NORTHWESTERN UNIVERSITY

Interfacial Engineering of

Energy Storage and Quantum Information Materials

A DISSERTATION

SUBMITTED TO THE GRADUATE SCHOOL
IN PARTIAL FULFILLMENT OF THE REQUIREMENTS

for the degree

DOCTOR OF PHILOSOPHY

Field of Materials Science and Engineering

By

Carlos G. Torres Castanedo

EVANSTON, ILLINOIS

June 2024

For my family.

ABSTRACT

Interfacial Engineering of Energy Storage and Quantum Information Materials

Carlos G. Torres Castanedo

This thesis centers on the interfacial engineering of materials as thin film systems with applications in lithium-ion batteries and superconducting qubits. The investigated materials include epitaxial lithium manganese oxide cathode subjected to different liquid electrolytes and an ionogel, epitaxial platinum thin films serving as current collector templates, and niobium hydrides generated through wet chemical etching.

First, lithium manganese oxide thin films were subjected to a conventional electrolyte, an ionic liquid electrolyte, and an ionogel. The ionic liquid effectively suppresses Mn dissolution, enhancing electrochemical and structural stability. In situ X-ray techniques monitor changes during operation. Ex situ techniques confirm the dissolution suppression and highlight the role of the irreversibility of overlithiated lithium manganese oxides. In the conventional electrolyte, Mn dissolution and overlithiated phases are exacerbated due to the nature of the electrolyte. The use of the ionogel prevents Mn dissolution but leads to the formation of the irreversible phase due to inadequate physical contact.

Second, platinum thin films were optimized to serve as current collectors. A two-step temperature process yields improved epitaxy while simultaneously maintaining ultra-smooth interfaces (<3 Å) and featuring high electrical conductivity (6.9×10^6 S/m). The platinum films were used as epitaxial templates for depositing and cycling lithium manganese oxide in an ionogel electrolyte.

Lastly, niobium hydrides were explored via fluorine-based etching processes, a standard step in fabricating superconducting devices. The rate of hydride formation depends on the fluoride solution acidity and the etch rate of the native oxide, which acts as a diffusion barrier for hydrogen. The resulting Nb hydrides detrimentally affect superconducting properties, increasing power-independent microwave loss in coplanar waveguide resonators. Notably, Nb hydrides show no correlation with two-level system loss or device aging mechanisms.

Results presented in this thesis offer significant insights into engineering strategies, unraveling the role of interfaces in different phenomena such as Mn^{2+} *dissolution, interfacial contact with gel electrolytes, growth optimization of platinum current collector, niobium hydride formation, and losses associated with niobium hydrides.*

ACKNOWLEDGMENTS

Looking back on my Ph.D., I reflect on the ups and downs, twists and turns experienced during these five and a half years. Like many of my graduate school peers, I went through “unprecedented” times during the COVID-19 pandemic. I learned to value the people around me and the importance of keeping healthy. I also needed to change my Ph.D. topic from Li-ion batteries to superconducting qubits during that time. Despite initial uncertainties, this change provided an excellent opportunity to broaden my research vision. The latter half of my Ph.D. was marked by personal milestones, including meeting my soulmate and welcoming two wonderful children into the world. Their presence was a constant source of motivation, propelling me toward the competition for this academic journey. Looking back, I feel fortunate to have navigated a spectrum of life experiences that contributed significantly to my growth and maturity.

Gratitude is owed to several individuals who played pivotal roles in my academic and personal journey. Professors Michael Bedzyk and Mark Hersam, my advisors, deserve special thanks for their guidance, support, and the direction they provided for my research. I appreciate Mike’s intellectual curiosity and daily support and Mark’s outstanding organization and focus on the research ideas. The co-advisory relationship with them proved to be an excellent choice.

I extend my appreciation to my committee members: Professor Vinayak Dravid, Professor Peter Voorhees, and Dr. Alexander Romanenko. They provided great feedback and were eager to join scientific discussions and collaborations. Vinayak was helpful in all the TEM aspects of the three projects presented in this thesis and was there to listen to me in times of worry.

Acknowledging the collaborative nature of my projects, I express gratitude to mentors and collaborators. From the Bedzyk group, I would like to thank Dr. Bruce Buchholz from the PLD facility, who supported me countless times. He was always there for me for extensive scientific discussion and helpful life advice. Dr. Guennadi Evmenenko was extremely valuable, especially at the beginning of my Ph.D. He taught me how to do X-ray measurements properly and the importance of being organized and investing enough time to analyze the data. He was a great office mate, and even though we had some difficult times, we always found time to learn from each other. From the Hersam group, I would like to thank Dr. Norman Luu, Dr. Kyu-Young Park, and Dr. Woo Jin Hyun, who helped me navigate Li-ion battery research. Their support was critical to unifying the X-ray studies to the Li-ion battery research in the group. Norman was always there to listen and help me build research ideas. Dr. Paul M. Das and Dr. Thang Pham supported the TEM research, a pillar for the three projects presented in this thesis. They were also friendly towards me and were open to talking and discussing life and work-related topics. Finally, Dr. Dominic Goronzy was a great companion in the qubit-related projects. His help was pivotal in covering many projects and focusing on the most relevant ones. I appreciate his leadership in the collaboration, which allowed me to focus more on exploring and implementing research ideas. I also value his friendship in these last years.

I thank other members of the Bedzyk, Hersam, and other labs whose scientific collaboration and friendship were constructive. I had the opportunity to collaborate with bright post-docs and students, including Guennadi Evmenenko, Achari Kondapalli, Yanna Chen, Beata Szydłowska, Vinod Sangwan, Dominic Goronzy, Thang Pham, Paul Das, Iqbal Bakti, Dimitry Lebedev, Woo-Jin Hyun, Kyu-Young Park, Selin Cetin, Anusheela Das, Elise Goldfine, Roger Reinersten, Joseph McCourt, David Garcia, William Mah, Norman Luu, Cory Thomas, Sonal Ragnekar, Anushka

Dasgupta, Stephanie Liu, Mike Park, Mitchell Walker, Celeo Diaz, Graham Pritchard, Kevin Ryan, Hadallia Bergeron, and Matthew Cheng. I especially thank Beata, Elise, Anushka, Norman, Roger, Sonal, Joey, Dominic, and Cory for being incredibly supportive. I greatly value your friendship and hope it lasts beyond grad school.

I want to acknowledge the funding sources vital for this research. First and more importantly, the Fulbright program supported my stay at Northwestern University for the first three years of the Ph.D. program. Different research funding helped me to continue my research through the years, which includes the Center for Electrochemical Energy Science and Energy Frontier Research Center (CEES-EFRC), the Materials Research Science and Engineering Center at Northwestern University (NU-MRSEC), and the Superconducting Quantum Materials and System Center (SQMS).

The contributions of Northwestern University staff and research centers were indispensable to my work, and I express my gratitude to all of them. At Northwestern University, I received immense help from Sumit Kewalramani and Jerry Carsello from the Cohen X-ray Diffraction Facility, Bruce Buchholz from PLD Core, Xinqi Chen from Keck-II, Tirzah Abbot from NUANCE, Rebeca Sponenburg from QBIC, Dieter Isheim from NUCAPT, and Michele McManmon from the MSE office. Also, scientists in the Advanced Photon Source and Argonne National Lab, including Denis Keane, Jenia Karapetrova, Mike Guise, Tim Fister, and Paul Fenter, were very supportive. Many thanks to scientists at Fermi National Lab, including Akshay Murthy, Jaeyel Lee, and Mustafa Bal, and at the National Institute of Standards and Technology, including Corey Rae McRae and Anthony McFadden. Finally, colleagues at Rigetti Computing, including Cameron Kopas, Jayss Marshall, Josh Mutus, and Ella Lachman.

To my roommate Norman – you were an outstanding friend, mentor, and collaborator. I will keep all our great memories as roommates, especially during the pandemic. The time we visited your family was very fulfilling and grounded me well. I appreciate your discussions about sports, Catan, science, and life.

To my friend Marco – even though you could not visit me in Chicago, I enjoyed the few times we could see each other during the breaks and the many times we talked on the phone.

To my parents – thank you for being my motor throughout all these years of studying. Thank you for always being there when I need someone to listen to and give me so much advice. Thank you for opening the door of your labs when I first became interested in science.

To my sister – thank you for being supportive and teaching me to be passionate and hard-working in what I like to do.

To my grandfather Valentin – thank you for all your invaluable lessons and care.

To Alex and Freddie – thank you for helping me discover my new facet as a father. I have enjoyed every second I have been with you and look forward to seeing you grow and discover the world. I commit to encouraging your curiosity about science.

Finally, to my partner Beata – thank you for being the most supportive partner I could have wished for. I am so glad that I can always have you by my side. Thank you for your scientific advice, too; it helped a lot to finish this Ph.D. Thank you for your guidance, patience, and love.

I look forward to our continued journey together.

LIST OF ABBREVIATIONS

3D	Three-dimensional
4D-STEM	Four-dimensional scanning transmission electron microscopy
AFM	Atomic force microscopy
BOE	Buffer Oxide Etch
CBED	Convergent beam electron diffraction
CPW	Coplanar waveguide
CV	Cyclic voltammetry
DI	Deionized
DMC	Dimethyl carbonate
DMD	Dissolution-migration-deposition
EC	Ethylene carbonate
EDS	Electron dispersive spectroscopy
EELS	Electron energy loss spectroscopy
EMIM-TFSI	1-ethyl-3-methylimidazolium bis(trifluoromethylsulfonyl)imide
FIB	Focused ion beam
FWHM	Full width at half maximum of the peak
GI-XRD	Grazing incidence X-ray diffraction
HAADF	High-angle annular dark-field
h-BN	Hexagonal boron nitride
HF	Hydrofluoric acid
HiPIMS	High-power impulse magnetron sputtering
ICP-MS	Inductively coupled plasma-mass spectrometry
IL	Ionic liquid
JJ	Josephson junction
LCO	Lithium cobalt oxide, $LiCoO_2$
LFP	Lithium iron phosphate, $LiFePO_4$
LIBs	Li-ion batteries
Li-IL/h-BN	Ionogel electrolyte based on h-BN matrix
$LiPF_6$	Lithium hexafluorophosphate

LMO	Lithium manganese oxide, $LiMn_2O_4$
L_z	Domain size
MBE	Molecular beam epitaxy
NH_4F	Ammonium fluoride
PI	Power-independent
QP	Quasi-particles
q	Scattering vector
RC	Rocking curve
RMS	Root mean square
RRR	Residual resistance ratio
SAED	Selected area electron diffraction
SEI	Solid electrolyte interphase
SRF	Superconducting radiofrequency
SRO	Strontium ruthenate, $SrRuO_3$
STO	Strontium titanate, $SrTiO_3$
T_c	Critical temperature
TEM	Transmission electron microscopy
TFSI	Bis(trifluoromethylsulfonyl)amide
TLS	Two-level system
TM	Transition metal
ToF-SIMS	Time-of-flight secondary-ion mass spectrometry
UHV	Ultra-high vacuum
XPS	X-ray photoelectron spectroscopy
XRD	X-ray diffraction
XRR	X-ray reflectivity
ZA	Zone axis

LIST OF FIGURES

LIST OF TABLES

TABLE OF CONTENTS

CHAPTER 1:

INTRODUCTION

1.1 Motivation and Thesis Statement

Well-understood interfaces are critical for the performance and functionality of materials within diverse scientific and technological domains. A single interface can often cause an intricate device with multiple materials to fail. This is observed in energy storage devices such as Li-ion batteries and quantum devices like superconducting qubits. Both are subject to extensive study and engineering efforts to improve their interfacial properties and enhance overall performance. These two areas are booming due to the increasing demand for energy storage and the promise of significant technological breakthroughs using quantum computing.

In Li-ion batteries, establishing a well-engineered and stable electrode/electrolyte interface is critical to the battery efficiency and lifetime. Additionally, a carefully designed electrode/current collector interface aids in achieving higher power rate capability. Given the intricate nature of these electrochemical systems, meticulous attention must be devoted to each interface to uphold the overall integrity of the battery. In this context, *in situ* experiments emerge as the preferred method for understanding the interfacial mechanisms that unfold during battery operation.

Similarly, interfaces play a critical role in superconducting qubits, hosting multiple loss mechanisms that can hinder the qubit's ability to persist long enough to perform a computation.

These losses may arise from various factors, including materials selection, fabrication processes, and environmental noise. Therefore, understanding and mitigating these interfacial losses is crucial for achieving high fidelity and scalability.

1.2 Thesis Organization and Roadmap

This thesis aims to comprehensively explore the interfacial and structural properties of various thin film systems, including epitaxial $LiMn_2O_4$ cathode material, epitaxial Pt current collector, and polycrystalline Nb superconducting material. The research delves into distinct aspects, with the first two materials employed in a LIB setup involving different liquid electrolytes and one gel electrolyte, while Nb undergoes exposure to diverse fluoride-based liquid etchings for application in Nb superconducting resonator devices. The thesis structure is organized into thematic chapters, where Chapters 3 through 5 are dedicated to LIB research, and Chapters 6 and 7 focus on superconducting qubits. Chapter 7 provides insights into ongoing work, while Chapter 8 shows the overall conclusions.

Chapter 2 provides a comprehensive overview of two synthesis and nine characterization techniques in the presented projects. Special attention is given to X-ray techniques, pivotal for the success of the projects.

Chapter 3 concentrates on LIBs, cathode materials, ionic liquid electrolytes, and current collectors. **Chapter 4** presents detailed studies on the interfacial and structural aspects of epitaxial $LiMn_2O_4$ when exposed to various electrolytes. The chapter explores Mn dissolution, electrolyte decomposition, formation of overlithiated $Li_2Mn_2O_4$, and physical contact through *in* situ and *ex* situ experiments. **Chapter 5** describes the growth optimization of Pt thin films for use as a current collector, employing various techniques to establish a suitable collector. The ultra-smooth film serves as an epitaxial template for depositing $LiMn_2O_4$ cathode, cycled in the ionogel electrolyte.

Chapter 6 transitions to superconducting qubits, examining loss mechanisms associated with materials selection and fabrication processes. Various sources of loss, such as substrates, tunnel junctions, metallic films, and surface treatments, are explored. **Chapter 7** investigates the impact of fluorine-based etching on film and resonator device properties, which is a common practice in superconducting qubits fabrication. The mechanism of Nb hydride formation and its connection to loss are established.

Chapter 8 spotlights ongoing projects related to interfacial engineering for superconducting qubits, focusing on interfaces like Nb/air and Nb/substrate to comprehend and mitigate loss mechanisms. **Chapter 9** concludes the thesis by summarizing key findings from the three main research projects.

CHAPTER 2:

METHODS

2.1 Pulsed Laser Deposition

Pulsed laser deposition (PLD) is a physical vapor deposition (PVD) method that utilizes a high-power pulsed laser focused on a target to induce an ablation process. This process occurs at sufficiently high energy densities (fluence), causing the laser to vaporize or ablate the material, creating a plume of particles, clusters, diatomic, atomic, and low-mass species.[1] The plume then reaches the substrate, forming a thin film. **Figure 2.1** illustrates a typical PLD system, often employing a UV excimer laser (KrF at 248 nm or ArF at 193 nm).

A PLD equipment includes a vacuum system and gas inlets (e.g., O_2, N_2, Ar), ensuring deposition in ultra-clean environments and enabling adjustments to film stoichiometry and different deposition rates. The sample holder's heating capability enhances crystallinity, while rotation aids in achieving uniform deposition. Various experimental parameters can be fine-tuned during thin film deposition optimization, such as substrate temperature, background gas and pressure, target-to-substrate distance, fluence, and repetition rate. Additionally, reflection high energy electron diffraction (RHEED) can be utilized to monitor the initial stages of thin film growth.

PLD offers numerous advantages over other thin film deposition techniques. First, its remarkable versatility allows the deposition of a wide range of materials, encompassing oxides, borides,

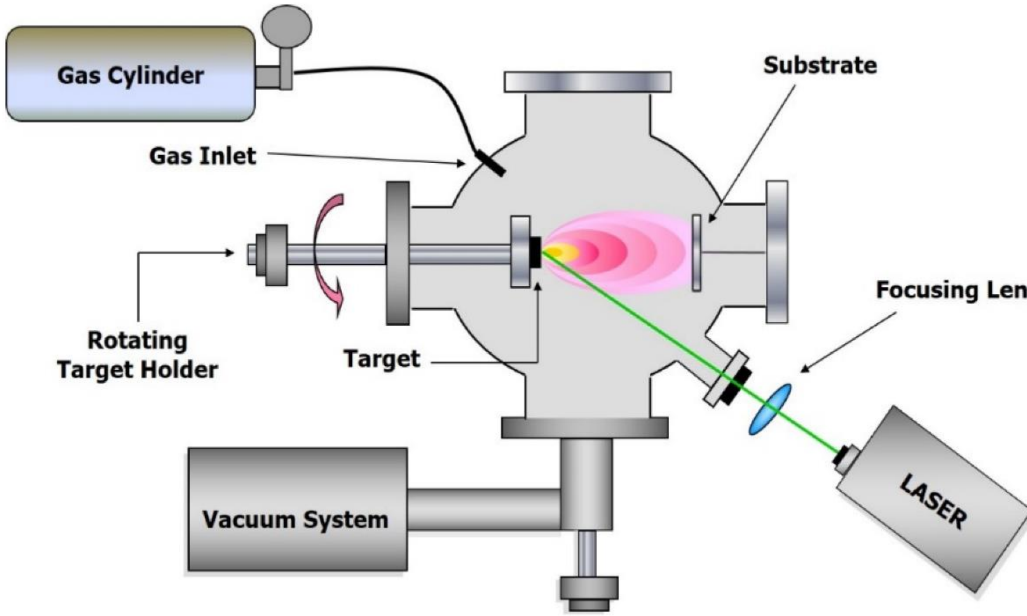

Figure 2.1. Schematic of a Pulsed Laser Deposition (PLD) system. Retrieved from Ref. [2]

carbides, metals, semiconductors, and complex compounds. Secondly, the deposited film closely mirrors the stoichiometry of a single target, which is particularly advantageous in the growth of complex oxides like perovskites. Lastly, PLD presents significant opportunities for synthesizing epitaxial heterostructures and superlattices.

Nevertheless, PLD has a few limitations associated, including relatively low deposition rates and challenges in large-area deposition. Overall, PLD is a versatile and impactful technique, valuable for thin film growth and the synthesis of complex materials. In this thesis, various thin films deposited by PLD at Northwestern University, including $LiMn_2O_4$, $SrRuO_3$ Pt, amorphous Nb_2O_5, TiN, and Au, are presented and discussed.

2.2 DC and High-Power Impulse Magnetron Sputtering

Sputtering is one of the most conventional PVD methods due to its ease of implementation and suitability for industrial-scale applications.[3] In direct current (DC) sputtering, a voltage ranging from 0 to 1000 V is applied across a rarified and inert gas, like Argon (Ar). When this gas breakdowns, it forms a glow discharge plasma. Subsequently, the positive ions generated from the plasma collide with the negatively charged electrode within the target. The transferred energy from these ions causes atoms/molecules to be ejected from the target surface, depositing them onto the substrate.

An integral component of the sputtering system is the magnetron source, which generates a magnetic field directing the electrons along elongated paths near or at the target's surface, increasing the likelihood of gas ionization. **Figure 2.2** demonstrates the principle of DC magnetron sputtering. The setup includes a vacuum system, magnetron, substrate holder, high-

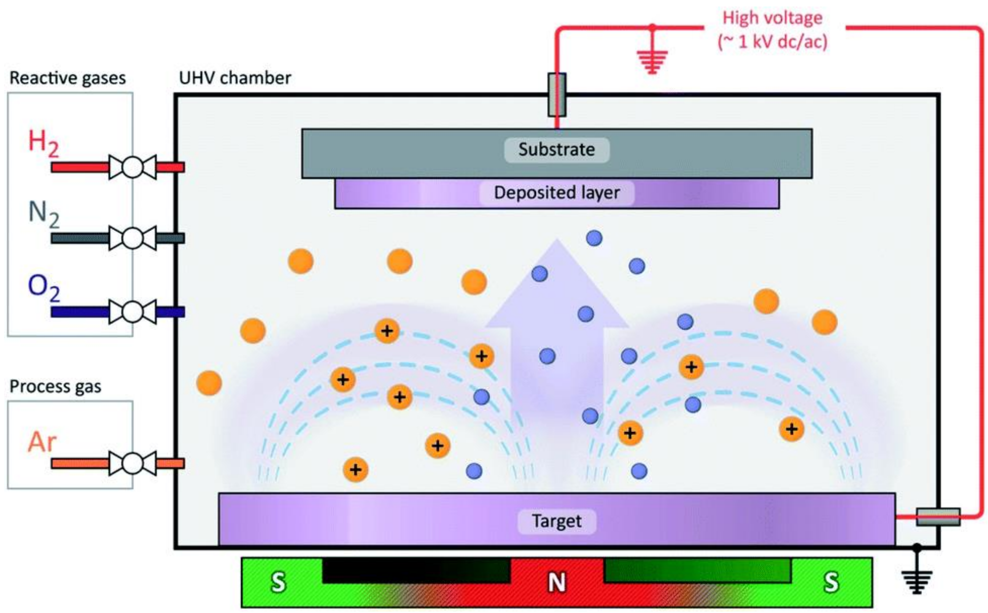

Figure 2.2. Schematic illustration of the principle of magnetron sputtering. Retrieved from Ref. [3]

voltage power supply, and working gases (Ar and reactive). Adjustments to parameters such as substrate temperature, reactive gas flow rate, sputtering power input, total gas pressure, substrate bias potential, and target-to-substrate distance enable the optimization of the thin film growth.

An alternative to DC sputtering involves the implementation of a pulsed high-voltage supply. High-power impulse magnetron sputtering (HiPIMS) employs a periodic voltage where the peak power significantly exceeds the time-averaged power compared to DC sputtering, usually by two orders of magnitude.[4] In HiPIMS, a higher proportion of the sputtered atoms become ionized, generating a highly ionized and energetic plasma. This distinctive plasma produces dense films with superior adhesion to those achieved with DC sputtering.[5] In this thesis, niobium (Nb) thin films were deposited by both methods at Northwestern University, NIST or Rigetti Computing. In addition, other materials, including tantalum (Ta) and titanium nitride (TiN), have been explored at Northwestern University.

2.3 X-ray Diffraction

X-ray diffraction (XRD) can examine numerous material properties, including crystalline phase, lattice parameters, degree of crystallinity, preferential orientation, epitaxy, grain size, residual stress, film composition, and density of dislocations.[6] Notably, XRD offers several advantages over other techniques. It is non-destructive, relatively fast, no sample preparation is needed, probes a large proportion of the area of the film, and *in situ* measurements are possible. However, it also has some drawbacks, such as poor spatial resolution and challenges to deconvolute multiple properties from XRD data.[6] Within this thesis, X-ray techniques, including different scan modes of XRD, are extensively used.

X-rays are a type of electromagnetic radiation with wavelengths (λ) in the order of Angstroms (Å), comparable to the interatomic distance in crystalline solids. These rays can be generated using different methods. For instance, conventional laboratories use a metal anode within a vacuum tube, and synchrotrons consist of circular storage rings covering over a kilometer in circumference, housing charged particles in motion.

When X-rays interact with an atom, they undergo scattering or absorption processes (as discussed in section 2.7). To understand the scattering effect, we can start with a free electron. The incident X-ray's electric field exerts a force on the electron, causing it to oscillate. This oscillation generates electromagnetic dipole radiation, with an intensity dependent on the incident polarization and the observer's location. The Thomson cross-section shows that the overall electromagnetic radiation for a free electron, without relativistic or quantum effects, remains constant (6.65×10^{-29} m^2), regardless of the incident light frequency.[7]

In the case of an atom, its electron cloud with charge distribution $\rho(\mathbf{r})$ will contribute to the total scattered radiation field. When the incident wave interacts with a volume element positioned at the origin and at a specific location $\mathbf{r}$ inside the atom (**Figure 2.3 A**), the wavevector $\mathbf{k}$ scatters from the atom to the direction specified by $\mathbf{k'}$. The wavevector transfer, or scattering vector, is represented by $\mathbf{Q}=\mathbf{k}-\mathbf{k'}$, and the scalar product of $Q \cdot r$ determines the phase difference. In an elastic event, where $|\mathbf{k}|= |\mathbf{k'}| =2\pi/\lambda$, the magnitude of Q is calculated as $2|\mathbf{k}| \sin\theta=(4\pi/\lambda) \sin\theta$, with θ representing the scattering angle.

Q and r exhibit a reciprocal relationship: the real space is represented by r, while the reciprocal space is by Q. The total scattering length of the atom includes $\rho(\mathbf{r})$ and the phase factor $e^{i\mathbf{Q}\cdot\mathbf{r}}$. Integrating these factors leads to the derivation of the atomic form factor, denoted as $f^0(\mathbf{Q})$,

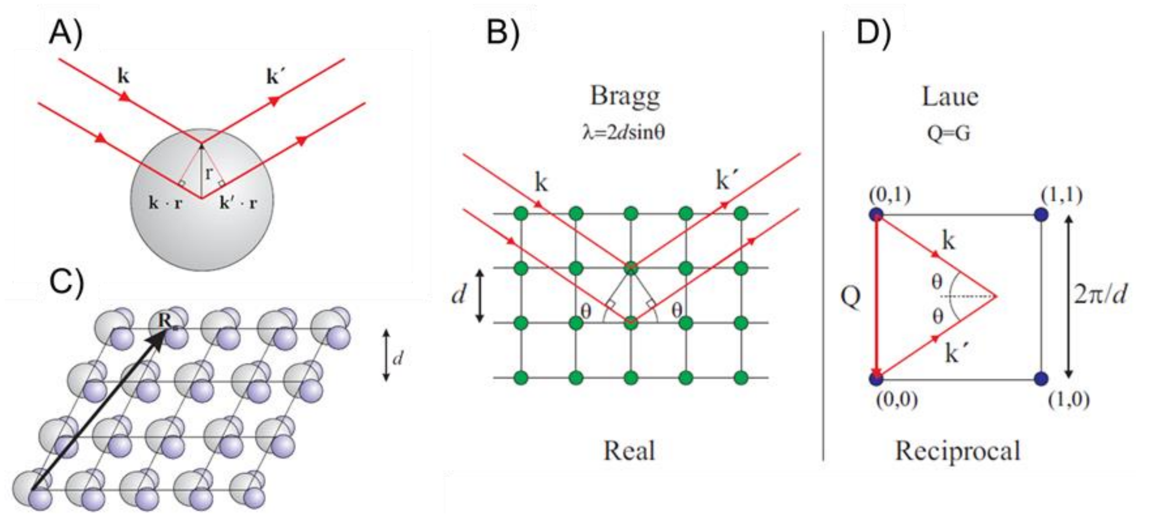

Figure 2.3. Principles of X-ray scattering. (A) Scattering from an atom and (C) a crystal. An X-ray with a wavevector k scatters from an atom to the specified direction by k′. The atoms/molecules are organized in a lattice with position vector Rn and a lattice plane spacing *d*. (B) Schematic illustrates Bragg's law in real space and its equivalence to the Laue condition in reciprocal space for a (D) 2D square lattice. Retrieved from Ref. [7]

describing the total scattering amplitude for an atom as a function of Q. For instance, when θ=0, $f^0(\mathbf{Q}=0)$ equals *Z* (atomic number) at its maximum and decreases as Q increases due to different volume elements scattering out of phase. The scattering factor also includes a dispersion correction ($f'(\hbar\omega)+if''(\hbar\omega)$) to account primarily when X-rays energy closely align with the energies of the scattered elements.

When X-rays interact with a crystal with a periodic arrangement of atoms, Bragg's law describes the condition for constructive interference:

$$n\lambda = 2d sin\theta \qquad \textbf{Eq. 2.1}$$

The diffraction of X-rays is visualized in **Figure 2.3 B** for an incident X-ray beam of wavelength λ at an angle θ onto a series of atomic planes of spacing d. n is an integer is referred to as the order of the diffraction maxima. Constructive interference occurs solely at specific Bragg angles (θ_B) corresponding to distinct interplanar spacings (d_{hkl}), where *hkl* denotes the Miller indices of the crystallographic plane.

While Bragg's law specifies the condition for constructive interference, calculating the scattering intensity requires the specification of atomic positions withing the lattice. The lattice vectors ($\mathbf{R_n}$) (**Figure 2.3 C**) and the position $\mathbf{r_j}$ of other atoms at any lattice sites are used to determine the position of any atom in the crystal for $\mathbf{R_n} + \mathbf{r_j}$. The scattering amplitude is given by:

$$F^{crystal}(\boldsymbol{Q}) = \sum_j f_j(\boldsymbol{Q}) e^{i\boldsymbol{Q}\cdot\boldsymbol{r}_j} \sum_n e^{i\boldsymbol{Q}\cdot\boldsymbol{R}_n} \qquad \textbf{Eq. 2.2}$$

The first term exclusively relates to the unit cell, while the second accounts for the sum over lattice sites. If $\mathbf{Q}\cdot\mathbf{R_n}=2\pi \times$ integer, the second term simplifies to the number of unit cells N. To obtain a unique solution, $\mathbf{R_n}=n_1\mathbf{a_1}+n_2\mathbf{a_2}+n_3\mathbf{a_3}$, where $\mathbf{a_i}$ denotes the basis vector, and n_i are integers, requires the introduction of the concept of a reciprocal lattice. For the reciprocal lattice vector, $\mathbf{G=ha_1^*+ka_2^*+la_3^*}$, to satisfy $\mathbf{G\cdot R_n}=2\pi \times$ integer, Q=G. This expression, the Laue condition, signifies that $F_{crystal}(\mathbf{Q})$ is non-zero only when $\mathbf{Q}$ coincides with the reciprocal lattice vector.[7] This condition aligns with Bragg's law and is illustrated in **Figure 2.3 D** for a 2D square lattice.

X-ray instruments generally contain five major components: X-ray source, detector, incident optics, receiving optics, and goniometer (**Figure 2.4 A**).[6] The X-ray source involves a heated tungsten cathode that creates electrons that further bombard the Cu anode (**Figure 2.4 B**). The

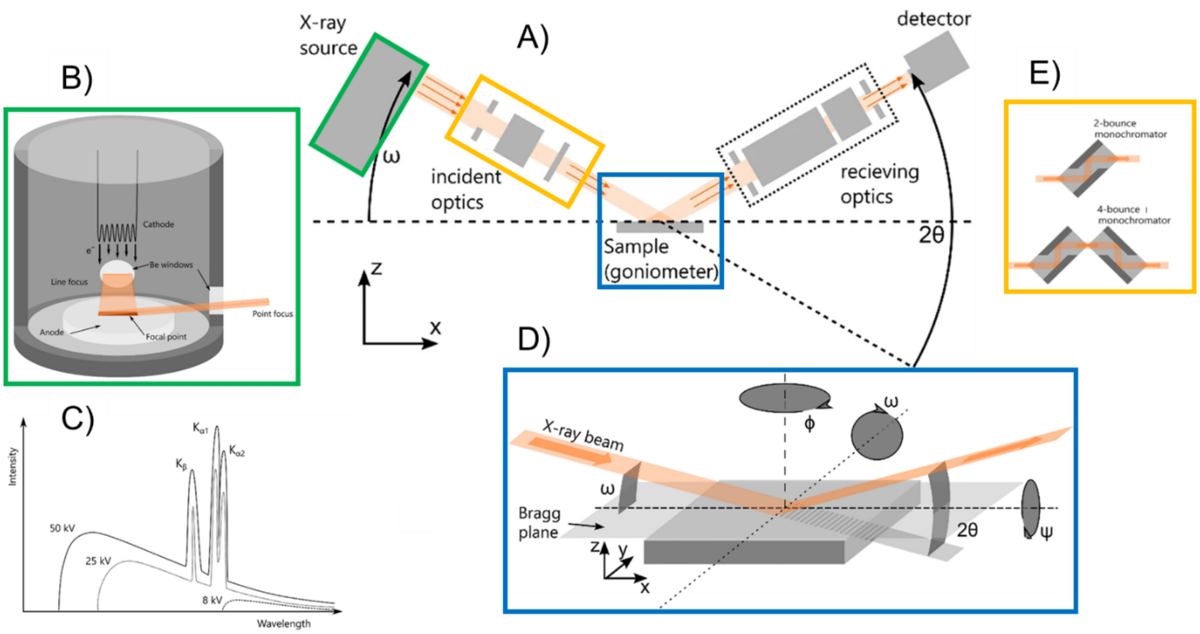

Figure 2.4. Overview of the components of a diffractometer. Schematics of: (B) Diffractometer, (C) X-ray tube and its (C) emission profile, (D) notation for the angles and degrees of freedom in a diffractometer, and. (E) 2-bounce and 4-bounce channel-cut crystal monochromators. Retrieved from Ref.[6]

ionization process produces an X-ray spectrum (**Figure 2.4 C**) consisting of a continuous part due to electron energy loss collisions (*Bremsstrahlung*) and discrete fluorescent lines (K_α and K_β) when electron vacancies in the K shell are filled by electrons from the L (2p) and M (3p) shells, respectively, of the Cu atom.

The detector converts X-rays to electronic signals and is often categorized as 0D, 1D, or 2D based on its detection dimensionality. Some detectors can discriminate a narrow energy window to reduce fluorescence.[8] The attenuator is crucial to avoid damaging the detector and non-linear response.

The goniometer (**Figure 2.4 D**) determines angles among the source, detector, and sample surface. A basic goniometer allows variation in the angle between the incident beam and the sample θ and between the incident beam and the detector 2θ. These two angles are coupled for powder diffraction but decoupled for thin films. In such a case, the incident angle is denoted ω. Additional degrees of freedom include φ (rotation or azimuthal angle) and ψ (tilting angle), granting access to in-plane and off-specular information, aiding in pole figure and epitaxy determination. A four-circle goniometer, offering four degrees of freedom, serves this purpose, while a five-circle goniometer, featuring an additional degree $2\theta\chi$ (in-plane 2θ angle), provides enhanced capabilities, like the Smartlab Gen 2 9kW equipment in the X-ray facility at Northwestern University.

The choice of incident and receiving optics in diffractometers primarily involves two modes: Bragg-Brentano and Parallel Beam. Bragg-Brentano, typical in powder diffraction, uses a divergent X-ray beam focused back to a single point in the receiving slit, but slight sample height *h* misalignments can shift the measured peaks. Parallel Beam mode is recommended for thin films, utilizing a parabolic mirror after the source to convert divergent X-rays into a parallel beam, reducing systematic errors. Despite losing intensity from the beam, the parallel nature of the X-rays guarantees the beam will reach the sample with the same incident angle. The parabolic mirrors can also reduce the K_β component and the *Bremsstrahlung* emission as they are designed to have limited efficiency in reflectivity wavelengths not close to Kα.[6] However, $K\alpha_1$ and $K\alpha_2$ are too close to discriminate. For higher-resolution XRD, monochromators remove $K\alpha_2$ and improve the $K\alpha_1$ resolution. Channel-cut crystal monochromators (**Figure 2.4 E**) commonly achieve a highly monochromatic beam. In these crystals, the X-rays diffract at least twice as they pass through the monochromator.

Various XRD scans elucidate the properties of thin films. For instance, $2\theta/\omega$ scans help determine thin film crystallography. In this type of scan, the Bragg plane is aligned to the crystallographic

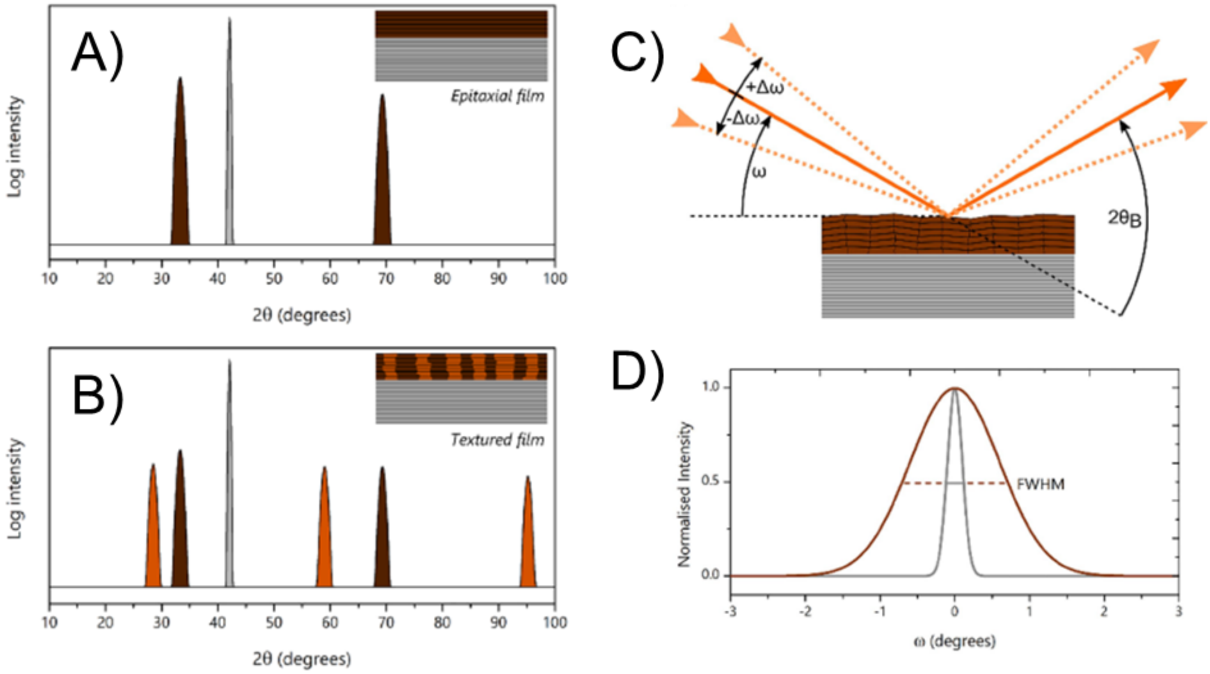

Figure 2.5. 2*θ*/*ω* and *ω* measurements in XRD. 2*θ*/*ω* patterns for (A) an epitaxial film and (B) a textured film. The insets show schematics of the microstructure. (C) Schematic of a rocking curve measurement and (D) example of the resultant curves for a film on a single-crystal substrate. Retrieved from Ref [6]

axis of the substrate and a symmetric scan is performed where ω is kept to half of 2θ. A single orientation is expected for epitaxial films with a single set of peaks in the pattern (**Figure 2.5 A**). In contrast, textured films enhance the relative intensity of some Bragg reflections and a reduction of others (**Figure 2.5 B**), compared to a powder diffraction pattern. Texture in films comes from various sources such as epitaxy, surface energy minimization during deposition, or the composition of different grains with different orientations.[6] A critical parameter to quantify the crystallinity of the films is the grain size. The higher quality film will have a bigger grain size. The crystallite or vertical domain size in epitaxial films (L_z) corresponds to the coherent volume in the material related to the diffraction peak. It can be calculated by the Scherrer's equation[9]:

$$L_z = \frac{k_s \lambda}{(cos\theta)\beta} = \frac{2\pi\ k_s}{\Delta q} \qquad \textbf{Eq. 2.3}$$

Where k_s is a shape factor (0.94), β the full width at half maximum of the peak (FWHM) of the Bragg peak in radians, and Δq the FWHM of the Bragg peak in q values ($Å^{-1}$). The calculation can include instrumental resolution via quadrature $\sqrt{\left(\Delta q_{film}^2 - \Delta q_{inst}^2\right)}$ in the denominator.

To comprehensively explain a film's epitaxy or texture, in-plane complement out-of-plane data. For instance, a thin film exhibiting texture exclusively in the out-of-plane orientation without any azimuthal dependence is classified as a fiber-textured polycrystalline film.[10] Another observed scenario in $2\theta/\omega$ scans is randomly oriented polycrystalline films lacking preferential orientation, aligning with the powder diffraction pattern of the material. Additionally, amorphous films manifest broad, low-intensity peaks (if present) in these scans, indicating their non-crystalline nature.

Another important XRD scan is the rocking curve (RC, ω scan), where the Bragg peak angle ($2\theta_B$) remains fixed at the centroid position from the $2\theta/\omega$ scan, and a sample tilting in the ω axis occurs (**Figure 2.5 C**). This scan measures peak sharpness (full-width half-maximum, FHWM), reflecting film quality. For instance, epitaxial films exhibit smaller FHWMs (few tenths of degrees) than textured (dew degrees) or randomly oriented (several degrees) films due to fewer disruptions in the lattice planes. **Figure 2.5 D** illustrates the FWHM difference between a single-crystal substrate (gray) and a thin film (brown). The width will depend on the spread of grains and the density of dislocations, disrupting the lattice planes' parallel nature. In this thesis, several rocking curve measurements were used to assess the quality of the deposited thin films.

2.4 X-ray Reflectivity

X-rays, a form of electromagnetic waves, exhibit refraction when encountering an interface between different media, each characterized by an index of refraction n. This phenomenon entails splitting the original X-ray wave into a transmitted (refracted) wave, which travels into the second medium, and a reflected wave, which propagates back into the first medium. Notably, in the high-frequency dispersion limit typical for X-rays, n is found to be slightly less than 1. Consequently, this leads to intriguing effects like a total external reflection at angles α below a critical angle α_c.[7]

Expressed as $n = 1 - \delta + i\beta$, the index of refraction is defined by δ and β. Here ,δ is remarkably small, approximately on the order of 10^{-6}, and can be computed as $2\pi\rho r_0/k^2$, where ρ represents the electron density of the material, k the wavevector ($2\pi/\lambda$), and r_0 the electron radius ($2.82\text{x}10^{-5}$Å). Meanwhile, β is associated with absorption processes within the medium leading to the attenuation of the X-ray intensity, and it is equal to $\mu/2k$, where μ and is the absorption coefficient. By disregarding the absorption factor and applying Snell's law at low angles, α_c can be approximated as $\sqrt{2\delta}$. Typically falling within the milli-radians range (0.2-0.5°), α_c holds a proportionality to the electron density of the material.[11]

The Fresnel equations, derived from boundary conditions at the interfaces, serve as a valuable tool to compute the intensity of ratios of incident X-ray waves with transmitted and reflected waves of two different media (**Figure 2.6 A**). The fraction of specularly reflected intensity denoted as $R(\alpha)$, is given by $I(\alpha)/I_0$, where I_0 represents the initial intensity of the incident X-rays. In the context of the momentum transfer along the z coordinate ($q_z = k_r - k_i = \frac{4\pi}{\lambda}\sin\alpha$), where k_r and k_i denote the wavevectors of the reflected and incident X-rays, respectively, the specularly reflected

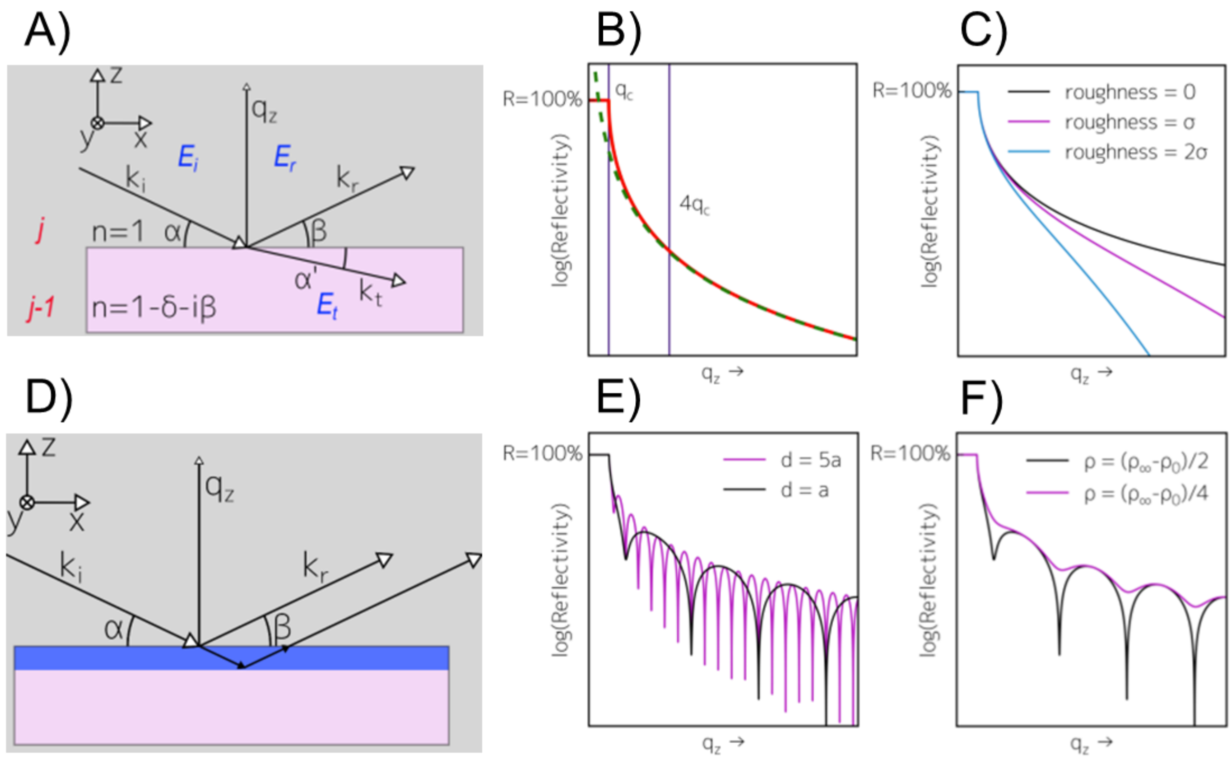

Figure 2.6. Principles of X-ray reflectivity. Refraction for X-rays above the critical angle between two media (A) and a thin film on a substrate (D). Effect of different parameters on the XRR data: B) Large *q* values, (C) roughness, (E) thickness, and (F) electron density contrast. Retrieved from Ref. [12]

intensity for the *j*-1 medium at an ideal interfaced, termed the Fresnel reflectivity (R_F), is determined is given by:

$$R(q_z) = |r_{j,j-1}|^2 = \left|\frac{k_{j,z} - k_{j-1,z}}{k_{j,z} + k_{j-1,z}}\right|^2 = \left|\frac{q_z - \sqrt{q_z^2 - q_c^2}}{q_z + \sqrt{q_z^2 - q_c^2}}\right|^2 = R_F \qquad \textbf{Eq. 2.4}$$

where q_c is the momentum transfer at α_c . For $q_z > 4q_c$, $R(q_z) \approx \frac{q_c^4}{q_z^4}$, resulting in a rapid decline in reflected intensity as q_z increases, a phenomenon depicted in **Figure 2.6 B**. When introducing surface roughness (σ), a Debye-Waller-like factor can be incorporated into the reflectivity equation as $R(q_z) = R_F e^{-q_z^2\sigma^2}$. This factor dampens the reflectivity, elucidated in **Figure 2.6 C**.

For scenarios involving a thin film on a substrate comprising three distinct media (**Figure 2.6 D**), X-rays reflected from different interfaces exhibit constructive and destructive interference based on the incident angle, forming Kiessig fringes. The spacing between the maxima, denoted as $\Delta q = 2\pi n_1/t$, is contingent upon the film's thickness (t). **Figure 2.6 E** illustrates the reduction in fringe maxima as the film's thickness increases.

Parrat's formalism provides a pathway to calculate reflection and transmission coefficients quantitatively.[13] Particularly for N=2 number of layers:

$$R(q_z) = \frac{r_{1,0}^2 + r_{2,1}^2 + 2r_{1,0}r_{2,1}\boldsymbol{cos2k_{z1}t}}{1 + r_{1,0}^2 r_{2,1}^2 + 2r_{1,0}r_{2,1}\boldsymbol{cos2k_{z1}t}} \qquad \textbf{Eq. 2.5}$$

Where $r_{j,j-1}$ is given in **Equation 2.4** for the air-film interface (1,0) and the film-substrate interface (2,1). This expression accounts for various factors, such as the oscillatory behavior determined by terms associated with electron density contrast, represented by the bolded terms.[13] **Figure 2.6 F** illustrates the impact of electron density contrast on fringe visibility; a higher contrast between the film and substrate results in more distinct fringes.

Parrat's formalism, employed through recursion schemes incorporating surface roughness at different interfaces, is often utilized in multiple XRR-fitting programs, such as Motofit.[14] Alternatively, an approach involving a density profile $f(z)$ at the interface can be employed to determine the reflectivity for a graded interface, following the equation:

$$\frac{R(q_z)}{R_F(q_z)} = \left| \int_{\infty}^{\infty} \left(\frac{df}{dz}\right) e^{iq_z z} dz \right|^2 Eq. 2 \qquad \textbf{Eq. 2.6}$$

This equation, known as the master formula, offers an analytical expression for the density profile at the interface, often resembling an error function whose derivative takes the form of a Gaussian. **Figure 2.7 A** demonstrates the electron density profile, its derivative as a Gaussian function, and the solution to Eq.2, with the dotted line indicating an ideal interface and the continuous line representing the graded interface. This formalism provides a closed-form equation, and it is relatively good for higher angles than α_c.[15]

X-ray reflectivity (XRR) is a valuable tool for swiftly analyzing various sample types. **Figure 2.7 B** showcases how XRR enables the determination of thin films' density, thickness, and roughness. Notably, XRR does not necessitate crystalline material but somewhat lateral homogeneity and relatively smooth interfaces. It can provide crucial insights into buried interfaces and interdiffusion non-destructively.[16] Moreover, with high resolution, XRR can measure thicknesses up to several

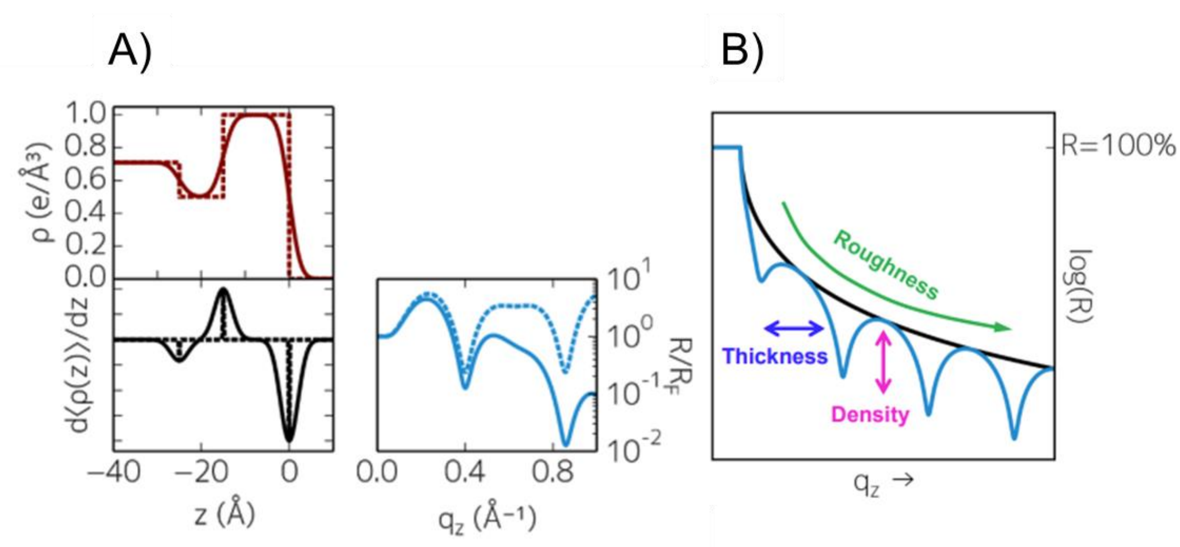

Figure 2.7. Reflectivity master equation and summary of obtained parameters. (A) Evaluation of the reflectivity master formula illustrating the electron density profile, its derivative, and the evaluation of the equation for an ideal and non-ideal interface. (B) Summary of obtained parameters in an XRR-fitting. Retrieved from Ref. [12]

hundred nanometers.[11] In this thesis, XRR extensively contributes to assessing interfacial quality, buried interfaces, and determining the thickness of numerous thin films.

2.5 Cyclic Voltammetry

Cyclic voltammetry (CV) is one of the most popular electrochemical techniques to explore reactions involving electron transfers, such as oxidation and reduction of a metal complex. This method involves varying the potential of an electrode in a solution while simultaneously tracking the resulting current. Throughout this process, the working electrode's potential is referenced against a specific electrode, such as Li^+/Li, in the context of LIBs.

Figure 2.8 visually explores the intriguing "duck" shape observed in cyclic voltammograms. It demonstrates concentration profiles (**A-G**) in relation to the distance from the electrode to the

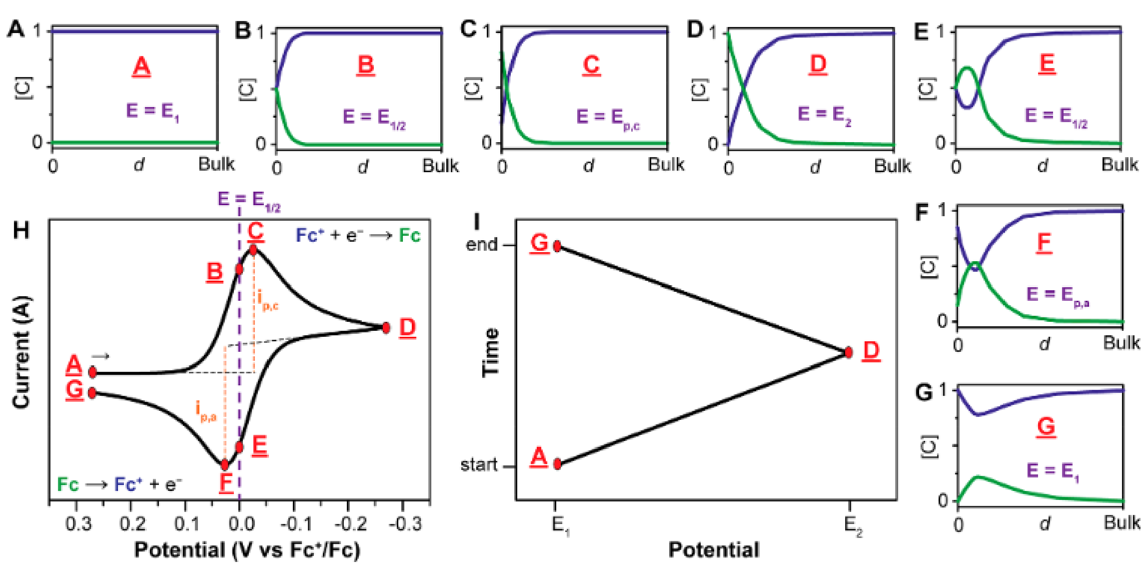

Figure 2.8. Principles of cyclic voltammetry. (A-G) Concentration profiles for Fc^+ (blue) and Fc (green) as a function of the distance from the electrode to the solution for different instances during the voltammogram (H). Applied potential as a function of time for such experiment (I). Retrieved from Ref.[17]

electrolyte during various phases of the voltammogram (**H**). Additionally, (**I**) depicts the applied potential versus time. During the CV, the concentration of the species near the electrode undergoes dynamical changes, following the Nernst equation.[18] The profiles (**A-G**) represent the ion (Fc^+ in blue) and the neutral compound (Fc in green). During the negative potential scan (**C-D**), Fc^+ is reduced locally at the electrode, resulting in a measurable current (e^-). The intricate interplay of species within the electrode during the reduction and oxidation process gives rise to the distinct "duck" shaped voltammogram.

It is essential to mention that **Figure 2.8** follows the US convention, where reduction appears at the top of the voltammogram towards lower potentials. Conversely, in LIBs, the IUPAC convention is followed, with oxidation observed at the top of the voltammogram towards higher potentials. The IUPAC convention was used in the CV experiments presented in this thesis, and the voltammograms were referenced vs Li^+/Li, the reference electrode.

2.6 In-situ Synchrotron X-ray and Electrochemical Setup

An *in situ* X-ray-compatible cell, designed by Dr. Timothy Fister from Argonne National Lab, was used to study the interfacial and structural evolution withing a LIB thin film setup. The cell, depicted in **Figure 2.9 A**, operates on the principle of transmission geometry", allowing X-rays to pass through the circular opening during the experiments. **Figure 2.9 B** displays the various components of the transmission cell. The cell is meticulously sealed inside an Ar glovebox using specific components, including an alumina-coated 75 μm Kapton window (**#1**), which is X-ray transparent, a Teflon flange (**#2**), and a Kel-f window clamp (**#3**), to ensure the integrity of the LIB materials such as the Li metal and the electrolyte.

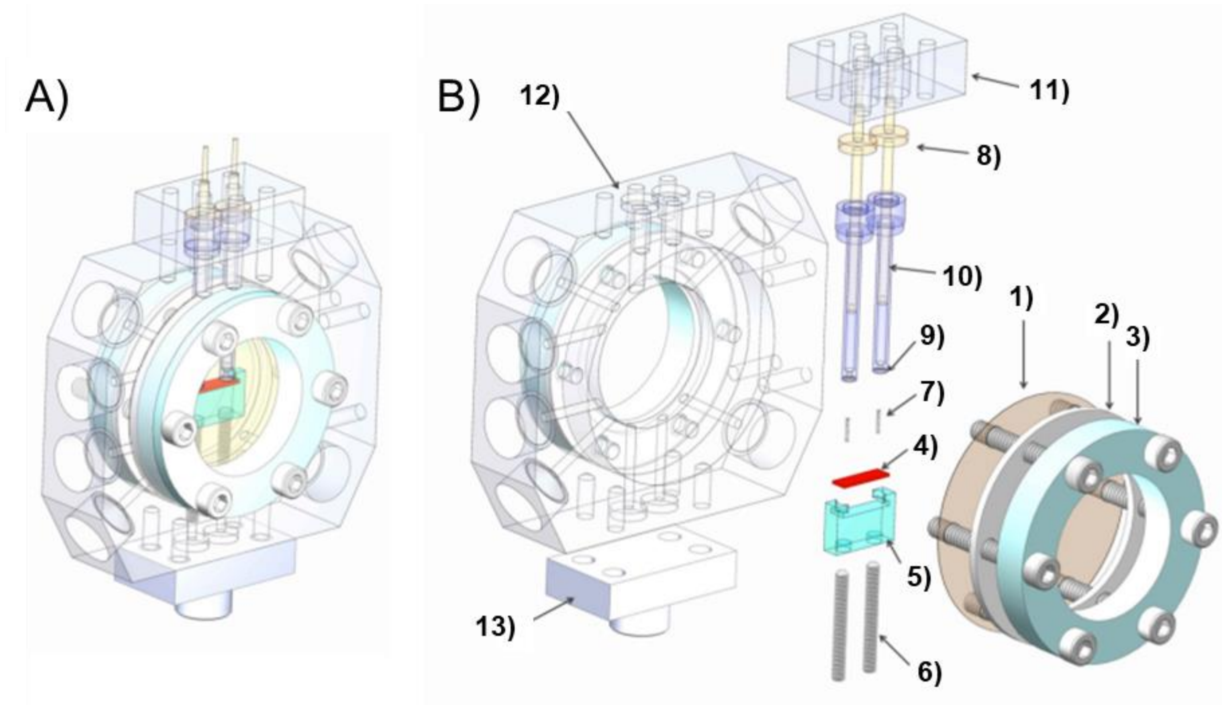

Figure 2.9. Transmission cell used for the *in situ* X-ray experiments. (A) Cell fully assembled and (B) with all the components labeled 1-13. Retrieved from Ref.[19]

The sample to analyze comprises a cathode thin film ($LiMn_2O_4$) deposited on a conductive electrode (*i.e.*, $SrRuO_3$ or Pt) atop a substrate ($SrTiO_3$ or Al_2O_3) (**#4**). The height position of the sample holder (**#5**) can be adjusted using two stainless steel (SS) screws (**#6**). The contact with the sample is established through two SS compression springs (Lee, CIM010ZA) (**#7**) and two working SS electrode plungers (**#8**). To prevent electrode contact with the liquid electrolyte inside the cell chamber (visible in yellow in **Figure 2.9 A**), two 20-30 kfm O-rings (PSI) (**#9**), two Kel-F plunger shells (**#10**), and one Kel-F working electrode clamp (#11) are employed. Finally, the cell assembly includes the Kel-F cell body (**#12**) attached to an Al goniometer adaptor (**#13**).

A CHI 760E potentiostat is connected to the thin film and the Li metal through inlets shown in **Figure 2.9 A**. CV is conducted at a sweep rate from 0.2 to 0.5 mV/s within the 3.5-4.3 or 2.5-4.3

V range *vs.* Li^+/Li. The setup utilizes a synchrotron X-ray beam and a Pilatus 2 D X-ray detector. The motivation behind employing synchrotron X-rays over lab-based X-rays is their extremely bright nature and flexibility in modifying the source wavelength. Synchrotrons like the Advanced Photon Source offer more than 10 orders of magnitude higher brilliance than a Cu X-ray rotating anode in a lab, allowing for the rapid collection of high-quality *in situ* data.[20]

Moreover, using 20 keV energy in the synchrotron results in fewer X-rays being absorbed by the electrolyte compared to the 8.04 KeV from the Cu anode. For instance, the electrolytes used in this thesis displayed only 1-4% of transmission at 8.04 keV, while 77-83% at 20 keV over a 3 mm path, the lower limit for the ionogel electrolyte. However, a lower transmission will be achieved for ionic liquids and carbonate electrolytes as the X-rays pass through the cell chamber (16 mm). For instance, compounds like Lithium hexafluorophosphate ($LiPF_6$), lithium perchlorate ($LiClO_4$), or h-BN exhibit approximately 20 times more absorption at 8.04 keV compared to 20 keV, highlighting the significant absorption disparity.[21]

2.7 X-ray Photoelectron Spectroscopy

When X-rays interact with an atom, they exhibit two primary outcomes: scattering, as detailed in section 2.3, or absorption, where an electron is expelled (photoelectron). (**Figure 2.10 A**). This process is termed photoelectric absorption. The absorption cross-section of a material is inversely dependent upon the photon energy ($\sim 1/E^3$) and proportional to the atomic number Z ($\sim Z^4$).[7]

During the photoelectric absorption, an electron ejected from an inner atomic shell (K) creates a void, leading to intriguing phenomena. For instance, when an electron from the outer shell (L) fills

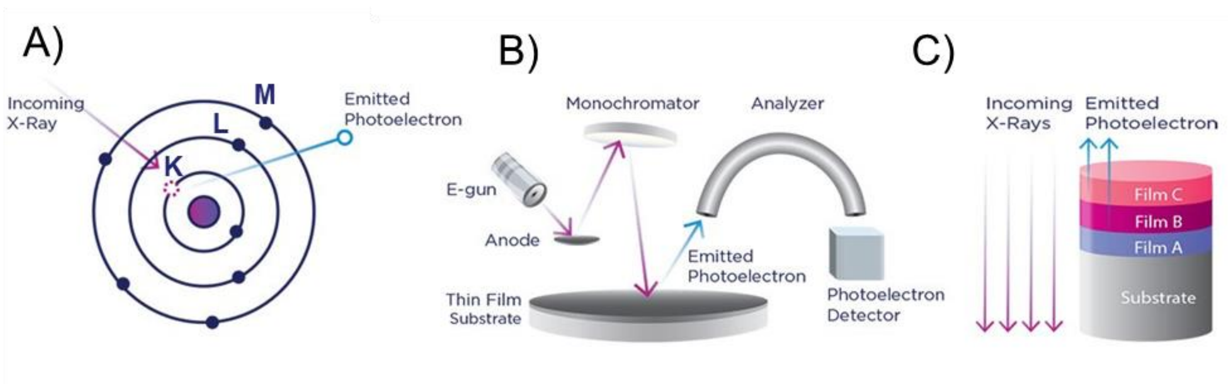

Figure 2.10. Principles of X-ray photoelectron spectroscopy. (A) Photoelectric effect, (B) instrument instrumentation, and (C) measurement. Retrieved from Ref.[22]

this vacancy in the K shell, it emits radiation, termed fluorescence, possessing an energy equivalent to the difference between the binding energies of the K and L electrons. Alternatively, the emitted photon can expel another electron from an outer shell M, an Auger electron.

The photoelectric effect can be capitalized with a spectrometer to discriminate the photoelectrons' kinetic energy (KE). Also, a monochromatic source with relatively low energy (hv), for instance, Al Kα=1487 eV or Mg Kα=1254 eV, is used, which sets the upper bound to KE. The binding energy (BE) of the electron, which inherently carries chemical information, is determined by the following equation:

$$BE = hv - KE - \Phi_{spec} \qquad \textbf{Eq. 2.7}$$

where Φ_{spec} is the spectrometer work function, which is a correction factor for the instrument. KE can be determined using the analyzer, and the BE can be determined.

Figure 2.10 B displays the instrumentation of an X-ray photoelectron spectrometer. This setup requires ultra-high vacuum (UHV) to prevent photoelectron scattering off air molecules and reduce surface contamination.[23] X-rays are generated by electron bombardment on an anode and then monochromated to eliminate excitation by additional X-ray lines and to increase the spectral resolution needed for chemical state differentiation. For instance, using a monochromator with an Al source decreases the linewidth from 0.9 eV to 0.25 eV.[24] Finally, the photoelectrons from the sample travel in electrostatic fields within a hemispherical analyzer, allowing only electrons of a given energy to arrive at the photoelectron detector.

X-ray photoelectron spectroscopy (XPS) is a surface-sensitive quantitative analysis technique as the photoelectrons are typically emitted from a few nm (**Figure 2.10 C**). XPS is highly effective in identifying the chemical environment of atoms, where the oxidation state or nearest neighbors of an element affect the binding energies of the photoelectron peak. Another advantage of XPS is that X-rays are less prone to damage the samples when compared to electron-based techniques like Auger electron spectroscopy.[25]

2.8 Time-of-flight Secondary Ion-Mass Spectroscopy

Secondary ion mass spectrometry (SIMS) is a powerful analytical technique that bombards a sample's surface with high-energy ions like Ar^+, Ga^+, Bi^+, or Cs^+. This bombardment triggers the emission of ionized particles, which are subsequently analyzed in a spectrometer. Although most ejected species are neutral, a spectrometer can detect and analyze the secondary ions. **Figure 2.11** illustrates the SIMS process. This technique is the most sensitive of all commonly used surface analytical tools. For instance, it can detect atomic dopant concentrations in silicon ranging from 0.2% to as low as $2x10^{-6}$ %.[26] However, this exceptional sensitivity comes with a downside, resulting in complex spectra due to detecting numerous masses of ions and ion fragments.

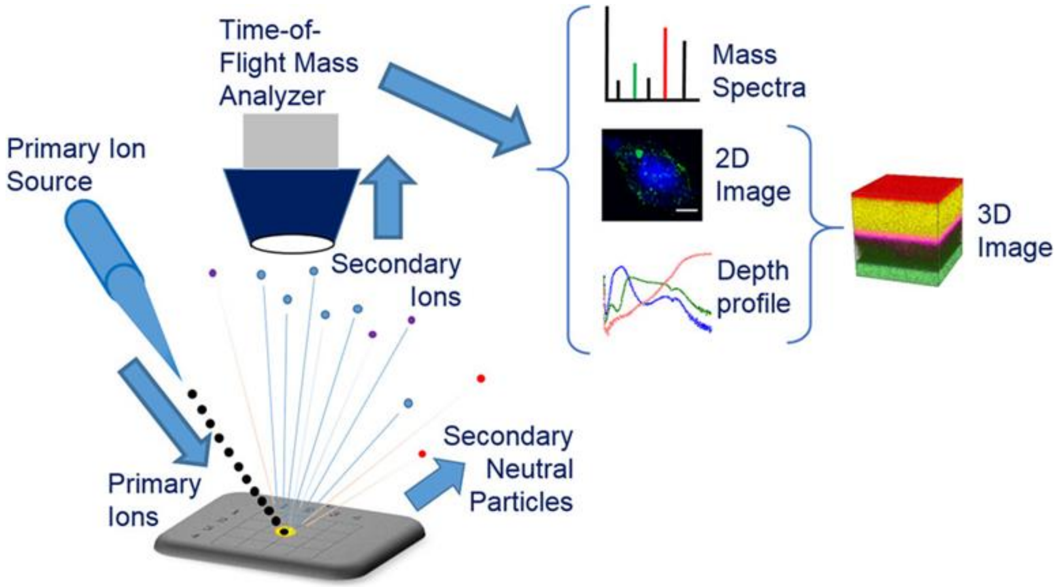

Figure 2.11 Principles and applications of secondary ion mass spectrometry. Retrieved from Ref.[27]

The instrumentation comprises a focused primary ion beam, initiating collisions that lead to neutral atoms/molecules, secondary ions, and electron emission. Subsequently, a time-of-flight (ToF) mass analyzer measures the time taken by each ion, accelerated by a pulsed voltage, to reach the detector in the scale of nanoseconds. For enhanced mass resolution ($m/\Delta m$), an ion reflector is sometimes employed instead of a linear analyzer. UHV is essential to increase the mean free path of the liberated ions.

SIMS can be operated in static or dynamic mode. In the static mode, an extremely low dose of primary pulsed ions ($<10^{13}$ ions/cm^2) minimizes surface damage ("a tickle"), affecting less than 1% of the top surface.[28] Conversely, dynamic mode employs a continuous higher-energy primary ion beam for rapid sputtering rates and improved counting statistics. Beyond its high sensitivity, SIMS offers superior spatial resolution (50-60 nm).[29] Crucially, it possesses a high dynamical rate, facilitating fast data acquisition for depth profiling of various ions and 2D/3D imaging.[27] However, SIMS does have some drawbacks. Its complexity lies in quantifying the obtained spectra due to matrix effects and the mixing and redistribution of elements caused by ion sputtering.[30] Proper reference samples are needed for accurate quantification. Additionally, its destructive nature potentially alters the sample surface during analysis.

2.9 Inductively Coupled Plasma-Mass Spectroscopy

Inductively coupled plasma-mass spectrometry (ICP-MS) is a versatile technique employed across diverse fields to precisely measure trace elements within samples. Its remarkable capability is detecting elements at very low concentrations, often down to part per trillion, while maintaining high spectral resolutions. The process begins with an ICP, where atoms within the sample undergo ionization in a high-temperature Ar plasma, reaching temperatures as high as 10,000°C.

The ionization sequence follows several stages. Initially, the aerosol sample undergoes desolvation, transforming into small solid particles. Then, these particles transverse the plasma, transitioning from a gaseous to a ground-state atomic form. Finally, ionization occurs primarily through collisions with energetic Ar electrons, converting the atoms into positively charged ions.[28] The resulting ions move toward the mass spectrometer, where they are sorted based on their mass-to-charge ratio. To ensure precision in quantification, commercially available certified multielement standards are indispensable.[31]

2.10 Atomic Force Microscopy

Atomic force microscopy (AFM) is a high-resolution imaging technique that uses a sharp tip that systematically scans across a sample. This process relies on the interplay of forces between the

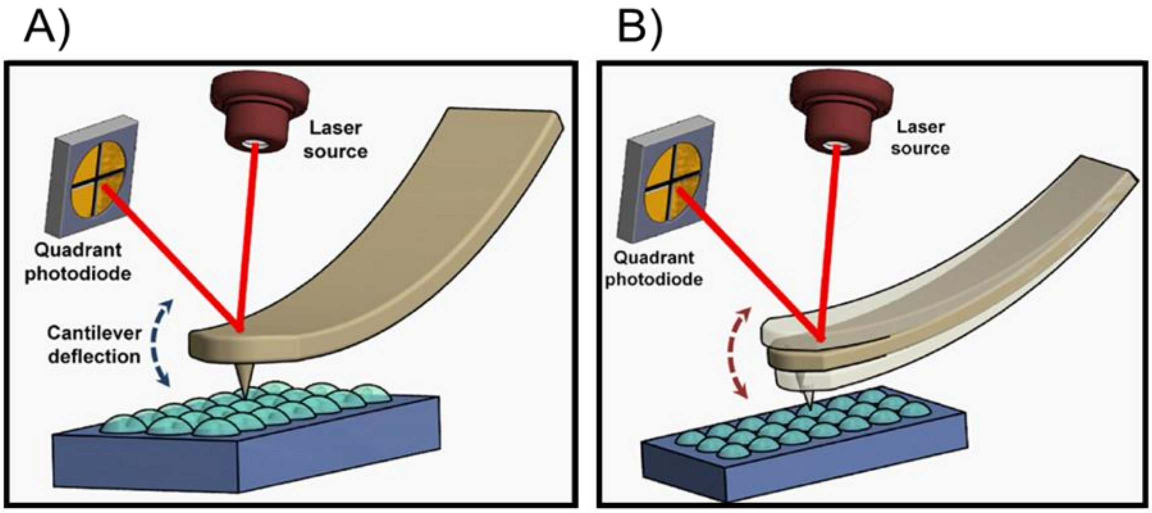

Figure 2.12. Schematic of a cantilever-based atomic force microscope. Two measurement modes are presented: (A) contact mode and (B) tapping mode. Retrieved from Ref.[32]

AFM tip and the cantilever's spring-like nature. The deflection is detected and measured using a laser reflected off the cantilever into a position-sensitive photodetector. A transducer, commonly a stack of piezo actuators, enables an electronic feedback loop, ensuring precise sample movement (XYZ Scanner).

Coulombic and Van der Waals (VdW) interactions govern the AFM cantilever deflection. Coulombic forces, being strong and short-ranged, originate from electron cloud repulsion, whereas the VdW forces, being long-ranged and attractive, emerge from fluctuating dipoles.[33] The AFM typically operates in contact (repulsion regime) and tapping mode (attractive regime). In contact mode (**Figure 2.12 A**), the electronic feedback loop maintains constant tip deflection, capturing the surface topography as a function of vertical motion. In tapping mode (**Figure 2.12 B**), the AFM cantilever oscillates near its fundamental frequency, essentially “tapping” the surface. The feedback loop maintains a constant oscillation amplitude, altering the tip-sample distance and generating a topographic image.

AFM offers numerous practical advantages over other microscopy techniques, as it operates without a vacuum and requires minimal to no sample preparation. Additionally, the electrical conductivity of the sample is not a prerequisite for imaging.[34] This relatively straightforward instrumentation has led to diverse developments in the technique. On the one hand, by modifying the instrumentation, various surface properties can be probed while simultaneously acquiring topography data.[35] Techniques like lateral, Kevin Probe, conductive, magnetic, and pulsed force microscopy are commonly utilized. On the other hand, AFM finds application in nanofabrication tasks, including atomic manipulation, local anodic oxidation, and deposition pattering. [36]

2.11 Transmission Electron Microscopy

Transmission electron microscopy (TEM) is a powerful technique involving an electron beam interacting with an ultra-thin sample, producing a highly magnified image with less than 0.1 nm resolution.[37] The resolution of this technique is impacted by the wavelength associated with the acceleration given to the electrons.[38] The sample must be very thin (<100 nm) to effectively use the TEM capabilities to enable forward scattering, including direct beam, elastic and inelastic scattering, and diffraction phenomena. The latter is attributed to the wave nature of the electrons.

The TEM instrument primarily comprises three key components: (1) a high-voltage electron beam and a condenser system that accelerate and focus the electrons onto the sample, (2) a series of lenses that focus the electrons that traversed the specimen to form an image, and (3) an image recording system which converts the electron-based image into a visual form.

Compared to XRD, TEM offers several advantages, particularly in nanomaterials and phase exploration.[39] Firstly, TEM possesses a significantly higher spatial resolution (a few nanometers) than XRD (hundreds of micrometers), enabling enhanced precision and detailing. Secondly, XRD demands more material due to the weak interaction between X-rays and matter. Lastly, routine XRD encounters limitations in probing non-periodic local structure features such as morphology, defects, grain boundaries, domain distribution, and phase segregation. In contrast, with its diffraction and spectroscopic capabilities, TEM is an unparalleled tool for correlating real-space imaging to chemical and structural properties with atomic-level spatial resolution.

TEM is broadly classified into two imaging modalities: TEM and scanning TEM (STEM). In TEM mode, as illustrated in **Figure 2.13 A**, a parallel beam illuminates the sample, forming a diffraction pattern at the back (I) of the focal plane (II). The diffracted region can be chosen by introducing an aperture just after the back of the focal plane. Selected area electron diffraction (SAED) offers valuable crystallographic insights from different sample regions.

An objective aperture in (I) forms an image using the transmitted and diffracted electron, which forms the essential signals of TEM. In the Bright Field mode (BF), only the transmitted electrons can pass through the objective aperture, while in the Dark Field mode (DF), only the diffracted electrons. Because of this, images in BF (DF) mode will appear dark (light) in areas of crystalline or high-mass material (more diffraction effect).[40] **Figure 2.13 A** illustrates the acquired information from electron diffraction and BF mode imaging.

In STEM mode (**Figure 2.13 B**), a convergent beam probes the sample using scanning coils, enabling rastering, imaging, and generation of secondary signals for spectroscopic analyses. For instance, energy-dispersive spectroscopy (EDS) facilitates elemental composition determination.

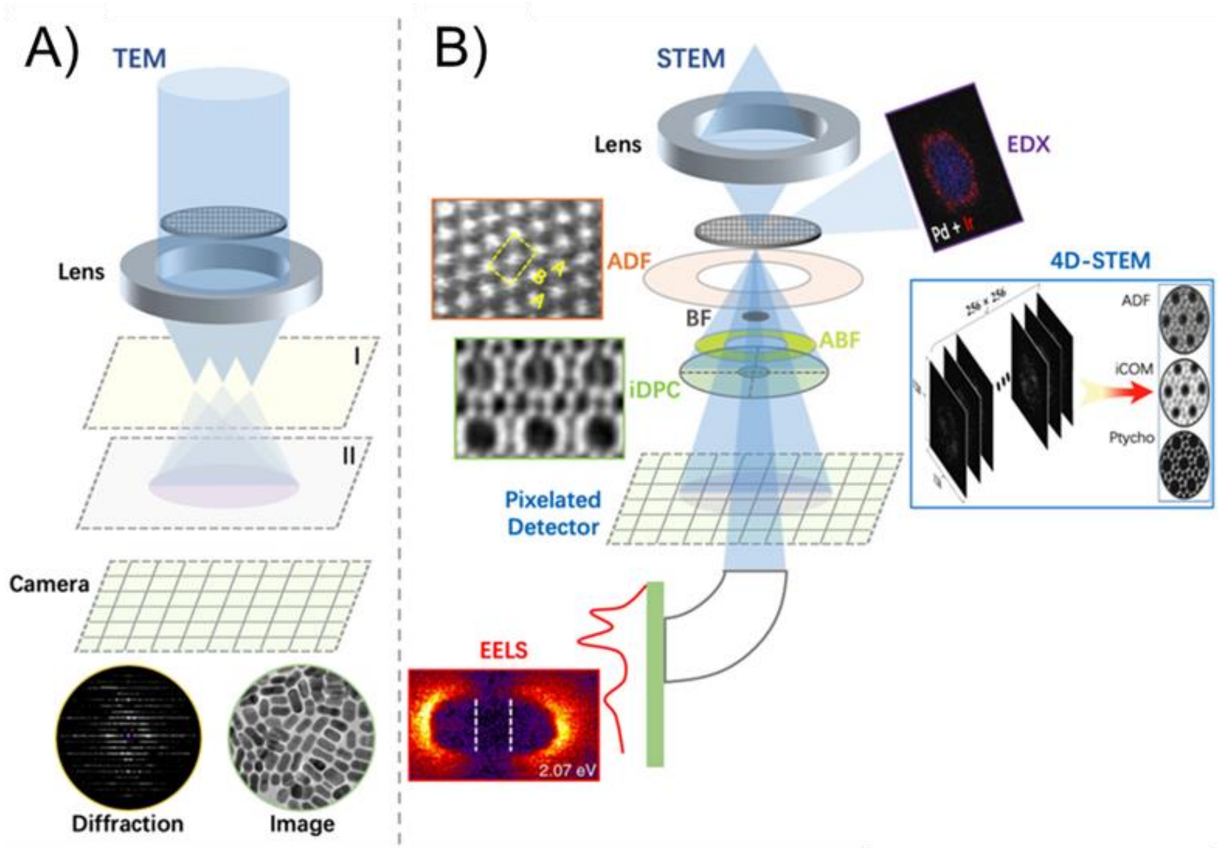

Figure 2.13. Overview of transmission electron microscopy techniques. (A) TEM and (B) STEM modes are presented. In TEM mode, reciprocal-space diffraction and real-space imaging are conjointly used. In STEM mode, various imaging modalities study the crystal structure, composition, and electronic structure. 4D-STEM provides the acquisition of multiple images in one data set. Retrieved from Ref.[39]

Various apertures can be used to acquire the generated scattered electrons: BF, annular BF (ADBF), annular dark-field (ADF), and high-angle ADF (HAADF). Of particular interest is HAADF, which captures information in the 50-200 mrad range, detecting inelastically scattered electrons (Rutherford scattering effect) as opposed to Bragg scattered electrons.[41] This technique allows the proper differentiation of elements as the contrast is given by $Z^{2,}$ where Z is the atomic number.

STEM can also be used for electron energy loss spectroscopy (EELS) (**Figure 2.13 B**), which is used to gather information about the sample's chemical bonding, valence states, and electronic structure.[42] These electrons interacted with the sample but suffered inelastic collisions. ELLS signal is significantly enhanced in conjunction with HAADF, as more electrons from the main beam reach the EELS detector.[43]

Similar to TEM mode, STEM is employed for diffraction purposes. Convergent beam electron diffraction (CBED) obtains diffraction patterns from regions smaller than one nm, enabling the study of strain mechanisms in materials.[44] Furthermore, 4D-STEM generates orientation and strain mapping by recording a 2D image of the diffracted electron beam for each probe position, ultimately forming a 4D data cube.[45] In this thesis, 4D-STEM was used to determine strain and phase mapping in different systems.

CHAPTER 3:

INTERFACIAL ENGINEERING OF ENERGY STORAGE MATERIALS IN LI-ION BATTERIES

3.1 Overview

Due to their high energy density, Li-ion batteries (LIBs) have emerged as the primary power source for small-scale portable electronics. In the more than three decades since their initial commercialization, LIBs have attracted extensive research attention, notably driven by initiatives promoting green energy technologies and the adoption of electric vehicles.[46] Despite their success, there is an urgent demand for batteries with higher stability and safety. This necessity is crucial for fully integrating LIBs into the transportation sector and electricity grids.[47]

This chapter introduces LIBs, which will be further explored in chapters 4 and 5 in two research directions. The LIBs presented in this thesis were developed in a thin film geometry to investigate interfacial and structural phenomena. Chapter 4 focuses on the stability of a $LiMn_2O_4$ cathode in various electrolytes, while Chapter 5 concentrates on optimizing a Pt thin film current collector. This introduction emphasizes the key components of LIBs relevant to this thesis, including cathode materials, ionic liquid electrolytes, and current collectors. Additionally, the importance of *in situ* X-ray characterization tools to elucidate the interfacial behavior is discussed.

3.2 Li-Ion Batteries

LIBs generally consist of two Li-hosting electrodes (cathode and anode), an electrolyte facilitating the migration of Li^+ ions, and a separator preventing electron flow through the electrolyte. Additionally, current collectors link the cell terminals, transmitting electric current to the electronic device. **Figure 3.1** illustrates the working principle of a LIB: during discharge, Li^+ ions move from the anode to the cathode through the ionically conductive electrolyte, resulting in an accumulation of electrons at the anode. These electrons traverse an external circuit to reach the cathode, maintaining electronegativity. The reversible process (charge) is achieved by forcing the Li^+ ions to return to the anode by applying a current or bias.

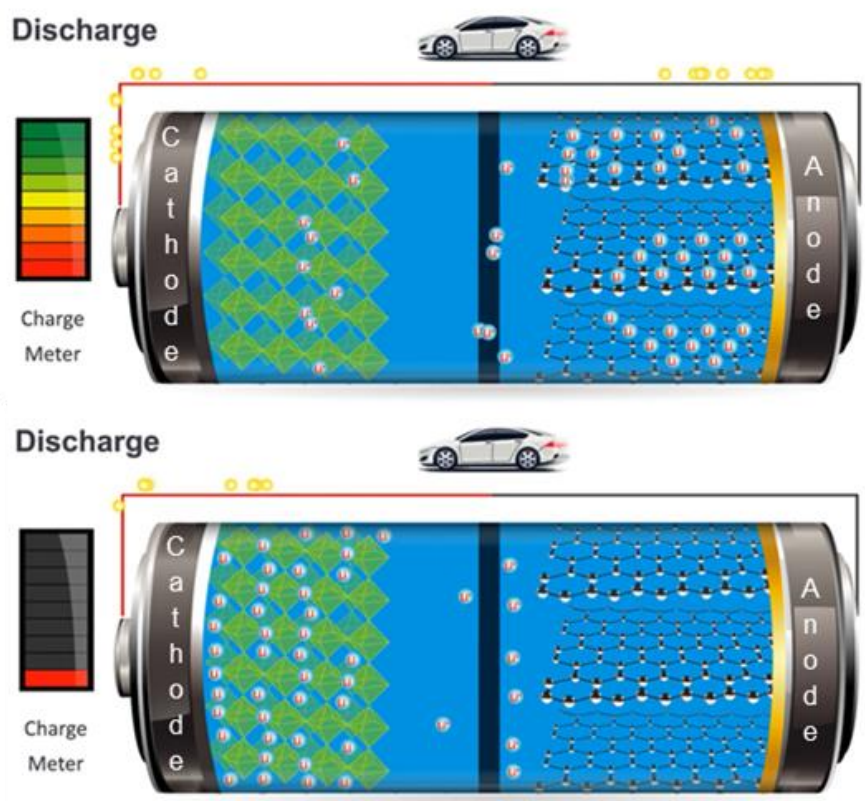

Figure 3.1. Schematic of the working principle of a Li-ion battery during discharge. Retrieved and adapted from Ref.[48]

3.3 Cathode Materials for Li-Ion Batteries

The cathode is the energy-limiting electrode due to its lower energy density.[49] Graphite, a commonly used and cost-effective anode material, possesses a theoretical capacity of 372 mAh/g, significantly surpassing the theoretical capacity of widely employed cathodes like $LiCoO_2$ (148 mAh/g). Most commercially available cathode materials function through an intercalation mechanism, reversibly incorporating ions into vacant sites. This particular mechanism often results in modest capacities but showcases exceptional cycling performance by minimizing volume changes and mechanical strain during cycling. [50]

Three primary types of cathode materials are categorized by their crystal structure, hosting distinct intercalation channels. (**Figure 3.2**). The first type comprises layered compounds represented by the formula $LiMO_2$ (M=Co, Mn, and Ni), exemplified by $LiCO_2$ (LCO) (**Figure 3.2 A**). LCO possesses a crystal structure $R\overline{3}m$ featuring three slabs of edge-sharing CoO_6 octahedra, offering a 2D pathway to diffuse Li^+ ions. This cathode exhibits a substantial specific capacity and good cycling stability. Nevertheless, there's a desire for cathodes without cobalt due to its toxicity, high cost, and detrimental social impact. The second type involves spinel-type compounds with the formula LiM_2O_4 (M=Co, Mn, and Ni), exemplified by $LiMn_2O_4$ (LMO) (**Figure 3.2 B**). LMO belongs to the $Fd3m$ space group and consists of an MnO_2 framework that allows for a 3D diffusion pathway for Li^+ ions. This cathode has excellent rate capability and is inexpensive and environmentally friendly. However, they are susceptible to substantial capacity loss, particularly at elevated temperatures. The third type comprises olivine represented by the form $LiMPO_4$ (M=Fe, Co, Ni, and Mn), such as $LiFePO_4$ (LFP) (**Figure 3.2 C**). LFP belongs to the space group $Pnma$ and consists of a framework of the FO_6 octahedra and PO_4 tetrahedra, facilitating Li^+ ion movement through 1D diffusion channels. This cathode is environmentally friendly, possesses moderate energy density with rapid charging capabilities, and is employed in producing the safest batteries. Still, it suffers from low electronic and ionic conductivities. **Figure 3.2** shows hexagonal spider graphs delineating the performance characteristics of these three major cathode materials. It is important to notice that each of the three cathodes presents a unique advantage that is not present in the others.

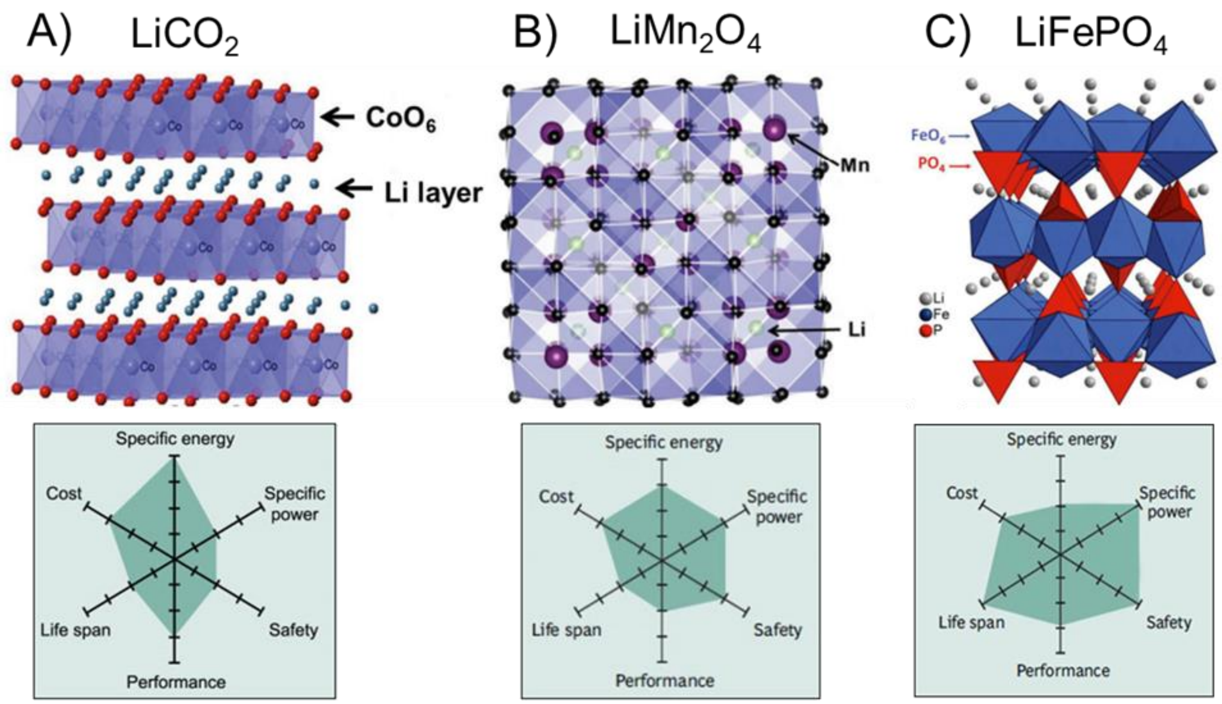

Figure 3.2. Crystal structure and performance for three common cathode materials. Here, (A) $LiCO_2$, (B) $LiMn_2O_4$, and (C) $LiFePO_4$ are presented with their respective hexagonal spider graphs performance. The performance of the cathodes is shown in terms of *specific energy* or capacity, *specific power* or ability to deliver high current, *safety*, *performance* at hot and cold temperatures, *life span* showing the longevity and cycle life, and *cost*. Retrieved and adapted from Refs. [51, 52]

3.3 Capacity Decay in $LiMn_2O_4$

Since its discovery in 1983 by Thackeray, spinel LMO has been extensively studied as a cathode material. Despite its potential, LMO suffers from severe capacity decay, especially under elevated temperatures and at high and low potentials. [53] Different degradation mechanisms occur in LMO: Firstly, Jahn-Teller distortion of Mn^{3+} species originates at deep discharge, causing a large and anisotropic volume change, damaging the cathode. [54] Secondly, the loss of active Mn ions due to dissolution arises from disproportionation reactions of Mn^{3+}, forming soluble Mn^{2+} ions. Thirdly, electrolyte decomposition triggered by trace amounts of H_2O generates HF, which erodes the cathode's surface. Other identified mechanisms include oxygen defects originating from materials synthesis or electrolyte decomposition, microcrack formation due to volume changes, and the deposition of Mn ions on the anode. **Figure 3.3** illustrates these mechanisms and their synergy to cause capacity loss in LMO.

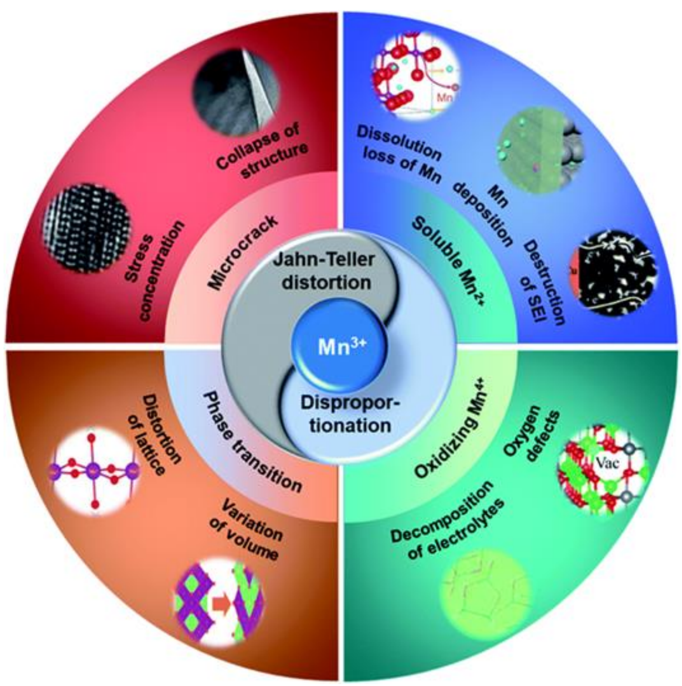

Figure 3.3. The synergic reaction of capacity decay in LMO. Retrieved from Ref. [53]

Liu *et al.* explained the connection between Mn dissolution and the dynamic phase stability in LMO.[55] Discharging the LMO results in a soluble Mn_3O_4 phase through the disproportionation reaction of Mn^{3+} ions and the emergence of an over-lithiated tetragonal $Li_2Mn_2O_4$ phase. The soluble ions exit the cathode, deteriorate its surface, and accumulate on the anode, obstructing Li^+ transport channels and damaging the solid electrolyte interphase (SEI). Simultaneously, transforming from cubic LMO to the $Li_2Mn_2O_4$ phase induces uneven volume changes, leading to irreversible phase alterations and particle cracking. Moreover, the electrolyte decomposition via hydrofluoric acid (HF) production continuously triggers Mn dissolution, further damaging the cathode. This cyclic process is accountable for the capacity decline observed in LMO.

Numerous strategies have been employed to mitigate the capacity loss observed in LMO. One approach involves doping or partially substituting Mn^{3+} to reinforce the unit cell by reducing Jahn-Teller distortion. Achieving enhanced cyclability through this method requires precise adjustments, wherein the guest ionic radius closely matches that of Mn^{3+}, an increase in manganese oxidation state above 3.5, and optimal concentration control.[56] Al^{3+} is one of the most promising options due to its abundance, environmental friendly, and low toxicity, which have shown potential.[57]. Several other elements have been proven effective, including Fe, Mg, Si, and B. Additionally, transition metals (TM) such as Ni^{2+} and Co^{2+} have been utilized to stabilize the LMO lattice.[58, 59] Anionic doping with elements like N, Cl, F, and S has demonstrated enhanced resistance to HF attack, notably in the case of fluorine.[60]

Several reactions occur at the cathode electrolyte interface (CEI), so different protective coating schemes have been proposed. Metal oxides like Al_2O_3[61], TiO_2[62], and ZrO_2[63], along with 2D-materials like graphene[64] or reduced graphene oxide[65], have shown promise in protecting the cathode from electrolyte decomposition reactions. Moreover, modifications in the electrolyte have been explored to counteract the rapid oxidation of electrolyte solvents. Strategies involve incorporating additives or substituting conventional electrolytes with ionic liquid and solid-state electrolytes.

3.4 Conventional Electrolytes and Ionic Liquid Electrolytes

Most state-of-the-art LIBs rely on organic liquid electrolytes known for their high ionic conductivities (10^{-3}-10^{-2} S/cm). These conventional electrolytes are composed of Li-salts and organic carbonate solvents like ethylene carbonate (EC), diethyl carbonate (DEC), and dimethyl carbonate (DMC). However, employing such electrolytes carries substantial safety risks, including toxicity, flammability, and the potential for explosion when the LIBs are exposed to harsh conditions such as high-temperature, short circuits, and high temperature.[66]

Furthermore, as mentioned in the previous section, these conventional electrolytes can decompose due to trace levels of H_2O and interaction with the cathode. Computational studies have shown that EC, for example, can decompose with TM oxides via electrophilic attack, followed by EC ring-opening, dissociation, and carbonate dehydrogenation. [67]

An ideal electrolyte should possess favorable ionic transport properties, chemical, and electrochemical stability during cycling, low melting and high boiling points, low vapor pressure, and the ability to form a passive SEI. [68] The SEI is crucial as its composition and evolution govern the ion’s (de)desolvation and transport into the electrode. Ionic liquids (ILs), molten salts with a melting point below 100°C and typically composed of a bulky asymmetric cation and a weakly coordinating anion, possess these desired properties. There is a significant interest in utilizing bis(trifluoromethylsulfonyl)amide ($TFSI^{-}$) as an anion in combination with various cations for the electrolyte due to its ability to form a robust SEI.[68] However, the adoption of Li-TFSI salt is hindered when used with organic solvents due to the anodic dissolution of the Al current collector.[69]

A promising alternative lies in a class of electrolytes known as ionogels, derived from ILs and a gelling matrix, which shows promise for solid-state LIBs. These electrolytes offer advantages over ILs alone, including enhanced mechanical strength owing to their gel-like nature. This improved strength helps prevent the growth of Li dendrites, eliminating the need for a separator.[70]

One such ionogel employs exfoliated hexagonal boron nitride (h-BN) as a gelling matrix to fabricate an ionogel composed of Li-TFSI salt and 1-ethyl-3-methylimidazolium bis(trifluoromethylsulfonyl)imide (EMIM-TFSI).[71] H-BN has many desirable attributes, such as chemical inertness, thermal stability, mechanical robustness, and electrical insulating nature. **Figure 3.4 A** demonstrates the preparation process of the ionogel, involving liquid phase exfoliation assisted with ethyl cellulose, followed by an annealing at 400°C for decomposition and, ultimately, gelation by mixing the h-BN nanoplatelets with the IL. **Figure 3.4 B** illustrates the use of this ionogel in a LIB without a separator, while **Figure 3.4 C** presents photographs of the ionogel.

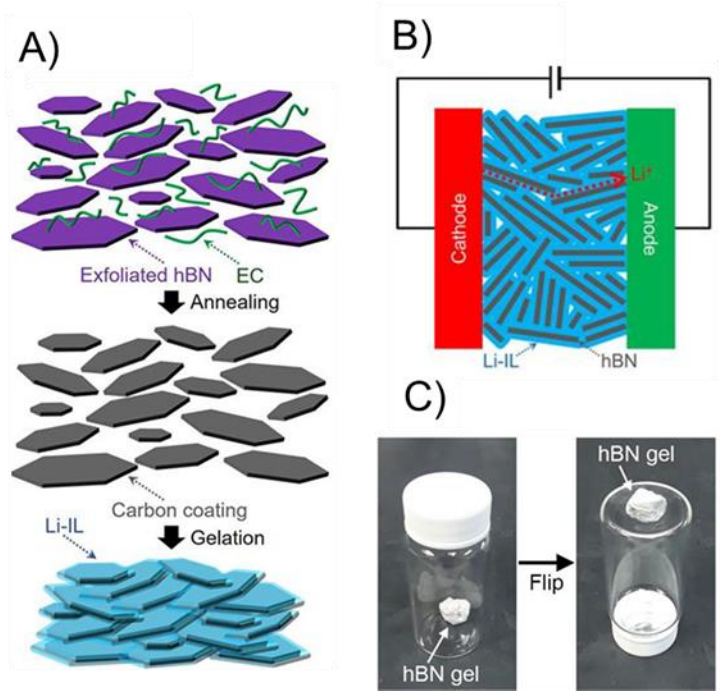

Figure 3.4. Schematic and working principle of a h-BN ionogel electrolyte. Schematics of the (A) h-BN ionogel electrolyte preparation and (B) **its use in LIBs.**(C) Photographs of a vial with the h-BN ionogel electrolyte before and after flipping. Retrieved and adapted from Ref. [71]

3.5 Current Collectors

Current collectors in LIBs bridge the electrical current generated in the electrodes with external circuits. Given that current collectors do not participate in the Li^+ intercalation reactions, there is a strong preference for thin and lightweight variants to enhance the volumetric energy density of the LIB. Significantly, these materials must exhibit chemical and electrochemical stability throughout battery operation.

Cu and Al are the most widely used commercial current collectors, as they generally demonstrate stability at anodic and cathodic potentials, respectively. Nevertheless, corrosion is still observed for both collectors under various operating conditions, both regular and extreme.[72] To address this issue, alternative materials, structures, and treatments, such as etchings and coatings, are needed to enhance LIB performance further.[73]

In the context of thin film batteries, the current collector functions as a template for the electrode's thin film growth. The electrochemical properties of the electrode are highly dependent on factors like crystallinity and crystal orientation, particularly evident in LMO.[74] Therefore, there is a need for optimized current collectors. Noble metals such as Pt and Au are of great interest due to their chemical stability, enabling the epitaxial deposition of electrode materials. Using such materials holds promise for enhancing the overall performance of thin film batteries.

3.6 *In situ* X-ray Techniques for Li-Ion Battery Research

In situ techniques have emerged in recent years as the preferred method for understanding mechanisms within LIBs. This approach involves monitoring the evolution of the different battery components and interfaces under real conditions, such as electrochemical cycling. *In situ* stands in contrast to *ex situ* experiments where the cell needs to be disassembled. *In situ* analysis allows instant probing, mitigating the risks associated with contamination or relaxation of metastable phases.[75] This methodology is necessary for solid-state batteries, where the removal of the electrolyte for post-mortem examination is prohibited.[76]

A specific phenomenon extensively investigated through *in situ* experiments is the dissolution of Mn ions in LMO cathodes, encompassing ion dissolution, migration to the electrolyte, and deposition on the anode (DMD process).[77] **Figure 3.5** illustrates four examples of *in situ* techniques applied to study the complex behavior and degradation associated with the DMD process. For instance, Uv-Vis spectroscopy detected the increase of soluble Mn^{2+} in the electrolyte during cycling (**Figure 3.5 A**).[78] In a separate experiment, X-ray fluorescence microscopy monitored the Mn^{2+} deposition of the anode (**Figure 3.5 B**). [79] AFM revealed an increase in roughness attributed to the dissolution of one or two atomic layers of LMO. (**Figure 3.5 C**).[80] Additionally, X-ray absorption spectroscopy indicated an increment of Mn^{3+} in the LMO cathode after one cycle, which further leads to more soluble Mn^{2+} ions due to the disproportionation reaction (**Figure 3.5 D**). [81]

Beyond the DMD, numerous other mechanisms can be explored using *in situ* configurations. **Figure 3.6** illustrates multiple *in situ* techniques employed to study a solid-state LIB. Ideally, some of these techniques can be used simultaneously with minimal to non-detrimental effects on the LIB performance. Microscopy techniques directly visualize changes in cell components, while X-ray and neutron scattering offer insights into phase evolution and impurity formation. EDS and

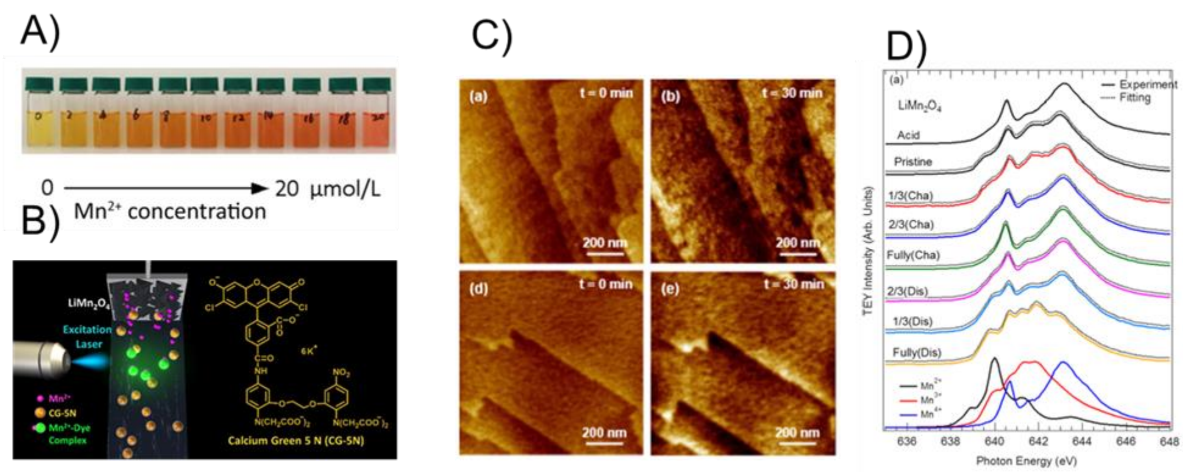

Figure 3.5. *In situ* techniques to study the Mn DMD process in LMO cathodes. Examples include: (A) UV-Vis spectroscopy, (B) X-ray fluorescence microscopy, (C) atomic force microscopy, and (D) X-ray absorption spectroscopy. Retrieved and adapted from Refs. [52, 78-81]

XPS offer elemental composition information about intermittent products, and dynamic electrochemical mass spectrometry provides residual gas evolution.[82] Due to the non-destructive nature of X-rays, X-ray-based techniques such as XRR and XRD offer a unique opportunity to monitor interfacial and structural evolution during cycling.[83]

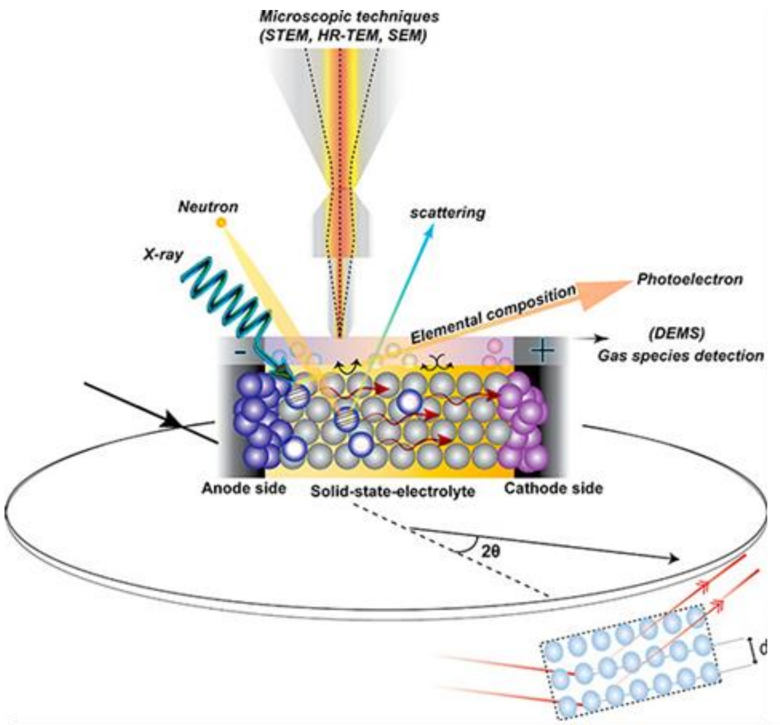

Figure 3.6. *In situ* techniques to explore the components and interfaces in solid-state LIBs. Retrieved from Ref.[82]

CHAPTER 4:

ELUCIDATING THE CATHODE/ELECTROLYTE INTERFACE IN THE EPITAXIAL $LiMn_2O_4$ (111) / ELECTROLYTE SYSTEM

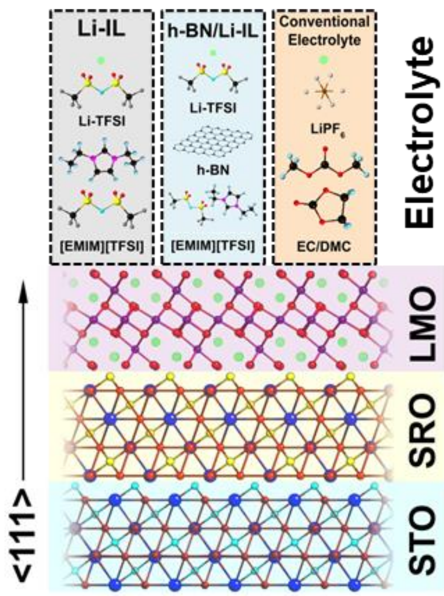

This chapter is adapted from:

Torres-Castanedo C. G., Evmenenko G., Luu N. S., Das P. M., Hyun W. J., Park, K. Y., Dravid, V. P., Hersam M. C. & Bedzyk M. J. (2023). Enhanced $LiMn_2O_4$ Thin-Film Electrode Stability in Ionic Liquid Electrolyte: A Pathway to Suppress Mn Dissolution. *ACS Applied Materials & Interfaces*, *15*(29), 35664-35673.

Torres-Castanedo C. G., Evmenenko G., Luu N. S., Hyun W. J., Park K. Y., Hersam M. C. & Bedzyk M. J. Interfacial and Structural Evolution of $LiMn_2O_4$ Electrode in h-BN Ionogel Electrolyte. *In Preparation.*

4.1 Overview

Spinel-type lithium manganese oxide ($LiMn_2O_4$) emerges as a promising LIB cathode material due to its high theoretical capacity, wide availability of Mn, eco-friendly sourcing, low toxicity, and strong stability. Yet an unresolved critical issue is the loss of capacity caused by Mn^{2+} dissolution from the lattice to the electrolyte, which causes structural damage to the spinel framework and irreversible phase transformations. *In situ* XRR and XRD offer a unique outlook to connect Mn dissolution with phase stability by accessing interfacial and structural information during cell operation. Such an approach is possible using a model LIB system composed of epitaxial $LiMn_2O_4$ thin films with high-crystal quality and ultra-smooth interfaces.

In this chapter, an ionic liquid replaces problematic organic carbonate-based electrolytes (i.e., $LiPF_6$+EC/DMC) to interrogate Mn dissolution and phase stability. The ionic liquid electrolyte is composed of LiTFSI salt and EMIM-TFSI ionic liquid. The *in situ* X-ray results, gathered during cyclic voltammetry (CV), and a comprehensive ex situ characterization, including XPS, XRD, ICP-MS, and TEM, show that the ionic liquid suppresses Mn dissolution during and after nine wide-range cycles (2.5-4.3 V *vs.* Li/Li^+). The organic carbonate-based ($LiPF_6$+EC/DMC) electrolyte was used as a baseline for this study.

Finally, an ionogel based on the same ionic liquid and exfoliated h-BN nanoflakes was used to study the cathode/gel interface. The *in situ* X-ray measurements show evidence of irreversible phase transformation with no Mn dissolution, which is attributed to improper interfacial contact. An ionic liquid interlayer was later introduced between the cathode and the gel to improve the contact, showing enhanced phase stability. These findings show the significant advantages of ionic liquids and gels in suppressing Mn dissolution in $LiMn_2O_4$ LIB cathodes and the physical contact challenge limiting the practical use of ionogel electrolytes.

4.2 Background

$LiMn_2O_4$ (LMO) exhibits a cubic-spinel structure ($Fd\bar{3}m$), with an average Mn oxidation state of +3.5 ($Mn^{3+/4+}$). Within this lattice arrangement, Li and Mn cations occupy tetrahedral (8a) and octahedral (16d) sites, respectively, in a cubic close-packed array of O anions (32e). The LMO lithiation process involves two Li^+ insertion events through the tetrahedral 8a and empty 16c octahedral sites. at ~4 V and ~3 V *vs.* Li/Li^+.[84] During Li^+ extraction ($x = 1 \rightarrow 0$), $Li_xMn_2O_4$ maintains its cubic symmetry (λ-MnO_2, $Fd\bar{3}m$) as Li^+ migrates out of the tetrahedral 8a sites at ~4 V *vs.* Li/Li^+. In deep discharge, Li^+ enters into the empty 16c octahedral sites at ~3 V *vs.* Li/Li^+, resulting in a structural conversion to a tetragonal phase ($Li_2Mn_2O_4$, $I4_1/amd$).[85, 86] This phase transformation results in Jahn-Teller distortion and substantial change in the unit cell volume (6%), compromising the structural integrity of the cathode.[84, 85] To circumvent this structural instability, the lower operating voltage cutoff has been empirically established above 3 V *vs.* Li/Li^+. However, this adjustment comes at a cost, sacrificing half of the available capacity for LMO.[87]

LMO exhibits capacity fade, even when cycled around 4 V *vs.* Li/Li^+.[88, 89] The Mn^{2+} dissolution, resulting from the disproportionation reaction $2Mn^{3+} \rightarrow Mn^{4+} + Mn^{2+}$, is considered as the root cause of capacity fades in LMO.[90] Following the dissolution, Mn^{2+} ions travel through the electrolyte, eventually depositing onto the anode, elevating the overall cell impedance.[77, 90] This process is identified as the dissolution-migration-deposition (DMD) mechanism.[77] Additionally, the loss of Mn ion potentially induces irreversible phase transformations and structural damage, leading to the formation of cracks, which also contribute to capacity degradation.[55]

The DMD mechanism in LMO has been widely studied, particularly in conventional electrolytes.[77] It is essential to understand the reactions occurring at the electrode/electrolyte interface to enhance LIB stability.[76, 91] *In situ* methods are the preferred approach for exploring the complex behavior and degradation linked to the DMD process.[78-81, 92] Among these methods, synchrotron X-ray experiments offer the ability to observe changes in the surface/interface, bulk structure, morphology, and chemical composition during operation with minimal impact on the sample.[83, 91]

Several strategies have been explored to mitigate Mn dissolution in LMO.[93] One approach involves using thin and robust coatings such as oxides (Al_2O_3, TiO_2, or ZrO_2) or graphene to create a barrier to minimize contact between LMO and the electrolyte.[61, 62, 64] Additionally, structural or surface modification through cationic substitution (e.g., $LiM_xMn_{2-x}O_4$, M=Ni, Co, Zn) aims to increase the average oxidation state of Mn, thus reducing the presence of Jahn-Teller active Mn^{3+} species.[88] Another explored method includes the use of HF/H_2O scavengers in the electrolyte or separator since conventional Li-salts such as $LiPF_6$ can quickly react with trace amounts of water, producing HF and deteriorating LMO.[94, 95]

Using alternative electrolytes to replace problematic organic carbonate electrolytes can be a practical approach to mitigate Mn dissolution. Among these alternatives, ionic liquids offer several advantages, such as non-flammability, minimal volatility, and high thermal and electrochemical stability.[96] Moreover, when integrated into a gelling matrix, ionic liquids can form a solid-state composite known as an ionogel, eliminating the need for additional liquid components or separators.[97, 98] These gel systems can address safety concerns and possibly prevent Li dendrite formation.[76] However, as long-term cyclic stability is influenced by interfacial behavior, comprehensively understanding the relationship between ionic liquids/gels and cathode interfaces during cycling is crucial to validate these electrolyte systems.

4.3 Thin Film Model System to Study the $LiMn_2O_4$/Electrolyte Interface

Epitaxial and smooth LMO (111) / $SrRuO_3$ (111) (SRO) thin films were deposited on $SrTiO_3$ (111) (STO) substrates using PLD. The choice of (111) orientation aimed to examine Mn dissolution, as particle fracture primarily occurs along the 111 planes.[99] The SRO thin film achieves epitaxy due to its minimal lattice mismatch (-0.1%) with the STO substrate while also functioning as a current collector.[100] Meanwhile, the epitaxy of the LMO thin film (a=8.251 Å, ICSD-50415) was achieved despite a more significant mismatch (2:1) of -5.5% with the SRO/STO lattice (a = 3.905 Å / 3.910 Å) of -5.5%. This investigation required ideal interfaces and high-crystal quality films for detailed structural and interfacial X-ray analysis during electrochemical operation.

Initial analysis of the LMO thin film's crystallinity, epitaxial nature, and interface involved *ex situ* X-ray characterization of pristine samples. (**Figure 4.1**) High-resolution XRD (HR-XRD) confirmed the single-crystal nature of the LMO (111) thin film, displayed an out-of-plane d-spacing close to the reported bulk value (d_{111exp} = 4.75 Å *vs.* $d_{111bulk}$ = 4.76 Å). The presence of Kiessig fringes in the longitudinal scan through the LMO (111) Bragg peak and a transverse ω-scan (rocking curve) showcasing an FWHM of 0.22° corroborated the high-crystal quality of the film. Grazing incidence XRD (GI-XRD) measurements revealed epitaxy in the LMO [1-10] || STO [1-10] in-plane orientation and LMO [100] || STO [100] off-specular orientation.

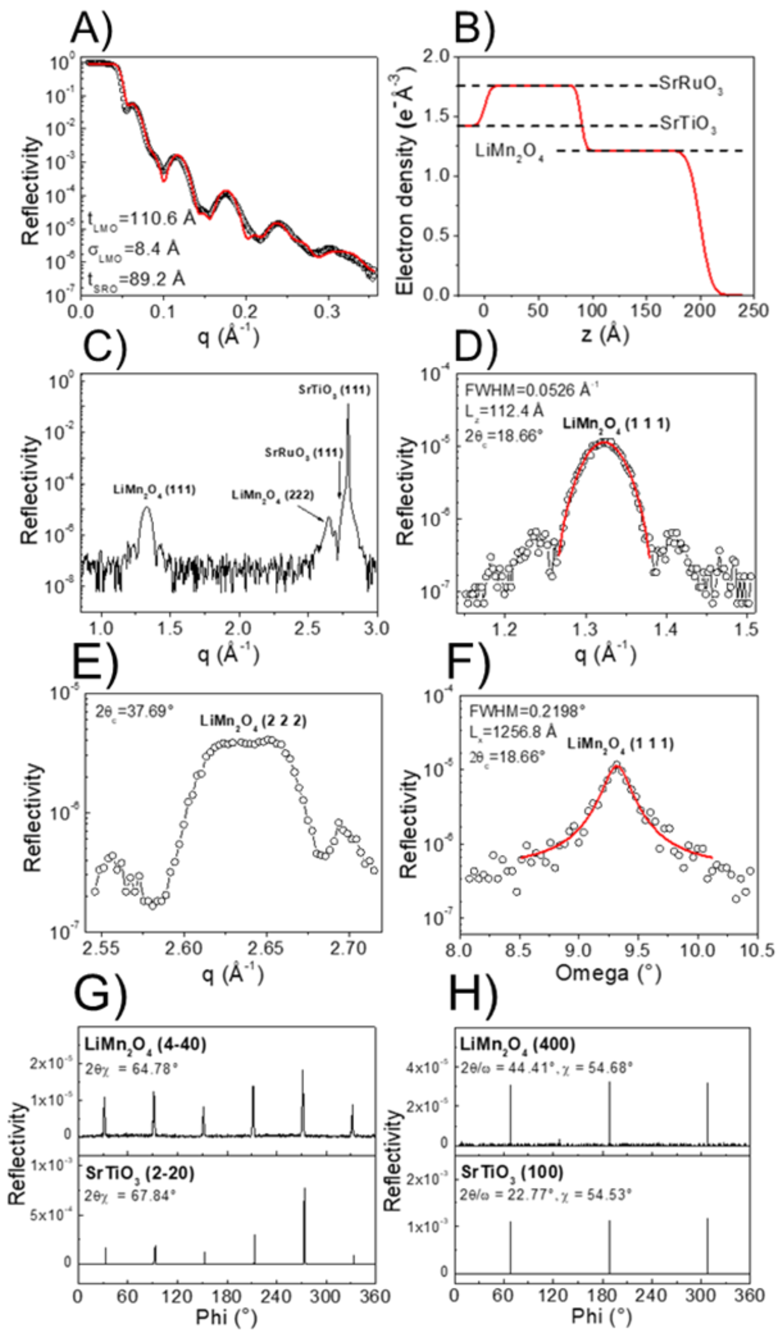

Figure 4.1. *Ex situ* X-ray characterization of the epitaxial LMO(111)/SRO(111)/ STO(111) sample. (A) X-ray reflectivity data (black circles) and model best fit (red line). (B) Electron density profile determined from the XRR fit. (C) High-resolution X-ray diffraction showing the LMO (111), LMO (222), and STO (111) Bragg peaks. Region of the (D) LMO (111) and (E) LMO (222) Bragg peaks. A Gaussian curve was utilized to calculate L_z in Equation 2.3. (F) Rocking curve of the LMO (111) Bragg peak. (G) Azimuthal φ-scan of the in-plane STO (2-20) and LMO (4-40) Bragg peaks. (H) Azimuthal φ-scan of the off-specular STO (100) and LMO (400) Bragg peaks.

XRR data fitting employed a slab model and the theoretical electron densities for LMO 1.21 $e^-/Å^{-3}$, SRO 1.76 $e^-/Å^{-3}$, and STO 1.42 $e^-/Å^{-3}$. The extracted thicknesses of the LMO and SRO films measured by XRR were 110.8 Å and 89.2 Å, respectively, with an overall roughness of 8.4 Å.

These precise measurements of the film thickness and overall roughness, obtained through XRR, are necessary to monitor and analyze the interfacial evolution.

4.4 Enhanced Interfacial and Structural Stability of $LiMn_2O_4$ in Li-IL

The CV profile of the LMO sample cycled for 2 D and 9 DD in the Li-IL electrolyte is illustrated in **Figure 4.2 A**. Within the 4 V region, distinct redox peaks were identified at 4.02 V and 4.16 V, demonstrating minimal polarization (0.01-0.02 V). Notably, the Li-IL electrolyte showed redox peaks at 2.92/3.80 V in the 3 V region with a negligible -0.02 V shift in polarization after 9 DD cycles. This result highlights the superior reversibility and enhanced kinetic properties of the Li-

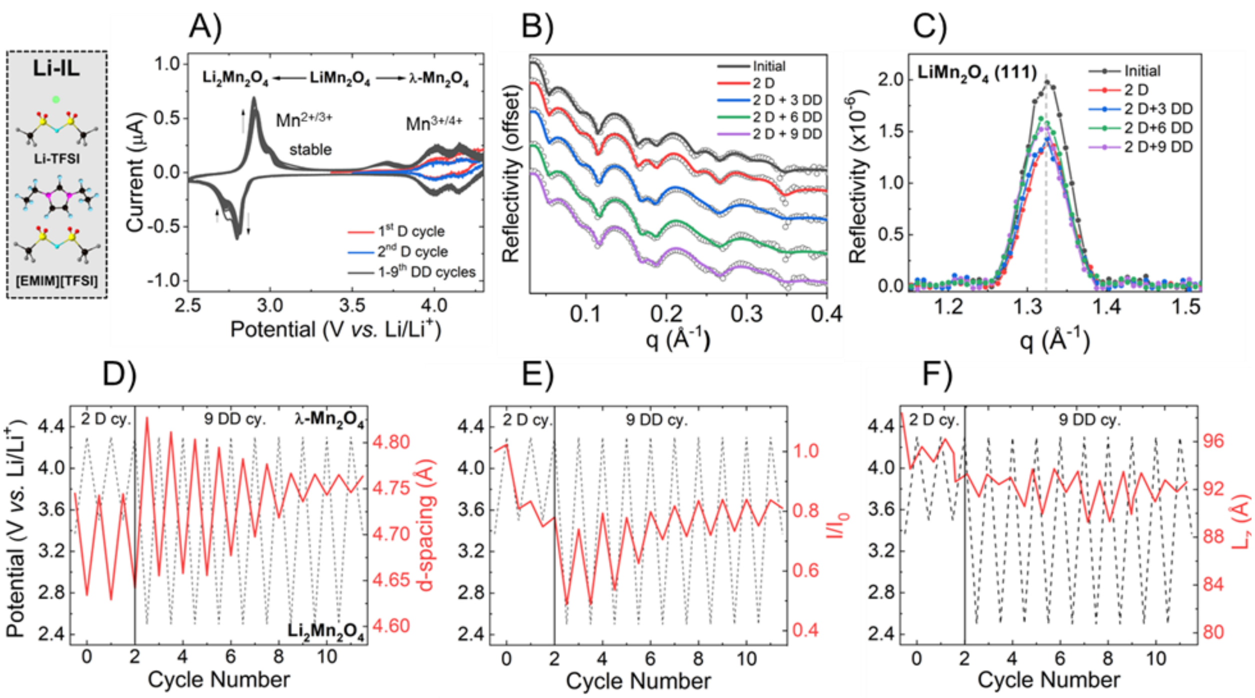

Figure 4.2. ***In situ*** **XRR/XRD of the LMO cycled in Li-IL electrolyte.** (A) Cyclic voltammetry of the L MO (111) cathode. (B) XRR with fit and (C) XRD as a function of the voltammetry cycles measured at ~3.5 V. Evolution of the (D) d-spacing, (E) domain size, and (F) integrated intensity from the LMO (111) Bragg peak during cyclic voltammetry. The *dashed lines* illustrate the voltage changes during cycling. shown for the LMO (111) Bragg peak.

IL electrolyte over the conventional counterpart when used with LMO, particularly in the context of DD cycles.[101]

Figures 4.2 B and **C** exhibit the *in situ* XRR and XRD results for the Li-IL electrolyte measured around 3.5 V across selected cycles. Analysis from XRR indicated a consistent thickness of both LMO and SRO films throughout the experiment, evidenced by the unchanging periodicity of fringes' minima. **Table 4.1** summarizes the XRR fittings parameters around 3.5 V vs Li/Li^+. Specifically, the LMO thickness exhibited a marginal 3% decrease (from 92.8 Å to 90.0 Å), potentially attributed to a slight increment in the LMO roughness (from 7.4 Å to 9.4 Å). These findings suggest a substantial inhibition of Mn dissolution into the electrolyte during cycling, even in the DD conditions. Examining the LMO (111) Bragg peak in **Figure 4.2 C**, its integrated intensity remained stable throughout the DD cycles. Additionally, the LMO (111) peak position for the Li-IL remained constant during cycling, indicating a proper (de)lithiation process and the absence of irreversible $Li_xMn_2O_4$ phases.

	t_{LMO} (Å)	ED_{LMO} ($e^-/Å^3$)	σ_{LMO} (Å)	t_{SRO} (Å)	$\sigma_{SRO\text{-}LMO}$ (Å)	$\sigma_{STO\text{-}SRO}$ (Å)
Initial	92.8	1.26	7.4	72.9	5.6	4.3
2 D	92.5	1.25	7.5	72.9	5.4	3.7
2 D + 3 DD	90.7	1.24	10.4	72.9	6.4	3.6
2 D + 6 DD	90.0	1.20	9.8	73.0	6.5	3.5
2 D + 9 DD	90.0	1.20	9.4	73.0	6.4	3.5

Table 4.1. XRR fitting parameters of the LMO cycled in the Li-IL electrolyte. The following electron densities were fixed in the fitting: STO (1.42 $e^-/Å^3$), SRO (1.76 $e^-/Å^3$), and Li-IL electrolyte (0.35 $e^-/Å^3$).

The evolution of the LMO (111) Bragg peak concerning *d-spacing*, integrated intensity, and vertical domain size (L_z) was monitored during electrochemical cycling (**Figures 4.2 D-F**). Solid red lines denote data points for half-integer and integer cycles, while dashed lines depict the voltage evolution. The *d-spacing* of the LMO (111) Bragg peak, expressed as $d=2\pi/q_{111}$, indicates the state of charge. This parameter reflects the lattice expansion or contraction within LMO, driven by the insertion or extraction of Li^+ ions. Notably, for LMO fully cycled with the Li-IL electrolyte, the *d-spacing* tended towards a stable intermediate value of approximately 4.75 Å, aligning with the initial state of the film. (**Figure 4.2 D**).

In examining the normalized integrated intensity ($I/I_{pristine}$, **Figure 4.2 E)** for LMO cycled with Li-IL, a decrease of 20% occurred after the initial two D cycles, suggesting an initial loss of crystallinity. However, this value stabilized during the subsequent DD cycles, converging to an $I/I_{pristine}$ value of 0.8. Similarly, the L_z, calculated from the FWHM using Eq. 4.1, displayed a comparable trend to $I/I_{pristine}$ (**Figure 4.2 F**). After 2 D + 9 DD cycles, L_z experienced only a 4% reduction, indicating sustained crystallinity for the LMO thin film during cycling. The observed behavior showcases robust cathode stability in the Li-IL electrolyte with a durable performance under demanding DD conditions.

Previously, Chen *et al.* observed a reduced LMO thickness and an overall crystallinity loss in LMO samples cycled in $LIPF_6$+EC/DMC electrolyte over 2 D + 3 DD cycles.[101] Here, an additional LMO sample was cycled for 2 D + 9 DD using the same electrolyte to compare directly with the Li-IL experiment. The CV **(Figure 4.3 A)** revealed two pairs of redox peaks within the 4 V region at 4.01 V and 4.17 V, with an additional pair in the 3 V region at 3.20/2.70 V. After subsequent

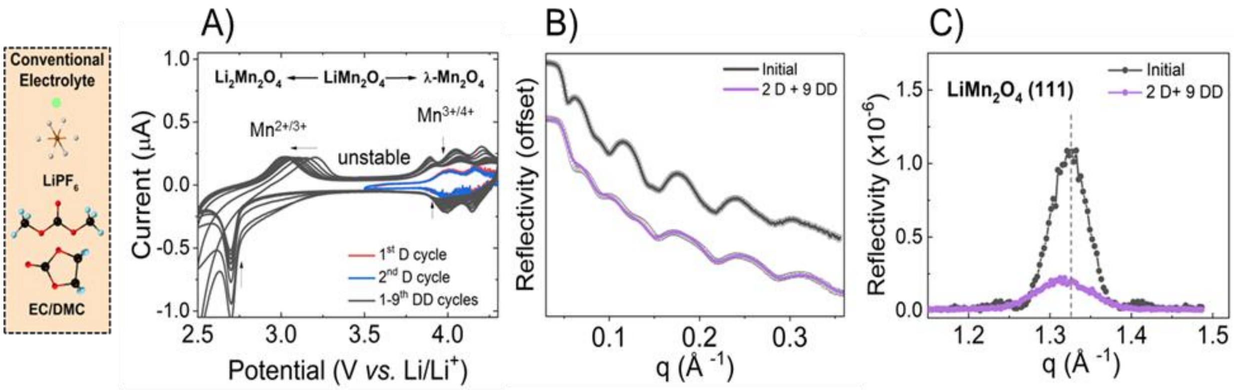

Figure 4.3. ***Ex situ*** **XRR/XRD of the LMO cycled in the conventional electrolyte.** (A) Cyclic voltammetry for this system. (B) XRR with fit and (C) XRD before and after 2 D + 9 DD cycles.

DD cycles, the system exhibited instability, evidenced by a continuous shift and reduction in the intensity of these redox peaks (as marked by arrows in **Figure 4.3 A**).

XRR and XRD measurements conducted before and after 2 D + 9 DD cycles (**Figures 4.3 B** and **4.3 C)** unveiled a 28% reduction in LMO thickness (from 111.3 Å to 80.4 Å) and a 67% increase in roughness (from 8.7 Å to 14.5 Å). **Table 4.2** summarizes the parameters used for the XRR fittings. On the other hand, L_z decreases by 32% (from 109.4 Å to 74.9 Å). The decrease in crystallinity was not solely a consequence of material loss but of the formation of irreversible $Li_2Mn_2O_4$ (220), which broadened the LMO (111) Bragg peak and consequently diminished the Lz value, as derived from Eq. S1. A summary of the XRR/XRD results for LMO after 2 D + 9 DD

	t_{LMO} (Å)	ED_{LMO} ($e^-/Å^3$)	σ_{LMO} (Å)	t_{SRO} (Å)	$\sigma_{SRO-LMO}$ (Å)	$\sigma_{STO-SRO}$ (Å)
Initial	111.3	1.21	8.7	91.0	5.2	1.5
2 D + 9 DD	80.4	1.02	14.5	88.8	3.5	5.4

Table 4.2. XRR fitting parameters used for the LMO cycled in the conventional electrolyte. The following electron densities were fixed in the fitting: STO (1.42 $e^-/Å^3$) and SRO (1.76 $e^-/Å^3$).

cycles and the percentage change for the two electrolytes is provided in **Table 4.3**. The main difference between the LMO samples cycled with the two different electrolytes was the considerable reduction in thickness, L_z, and integrated intensity in the $LiPF_6$+EC/DMC electrolyte. This result suggests a severe chemical and structural compatibility issue induced by cycling. In contrast, the LMO cycled in Li-IL electrolyte showed notably higher interfacial and structural stability following the 2D + 9 DD cycles.

		Li-IL			$LiPF_6$+EC/DMC		
		Pristine	Cycled	Change	Pristine	Cycled	Change
XRR	LMO thickness (Å)	92.8	90.0	**-3%**	111.3	80.4	**-28%**
	LMO roughness (Å)	7.4	9.4	+27%	8.7	14.5	+67%
XRD	Vertical Domain Size L_z (Å)	96.7	92.6	**-4%**	109.4	74.9	**-32%**
	Change in area of LMO (111)	-20%			-72%		
ICP-MS	Mn loss in electrolyte	**-3.9%**			**-22.7%**		

Table 4.3. XRR/XRD and ICP-MS of the LMO samples cycled in the two liquid electrolytes. Mn loss from the films based on ICP-MS analysis of the electrolytes. (*see Table 4.4 for details*)

4.5 Mn Dissolution and Phase Stability in Li-IL *vs.* Organic-based Electrolyte

The dissolution of Mn and its connection to LMO phase stability post CV was approached systematically. The methodology encompassed an electrolyte analysis using inductively coupled plasma mass spectrometry (ICP-MS) and a comprehensive examination of the surface and bulk of LMO thin films using diverse characterization techniques. The measurements were conducted after the 2 D + 9 DD cycles at a state of charge of 3.5 V vs Li/Li^+.

Initially, the suppression of Mn dissolution into the electrolyte was studied by ICP-MS. The Mn concentration in the electrolyte was measured by ICP-MS to compute the film thickness loss, as detailed in **Table 4.4**. The film loss for LMO cycled with the $LiPF_6$+EC/DMC electrolyte (-22.7%)

is close to that from XRR (-28.0%). For the LMO cycled in Li-IL, a notably lower Mn concentration corresponded to only a 3.9% loss in LMO thin film thickness (**Table 4.3**). An additional ICP-MS experiment was performed on pristine LMO powder samples to investigate the Mn dissolution suppression in the Li-IL. These samples were immersed in Li-IL and $LiPF_6$+EC/DMC at 60°C for seven days to accelerate Mn dissolution.[102] The resulting Mn concentrations were 106 ppb and 3530 ppb for the $LiPF_6$+EC/DMC and Li-IL electrolytes, respectively. The dissolution in the $LiPF_6$+EC/DMC electrolyte was induced in the absence of cycling, driven by the production of HF via hydrolysis of $LiPF_6$.[103] This finding supports the XRR results, consistently indicating a substantial reduction in Mn dissolution within the Li-IL electrolyte.

Previously, various lithium salts were proposed to enhance the performance of LIBs by mitigating dissolution. For instance,, lithium-imide salts such as LiTFSI and lithium bis(fluorosulfonyl)imide

	Li-IL	**$LiPF_6$ + EC/DMC**
LMO thickness (Å)	95.3	110.6
Mn mass in the thin film (ng)	291.86	330.63
Total mass of the electrolyte (g)	2.22	3.25
Mn in the electrolyte (ng/g)	5.12	23.07
Mn mass in the electrolyte (ng)	11.37	75.07
Loss of Mn from the thin film (%)	**-3.9**	**-22.7**

Table 4.4. ICP-MS quantification of Mn in the liquid electrolytes after 2 D + 9 DD cycles. The following density values (in g/cm^3) were used in the calculation: ρ_{LMO} = 4.020, $\rho_{Li\text{-}IL}$ = 1.478, and $\rho_{LiPF6+EC/DMC}$ = 1.356. An LMO area of 0.3 × 0.4 cm^2 was utilized to calculate the total Mn mass in the thin film.

(LiFSI), known for their reduced susceptibility to hydrolysis compared to $LiPF_6$ were used to enhance the electrochemical and thermal stability of $LiFePO_4$ and $LiNi_{0.5}Mn_{1.5}O_4$, respectively.[104, 105] In the case of $LiPF_6$-based electrolytes, the presence of trace amounts of water triggers the decomposition of this salt into HF, exacerbating Mn dissolution.[106] Previously, the hydrolysis potential of fluorine ions such as $[PF_6]^-$ in 1-butyl-3-methylimidazolium (BMIM) ionic liquid has been discovered.[107] In contrast to $LiPF_6$, LiTFSI salt, when used in the Li-IL electrolyte, reduces the likelihood of salt breakdown, stabilizing the LMO cathode's electrochemical performance.

Moreover, compared to organic carbonate solvents such as EC/DMC, EMIM-TFSI ionic liquids provide enhanced resistance to solvent decomposition, especially at high states of charge and during deep discharge. Specifically, the interaction of EC molecules with the LMO surface oxygen leads to solvent decomposition, forming hydroxyl groups.[108] This superior oxidative stability was further exemplified in the ionic liquid Pyr_{13}TFSI using LiTFSI salt. Qiao *et al.* showed a reduction in Mn/Ni dissolution in $LiNi_{0.5}Mn_{1.5}O_4$ cathodes when compared to $LiPF_6$+EC/DEC.[79]

During the electrochemical cycling of $Li_xMn_2O_4$ $(0 < x < 2)$, both the Jahn-Teller distortion and Mn dissolution processes have been identified to trigger the formation of overlithiated $Li_2Mn_2O_4$. Such transformation can be irreversible due to damage in the spinel framework.[55, 74] This formation of this impurity phase has been observed at 3.5 V in the surface and cracks of particles after cycling in the standard range (3.4-4.3 V).[55] If this tetragonal phase is found after cycling in a potential window where only stoichiometric $LiMn_2O_4$ is expected to be redox active, these regions of $Li_2Mn_2O_4$ will likely endure. The persistence of $Li_2Mn_2O_4$ leads to an overall reduction in the $Mn^{3.5+}$ oxidation state. Therefore, a lower oxidation state than 3.5 would indicate irreversibility and the presence of overlithiated LMO.

This correlation was examined in the LMO samples by analyzing the Mn 2p and Mn 3s core levels using XPS, as seen in **Figure 4.4 A**. The Mn oxidation state was obtained by fitting the $2p_{3/2}$ core level with two peaks at 641.5 eV (Mn^{3+}) and 643.1 eV (Mn^{4+}). For the pristine LMO sample, the observed Mn oxidation state was approximately 3.5 (Mn^{3+} = 50.6%, Mn^{4+} = 49.4%), consistent with stoichiometric LMO. After 2 D + 9 DD cycles, the sample cycled with Li-IL exhibited a marginally higher oxidation state (Mn^{3+} = 48.6%, Mn^{4+} = 51.4%). In contrast, the sample cycled in the conventional electrolytes displayed a decreased oxidation state (Mn^{3+}=58.9%, Mn^{4+}=41.1%).

The reduced oxidation state was also observed in the multiplet separation (ΔE) of the Mn 3s peak (**Figure 4.4 B**).[109] This separation arises from coupling the 3s and 3d electrons during

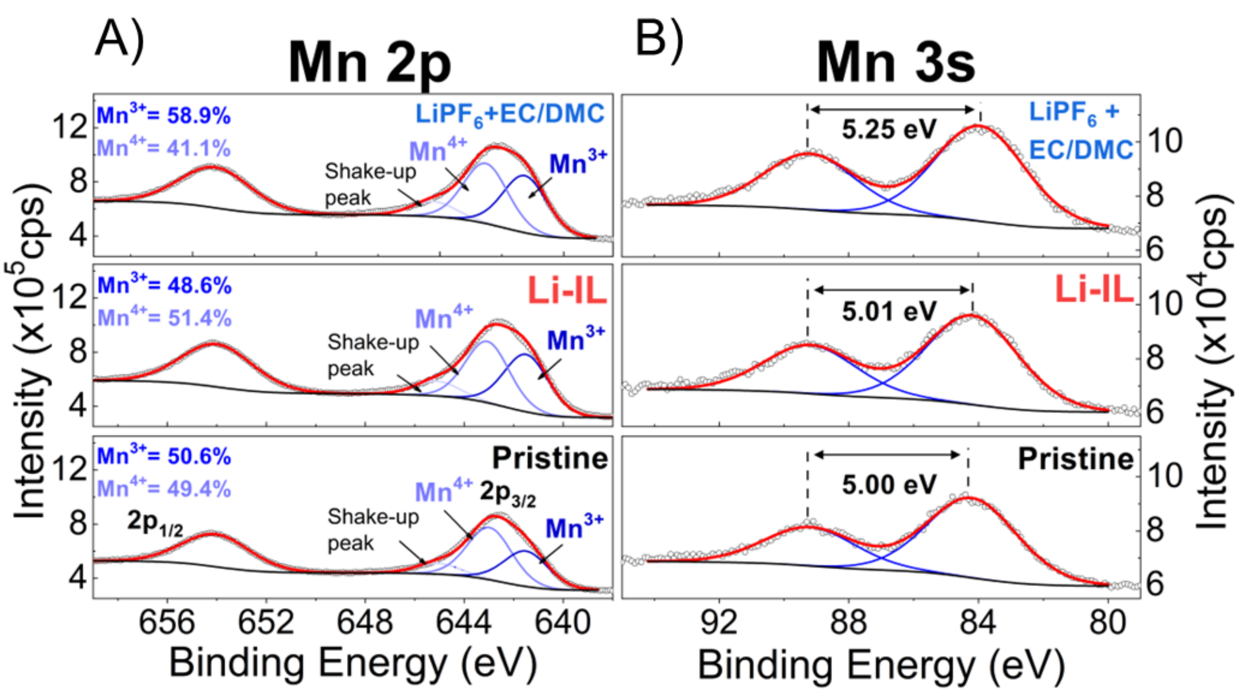

Figure 4.4. XPS of the LMO samples cycled in the two liquid electrolytes. (A) Mn 2p and (B) Mn 3s binding energies of LMO samples. The XPS is shown for the pristine LMO sample and for the samples cycled 2D + 9DD cycles in the two electrolytes.

photoelectron ejection and increases with decreasing oxidation state, as lower valence implies more electrons in the 3d orbital. The separation for the pristine samples was found to be 5.00 eV, corresponding to an ~3.5$^+$ oxidation state when compared to Mn_2O_3 (5.41 eV,$^{3+}$) and MnO_2 (4.78 eV,$^{4+}$), representing the Mn^{3+} and Mn^{4+} oxidation states, respectively.[110] The sample cycled with Li-IL showed a similar value (5.01 eV) to the pristine case, indicating stabilization of the film surface after cycling, consistent with the results obtained from the X-ray characterization. In contrast, for the $LiPF_6$+EC/DMC electrolyte, ΔE increased (5.25 eV), corresponding to a reduced oxidation state and the formation of overlithiated LMO.

To investigate the presence of crystalline tetragonal $Li_2Mn_2O_4$, XRD was performed in the vicinity of the LMO (222) Bragg peak for the pristine sample, and the samples cycled in the two electrolytes after 2 D + 9 DD cycles (**Figure 4.5**). The gray dotted lines represent the anticipated position of the cubic $LiMn_2O_4$ (222) and the tetragonal $Li_2Mn_2O_4$ (022) Bragg peaks. The sample

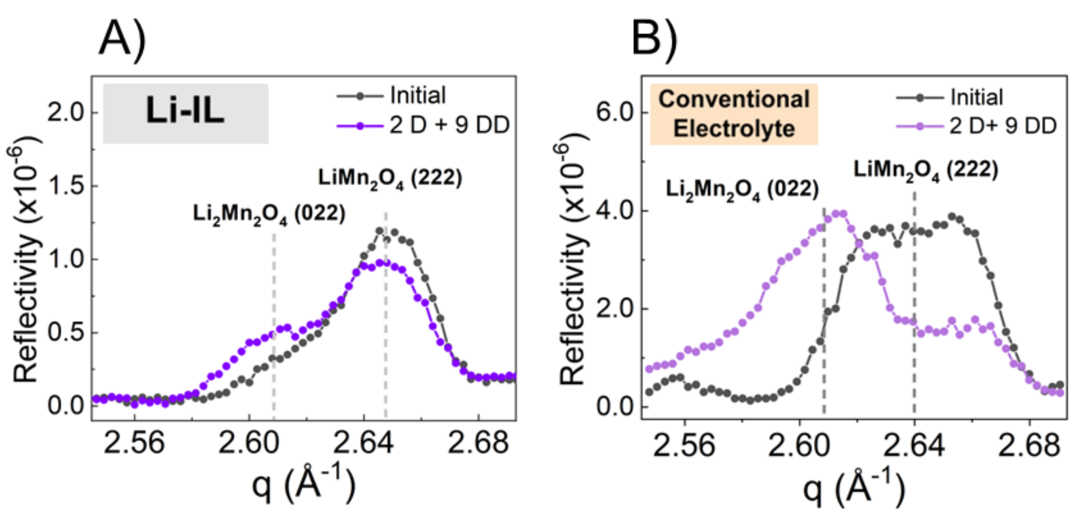

Figure 4.5. LMO (222) Bragg peak before and after cycling in the two electrolytes. LMO (222) Bragg peak after 2D + 9 DD cycles for the (A) Li-IL and the (B) conventional electrolyte. The dotted lines indicate the initial position of the cubic LMO (222) Bragg peak and the tetragonal $LiMn_2O_4$ (022) Bragg peak.

cycled in Li-IL showed a slight decrease in the $LiMn_2O_4$ (222) peak intensity and a subtle presence of $Li_2Mn_2O_4$ (022). In contrast, the LMO cycled with $LiPF_6$+EC/DMC electrolyte exhibited a higher proportion of irreversible $Li_2Mn_2O_4$. This is primarily attributed to Mn dissolution, which caused severe structural damage (together with Jahn-Teller distortions) and uneven Li diffusion in the lattice.[55] In the case of powder LMO, the appearance of this overlithiated phase was previously reported after 25 cycles in the D cycle regime (3.4-4.3 V *vs.* Li/Li^+).[55] . The irreversibility was observed after 2 D + 9 DD cycles since the DD cycles encourage more Jahn-Teller active Mn^{3+} and a further increase in the volume change of the lattice.

The dissolution of Mn and the overlithiated LMO phase presence were further investigated using HAADF STEM imaging ELLS, respectively. First, the LMO film subjected to cycling in the Li-IL electrolyte showed no dissolution, as evidenced by a film thickness close to its initial thickness before cycling (**Figure 4.6 A**, refer to **Table 4.1**). In contrast, cross-sections of the LMO cycled in the $LiPF_6$+EC/DMC revealed partial film loss in various regions within the LMO/air interface (**Figure 4.6 B**). Beyond the loss of LMO, discernible cracks in the LMO film were observed when cycled in the $LiPF_6$+EC/DMC electrolyte (**Figures 4.6 C** and **D**). These cracks have been associated with overlithiated LMO phases and exacerbated Mn dissolution.[55] Secondly, horizontal EELS line scans conducted across 200 nm-long regions of LMO films cycled in the $LiPF_6$+EC/DMC electrolyte evidenced an overlithiated phase near the LMO/air interface (**Figure 6 E** and **F**). The Mn-L_2 and Mn-L_3 edges displayed energy redshifts of 1.3 eV and 0.5 eV, respectively, for the over-lithiated location (close to the grain edge) compared to the bulk. These energy shifts are consistent with previous EELS studies of LMO cycled in $LiPF_6$+EC/EMC and

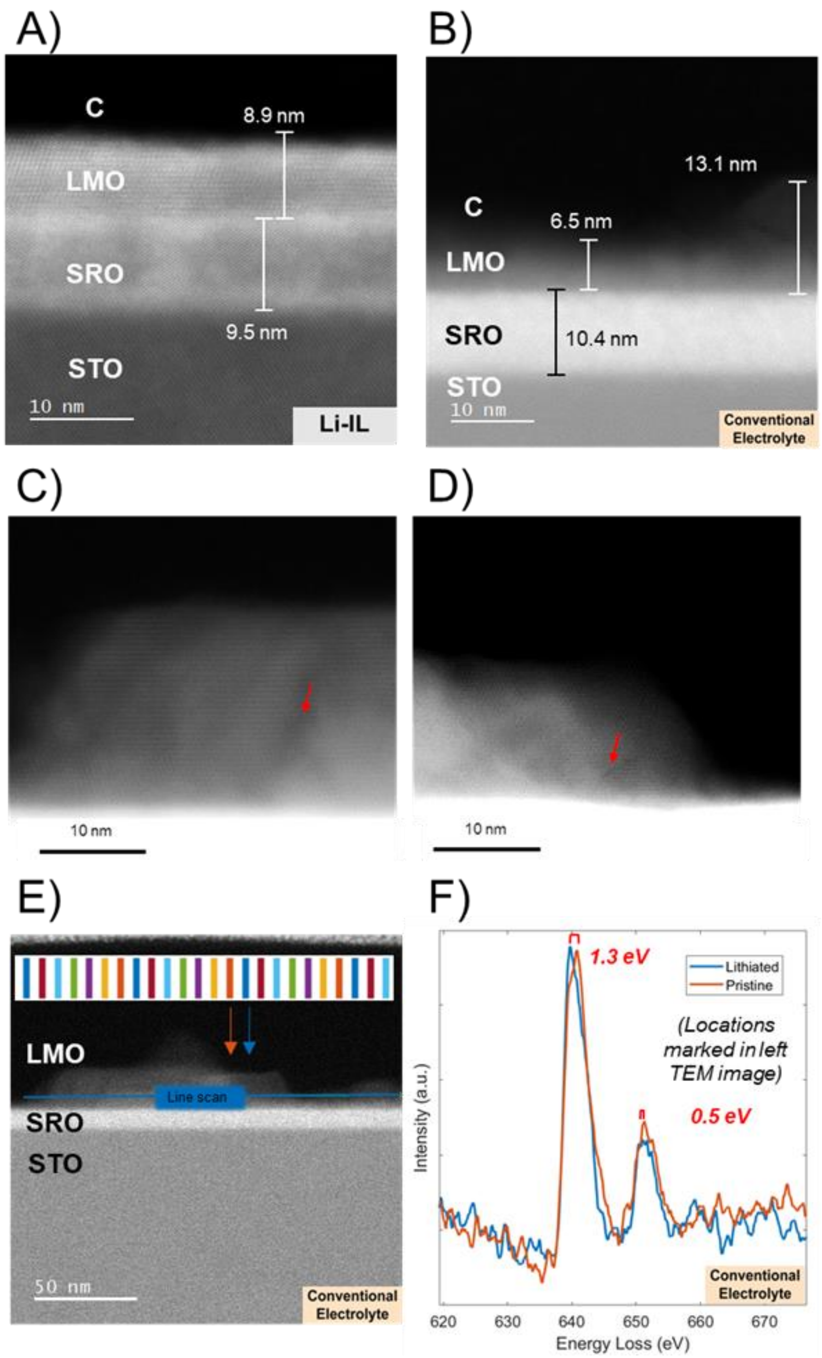

Figure 4.6. STEM/EELS of the LMO samples cycled in the liquid electrolytes. Cross-section STEM of the LMO samples cycled in the (A) Li-IL and (B) $LiPF_6$+EC/DMC electrolytes. (C) and (D) show cracks in the LMO cycled in $LiPF_6$+EC/DMC electrolyte**.** (E) EELS horizontal profile of the sample cycled in the $LiPF_6$+EC/DMC electrolyte. (F) Selected EELS spectra of two locations of the LMO sample showing a lithiated and non-lithiated phase.

EC/DMC[55, 111] and further support the XRD data indicating the generation of overlithiated $Li_2Mn_2O_4$. In contrast, the sample cycled in Li-IL showed high structural stability and no presence of such a phase.

4.6 Stability of $LiMn_2O_4$ in h-BN Ionogel Electrolyte

The interfacial and structural evolution of the LMO was investigated in an ionogel composed of h-BN nanoplatelets and the identical Li-IL electrolyte employed previously (Li-TFSI + EMIM TFSI). This ionogel, denoted as h-BN/Li-IL, was used to cycle the epitaxial LMO thin film 2 D + 9 DD cycles. The CV profile (**Figure 4.7 A**) shows two redox peaks in the 4 V region with minimal

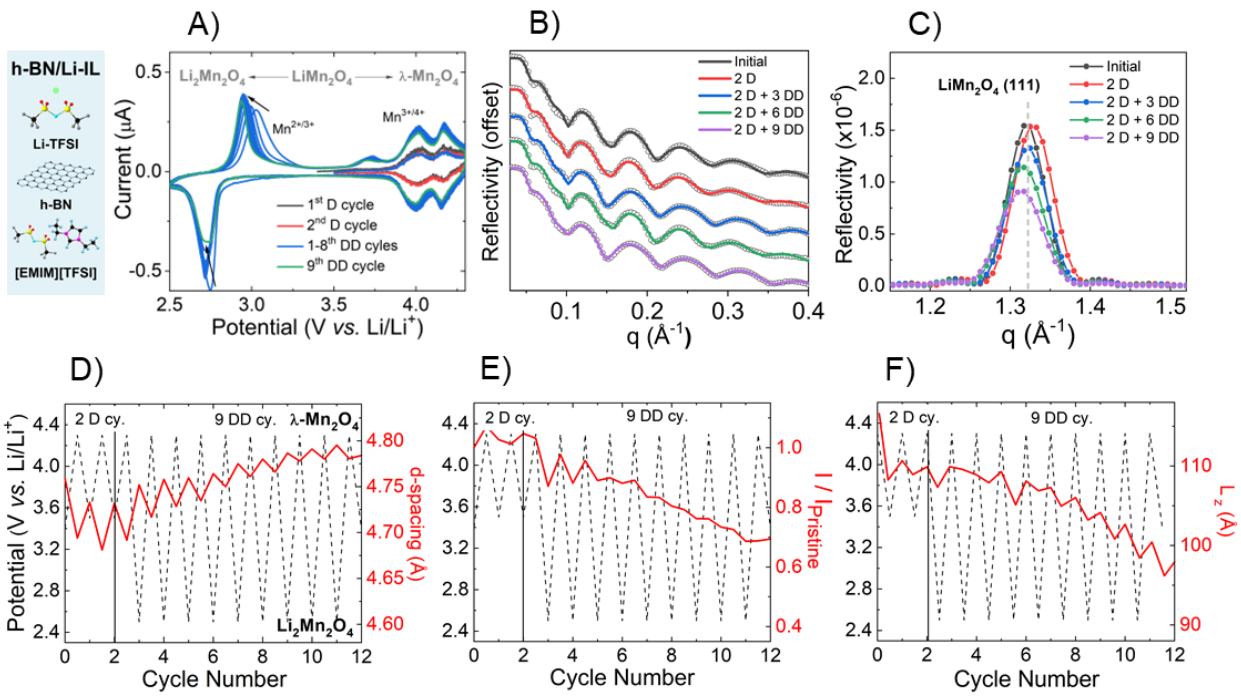

Figure 4.7. ***In situ*** **XRR/XRD of the LMO cycled in the h-BN/Li-IL electrolyte.** (A) Cyclic voltammetry of the LMO (111) cathode. (B) XRR with fit, and (C) XRD as a function of the voltammetry cycles measured at 3.5 V. The XRR plot includes the fitting. Evolution of the (D) d-spacing, (E) domain size, and (F) integrated intensity from the LMO (111) Bragg peak during cyclic voltammetry. The *dashed lines* illustrate the voltage changes during cycling. shown for the LMO (111) Bragg peak.

polarization (0.01 V). However, within the 3 V region, the redox peaks at 3.03/2.72 V exhibited an increase of polarization after 9 DD cycles (0.03-0.08 V).

The *in situ* XRR and XRD results for the LMO cycled in h-BN/Li-IL around 3.5 V across selected cycles are depicted in **Figures 4.7 B** and **C**, respectively. The XRR analysis showed no evidence of changes in the LMO thickness, accompanied by a subtle increment of 24% in roughness, indicative of complete suppression of Mn dissolution. **Table 4.5** summarizes the XRR fittings parameters around 3.5 V vs Li/Li^+. The fitted parameters include the electron density (ED) of the LMO, the thickness (t) of the LMO and SRO, and the roughnesses of the different interfaces (σ). However, the LMO (111) Bragg peak shows a 30% reduction in the integrated intensity after 2 D + 9 DD cycles. This decline is attributed to an overall loss in film crystallinity and mosaicity, which is evident through the broadening of the (111) Bragg peak and respective RC. Estimations of L_z (Eq. S1) and L_x (Eq. S2) revealed a 15% decrease in L_z and a 26% decrease in L_x post 2 D + 9 DD cycles. **Table 4.6** summarizes the XRR and XRD results for the sample before and after 2 D + 9 DD cycles, including the observed changes in thickness, roughness, crystalline domain size, and mosaicity.

	t_{LMO} (Å)	ED_{LMO} (e/Å^3)	σ_{LMO} (Å)	t_{SRO} (Å)	$\sigma_{SRO\text{-}LMO}$ (Å)	$\sigma_{STO\text{-}SRO}$ (Å)
Initial	104.6	1.16	10.9	91.4	3.5	5.2
2 D	105.3	1.12	10.5	92.6	3.3	5.6
2 D + 3 DD	104.2	1.17	13.0	90.2	3.4	4.8
2 D + 6 DD	104.3	1.13	10.0	92.6	3.5	5.5
2 D + 9 DD	105.2	1.20	15.4	89.3	3.1	4.8

Table 4.5. XRR fitting parameters of the LMO cycled in the h-BN/Li-IL electrolyte. Two parameters were fixed in the fitting: The following electron densities were fixed in the fitting: STO (1.42 $e^-/Å^3$), SRO (1.76 $e^-/Å^3$), and h-BN/Li-IL electrolyte (0.45 $e^-/Å^3$).

The evolution of the LMO (111) Bragg peak, including the d-spacing, I/Ipristine, and L_z, was tracked during electrochemical cycling (**Figure 4.7 D-F**). For clarity, only data points corresponding to half-integer and integer cycles are shown in solid red lines, while the voltage progression is depicted in dashed lines. The d-spacing of the LMO (111) Bragg peak ($d=2\pi/q_{111}$) indicates the lattice's lithiation state during electrochemical cycling. Three zones can be distinguished during the continuous (de)lithiation process of the $Li_xMn_2O_4$: Mn_2O_4, $LiMn_2O_4$, and $Li_2Mn_2O_4$. The latter one is accessible during DD cycles. The evolution of the d-spacing (**Figure 4.7 D**) exhibits an oscillatory behavior reflective of the (de)lithiation process during the D and DD cycles. However, upon subsequent entry into the DD regime, a reduction in the overall (de)lithiation amplitude and an increase in the d-spacing are observed. This behavior suggests the formation of a non-reversible overlithiated $Li_xMn_2O_4$ phase.

Additionally, the normalized integrated intensity (**Figure 4.7 E**) and L_z (**Figure 4.7 F**) show a consistent decrease, evidence of loss of crystallinity and an irreversible mechanism occurring within the lattice. Previously, our studies on the Li-IL liquid electrolyte with no h-BN showed no Mn dissolution but less impact on the crystallinity when compared to the ionogel.[112] Previously, using a metal-ion chelating polymer (Pyd-PVA-CN) gel electrolyte improved LMO's capacity

		h-BN/Li-IL		
		Pristine	Cycled	Change
XRR	LMO thickness (Å)	104.0	103.9	**0%**
	LMO roughness (Å)	14.0	17.4	+24%
XRD	Vertical Domain Size L_z (Å)	110.0	95.5	**-15%**
	Horizontal Domain Size L_x (Å)	1050	780	-26%
	Change in area of LMO (111)	-30%		

Table 4.6. XRR/XRD results of the LMO cycled in the h-BN/ Li-IL electrolyte.

retention by mitigating Mn ions' dissolution.[113] **Table 4.6** summarizes the XRR/XRD before and after 2 D + 9 DD cycles in the h-BN/Li-IL electrolyte.

The LMO cycled in h-BN/Li-IL electrolyte revealed no indication of Mn dissolution but exhibited pronounced irreversibility in its structural properties. One plausible explanation for such irreversibility is the Jahn-Teller distortion from the cubic $LiMn_2O_4$ to the tetragonal $Li_2Mn_2O_4$ during DD cycles. The persistence of such phase was validated by *in situ* XRD measurements conducted near the LMO (222) Bragg peak during operation around 3.5 V and confirmed by *ex situ* XPS measurements after cycling.

Figure 4.8 depicts a marginal decrease in the LMO (222) Bragg peak after 2 D cycles, followed by the emergence of $Li_2Mn_2O_4$ (022) after the 9 DD cycles. Such a phase is irreversible as it deviates from the expected phase at the state of charge of 3.5 V. Moreover, the *ex situ* XPS spectra for the Mn 2p and Mn 3 s peaks (**Figures 4.8 B** and **C**) demonstrate an increased Mn^{3+} oxidation

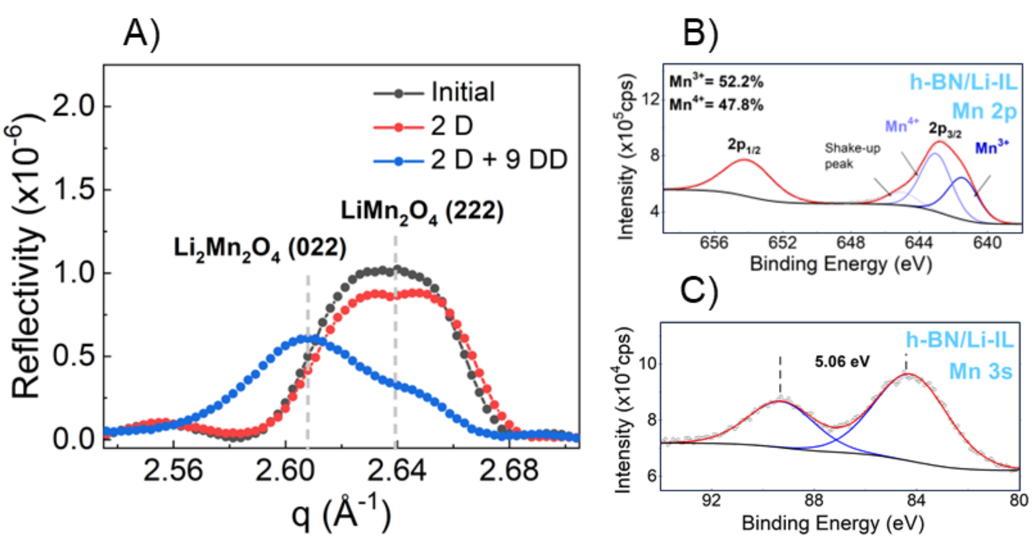

Figure 4.8. Formation of $Li_2Mn_2O_4$ after cycling in the h-BN/Li-IL electrolyte. (A) *In situ* LMO (222) Bragg peak measurements at three stages during cycling. The dotted lines indicate the initial position of the cubic $LiMn_2O_4$ (222) Bragg peak and the tetragonal $Li_2Mn_2O_4$ (022) Bragg peak. *Ex situ* (B) Mn 2p and (C) Mn 3s spectra of the LMO sample after 2 D + 9 DD cycles.

state, characteristic of $Li_2Mn_2O_4$. The Mn 2p fitting reveals a slight increase in the Mn^{3+} (52.2 %) and a 5.05 eV separation in the Mn 3s. For stoichiometric $LiMn_2O_4$, Mn^{3+} is anticipated at 50%, and the Mn 3s peak separation is at 5.00 eV. Notably, our previous study on the Li-IL (i.e., liquid and without h-BN) exhibited no discernible increment in the presence of Mn^{3+} or splitting in the Mn 3s peak.[112]

The generation of $Li_2Mn_2O_4$ is commonly associated with Mn dissolution, typically observed in carbonate-based electrolytes. Previously, our group demonstrated such presence via *ex situ* XRD, STEM, and XPS.[112] Liu *et al.* elaborated on the mechanism, proposing that surface Mn dissolution leads to structural damage and uneven Li diffusion, thereby triggering irreversible $Li_2Mn_2O_4$ generation via Jahn-Teller distortion, particularly when accessing DD cycles.[55] This phase transformation is particularly noticeable within surface cracks, where uneven Li diffusion is expected.

However, in the context of the h-BN/Li-IL, where the Li-IL electrolyte suppresses Mn dissolution[112], an alternative explanation is required for the occurrence of $Li_2Mn_2O_4$. One explanation lies in the inadequate wetting behavior of gel-based electrolytes, causing challenges in establishing intimate contact between the electrode and the electrolyte.[114] The voids along the LMO-hBN/Li-IL interface result in localized areas experiencing high Li current densities, thereby facilitating the formation of $Li_2Mn_2O_4$ despite the absence of Mn dissolution.

Figure 4.9 depicts the schematic detailing the mechanisms involved in the $Li_2Mn_2O_4$ formation mechanisms during electrochemical cycling, explicitly considering the absence of Mn dissolution. As Li^+ ions undergo diffusion throughout the (dis)charging processes, they navigate through regions of high density, particularly near the voids in the electrode/electrolyte interface. This

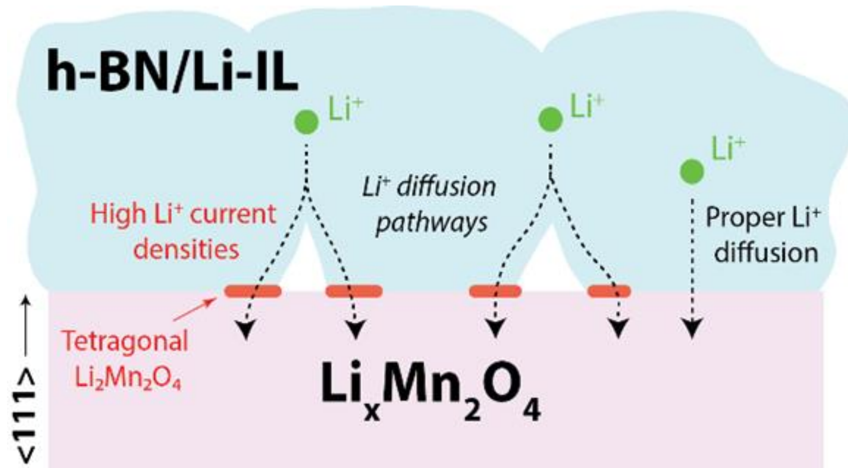

Figure 4.9. Schematic of the irreversible phase transition in LMO cycled in the ionogel. The transition occurs from cubic $LiMn_2O_4$ to tetragonal $Li_2Mn_2O_4$ in regions of poor contact when using the h-BN/Li-IL electrolyte.

movement through high-density pathways can promote the localized generation of $Li_2Mn_2O_4$. Similar behavior has been observed in a nanowire battery system employing an ionic liquid electrolyte consisting of Li-TFSI salt and PP13TFSI ionic liquid.[115] There, the formation of the $Li_2Mn_2O_4$ phase was observed through *in situ* electron diffraction near the interface, proximal to the ionic liquid. This observation was attributed to the localized accumulation of Li^+ around the nanowire base, suggesting that high Li^+ concentration regions prompt the generation of $Li_2Mn_2O_4$.

The void problem found in the sample cycled with h-BN/Li-IL can be alleviated by improving the interfacial contact. A Li-IL layer was introduced between the LMO and the h-BN/Li-IL to wet the LMO thin film. I*n situ* XRR/XRD was performed for 2 D + 3 DD due to beamline time limitations (**Figure 4.10 A-C**). **Table 4.7** summarizes the XRR fittings parameters around 3.5 V vs Li/Li^+. **Figure 4.10 D-F** depicts the evolution of the d-spacing, I/Ipristine, and L_z for the sample with the Li-IL interlayer (Li-IL+h-BN/Li-IL). Compared to the LMO cycled in the h-BN/Li-IL electrolyte (**Figure 4.10 D-F**), all the parameters tend to an equilibrium position. First, there is no evidence of over-lithiation after 2 D + 3 DD cycles in the Li-IL+h-BN/Li-IL, and the amplitude of the

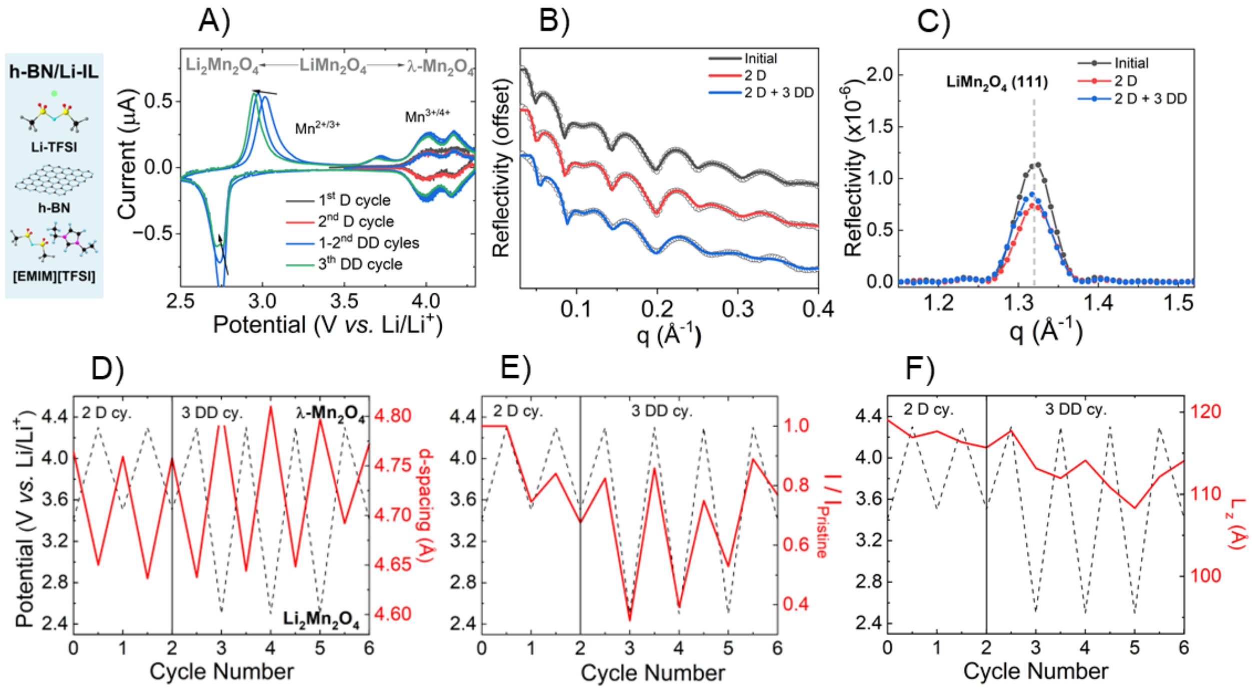

Figure 4.10. *In situ* XRR/XRD of the LMO cycled in the Li/IL+h-BN/Li-IL electrolyte. (A) Cyclic voltammetry of the LMO (111) cathode. (B) XRR with fit and (C) XRD as a function of the voltammetry cycles measured at 3.5 V. D Evolution of the (D) d-spacing, (E) domain size, and (F) integrated intensity from the LMO (111) Bragg peak during cyclic voltammetry. The *dashed lines* illustrate the voltage changes during cycling. shown for the LMO (111) Bragg peak.

(de)lithiation is broader and constant. The I/Ipristine and L_z values slightly decrease after the 2 D cycles but tend to be in equilibrium, differing from the h-BN/Li-IL, where the values continually decrease after cycling.

	t_{LMO} (Å)	ED_{LMO} (e^-/Å^3)	σ_{LMO} (Å)	t_{SRO} (Å)	$\sigma_{SRO\text{-}LMO}$ (Å)	$\sigma_{STO\text{-}SRO}$ (Å)
Initial	114.2	1.28	6.6	66.9	3.3	6.4
2 D	113.5	1.30	7.5	66.9	3.5	6.5
2 D + 3 DD	112.0	1.33	9.8	67.5	3.0	6.2

Table 4.7. XRR fitting parameters used for the LMO cycled in the Li/IL+h-BN/Li-IL electrolyte. The following electron densities were fixed in the fitting: STO (1.42 e^-/Å^3), SRO (1.76 e^-/Å^3), and h-BN/Li-IL electrolyte (0.45 e^-/Å^3).

Table 4.8 compiles the XRR/XRD results for the cycling experiment employing Li-IL+h-BN/Li-IL. As anticipated, there was no effect from Mn dissolution, evident in a marginal thickness reduction of only 2 Å, potentially attributed to the observed increase in roughness (from 6.7 Å to 10.3 Å). The crystalline domain sizes, both L_z and L_x, experienced a moderate decrease of 7% and 13% after 2 D + 3 DD cycles, while I/Ipristine decreased 23%. These outcomes imply that incorporating a Li-IL interlayer contributes to increasing the stability of the LMO cathode within the h-BN/Li-IL system. This arrangement improves the interfacial contact between the LMO electrode and the h-BN/Li-IL electrolyte, enhancing the overall structural stability during cycling.

4.7 Summary

The stability of single-crystal epitaxial LMO (111) thin films was studied for two different electrolytes: 1 M LiTFSI in EMIM-TFSI (Li-IL) and 1 M $LiPF_6$+EC/DMC (50/50 v.%) (conventional electrolyte). The films were cycled nine times in the 2.5-4.3 V range to access two Li^+ extraction/insertion processes in LMO and to enhance the formation of Mn^{3+}, which is prone to dissolution. The LMO cycled with Li-IL-based electrolytes showed considerably higher

		h-BN/Li-IL + Li-IL		
		Pristine	**Cycled**	**Change**
XRR	LMO thickness (Å)	114.0	112.0	**-2%**
	LMO roughness (Å)	6.7	10.3	+54%
XRD	Vertical Domain Size L_z (Å)	114.8	106.8	**-7%**
	Horizontal Domain Size L_x (Å)	300	260	-13%
	Change in area of LMO (111)	-23%		

Table 4.8. XRR/XRD of the LMO cycled in the Li-IL+h-BN/Li-IL electrolyte.

electrochemical and structural stability than its conventional electrolyte counterparts. The source of this improvement was attributed to the suppression of Mn dissolution in the Li-IL-based electrolyte, which is due to the reduced susceptibility of salt hydrolysis and solvent decomposition. *In situ* XRR/XRD showed stability in the thickness and crystallinity of the film when accessing the 2.5-4.3 V voltage range in the Li-IL electrolyte. ICP-MS analysis and STEM inspection of the LMO cycled in Li-IL showed negligible loss of Mn after cycling.

In contrast, the LMO cycled in the conventional electrolyte was unstable due to severe Mn dissolution. Through extensive *ex situ* characterization, including XRD, XPS, and EELS, we found that the Mn dissolution triggers overlithiated and irreversible LMO phases, which deteriorates the cycling performance of the cathode. Overall, these results show the importance of electrolyte selection and compatibility as critical factors that control the chemical and structural stability of transition metal LIB cathodes.

Apart from utilizing the two liquid electrolytes, an ionogel formulation (h-BN/Li-IL) composed of the same ionic liquid and h-BN nanoplatelets was employed to investigate the interfacial and structural evolution of the LMO cathode. Similar to the Li-IL electrolyte, the ionogel prevented Mn dissolution. However, irreversible $Li_2Mn_2O_4$ was unexpectedly observed after 2 D + 9 DD cycles. This finding was attributed to inadequate contact between the gel and the surface of the LMO, leading to the creation of voids where high Li^+ current densities are concentrated, consequently facilitating the localized generation of $Li_2Mn_2O_4$. Beyond the formation of the overlithiated phase, the inadequate contact adversely impacted the overall crystallinity of the LMO and compromised its reversibility during cycling. Incorporating a Li-IL interlayer addressed the issues associated with inadequate contact, improving the structural integrity of the LMO cathode and enhancing its stability during cycling.

4.8 Experimental Methods

4.8.1 Sample Preparation

LMO (111) / SRO (111) thin films were grown by PLD on 10 mm × 3 mm STO (111) substrates (MTI Corp.). The substrates were etched in buffered oxide etch BOE (7:1) solution for 30 s, rinsed with DI water, and annealed at 1050 °C for 3 hr in oxygen flow. This procedure allowed a Ti-terminated and step-terraced STO surface.[116] The deposition was performed in a PVD Products nanoPLD 1000, which employed a 248 nm KrF excimer laser focused onto a rectangular 1.5 mm × 3.5 mm spot. The conductive SRO layer (9 mm × 3 mm) was deposited from a stoichiometric target (QS Advanced Materials) at 60 mJ/pulse and 1 Hz. The SRO deposition was accomplished at 550°C in 50 mTorr O_2 and further annealing at 100 Torr O_2 for one hr at the same temperature. The LMO layer (4 mm × 3 mm) was deposited on the SRO/STO sample from an LMO target (Kurt J. Lesker) containing 30% excess of Li_2O ($Li_{1.3}Mn_2O_{4.14}$) to account for the Li loss during ablation at 140 mJ/pulse and 5 Hz. The LMO deposition was accomplished at 400°C in 75 mTorr O_2 and further annealing at 75 mTorr of O_2 atmosphere for one hr at the same temperature.

The Li-IL was prepared by dissolving 1 M lithium bis-(trifluoromethylsulfonyl)imide (LiTFSI) (99.95%, trace metal basis, Sigma-Aldrich) salt in 1-ethyl-3-methylimidazolium bis(trifluoromethylsulfonyl) imide (EMIM-TFSI) ($H_2O \leq 500$ ppm, Sigma-Aldrich) by stirring at 120°C for 24 hr. The h-BN nanoplatelets were produced following prior work, which was then mixed with the Li-IL (Li-IL/h-BN=60%/40% wt.) using a mortar and pestle.[71] The conventional electrolyte ($LiPF_6$+EC/DMC) is composed of 1 M lithium hexafluorophosphate ($LiPF_6$) in 50/50 v/v ethylene carbonate/dimethyl carbonate (Millipore Sigma). The electrolyte preparation and cell assembly were performed in an argon-filled glovebox.

4.8.2 Cyclic Voltammetry

The LMO/SRO/STO (10 mm × 3 mm) samples were individually sealed in X-ray transmission cells inside an Ar glovebox. The LMO thin films were fully immersed in the liquid electrolytes (~8 mL). For the ionogel, a spatula was used to manually put the electrolyte (~ 0.1 g) on top of the film to achieve ionic contact with a Li metal counter electrode (0.75 mm thick, Alfa Aesar) located approximately 5 mm above the sample.[42,43] The transmission cell was removed from the glovebox and connected to an electrochemical workstation (CHI760E) to perform cyclic voltammetry. Details about the cell setup, including a schematic and an image showing the acquisition/measurement procedure, can be found in **Figure 4.11**. The CV was performed in two different voltage ranges: standard discharge (D) cycles between 3.5 V and 4.3 V *vs.* Li/Li^+ ($0 < x < 1$) at 0.2 mV/s and deep discharge (DD) cycles between 2.5 V and 4.3 V *vs.* Li/Li^+ ($0 < x < 2$) at 0.5 mV/s. After the last cycle, a final discharge from 4.3 to 3.5 V was performed to return to the initial state of charge.

4.8.3 *In situ* X-ray Characterization

In situ XRR and XRD were performed at beamline 33BM-C at the Advanced Photon Source. The cells were mounted on a four-circle diffractometer with incoming X-rays (λ = 0.6199 Å) collimated into a 0.2 mm × 1 mm beam. The data were continuously acquired with a Pilatus 100k 2D detector during electrochemical cycling (**Figure 4.11C)**. All the XRR analyses were done using Motofit with a multiple-slab model and fixed electron densities.[14]

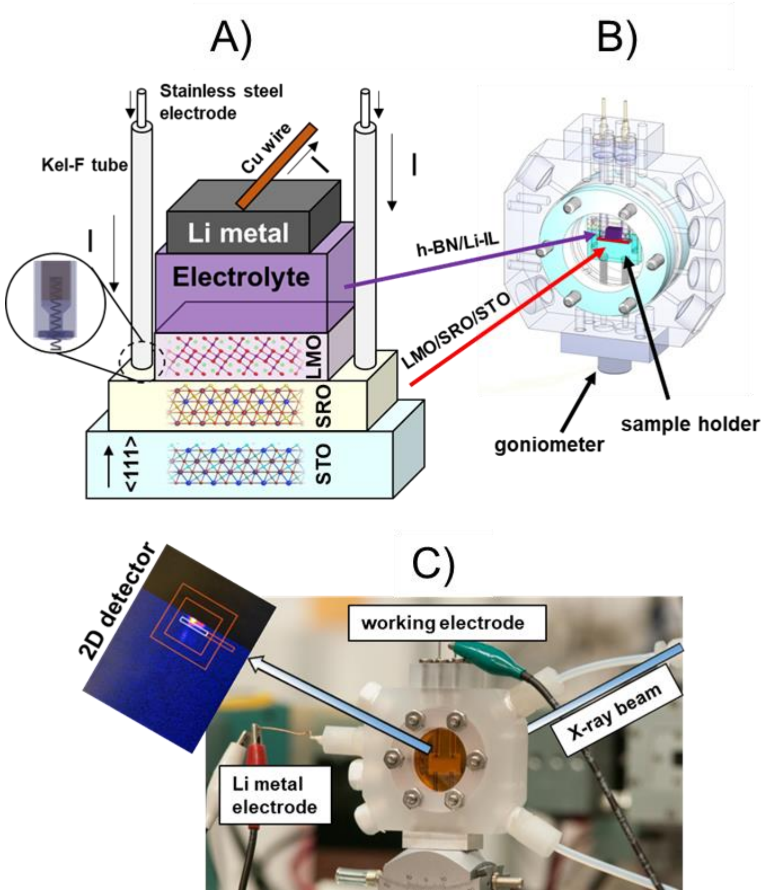

Figure 4.11. *In situ* XRR/XRD experimental setup for LIB characterization. (a) Schematic of the thin film model system used to study the LMO/electrolyte interface by *in situ* XRR/XRD (a). (b) Schematic of the electrochemical cell. (c) Photograph of the electrochemical cell and schematic of the incident and reflected X-ray beams, and the 2D detector (c). The data is acquired during continuous cycling while rotating the *2θ* axis (detector) and the axis (electrochemical cell). The specular scattering is integrated into the white rectangle area while and background is collected in the red rectangle.

4.8.4 *Ex situ* X-ray Characterization

Ex situ XRR and XRD measurements were performed in a Rigaku ATXG diffractometer with an 18 kW Cu rotating anode (λ = 1.5418 Å) and a 0.1 mm × 2 mm collimated beam. High-resolution measurements were achieved using a Ge (220) 2-bounce monochromator (λ = 1.5406 Å). All the measurements were normalized to the measured incident beam intensity, and the results are plotted in terms of the scattering vector $q = 4\pi \frac{Sin(\theta)}{\lambda}$. XRR data were corrected for footprint and diffuse scattering signal. Off-specular φ scans were performed in a Smartlab Gen 2 diffractometer equipped with a 9 kW Cu rotating anode (λ = 1.5418 Å) and a χ circle using a 0.05 mm × 2 mm collimated beam and two 0.5° Soller slits.

4.8.5 X-ray Photoelectron Spectroscopy

Spectra were acquired in a Thermo Scientific ESCA Lab 250Xi XPS spectrometer equipped with a monochromated Al Kα X-ray source (E = 1486.6 eV). The samples were analyzed with a spot size of ~500 μm and a flood gun for charge compensation. The Mn 2p and 3s spectra consisted of an average of eight spectra with a pass energy of 50 eV and dwell time of 75 s and 120 s, respectively. The analysis was performed using the Avantage (Thermo Scientific) software in which the core levels were fitted using a modified Shirley background correction and Gaussian-Lorentzian product (70% Gaussian and 30% Lorentzian). All the peaks were charge-corrected to adventitious carbon (C 1s) at 284.8 eV. The Mn oxidation state was analyzed by quantifying the $Mn^{3+/4+}$ area in the $2p_{3/2}$ peak and the multiplet split of the Mn 3s peak. For the $2p_{3/2}$ fitting, the position corresponding to Mn^{3+} and Mn^{4+} was located at 641.5 eV and 643.1 eV, respectively, allowing a shift of only ±0.1 eV.

4.8.6 Inductively Coupled Mass Spectroscopy

Quantifying manganese in the liquid electrolytes after cycling was accomplished using ICP-MS. After electrochemical cycling, the electrolytes were digested in concentrated trace nitric acid (> 69%, Thermo Fisher Scientific) at 65°C for 3 hours and at room temperature overnight to allow full digestion. Ultra-pure H_2O (18.2 MΩ·cm) was then added to produce a final solution of 3.0%

nitric acid (v/v) in a total sample volume of 5 mL (100 μL digested sample, 150 μL HNO_3 and 4.75 mL H_2O). Quantitative standards were made using a 100 μg/mL Mn elemental standard (Inorganic Ventures), which was used to create a 20 ng/mL mixed element standard in 3.0% nitric acid (v/v) in a total sample volume of 50 mL. ICP-MS was performed on a computer-controlled (QTEGRA software) Thermo iCapQ ICP-MS (Thermo Fisher Scientific) operating in KED mode and equipped with an ESI SC-2DX PrepFAST autosampler (Omaha). The internal standard was added inline using the prepFAST system and consisted of 1 ng/mL of a mixed element solution containing Bi, In, ^{6}Li, Sc, Tb, and Y (IV-ICPMS-71D from Inorganic Ventures). Finally, LMO (Sigma Aldrich) powders (~4 mg each) were immersed in 1 mL of ionic liquid and conventional electrolyte.

4.8.7 Transmission Electron Microscopy

Cross-sectional TEM lamellas were prepared using a dual-beam FIB FEI Helios Nanolab 600 operating at 30 kV with a Ga source. A set of C and Pt layers protected the samples from beam damage. High-resolution STEM images were obtained using an aberration-corrected JEOL ARM200CF microscope at 200 kV. Images were collected using a JEOL HAADF detector (90-370 mrad) with an 8 µs dwell time. In addition, EELS was acquired with a Gatan DualEELS detector (~0.1 eV energy resolution) to analyze the Mn-$L_{2,3}$ edges at different locations of the samples to detect lithiated and non-lithiated LMO.

CHAPTER 5:

ULTRA-SMOOTH EPITAXIAL PT THIN FILM ELECTRODES DEPOSITED BY PULSED LASER DEPOSITION

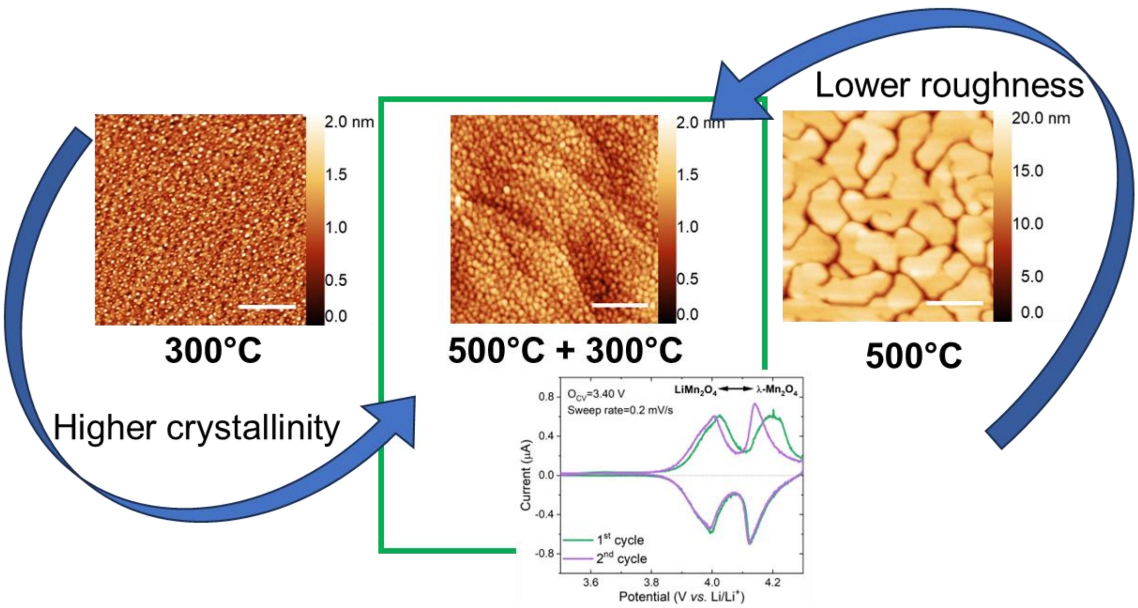

This chapter is adapted from:

Torres-Castanedo C. G., Buchholz D. B., Pham T., Zheng L., Cheng M., Dravid V. P., Hersam M. C. & Bedzyk M. J. (2024). Ultra-Smooth Epitaxial Pt Thin-Films Grown by Pulsed Laser Deposition. *ACS Applied Materials & Interfaces, 16*(1), 1921-1929.

5.1 Overview

Platinum (Pt) thin films are useful in applications requiring electrodes with high conductivity and excellent thermal and chemical stability. In the context of LIBs, these films act as current collectors, facilitating the efficient flow of electrons during electrochemical cycling, thereby ensuring optimal battery performance. Additionally, ultra-smooth and epitaxial Pt thin films offer the advantage of serving as optimal templates for the subsequent growth of heteroepitaxial structures, such as active electrode materials utilized in LIBs.

This chapter focuses on achieving epitaxial growth of Pt (111) electrodes on sapphire (α-Al_2O_3 (0001)) substrates via PLD. In the previous chapter, SRO (111) thin films were used as electrodes in the different LIB setups, facing challenges such as forming islands and bunched surfaces depending on the deposition conditions.[117] The morphology of SRO strongly relies on the deposition rate and temperature, nominal thickness, and miscut of the substrate.[118] Additionally, the limited availability of large-wafer STO substrates posed constraints for commercial applications, hence the motivation to explore Pt on wafer-scale sapphire.

The investigation encompassed experimentation with various gaseous environments and temperatures to achieve epitaxial growth while ensuring minimal surface roughness. Employing a two-step growth process of 500°C and 300°C yielded films with improved epitaxy, maintaining ultra-smooth interfaces (<3 Å) and featuring high electrical conductivity (6.9×10^6 S/m). Subsequently, these Pt films were used as current collectors and templates for the epitaxial growth of lithium manganese oxide ($LiMn_2O_4$ (111)) thin films, a cathode material used in LIBs. These films demonstrated high stability when subjected to electrochemical cycling in the range of 3.5-4.3 V *vs.* Li/Li^+ in a novel solid-state ionogel electrolyte.

5.2 Background

Pt possesses high electrical conductivity alongside exceptional thermal and chemical stability. These unique properties make Pt thin films pivotal in fundamental research, serving multiple roles as catalyst[119, 120], adatom templates[121, 122], seeding layers[123-126], and current collectors[125, 127-132]. Diverse techniques exist for growing high-quality Pt thin films, such as molecular beam epitaxy (MBE)[123, 133-137], metalorganic chemical vapor deposition (MOCVD)[138, 139], sputtering[132, 137, 140-143], and pulsed laser deposition (PLD).[125, 144-147]

Smooth epitaxial Pt thin films serve as excellent templates for the subsequent high-quality thin films. Pt has proven effective in facilitating the epitaxial growth of various thin films, including Fe_2O_3[124], $LuFeO_3$[125], ZnO[148], Fe_3O_4[149], graphene[150], and diamond[151]. In several cases, the Pt interlayer reduces the dislocation density[124] and strain[125] in subsequent films compared to direct deposition on a non-conductive single-crystal substrate. The appropriate substrate with low lattice mismatch is needed to achieve highly crystalline Pt films. Notably, Pt has been successfully grown epitaxially on substrates like MgO[140, 145, 146, 152], $SrTiO_3$[137, 152, 153], $LaAlO_3$[152], YSZ,[132, 147, 154] and α-Al_2O_3 (sapphire)[134-136, 155-158]. The commercial availability of wafer scale α-Al_2O_3 has led to its extensive use as a substrate for Pt growth, resulting in (111) orientation upon deposition on α-Al_2O_3 (0001). The epitaxy is facilitated by a low lattice mismatch (0.9%) between Pt (111) and α-Al_2O_3 (0001), reducing the dislocation density at the interface.[155]

Despite considerable advancements, achieving epitaxial, ultra-thin, and smooth Pt film growth remains challenging. For instance, increasing the deposition temperature to enhance crystallinity results in three-dimensional (3D) island formation and increased surface roughness.[147] Post-deposition annealing procedures are often employed to convert the island morphology into a better-defined thin film to address this issue.[155] However, this approach requires relatively thick films (ranging from 200 nm to 1 μm),[132, 155] which are incompatible with thin-film current collector applications.

Other strategies for Pt film growth involve introducing oxygen during deposition, which aids epitaxy by promoting a single in-plane orientation necessary to eliminate additional parasitic twining of the Pt crystallites.[137, 155] Alternatively, Pt electrodes have been grown using a Ti adhesion layer.[159] Nevertheless, rapid diffusion of Ti atoms through the Pt electrodes can lead to a Ti-rich Pt surface, prone to oxidation, compromising subsequent Pt deposition at high temperatures.[137, 159] These limitations underscore the need for alternative strategies to achieve smooth, thin, high-quality Pt films.

5.3 Optimization of Epitaxial and Ultra-Smooth Pt Electrodes Grown by PLD

The deposition of Pt thin films was studied under two distinct atmospheres (10 mTorr Ar and 10 mTorr 67%Ar + 33%O_2) across three different deposition temperatures (25°C, 300°C, and 500°C). Surface morphology was examined using AFM (**Figure 5.1**). Overall, the roughness of the films' root mean square (RMS) increases with temperature (**Table 5.1**). Specifically, Pt films deposited at 25°C exhibited a minimal roughness of less than 2 Å, resembling the sapphire substrate. At 300°C, the roughness increased to less than 6 Å. Notably, films grown at 500°C displayed a distinct percolating network of elongated islands, indicative of 3D island growth mode[147]. This morphology contributed significantly to an elevated RMS (>20 Å) due to the inhomogeneity of the films, resulting in 10-15 nm deep trenches. Notably, the sample deposited in Ar at 500°C displayed more coalesced grains than those in Ar+O_2. The grain morphology of the 300°C samples

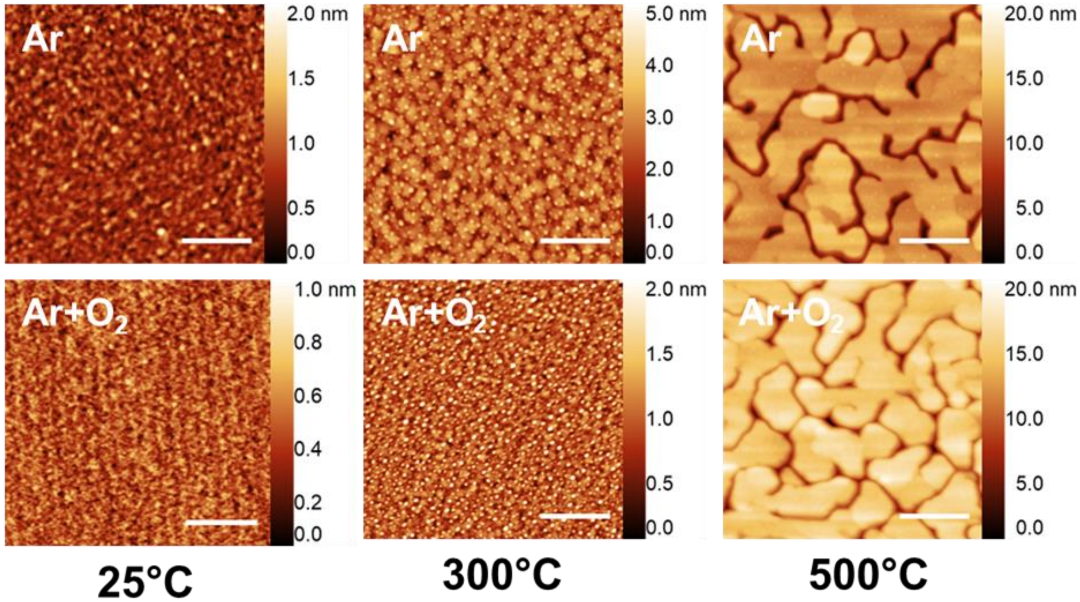

Figure 5.1. AFM of Pt thin films deposited at different atmospheres and temperatures. The samples were deposited in Ar (top) and Ar+O_2 (bottom) atmospheres at different temperatures. All scale bars are 250 nm.

demonstrated an intermediary state, displaying characteristics between uniformly small grains observed at 25°C and non-uniform larger grains at 500°C.

		AFM	XRR				XRD					4-probe
T_s (°C)	Gas	RMS (Å)	t (Å)	σ_{Pt} (Å)	$\sigma_{Pt/Al2O3}$ (Å)	ρ/ρ_{Pt}	$Mos_{\perp}$ (°)	$L_{\perp}$ (Å)	$Mos_{\|\|}$ (°)	Strain($\perp$,$\|\|$)	RC_{sharp} (%)	σ (MS/m)
25	Ar	1.9	265.0	2.7	2.1	1	-	-	- / -	+0.58/-	-	5.868
25	Ar+O_2	1.1	232.3	2.6	1.9	1	-	-	- / -	+0.76/-	-	2.600
300	Ar	5.8	292.9	5.5	8.6	1	0.10	241.1	4.06	+0.18./+0.41	10.51	6.090
300	Ar+O_2	3.0	267.5	2.3	1.6	1	0.08	273.6	1.39	+0.36/+0.58	60.45	6.876
500	Ar	24.1	336.3	9.4	9.0	0.82	0.09	299.2	0.71	+0.14/+0.28	59.00	1.010
500	Ar+O_2	22.3	340.4	11.4	7.1	0.79	0.10	321.2	0.60	+0.11/+.0.38	32.96	0.007
500/300	Ar+O_2	2.0	241.0	2.9	2.1	1	0.08	247.7	1.02	+0.32/+0.38	45.32	6.882

Table 5.1. Results of the Pt thin films deposited at different atmospheres and temperatures. The RMS roughness was extracted using AFM. The thickness (t), surface roughness (σ_{Pt}), interfacial roughness ($\sigma_{Pt/Al2O3}$), and normalized film density (ρ/ρ_{Pt}) were fitted by XRR. The mosaicity and strain in the (111) direction ($Mos_{\perp}, Strain_{\perp}$) and in the (220) direction ($Mos_{||}, Strain_{||}$), the domain size in the (111) direction ($L_{\perp}$) and the sharp component of the rocking curve (RC_{sharp}) were calculated by XRD. The electrical conductivity of the samples is also included.

The interfacial roughness and film thickness of the samples were studied by XRR. The obtained XRR data, shown in **Figure 5.2** along with the fitted curves, were modeled using an electron density profile incorporating various parameters such as Pt thickness (*t*), Pt/air surface roughness (σ_{Pt}), Pt/Al_2O_3 interfacial roughness ($\sigma_{Pt/Al2O3}$), and Pt film density (ρ_{Pt}). These fitted parameters for all the samples are summarized in **Table 5.1**. Analyzing the Kiessig fringe periodicity in the XRR data unveiled film thicknesses spanning 23 to 34 nm. Consistent with AFM observations, σ_{Pt} increases with higher process temperature, irrespective of the deposition atmosphere. In samples grown at 500°C, XRR-measured roughness appeared lower than AFM, possibly attributed to the Pt films' inhomogeneity characterized by flat grains and numerous trenches. Consequently, the ρ_{Pt} values were approximately 80% of the ideal bulk Pt density (21.4 g/cm^3). A two-layer fitting model accounted for the irregular Pt surface, incorporating an additional surface layer equivalent to 50% of the expected ρ_{Pt}. Nefedov *et al.*[158] used a similar strategy for fitting XRR data of Pt (111)/Al_2O_3

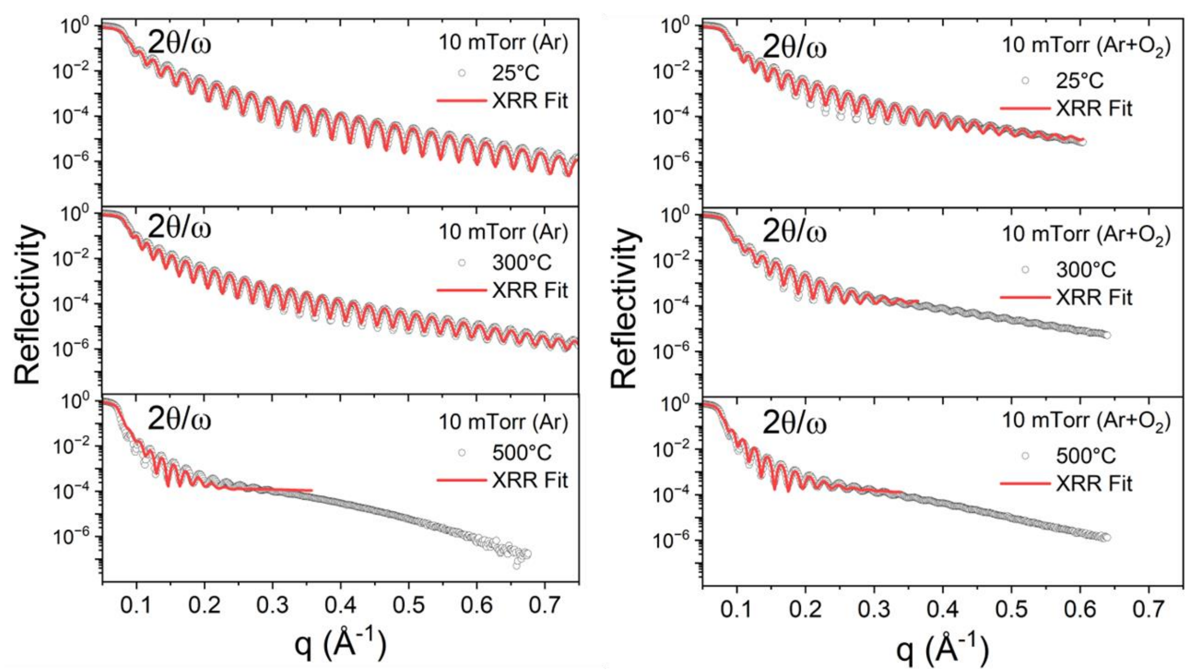

Figure 5.2. XRR of Pt thin films deposited in the two atmospheres and different temperatures. The red line shows the XRR fit with the parameters listed in Table 1.

(11$\bar{2}$0) deposited at 600°C, where a surface layer accounted for a surface 42% of the expected ρ_{Pt}. Including O_2 during the deposition led to a systemic interfacial decrease in $\sigma_{Pt/Al2O3}$ for all growth temperatures. Prior studies have highlighted that a high O_2 partial pressure aids in achieving uniform Pt deposition via atomic layer deposition, as the O_2 presence enhances the diffusion of Pt atoms in the form of PtO_x species.[160]

XRD investigated the crystalline and epitaxial properties of the Pt samples. All analyzed exhibited a Pt (111) Bragg peak without additional crystallographic orientations along the surface normal direction. **Figure 5.3** illustrates the specular *2θ/ω* and rocking curve (RC) *ω* scans. The films deposited at 25°C displayed textured polycrystalline behavior, evident from the weak Pt (111) Bragg peaks and broad rocking curves. The films grown at 300°C and 500°C in both atmospheres displayed Laue oscillations (corresponding to the thickness of the crystalline layer) in the *2θ/ω*

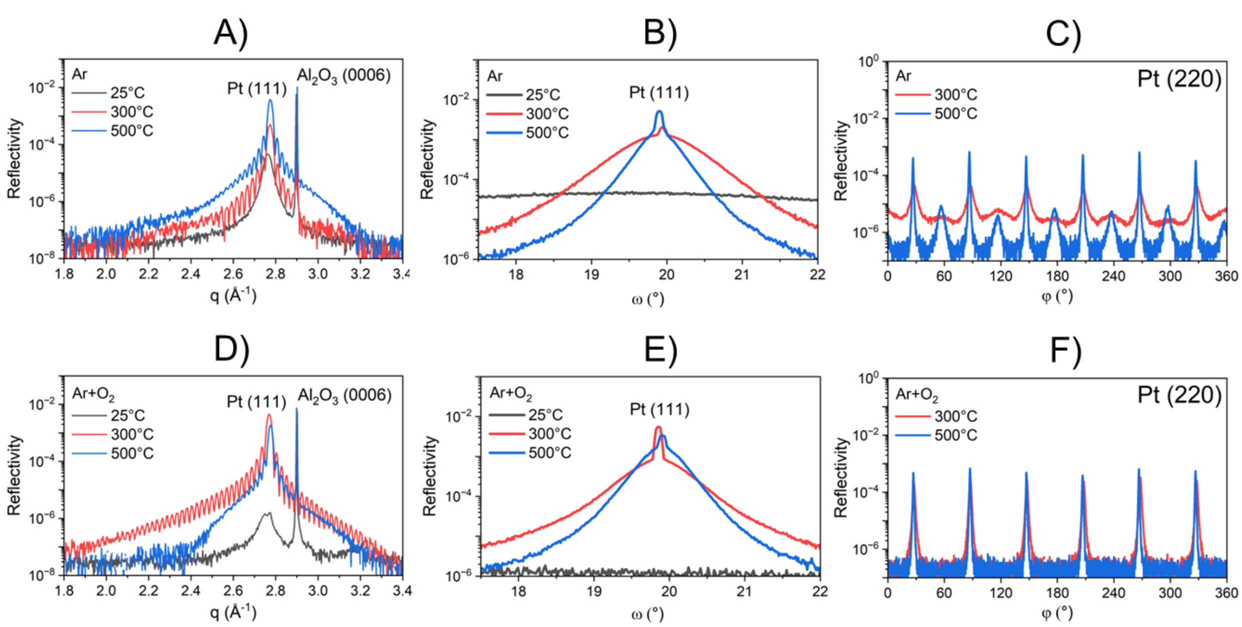

Figure 5.3. XRD of Pt thin films deposited in the two atmospheres and different temperatures. Specular XRD for the samples deposited in (A) Ar and (D) Ar+O_2. Rocking curves of Pt thin films deposited in (B) Ar and (E) Ar+O_2. Off-specular X-ray diffraction of Pt thin films deposited in (C) Ar and (F) Ar+O_2.

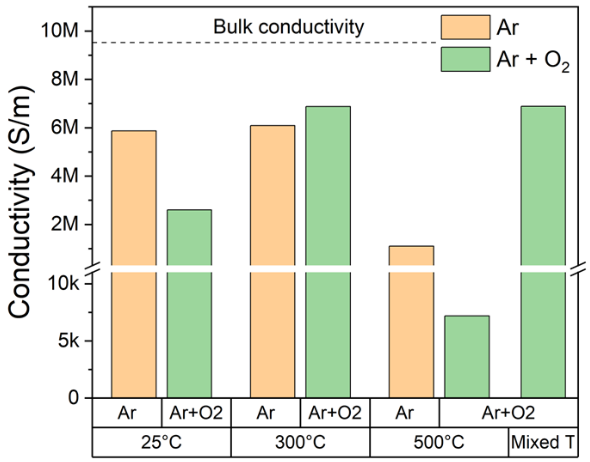

Figure 5.4. Electrical conductivity of the Pt thin films deposited in different atmospheres and temperatures.

scans. The 300°C sample deposited in Ar+O_2 displayed superior crystal quality with extended oscillations. The out-of-plane domain size ($L_{\perp}$), determined from Scherrer's equation, closely match the thickness determined by XRR (t), confirming no additional thickness above or beneath the coherently diffracting domains.[161] The conductivities of the samples deposited at 300°C ranked among the highest in this study, surpassing 6×10^6 S/m. The conductivity for all samples is depicted in **Figure 5.4**. The intensity of the Pt (111) Bragg peak generally increases with temperature, except for the sample deposited at 500°C in Ar+O_2, due to the inadequate grain coalescence observed in AFM (**Figure 5.1**). As presented in **Table 5.1**, this morphology significantly impacted the sample conductivity, resulting in values as low as 1.01×10^6 S/m and 0.01×10^6 S/m.

The rocking curves exhibited one broad and one sharp component, indicating a mixture of disordered grain nature and higher orderliness. The broad component is attributed to structural defects and local deformation within the Pt lattice planes.[123, 158] The rocking curve fitting (**Table 5.1**) revealed that the sample deposited at 300°C in Ar+O_2 had the highest sharp component (60.5%) and the lowest spread in the specular component of the rocking curve (0.8°), indicative of superior crystal quality. Similarly, the 500°C Ar-deposited sample also presented a high (59.0%) and sharp (0.9°) specular component, benefiting from the high-temperature deposition and improved coalescence in comparison to the 500°C in Ar+O_2-deposited sample, which displayed only a 33% specular component.

Off-specular φ-scans were conducted to assess the in-plane epitaxial characteristics of the films. To determine the in-plane epitaxial nature of the film. As depicted in **Figure 5.3 C**, the films deposited in Ar show two sets of Pt (220) reflections with a three-fold symmetry, complemented by lower-intensity twins rotated by 30°. These sets align with the Pt $[1\bar{1}0]$ || Al_2O_3 $[10\bar{1}0]$ epitaxial orientation, while the additional 30° rotated domains correspond to Pt $[1\bar{2}1]$ || Al_2O_3 $[10\bar{1}0]$.[153, 155] These additional twinning, particularly noticeable at 500°C, compromises the quality of subsequent heteroepitaxial film growth by generating more domains.[155] As expected, the Pt $[220]$ mosaicity improves as temperature increases (4.06° to 0.71°).

In contrast, the samples deposited in Ar+O_2 (**Figure 5.3 F**) show no additional twinning, with improved overall mosaicity observed at 300°C and 500°C (1.49° and 0.60°, respectively). This improved crystallinity and epitaxy are attributed to induced layer-by-layer (2D) growth as the oxygen reduces the barrier height for the motion of Pt adatoms across step edges.[162] Furthermore, an elevation in deposition temperature reduces the specular and off-specular strain in the samples, indicating an improvement in the Pt/Al_2O_3 heteroepitaxy (**Table 5.1**).

The findings collectively suggest that oxygen in the background gas and an increase in deposition temperature enhance crystallinity and mosaicity if 3D island growth is avoided. Considering these results, a proposed strategy involves a two-step deposition in Ar+O_2, where the initial 5% of the total film is deposited at 500°C, followed by the remainder at 300°C. This approach anticipates

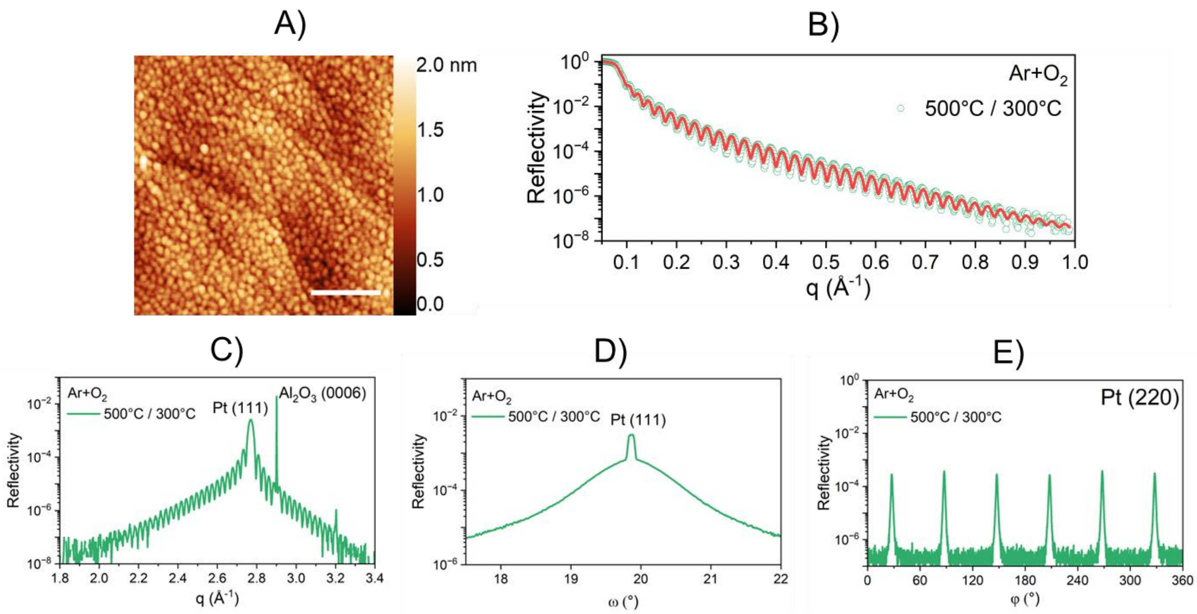

Figure 5.5. Characterization of the two-step Pt thin film. (A) Atomic force microscopy, (B) X-ray reflectivity, (C) specular X-ray diffraction, (D) rocking curve, and (E) off-specular X-ray diffraction.

the first 5% of the film to act as a seeding layer to improve the crystallinity of the subsequent film deposited at 300°C.

Figure 5.5 shows the AFM, XRR, and XRD results for this optimal thin film, as detailed in **Table 5.1**. The film morphology displays remarkable ultra-smooth roughness with an RMS of only 2 Å. The XRR fitting demonstrates near-ideal Pt/Al_2O_3 and Pt/air interfaces with interfacial roughness as minimal as 2-3 Å. Notably, the out-of-plane domain size of the film closely aligns with the thickness determined by XRR. The XRD reveals Laue oscillations, a two-component rocking curve, and a two-set of three-fold symmetry of the Pt (220) without additional twining (**Figure 5.5 C- E**). The overall crystallinity surpasses the samples deposited at 500°C due to higher uniformity, and those deposited at 300°C as the initial higher-temperature growth favors epitaxy. As indicated in **Table 5.1,** the out-of-plane (111) and in-plane (220) mosaicity and strains are measured at 0.08°/0.32% and 1.02°/0.38%, respectively. The sharp component of the rocking curve accounts for 45%, falling between 300°C (60.5%) and 500°C (33.0%) samples deposited in Ar+O_2 (**Table 5.1**).

The two-step deposition in Ar+O_2 presents the highest reported electrical conductivity in this study (6.9×10^6 S/m), comparable to the sample deposited at 300°C in Ar+O_2. The similarity arises because 95% of the two-step deposition film comprises Pt deposited at 300°C. The conductivity enhancement over the 500°C samples is attributed to the film's uniformity (**Figure 5.5 A** and **Figure 5.1**). Although the conductivity does not reach the bulk values of Pt (10.6×10^6 S/m), it closely matches Pt films deposited at higher temperatures (660°C) with similar thickness (24 nm) using MBE (~7.7×10^6 S/m).[134] Additionally, the conductivity reported surpasses that of hole-free Pt films (~120 nm thick) deposited by PLD on sapphire at 300°C and 500°C ($2.0\text{-}3.2\times10^6$ S/m).[163]

The crystallinity and strain of the Pt films synthesized via the two-step deposition method were further examined using TEM. A representative atomic-resolution TEM image in **Figure 5.6 A** reveals a highly crystalline Pt film, approximately 25 nm thick. Convergent beam electron diffraction (CBED), generated by integrating pixels from the complete 4D-STEM dataset covering the film and substrate regions (insets in Figure 5.6 A), reveals their respective structures and crystallographic alignment.[164] The Pt film is viewed along the $[11\bar{2}]$ zone axis (ZA), while the Al_2O_3 substrate is in the Al_2O_3 $[10\bar{1}0]$ ZA. Consequently, their epitaxial relationship is established as Pt $[111]$ || $Al_2O_3[0001]$ and Pt $[1\bar{1}0]$ || $Al_2O_3[10\bar{1}0]$, in agreement with the φ-scans XRD results.

To assess the strain within the Pt film deposited via the two-step process, a newly developed method utilizing 4D-STEM is applied for precise mapping and quantification of strain using CBED

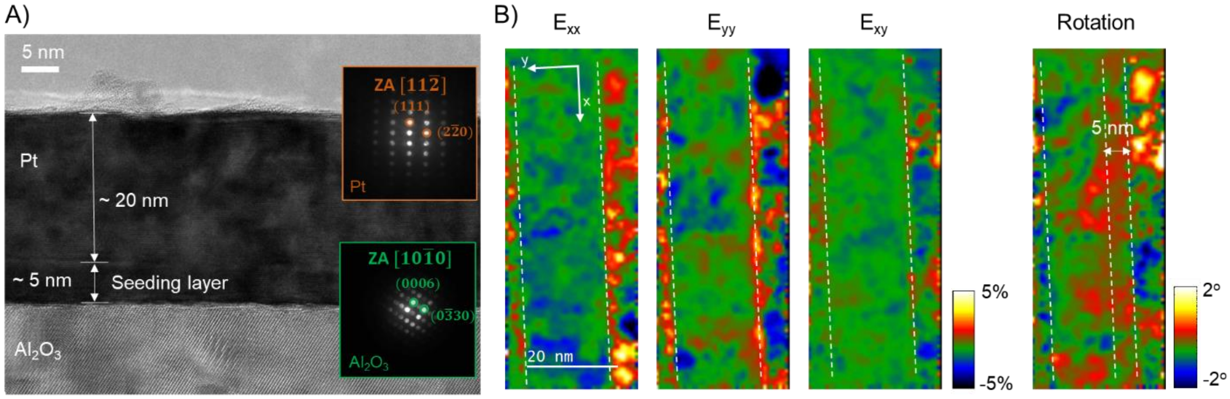

Figure 5.6. Structural analysis of the two-step deposited Pt films by TEM. (A) Atomic-resolution TEM image of the Pt film deposited on Al_2O_3. The 5 nm seeding layer is indicated. (Insets) CBED patterns of the Pt film in the [$\mathbf{11\bar{2}}$] ZA and of the Al_2O_3 substrate in the [$\mathbf{10\bar{1}0}$] ZA. B) Relative strain (left) and rotation (right) distribution through the Pt film. The rotation mainly occurs at the seeding layer. In (B), the film was rotated ~90° counterclockwise to the image in A), and the scan was carried out over ~30 nm x 60 nm area for the strain analysis.

patterns collected at each scanning probe.[45] This method has demonstrated its efficacy in a larger field of view compared to other techniques, such as Geometrical Phase Analysis.[165] The strain maps are generated based on these calculations and are shown in **Figure 5.6 B**. A line profile along the Pt region near the film-substrate interface reveals 0.5-1.5% strain in E_{xx}, E_{yy}, and E_{xy}. Notably, the rotation map shows that film rotation primarily occurs within the initial 5 nm of the film from the substrate. This observation aligns with the atomic-resolution TEM image shown in **Figure 5.6 A**, displaying a linear feature (indicated by a white arrow) located at the film's bottom with a slightly distinct contrast. These findings imply potential structure variations and grain size distribution within the bottom section of the film, likely attributed to the two-step deposition.

The growth evolution of the two-step deposited Pt film was examined by analyzing three additional samples of varying thicknesses (2.7 nm, 5.7 nm, and 10.1 nm). The RC of these samples with the extra 24.8 nm sample is shown in **Figure 5.7**. Analysis of the RC reveals a general reduction in

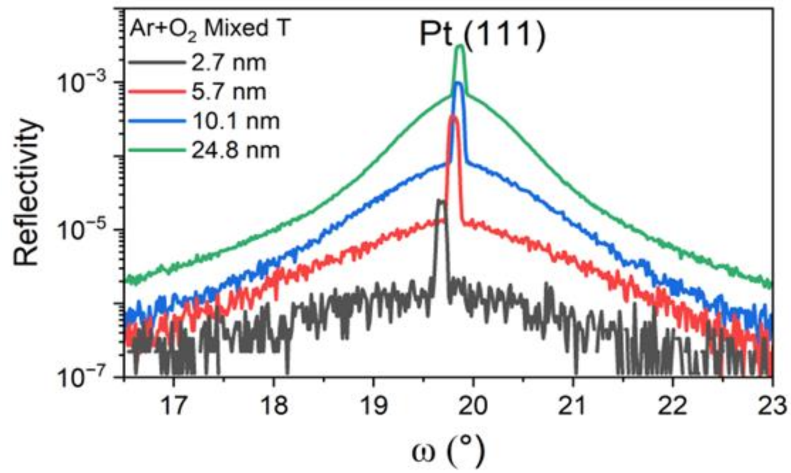

Figure 5.7. RC of the two-step deposited Pt film for different thicknesses.

the width of the broad component, as detailed in **Table 5.2**. This behavior, previously observed in the growth of Nb (110) || Al_2O_3 (11$\bar{2}$0), is explained as an initial 3D growth (Vollmer-Weber type), transitioning to an island coalescence.[166] The lateral domain size at the interface is small and increases with the thickness, contributing to the reduction in the wide component of the rocking curve. These results corroborate the increase in the rotation distribution near the Pt/Al_2O_3 interface.

5.4 Deposition of $LiMn_2O_4$ cathode thin film on Ultra-Smooth Pt Electrodes

The ultra-smooth Pt film deposited using the two-step growth method was used as a current collector in a LIB setup. For this purpose, an epitaxial LMO (111) thin film cathode was grown on the Pt (111) / Al_2O_3 (0006) template. A +4.05% lattice mismatch between the cubic $LiMn_2O_4$ unit cell (a=8.149 Å) and Pt (a=3.916 Å) favored 2:1 epitaxial growth. **Figure 5.8 A** shows the LMO (111) Bragg peak at 1.322 $Å^{-1}$, revealing 1% strain and a domain size of 4 nm. A subtle increase in intensity is noticeable in the Pt (111) Laue oscillations, corresponding to the $LiMn_2O_4$ (222) Bragg peak.

Thickness (nm)	FWHM wide (°)
2.7	2.38659
5.7	1.57768
10.1	1.0662
24.8	0.70881

Table 5.2. FWHM of the broad component of the RC using the of the two-step deposited Pt film for different thicknesses.

The RC FWHM of the LMO (111) was 1.16°, higher than the 0.08° mosaicity from the Pt (111) (**Figure 5.8 B**). Despite this, the LMO (111) FWHM is lower than that reported for LMO (111) deposited on Pt (111) / MgO (001) using PLD (2°), reflecting the higher crystal quality of the two-step growth Pt.[145] The epitaxy was investigated with off-specular φ-scans of the LMO (400) and Pt (400) Bragg peaks (located at 43.04° and 103.78° in 2θ, respectively), confirming the LMO $[1\bar{1}0]$ || Pt $[1\bar{1}0]$ in-plane epitaxial orientation. A two-set of three-fold symmetry peaks, 60° apart, aligns with the Pt twinning (**Figure 5.8 C**). The LMO (400) mosaicity in the φ-scan was 1.07°, which is lower than the reported for LMO (111) deposited on Pt (111) / MgO (001) by PLD (1.7°).[145]

Finally, the LMO cathode underwent electrochemical cycling utilizing a solid-state h-BN ionogel electrolyte containing h-BN nanoflakes and EMIM-TFSI ionic liquid.[71] The cyclic voltammetry depicted in **Figure 5.8 D** displays the characteristic Mn^{3+}/Mn^{4+} redox peaks specific for $LiMn_2O_4$. The cyclability in the 3.5-4.3 V vs. Li/Li^+ range demonstrates the effectiveness of employing the two-step growth Pt thin film as a current collector for LIB applications.

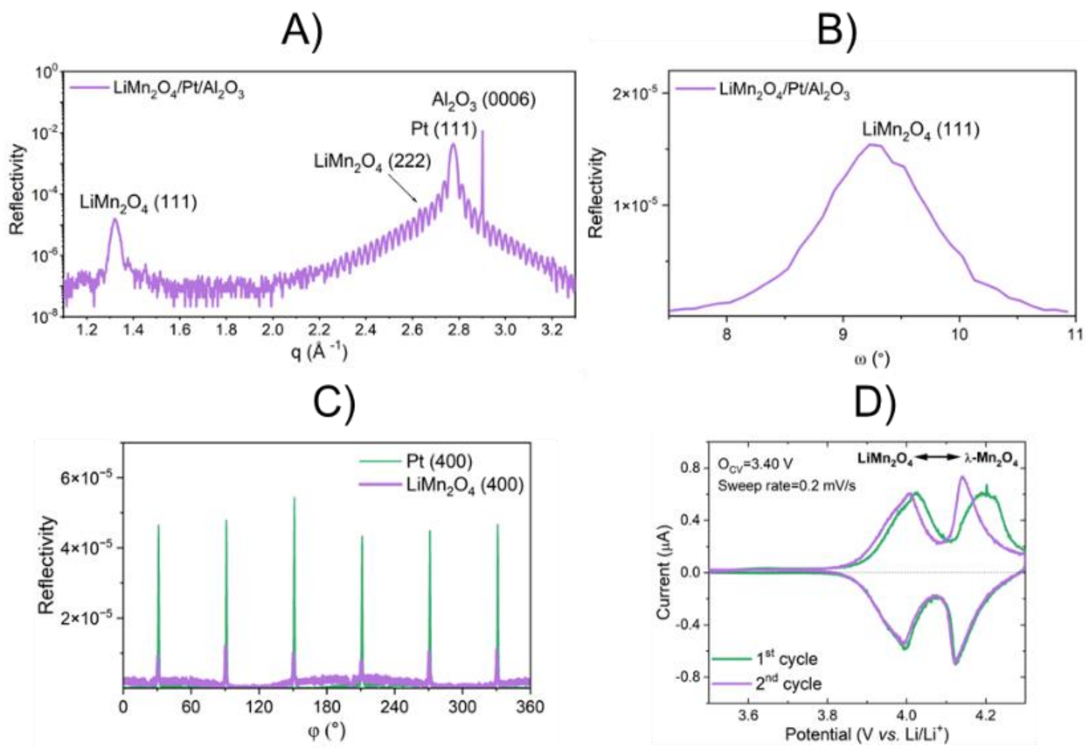

Figure 5.8. Characterization of the LMO film grown on the two-step deposited Pt thin films. (A) Specular XRD, (B) RC, and (C) off-specular XRD of this sample. (D) Cyclic voltammetry of the LMO thin film using the Pt thin film as the current collector.

5.5 Summary

This study focused on optimizing and using Pt (111) thin films as a current collector in LIB application. The films were deposited by PLD on Al_2O_3 (0001) substrates under various atmospheres and deposition temperatures. The film growth was optimized based on their morphological, structural, and interfacial properties. Following these results, a two-step temperature process (500/300°C) in an Ar+O_2 atmosphere emerged as the optimal condition, showcasing improved film crystallinity and mitigated 3D island growth. This procedure involved depositing the first 5% of the film at a higher temperature. The optimized process yielded ultra-smooth films (<2 Å), exhibiting high conductivity (~7 × 10^6 S/m) and a high degree of epitaxy, serving as excellent templates for subsequent epitaxial growth.

Detailed analyses using 4D-STEM unveiled the film's grain evolution and strain distribution. Notably, a thin interfacial layer displayed considerable rotational strain, attributed to the initial 3D growth transitioning into island coalescence. Furthermore, LMO (111) was grown epitaxially on the optimized Pt (111) template and successfully cycled in a LIB setup utilizing a solid-state h-BN ionogel electrolyte.

5.6 Experimental Methods

5.6.1 Sample Preparation

The Pt thin films were deposited by PLD on sapphire α-Al_2O_3 (0001) substrates (University Wafer, Inc.). Initially, the substrates were cleaned with acetone and isopropanol and annealed at 1100°C for two hours in air. The substrate miscut was 0.2° as measured by X-ray diffraction (XRD). The depositions were performed in a PVD Products NanoPLD 1000 with a 248 mm KrF excimer laser, focused to1.5 mm × 3 mm on a metallic Pt target (Refining Systems, Inc.) with a final energy of 175 mJ/pulse at 5 Hz. Initially, thin films were deposited in 100% Ar and a mixture of 67% Ar + 33%O_2 (Ar+O_2) at three different deposition temperatures: 25°C, 300°C, and 500°C. Subsequently, a two-step temperature growth process (500°C/300°C) was implemented in the Ar+O_2 mixture at 500°C for the initial 5% of the total film and 300°C for the remaining film. All the Pt films were approximately 30 nm in thickness. The LMO cathode thin film was deposited on the two-step temperature Pt film in the same PLD instrument employing a $Li_{1.3}Mn_2O_{4.14}$ target

(Kurt J. Lesker) at 140 mJ/pulse at 5 Hz. The deposition was performed at 400°C under an O_2 partial pressure of 75 mTorr, followed by a one-hour annealing under the same conditions.

5.6.2 Atomic Force Microscopy

The surface morphology of the Pt films was analyzed by AFM using Asylum Cypher AFM with a Si cantilever used in tapping mode at a scanning rate of 1 Hz.

5.6.3 X-ray Reflectivity and Diffraction

X-ray characterization was performed to investigate various aspects of the thin film, including interfaces, crystal orientation, and epitaxy. XRR measurements were performed in a Rigaku ATXG diffractometer with an 18 kW Cu rotating anode (λ = 1.5418 Å) with a 0.1 mm × 2.0 mm collimated beam. The XRR data were corrected for footprint and background signal, followed by further analysis using MotoFit Software[14]. Specular (2θ/ω), off-specular (φ), and rocking curve (ω) X-ray diffraction (XRD) measurements were conducted in a Smartlab Gen 2 9 kW 5-circle diffractometer equipped with a Ge (220) 2-bounce monochromator (λ = 1.5406 Å) with a 0.5 mm × 2 mm collimated beam. The rocking curves obtained at the film Bragg peaks underwent fitting procedures utilizing two Gaussians, a sharp peak on top of a broad diffuse peak. All the XRR and XRD measurements were normalized with the corresponding straight-through-beam intensity and plotted as a function of the scattering vector $q = 4\pi Sin\theta/\lambda$.

5.6.4 Four-probe resistivity

The electrical conductivity was measured with a 4-probe configuration using a Keithley 2450 source meter.

5.6.5 Transmission Electron Microscopy

Cross-section TEM samples were prepared using a dual-beam FIB) FEI-SEM Helios Nanolab. The process involved a lift-off performed at 30 kV Ga^+ ions and a cleaning step at 2 kV to remove surface damage in the area of interest. The resultant sample thickness was reduced to below 100 nm. TEM and scanning transmission electron microscopy (STEM) data were collected using a probe-corrected JEOL ARM200 S/TEM operating at 200 kV. The annular dark-field-STEM (ADF-STEM) imaging employed a convergent angle of 25 mrad. Electron dispersive spectroscopy (EDS) was acquired at 200 kV. Furthermore, a four-dimensional STEM (4D-STEM) approach was adopted using a OneView camera with a software bin size of 512 × 512 or 256 × 256 pixels. During the 4D-STEM experiments, a convergent angle of 3.5 mrad was utilized, with a camera length of 20 cm and a step size maintained between 5-10 Å.

Data processing encompassed analyses such as EDS chemical mapping, strain mapping, and quantification via 4D-STEM. Such procedures were done using Gatan GMS software and an open-source py4DSTEM package.[45] The 4D-STEM strain mapping and quantification process relied on the methodology presented by Ozdol *et al*.[165] In summary, this method involved the assignment of two principal orientations (diffraction disks) within the film (e.g. $[1\bar{1}0]$ and $[111]$), tracking the displacement of their center (vectors $\mathbf{g_1}$, $\mathbf{g_2}$) from an "unstrained" area (vectors $\mathbf{g^*_1}$, $\mathbf{g^*_2}$). The transformation matrix ($\boldsymbol{T}$) was calculated using $\mathbf{g} = \boldsymbol{T} \cdot \mathbf{g^*}$ for each diffraction pattern as the probe scanned the sample. The $\boldsymbol{T}$ matrix was then separated into a rotation matrix ($\boldsymbol{R}$) and a symmetric strain matrix ($\boldsymbol{U}$) through a polar decomposition $\boldsymbol{T} = \boldsymbol{RU}$. The planar strains were computed by $E_{xx} = 1 - U_{00}$ and $E_{yy} = 1 - U_{11}$, shear strain by $E_{xy} = 1 - U_{01}$, and rotation by $\theta = \cos^{-1}(R_{00})$. Gatan GMS Software or the open-source py4DSTEM package regularized the strain calculations.

In our study, the unstrained area is chosen to be in the middle of the film (5 × 5 nm), far away from any interfaces or an average value of the entire film; both give similar results.

5.6.6 Cyclic Voltammetry

The LMO/Pt/Al_2O_3 sample was hermetically sealed inside an Ar-filled glovebox within an X-ray transmission cell.[112] A hexagonal boron nitride (h-BN) ionogel electrolyte[71, 167-170] and a Li metal counter electrode (0.75 mm thick, Alfa Aesar) were employed to assess the electrochemical performance of the $LiMn_2O_4$ cathode and evaluate the efficacy of the Pt current collector. The cell was connected to an electrochemical workstation (CHI760E) for cyclic voltammetry conducted at a scan rate of 0.2 mV/s, in the potential range of 3.5-4.3 V vs. Li/Li^+.

CHAPTER 6:

INTERFACIAL ENGINEERING OF QUANTUM INFORMATION MATERIALS IN SUPERCONDUCTING QUBITS

6.1 Overview

After decades of continuous advancements, the field of computing is now entering a maturity phase. Despite the inherent complexities involved in manufacturing and operating modern quantum computers, which require extremely low temperatures, quantum computers are now accessible to users globally.[171] Major companies like IBM, Google, Microsoft, and Amazon offer remote access to their quantum computer resources, offering a platform for conducting experiments that were once considered classically intractable.[172] The significance of quantum technology has risen, making it a priority in economic and national security sectors. In the United States, the National Quantum Initiative Act, signed in 2018, has empowered the National Science Foundation (NSF) and the Department of Energy (DOE) to establish new research centers and institutes to expedite the development of quantum computing technology.[173]

Quantum algorithms utilize qubits, distinct from classical bits, as they can represent a superposition of multiple states. This unique characteristic allows qubits to surpass the capacity of binary logic in traditional computing. In the case of a single qubit, it can represent the state of two bits, $|0>$ and $|1>$, each assigned a probability coefficient. With two qubits, the representation expands to four possible bit states: $|\,0\,0\,\rangle$, $|\,0\,1\,\rangle$, $|\,1\,0\,\rangle$, and $|\,1\,1\,\rangle$. The accessible computational space grows as 2^N for N qubits, a surprisingly high number considering that 80 qubits can represent approximately all the information stored in all the matter particles in the observable universe.[174]

Quantum computers excel in specific computational tasks where classical computers fall short, particularly in managing large datasets or complex systems. Algorithms like Shor's for factoring large numbers and Grove's for database searching demonstrate significant advantages over classical counterparts.[175] The impact of quantum computing extends across diverse fields, including artificial intelligence, cybersecurity, logistics, meteorology, and molecular modeling. For example, understanding the nitrogenase mechanism in natural nitrogen fixation remains a mystery.[176] Quantum computers could potentially unravel this mystery, offering an alternative to the energy-intensive Haber-Bosch method, which currently consumes 2-3% of the world's energy.[177]

Superconducting qubits represent a mature quantum platform for building multi-qubit quantum processors. Here, the fabrication of the circuit elements involves standard fabrication processes, including lithography, etching, and metal deposition of superconductive materials.[178] However, these processes introduce defects that impact the circuit performance. Enhancing coherence, the ability of a qubit to maintain its state is a primary challenge at mK temperatures, where two-level systems (TLS) dominate decoherence sources.[179] Despite the unclear microscopic origins of TLS, amorphous surface dielectrics like SiO_2 or Nb_2O_5 are known to host them.[180] Additionally, quasiparticles and magnetic flux noise are other noise sources that can affect decoherence in qubits. Efforts to identify, understand, and mitigate these sources of decoherence, most of the time located at interfaces, are necessary to enhance quantum computing performance.

6.2 Quantum Computing and Superconducting Qubits

Various physical systems have been demonstrated for qubit generation, such as electron spins in silicon,[181] and quantum dots,[182] trapped ions,[183] nitrogen-vacancies in diamond,[184] molecular systems,[185] and polarized photons.[186, 187] Quantum information in these processes is encoded in a two-level system (TLS) associated with a microscopic state of the system like charge, spin, or polarization.

An alternative approach involves superconducting qubits based on macroscopic superconductive quantum circuits, lithographically defined, where the TLS originates from an anharmonic oscillator.[188] Josephson junctions (JJs) play a crucial role in superconducting qubits. When two superconductors are connected by a thin insulating layer, a non-dissipative and non-linear JJ is formed, enabling coherent tunneling of Cooper pairs.

JJs have found applications since their demonstration in 1962,[189] including superconducting quantum interference devices (SQUID)[190] and qubit generation[191]. **Fig. 6.1 A** illustrates a JJ's schematic and circuit element representation. Favored by its fabrication simplicity, numerous types of JJs have been developed, $Al/AlO_x/Al$ being one of the preferred choices due to well-controlled deposition and oxidation methods.[192, 193] **Fig. 6.1 B** shows an SEM image of a typical JJ. Another circuit element, a superconducting resonator, comprises inductive (L) and capacitive (C) components. **Fig. 6.1 C** shows an optical image of a resonator. Superconducting quantum devices utilize these two basic components for qubit generation, protection, and readout.[194]

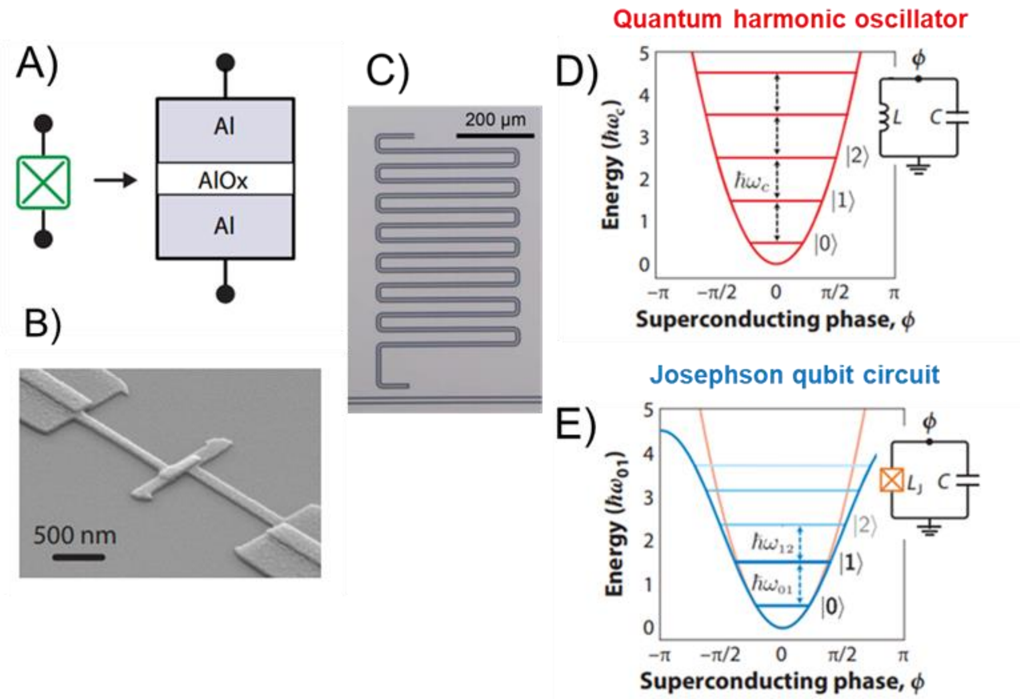

Figure 6.1. Superconducting circuit overview. (A) Element representation of a Josephson junction consists of two layers of aluminum separated by an aluminum oxide thin barrier.[195] (B) SEM image of a bridge-free Josephson junction.[195] (C) Optical image of an Al on Si resonator capacitively coupled to a feed-line.[196] (D) Circuit of an LC resonator with its equivalent energy potential corresponding to a quantum harmonic oscillator.[197] (E) Circuit of a Josephson qubit circuit with its sinusoidal (blue line) potential, which differs from the quadratic potential (orange line).[197, 198] Retrieved from Refs.[195-197, 199]

The LC circuit is quantized as a quantum harmonic oscillator with a resonant frequency. $\omega_c = \sqrt{1/LC}$ faces a challenge as it cannot operate as a qubit due to equidistant energy levels, as shown in **Fig 6.1 D**. To address this, a JJ replaces the linear inductor, creating non-equidistant energy levels and isolating the lowest energy levels states $|0\rangle$ and $|1\rangle$ with a unique transition frequency of $\hbar\omega_{01}$.

Different superconducting qubits can be designed by incorporating JJs, linear inductors, and capacitors in different configurations. The three fundamental superconducting qubits are the charge qubit,[200] flux qubit,[201] and phase qubit[202]. The charge qubit involves a charge box controlled by an external voltage (V_g), the flux qubit operates through an external magnetic flux (Φ_{ext}), and the phase qubit is connected to a static bias (I_b).[203]

For instance, the charge qubit circuit (**Fig. 6.2 A**) excludes a linear inductor and is based on a Cooper pair box (CPB). The CPB consists of a small superconducting island (black dot with node flux Φ) connected via a JJ to a large electrode, called a bulk or reservoir (**Fig. 6.2 B**).[200, 204] Cooper-pairs can tunnel on and off through the island, and an external voltage (V_g) through a gate capacitance (C_g) is used to determine the charge offset $n_g = C_g V_g / 2e$ which is used to tune the qubit frequency. The Hamiltonian for a charge qubit is given by:

$$H = 4\, E_C\, (\hat{n} - n_g)^2 - E_J\, cos\hat{\varphi} \qquad \textbf{Eq. 6.1}$$

Here, $\hat{n}$ denotes the excess of Cooper pairs on the island, and $\hat{\varphi}$ the phase difference across the JJ. The key parameters include E_J, the junction energy is given by $E_J = \hbar^2/(4e^2 L_J)$, and E_C, the charging energy is given by $E_C = e^2/(2C_Q)$, where L_J is the JJ inductance, and C_Q is the total qubit capacitance, incorporating the JJ and shunting capacitor.

In the case of a CPB, the ratio E_J/E_C is approximately 1, leading to high sensitivity to noise and significant large device-to-device variability.[197, 205] To address this, the transmon qubit is introduced, operating in the $E_J/E_C > 30$ regime.[206] This is achieved by increasing the island size, adding more shunting capacitance, and effectively decreasing E_C.[205] The transmon (**Figure 6.2 C**) consists of a JJ connected to two shunting capacitor (C) paddles (*purple*), capacitively coupled (C_C) to a resonator (*green*). Its circuit diagram is shown in **Figure 6.2 D**. Improved isolation from

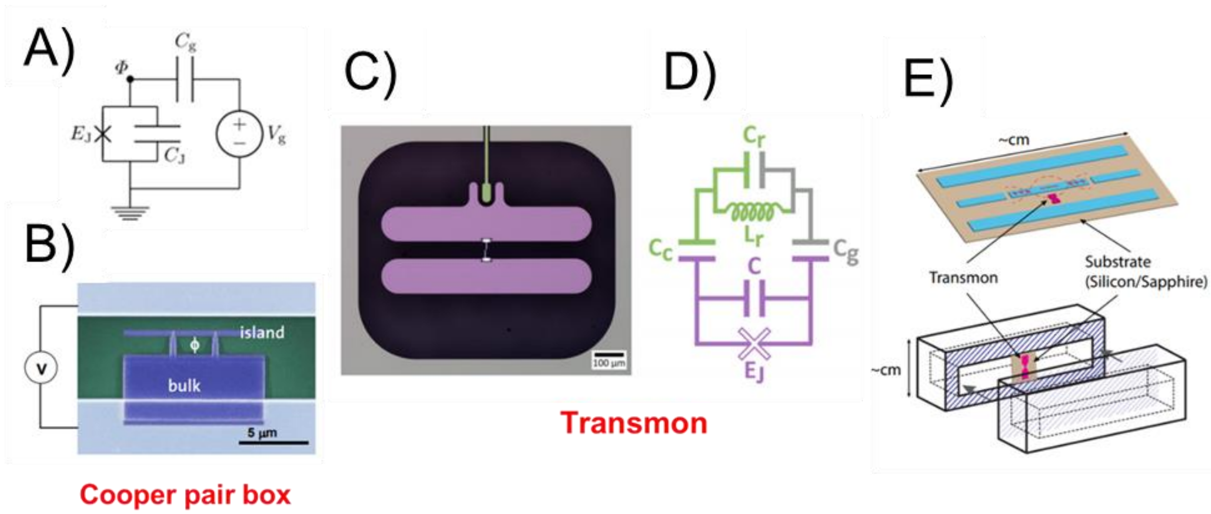

Figure 6.2. Charge qubit and transmon overview. (A) Josephson junction charge qubit circuit.[203] (B) False-color SEM image of a Cooper pair box (blue) fabricated on a silicon substrate (green) capacitively coupled to a resonator (light blue).[204] (C) False color optical image of a transmon qubit. Niobium regions include the CPW resonator (green), the transmon capacitor pads (purple), and the ground plane (gray). The black area indicates the sapphire substrate.[209] (D) Circuit diagram of a transmon qubit coupled with a resonator.[209] (E) Transmon devices dispersive coupled to a superconducting cavity in either 2D coplanar waveguide and 3D configuration.[195, 210]. Retrieved and adapted from Refs. [195, 203, 204, 209, 210]

the external environment is achieved by coupling the transmon to a 2D coplanar waveguide (CPW)[194, 206], or a 3D cavity,[207, 208] leveraging weaker electric fields at different interfaces. **Figure 6.2 E** shows a physical realization of transmon dissipative coupled to 2D and 3D systems. Processors based on superconducting transmons have been scaled up, with examples reaching 65 fully programmable qubits on a single chip, demonstrating high fidelity.[211, 212]

The TLS of a qubit is illustrated through a Bloch sphere (**Figure 6.3 A**), wherein a Bloch vector $|\Psi\rangle = \alpha^2 |0\rangle + \beta^2 |1\rangle$ represents the qubit state. The quantization of the qubit is depicted along the longitudinal axis with an additional transverse axis, representing relaxation and pure

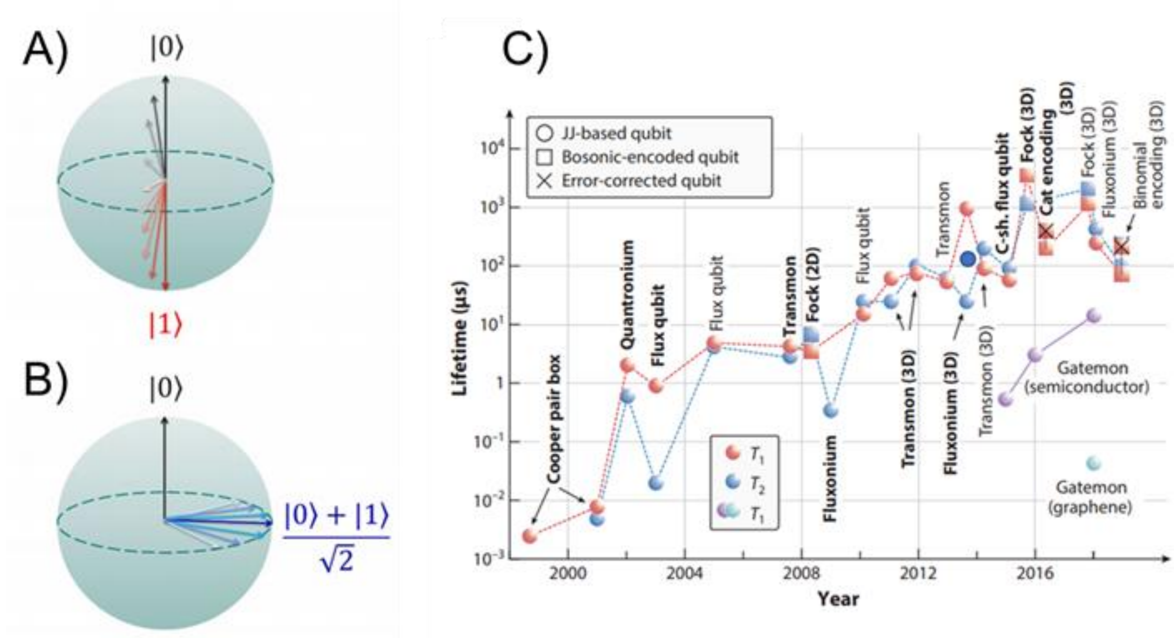

Figure 6.3. Qubit relaxation mechanism and lifetime evolution in recent years. (A) Bloch-sphere representation of the energy relaxation of a qubit (T_1) and (B) dephasing of a qubit which together with T_1, contributes to the decoherence time T_2.[213] (C) Evolution of lifetimes and coherence times in superconducting qubits.[197]

dephasing, respectively. For a more detailed explanation of noise and decoherence models, refer to a review from Krantz.[188]

The transverse relaxation T_2 describes the decoherence of a superposition state and is derived from the longitudinal relaxation T_1 and the pure dephasing time T_φ, as expressed by the equation:

$$\frac{1}{T_2} = \frac{1}{2T_1} + \frac{1}{T_\varphi} \qquad \textbf{Eq. 6.2}$$

T_1 and T_2 serve as crucial metrics for assessing the qubit's energy relaxation (energy dissipation to the environment) and dephasing (loss of information). Experimental measurements involve observing the decay of an excited qubit for T_1 and utilizing Ramsey interferometry for T_2 evaluation.[214, 215] **Figure 6.3 C** illustrates a consistent increase in coherence time across various superconducting qubits over the years. A notable improvement of four orders of magnitude in T_1 is observed for a 2D transmon compared to a Cooper pair box. Recent advancements have reported 2D transmons qubits based on Ta superconductors coherence times surpassing 300 μs[216] and 500 μs.[217]

6.3 Loss Mechanisms in Superconducting Qubits

Superconducting qubits face challenges from various source mechanisms that can impact their coherence and overall performance. These losses reside in the bulk materials, surface and interfaces, and the external environment. Notably, significant research has been dedicated to understanding two primary sources of losses: TLS losses in dielectrics and non-equilibrium quasiparticles (QPs) in the superconductor. [218]

Figure 6.4 A provides a schematic of a 2D transmon, highlighting the diverse bulk materials (superconducting metal, insulating substrate, and dielectric amorphous layers) and interfaces (metal/air, metal/substrate, and substrate/air), along with the different loss sources. The JJ within the transmon can contribute to TLS losses attributed to amorphous oxides and QPs tunneling (**Figure 6.4 B** and **C**). Additionally, TLS losses may be present on the substrate, manifesting as lossy surfaces, and on the metal as native oxides. The metal can also present QP losses in the form of resistive losses. Furthermore, the substrate and interfaces can also lead to dissipation when high-loss tangent materials are present. Finally, surface spins cause flux noise (**Figure 6.4 D** and **E**).

TLS losses have attracted substantial interest because they are the dominant form of dielectric loss at mK temperatures.[180] While the precise microscopic nature of TLS loss remains a subject of

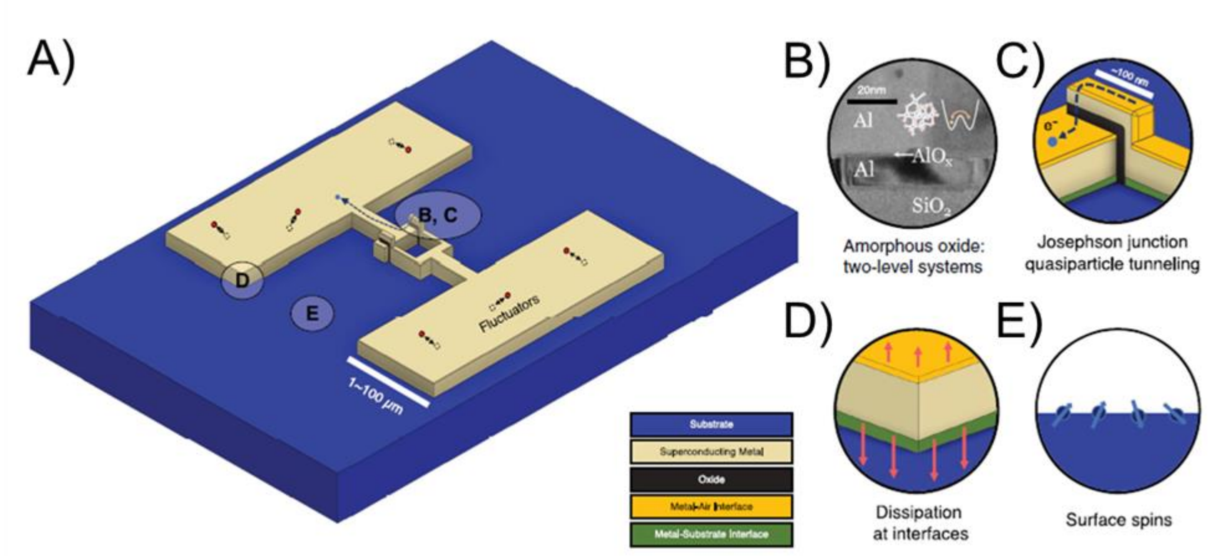

Figure 6.4. Loss sources in superconducting qubits. (A) Schematic of a superconducting transmon qubit. , showcasing the different bulk materials and interfaces. (B-E) Loss mechanisms in transmon qubits: (B) TLS system arising from the amorphous oxide (*inset*), (C) QP tunneling through the junction and transport across the superconductor, (D) Lossy dielectrics lead to dissipation at the different interfaces, and (E) surface spins lead to flux noise. Retrieved from Ref. [218]

debate,[179] it is acknowledged that it occurs through the interaction of an electromagnetic field with bulk dielectrics,[180, 219] surface oxides,[220] and interfaces.[221] Amorphous materials, particularly, are a primary candidate for hosting TLS. For example, in the fabrication of Al/AlO_x/Al JJ, the formation of an amorphous surface AlO_x, a high-loss material[222] (**Figure 6.5 A**), is integral once the JJ exists in the deposition chamber or undergoes intentional oxidation to create the barrier.

Various models of TLS formation in the JJ involve tunneling atoms, dangling bonds, and trapped charges (**Figure 6.5 B**).[179] Martinis *et al.* [180] identified dangling OH defects as a predominant source of TLS in amorphous SiO_2 and AlO_x grown by Chemical Vapor Deposition (CVD). Notably, a higher concentration of these defects was observed in SiO_2 than in a SiNx dielectric, attributed to the SiH_4 and O_2 precursor gases used in the CVD. The Rabi oscillations for a phase

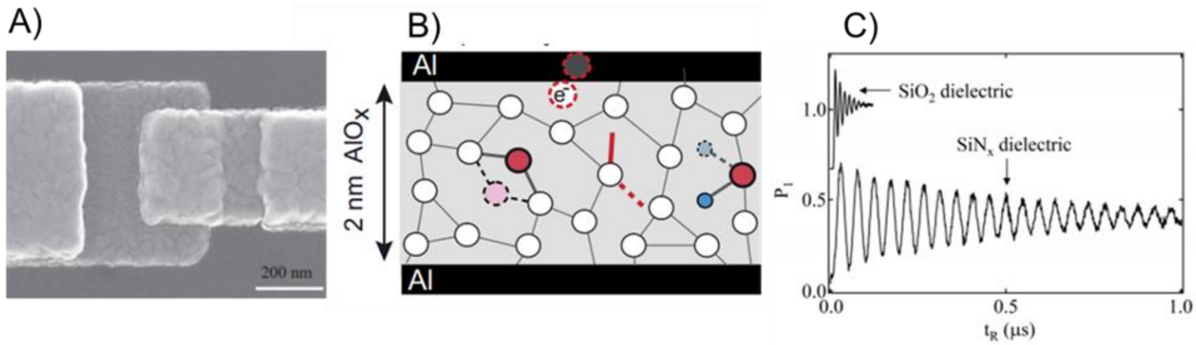

Figure 6.5. TLS losses associated with the dielectric in the JJ. (A) SEM image of an Al/AlO_x/Al JJ.[193] (B) Sketch of a JJ formed by two Al electrodes separated with a 2 nm amorphous AlO_x dielectric. TLS mechanisms are illustrated here, including tunneling atoms, dangling bonds, and trapped charges.[198] (C) Rabi oscillations for two qubits working with SiO_2 and SiN_x dielectric. The decay represents the relaxation time T_1.[180] Retrieved from Refs. [193, 198]

qubit (**Figure 6.5 C)**, utilized for T_1 calculation, indicate a substantial increase in T_1 (20 times) upon switching from SiO_2 to SiN_x, elucidating the importance of using low-loss dielectrics.[180]

The interaction between the different areas of the transmon and the external electric field leads to dissipation at interfaces, known as dielectric loss. In **Figure 6.6 A**, the impact of an electric field generated by a transmission-line resonator on TLS sources at various interfaces (substrate-vacuum (SV), metal-substrate (MS), and metal-vacuum (MV)) is illustrated. Generally, amorphous materials possess a higher dielectric loss than their crystalline counterparts due to the elevated density of TLS.[223]

Optimizing geometry parameters, focusing on minimizing the participation of lossy interfaces, offers a promising avenue to enhance decoherence in superconducting devices.[224] Dielectric loss participation ratios (P_i) for the different interfaces has been approximated by considering the boundary conditions at the interfaces using finite-element electromagnetic simulation analysis (**Figure 6.6 B**).[210, 225] Studies indicate that for coplanar architectures, the participation ratio of SV

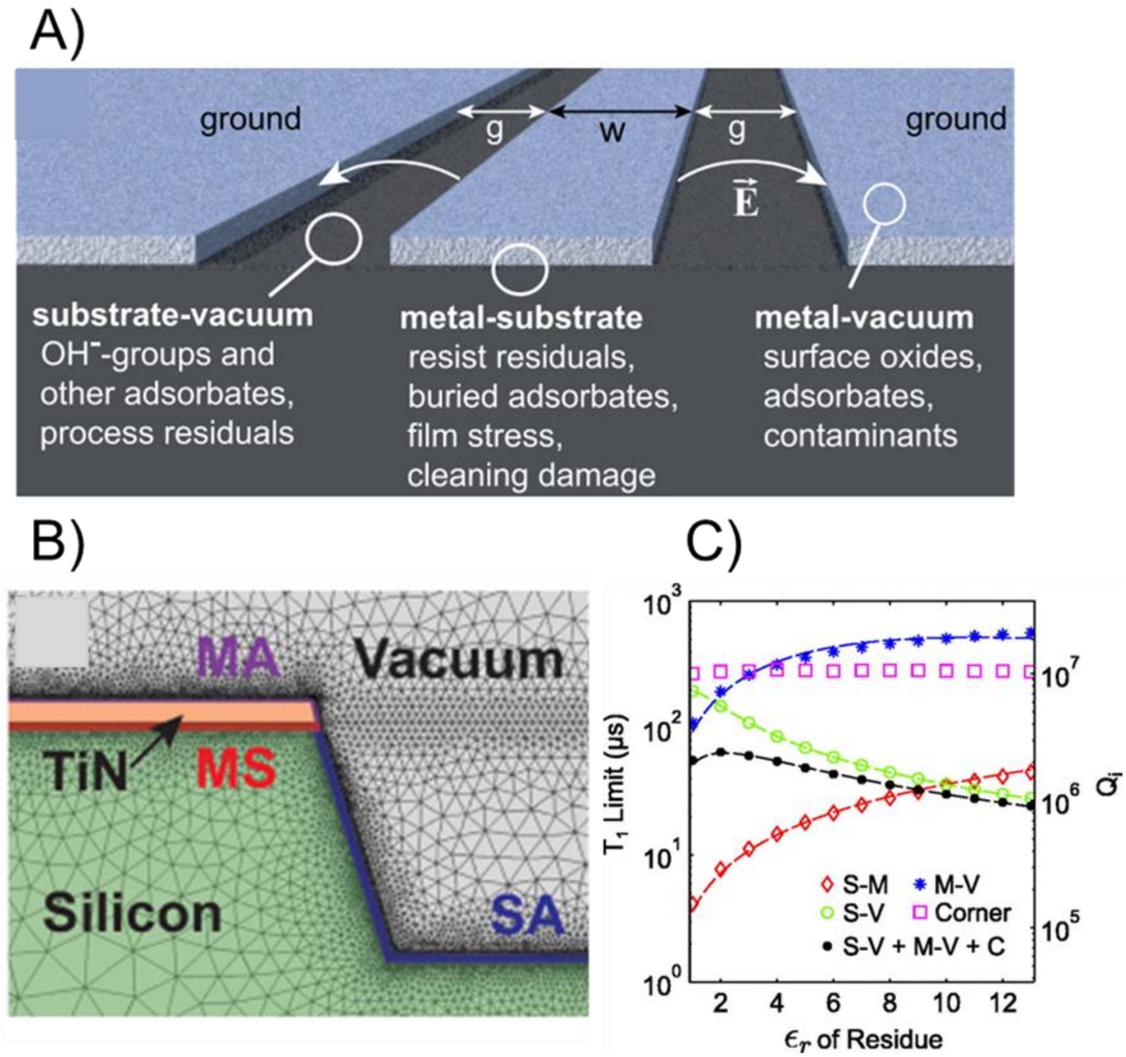

Figure 6.6. Participation of the different interfaces and respective loss sources. (A) Schematic of a coplanar transmission-line resonator and an overview of mechanisms associated with TLS formation at the three main interfaces (circles).[179] (B) 2D finite-element mesh used to calculate participation ratios of the dielectric regions: metal-substrate (MS in red), substrate-air (SA in blue), and metal-air (MA in purple).[210] (C) $\boldsymbol{T_1}$ limit at 6 GHz due to the loss for the three different interfaces in a CPW resonator.[199] Retrieved and adapted from Refs. [179, 199, 210]

and MS interfaces is significantly larger (~100 times) than that of MV. A similar result was found by Murray *et al.* with an additional hypothetical contamination layer thickness in the three different interfaces.[226] Quintana *et al.* pointed out that at low permittivity interface layer ($\varepsilon_r \sim 2$)

corresponding to the permittivity of a copolymer resist, MV and SV interfaces contribute similarly, while MS still exhibits the highest P_i (**Figure 6.6 C**).[199]

Beyond TLS and interfacial dissipation losses, the presence of QPs affects superconducting devices. The losses are associated with non-equilibrium QPs behaving like particles with energy and charge in the superconductor, causing dissipation and reducing the coherence. QPs generation can occur from Cooper-pair breaking from various sources such as infrared radiation,[227] ionizing radiation (β-particles, γ-rays, and X-rays),[228], and cosmic rays.[229] Additionally, QPs can be generated by microwave read-out devices when the frequency is below the gap frequency of the superconductor. [230]

CPW resonators serve as a convenient qubit proxy for assessing performance and studying different loss mechanisms, including TLSs and QPs. [231] Due to its fabrication simplicity compared to superconducting qubits, CPW can be geometrically tuned to increase the participation ratio of

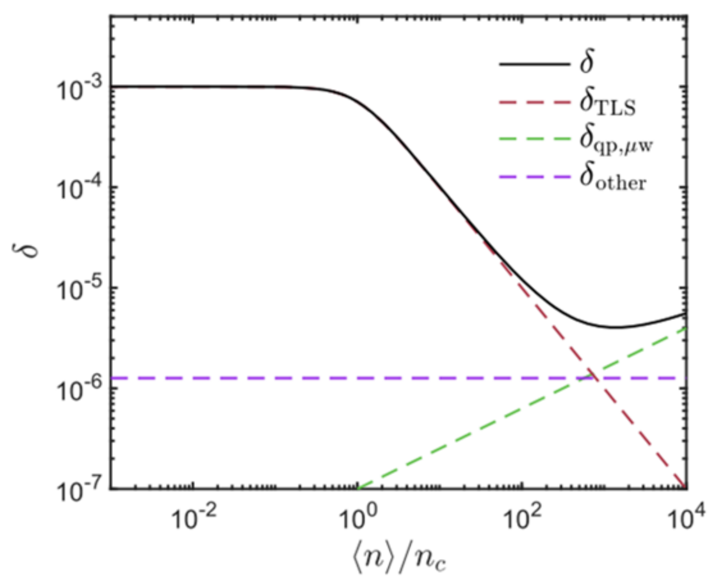

Figure 6.7. Loss versus power plot for a CPW resonator. The power of the resonating microwaves, proportional to $\langle n \rangle / n_c$ where $\langle n \rangle$ is the number of photons and n_c is the critical number of photons, below which TLS loss dominates. Retrieved and adapted from Ref. [231]

the different interfaces. Notably, loss channels can be distinguished during power-sweep measurements. **Figure 6.7** illustrates the power dependence and relative distributions of the various loss channels contributing to the total loss in the resonator: TLS loss (δ_{TLS}), QP loss due to microwave-induced pair-breaking ($\delta_{qp,\mu w}$), and the sum of all power-independent losses (δ_{other}). In the single photon regime, losses are dominated by dominated by δ_{TLS}, while at higher powers, $\delta_{qp,\mu w}$ becomes a relevant contributor.

6.4 Materials Matter in Superconducting Qubits

The challenge in superconducting qubits is constructing nearly perfect devices from inherently defective materials. Mitigating or minimizing loss mechanisms in bulk materials and interfaces is crucial. Various strategies have been explored, such as eliminating lossy dielectrics, using less reactive superconducting materials, optimizing fabrication recipes to diminish TLS losses at interfaces, and fabricating crystalline electrodes and tunnel junctions.[179] The following summarizes the latest advances in materials addressing these challenges.

6.4.1 Bulk Substrates

Low-loss substrates are crucial in coplanar geometries as most of the electric energy resides there (~90%).[195] The resonator quality (Q) and T_1 are inversely proportional to the loss tangent ($tan\delta_0$).[196] Sapphire and high-resistivity Si (>1000 Ω-cm) have been proven to be substrates with long coherence times.[232] While sapphire has a lower loss tangent ($tan\delta_0 = 10^{-8}$) compared to for high-resistivity Si ($tan\delta_0 = 10^{-6}$), there is no significant trend in TLS loss between fabrication devices deposited on sapphire and silicon.[196] Still, high-quality with low-impurities substrates are essential for achieving high-coherence times. Advancement in sapphire and Si single crystal growth have minimized their attributed loss.[233, 234] Studies comparing substrate quality and superconducting qubit properties reveal that Si doping reduces the Nb resonator performance,[235] float zone melting method for purified ^{28}Si substrates improves Si loss tangent,[236] and sapphire substrates grown by the heat exchange method result in higher quality transmons than those grown by the edge-defined film-fed method.[219]

Crystalline materials exhibit several orders of magnitude loss rates lower than their disordered counterparts. **Figure 6.8 A** depicts the loss tangent between different crystalline substrates, and **Figure 6.8 B** between different amorphous and dielectric thin films.[213] Ion milling processes, necessary for removing underlying lossy dielectrics such as SiO_2 for improving contact, [199] can increase loss tangent several orders of magnitude (**Figure 6.8 A**).

6.4.2 Tunnel Junctions

To date, creating a tunnel barrier in superconducting qubits is most effectively achieved through the oxidation of the superconducting metal or room-temperature oxide deposition. These two methods produce an amorphous layer that hosts TLS losses. As seen in **Figure 6.8 B**, the loss tangent of dielectrics varies with the deposition technique due to the different chemistries and physical effects involved. TLS sources such as OH- radicals in SiO_2 and Al_2O_3,[180, 237, 238] amorphization of Si,[239] and increment in the nitrogen concentration in SiN,[240] all increase the dielectric contribution to the loss.

Crystalline and epitaxial tunnel barriers have been explored to decrease losses, with examples like Al_2O_3 crystalline barrier[241] in a Re/Ti-Al_2O_3-Al JJ exhibiting lower losses ($tan\delta_0 = 6 \times 10^{-5}$) compared to conventional amorphous[242] Al_2O_3 in an Al-AlO_x-Al ($tan\delta_0 = 1 \times 10^{-3}$). Cubic AlN

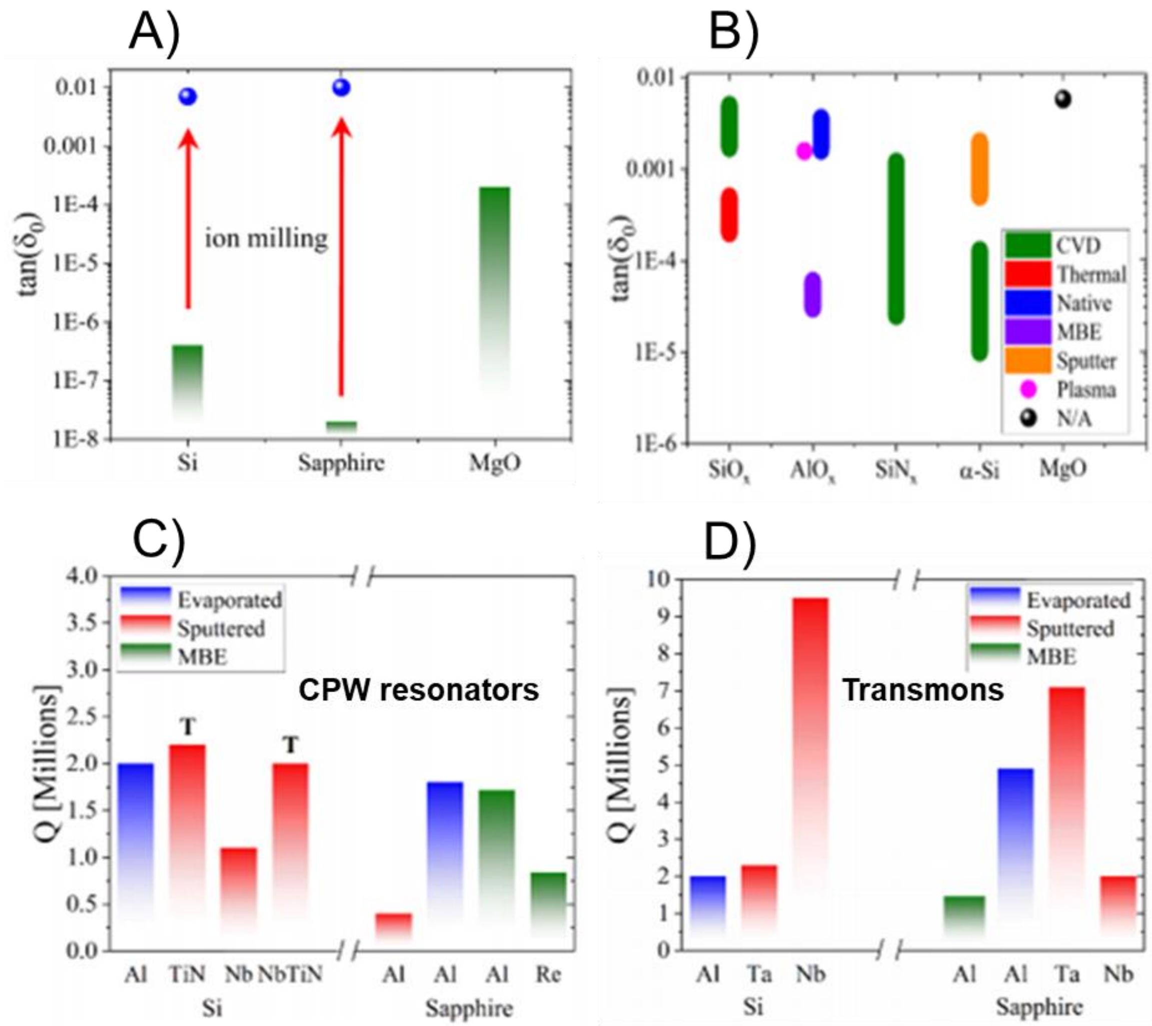

Figure 6.8. Overview of the use of materials in fabricating CPW resonators and transmons with different figures of merit. (A) Comparison of loss tangents for single crystal substrates and (B) dielectric films measured below 100 mK. (C) Comparison of quality factors of CPW resonators for three different deposition methods on Si and sapphire. (D) Comparison of quality factors of transmon qubits fabricated using various deposition methods and superconducting metallization. Retrieved and adapted from Ref. [245]

in NbN-AlN-NbN trilayer on Mg (100) resulted in a lower T_1 of 250-450 ns compared to shadow-evaporated junctions.[243] MgO, while possessing a higher loss tangent than Si and Al_2O_3 (**Figure 6 A**), was attributed to the low relaxation time. Recently, Kim *et al.* [244] addressed the use of MgO by introducing a TiN buffer layer on Si, obtaining a qubit relaxation time of 16.3 μs. Other try-outs, such as Al/GaAs/Al trilayer[246], evidenced the need to use non-piezoelectric materials to avoid loss due to phonon radiation.[247]

6.4.3 Metallic Films

The deposition and subsequent processing of metallic films intricately influence the overall performance of superconducting devices. The composition, impurity level, disorder, stress, stoichiometry, and crystal growth method can impact the TLS loss.[196] Aluminum, the most used superconductor, owes its popularity to the robust oxide layer, allowing precise control in JJ fabrication using simple shadow mask evaporation.[193] As shown in **Figure 6.8 C**, evaporated Al films show a similar quality factor Q in CPW resonators to those deposited by MBE. This suggests that different factors are involved besides the deposition process. Regarding the quality factor in transmons (**Figure 6.8 D**), Sputtered-deposited Nb has provided the best performance, even though MBE must offer an overall better crystal quality. In a comparative study, Kamal *et al.*[248] found that the lateral grain size of the MBE-grown Al film was more significant (0.3-1 μm) than the evaporated Al (0.1-0.3 μm). Additionally, an interlayer was observed in the evaporated-Al/Al_2O_3 interface (0.5 nm). These two factors should have caused the MBE-Al-based transmon to surpass the evaporated one. However, the main factor that increased the performance of these transmons was the substrate annealing prior deposition since the as-received substrate caused the thickest

Al_2O_3/Al interfaces (1.2-1.5 nm) and the lowest $T_1's$ (0.2-0.3 μs), independently of the deposition method. Additionally, Megrant *et al.*[249] concluded that the substrate surface cleaning and high-temperature annealing were the leading causes of improving the quality factor of Al films deposited by MBE and Sputtering

Considering the low critical temperature (T_c) and superconducting gap energy of Al, susceptibility quasiparticle excitation is observed.[213] Other superconducting materials with higher T_c such as Nb (9.2 K), Ta (4.5 K), Re (3 K), NbN (16 K), TiN (5.6 K), and Re-Mo alloys (10 K) have been explored. Sage *et al.*[250] compared Q values for resonators fabricated from polycrystalline Nb, Al, and TiN, as well as epitaxial Al and Rh. Nb/Si had the highest loss (1.5×10^{-5}) while TiN/Si had the lowest (9.6×10^{-7}). In TiN, the Q values in resonators patterned with preferential (200) direction were 10 times higher than (111).[251] Additionally, an optimized TiN resonator was obtained by reducing the strain in a film by increasing the N_2 pressure during the sputtering deposition.[252] Transmons fabricated with Ta demonstrate the highest performance, with T_1 exceeding 300 μs.[216] The hypothesis is that Ta forms a very thin and chemically robust oxide, contrasting with niobium. Epitaxial films such as Re (0002)[253] and Al (111)[254] aim to mitigate microstructural defects due to their close mismatch to Al_2O_3 (006) and both Si (111) and Al_2O_3 (006), respectively. However, it is challenging to attribute losses to only one study parameter since materials will have different properties considering the growth technique and growth parameters optimization, leading to different morphologies.[209] To date, the best quality factors have been achieved using polycrystalline metallic films and amorphous tunnel barriers.[213]

6.4.5 Surface Treatments

Efficient surface treatments are pivotal to mitigating surface-related losses that arise from uncontrolled surface states, oxides, and contamination. Pre-deposition cleaning of substrates, for instance, in Si-based systems, commonly involves an HF-dip to remove native oxides, reducing TLS losses.[255] Additional treatments, such as RCA-1 and high-vacuum annealing (880-950°), have been explored in Al/Si resonators.[256] Also, hexamethyldisilazane (HMDS) for creating a hydrophobic surface has improved the quality factor in NbTiN CPW resonators[257] and transmons qubits with $T_1 > 100\ \mu s$[258]. High-temperature annealing (>1000°C) eliminates organic residue and reconstructs the surface for sapphire substrates.[248] The use of oxygen plasma over Ar-ion milling for cleaning is preferred. Quintana *et al.* [199] found that intense Ar-ion milling degrades the substrate quality by incorporating Ar-ions.

Post-deposition cleaning and etching procedures play a crucial role in device fabrication. For example, HF treatment significantly improves the quality factor of Nb-based resonators by removing the Nb_2O_5 ($tan\delta_0 \sim 10^{-2}$), a significant source of microwave loss.[259] Buffered oxide etchant (BOE) has been employed for post-fabrication interface modification, enhancing CPW Nb/Si resonator performance.[260] **Figure 6.9 A** and **B** show the material's etching effect on the CPW Nb resonators at different etching times. For the non-etched CPW, XPS and CS-TEM showed that the thickness of the amorphous NbO_x layer is 4.5 nm while the SiO_x is 3 nm. As the time of BOE (5:1) dip-etching increases, the NbO_x and SiO_x are reduced in size. As seen in the XPS spectra and CS-TEM, the SiO_x was eliminated after only 30 s of etching, while the NbO_x was removed entirely after 1200 s. After CPW measurements, the main finding was that the SV interface is the main contributor to δ_{TLS} since after only 30 seconds, the δ_{TLS} are severely reduced, while the MV is the primary source of δ_{other} since more time is needed to reduce it (**Figure 6.9 C)**. The relationship

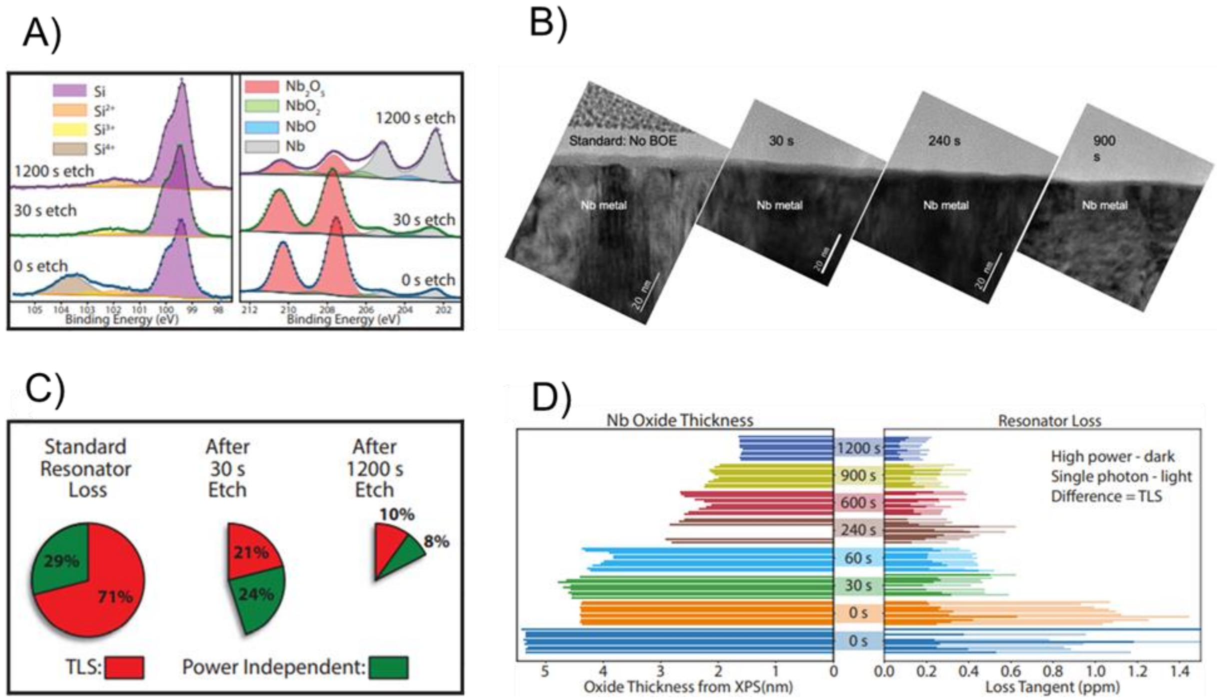

Figure 6.9. BOE etch effect on CPW Nb resonators. (A) XPS spectra comparing the MV and SV interfaces after BOE etching treatments. (B) CS-TEM of the MV interface after etching treatments. (C) Pie plots comparing loss distributions of TLS and high- power loss. (D) Histograms correlating the NbO_x thickness, determined by XPS, and the resonator loss. resonator loss. Retrieved from Ref. [262]

between Nb oxide thickness for different etching times and overall resonator loss can be seen in **Figure 6.9 D**. Clearly, the reduction of amorphous oxide enhances the performance of the CPW resonators.

Dry etching processes such as inductively coupled plasma (ICP) and reactive ion etching (RIE) based on SF_6 and CF_4 chemistries [261] were used to etch Ta films. The longer coherence time transmons were achieved using these dry etching processes.[217] Lift-off processes and the use of bandages for connecting Al electrodes have also seen continuous optimization.[258, 263]

In integrating 2D transmons with 3D architectures to enhance coherence time, addressing Nb_2O_5 and Nb hydrides is crucial. Surface treatments through chemical etching and annealing processes are of great interest in 3D niobium superconducting radiofrequency (SRF) cavities. Removal of Nb_2O_5 was achieved by in situ UHV annealing at 340-450°C, reducing the participation of TLS loss to obtain photon lifetimes of up to 2 seconds.[264] Polishing methods to improve surfaces in SRF cavities include BOE and electropolishing. These methods exposed the Nb metal to the solutions and air, which quickly caused hydrogen to be absorbed.[265] The presence of niobium hydrides is detrimental in SRF cavities since they are non-superconducting at $T_c > 1.3\ K$ and are responsible of the hydrogen Q-disease which refers to a large decrease in Q when hydrides form on the inner surface of the SRF cavity.[266]

CHAPTER 7:

FORMATION AND MICROWAVE LOSSES OF HYDRIDES IN NIOBIUM FROM WET CHEMICAL PROCESSING

This chapter is adapted from:

Torres-Castanedo C. G.*, Goronzy D. P., Pham T., McFadden A., Materise N., Das P. M., Cheng M., Lebedev D., Ribet S. M., Walker, M. J., Garcia-Wetten D. A., Kopas C. J., Marshal J., Lachman E., Zhelev N., Sauls J. A., Mutus J. Y., McRae C. R. H., Dravid, V. P., Bedzyk M. J. & Hersam M.C. Formation and Microwave Losses of Hydrides in Superconducting Niobium Thin Films Resulting from Fluoride Chemical Processing. *Submitted*.

*Equal contribution

7.1 Overview

Superconducting Nb thin films have attracted a revival of attention due to their utility in quantum information technologies. During the processing of these thin films, fluoride-based chemical etchants are employed to eliminate surface oxides, which are known to affect superconducting quantum devices adversely. However, these etchants can introduce hydrogen, forming Nb hydrides and potentially impacting microwave loss performance. This study comprehensively characterizes Nb hydrides formed in Nb thin films as a function of fluoride chemical treatments, utilizing secondary-ion mass spectrometry, X-ray scattering, and transmission electron microscopy to reveal the spatial distribution and phase transformation. The rate of hydride formation depends on the fluoride solution acidity and the etch rate of Nb_2O_5, which acts as a diffusion barrier for hydrogen. The resulting Nb hydrides detrimentally affect superconducting properties, increasing power-independent microwave loss in coplanar waveguide resonators. Notably, Nb hydrides show no correlation with two-level system loss or device aging mechanisms. In summary, this research offers valuable insights into Nb hydride formation and its impact on microwave loss, guiding ongoing efforts to enhance coherence time in superconducting quantum devices.

7.2 Background

Given their high fidelity and scalability, superconducting qubits hold great promise for quantum information technologies.[218, 267] Despite significant advancements in their performance over the past two decades, further improvement in coherence times is imperative for achieving scalable quantum computing.[268-270] Fabrication processes, often decoherence sources, can introduce impurities or defects in qubits, particularly influencing microwave loss mechanisms like two-level systems and excess unpaired quasiparticles.[218, 231, 245]

Superconducting qubits are produced using clean room techniques borrowed from the complementary metal-oxide-semiconductor (CMOS) industry to leverage existing fabrication processes.[271, 272] The extensive use of niobium (Nb) as the primary superconductor in these qubits is attributed to its compatibility with industrial-scale fabrication techniques and favorable superconducting properties, such as relatively high superconducting critical temperature (T_c ~ 9.2 K) and a low number of equilibrium quasiparticles at 10-20 mK.[273]

However, investigations into 2D resonators and 3D cavities have pinpointed the native Nb surface oxide as a detrimental source of microwave loss.[274, 275] Commonly employed fabrication protocols for surface cleaning and oxide removal utilize wet chemical fluoride-based etchants, such as hydrofluoric acid (HF) and the associated buffered oxide etchant (BOE). These etchants are integrated into various steps of qubit fabrication, including substrate cleaning before metallization and Josephson junction (JJ) deposition. They are also applied just before cryogenic cooling in the case of resonator measurements.[272, 276-278]

Notably, studies have demonstrated that using BOE to reduce amorphous surface oxides in Nb-based devices enhances resonator performance.[262] However, a potential concern arises as acidic solutions may introduce hydrogen into bulk Nb once the Nb_2O_5 top layer is removed.[279] The formation of Nb hydrides is potentially concerning for superconducting qubits, as these hydrides have been identified as a critical factor in reducing the quality factor in 3D superconducting radio frequency (SRF) Nb cavities. Different processing treatments introduced Nb hydrides to the Nb surface in this context.[280-282] Recently, similar hydride features have also been identified in Nb 2D superconducting qubits, raising further concerns.[283]

This chapter investigated the impact of fluoride-based chemical etching on forming Nb hydrides in Nb thin films at room temperature and their subsequent effects on Nb CPW resonator performance. Various etchants, including NH_4F, BOE, and HF, with concentrations ranging from 2% to 33%, were used to vary the hydrogen loading in b thin films. ToF-SIMS, XRD, TEM, and XRR are employed to track the incorporation of hydride species, identify crystallographic phases, and determine the etch rate of native Nb_2O_5. These experiments revealed an enhanced Nb hydride formation with the acidity of the etchant following a complete removal of Nb_2O_5.

Regarding superconducting properties, the formation of Nb hydrides correlates with suppressed T_c and residual resistance ratio (RRR). Microwave characterization of CPW resonators reveals increased power-independent loss in the presence of Nb hydrides. Conversely, two-level system (TLS) losses in the CPW resonators are not markedly affected by the presence of hydrides. Instead, nominal changes in TLS loss are more likely associated with variations in Nb_2O_5 layer thickness due to roughening of the Nb surface, as measured by AFM. By providing insights into the effects of fluoride-based etchants on hydride incorporation and superconducting properties, this research will help guide ongoing efforts to enhance Nb superconducting quantum device performance.

7.3 Formation of Nb Hydrides Resulting from Wet Chemical Processing

To explore the incorporation of hydrogen into niobium from fluoride-based chemical etchants, ~80 nm thick Nb films were exposed to the following range of fluoride-based aqueous solutions listed in order of increasing acidity: NH_4F, BOE, and HF (2%, 5%, 8%, 33%). Following a 20-minute immersion in each solution, the samples were characterized after air exposure. Air exposure stopped further hydride formation by facilitating the formation of native oxide Nb_2O_5, which functions as a hydrogen barrier.[279]

ToF-SIMS tracked the NbH^- ions as a function of depth into the film, as shown in **Figure 7.1 A**. The untreated sample showed the NbH^- ion signal peaking just below the Nb_2O_5, decreasing rapidly within the initial ~8 nm of the film (**Figure 7.2**). This observation is consistent with a report by Lee *et al.* [283], where the presence of hydrides in Nb thin films with no etching processes was observed. The NH_4F-treated film exhibited characteristics almost identical to the control film. (**Figures 7.1** and **7.2**) In contrast, the BOE-treated sample showed a deeper NbH^- signal. This trend of increasing depth persists as the etchant acidity increases. The hydride signal peaks and then rapidly decreases for the untreated control, NH_4F, BOE, and 2% HF samples. Conversely, the 5% HF, 8% HF, and 33% HF samples displayed a hydride signal reaching a plateau, followed by a slower decay. The extension of these plateaus correlated with the introduced hydrogen content.

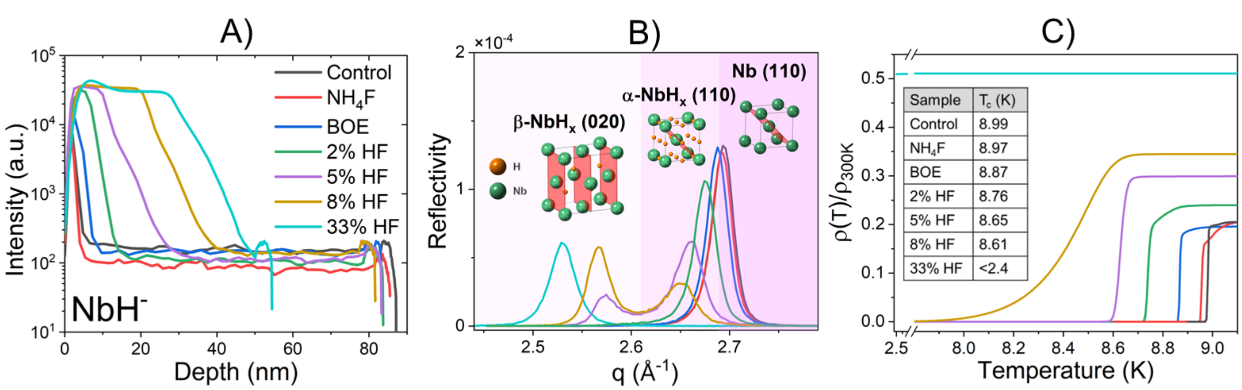

Figure 7.1. Nb hydride formation and properties. (A) NbH^- SIMS profiles, (B) XRD patterns, and (C) superconducting critical temperature measurements for a series of Nb thin films after 20 min fluoride-based etching treatments. The inset table in (C) shows the superconducting critical temperatures of the films. The line color legend in (A) also applies to (B) and (C).

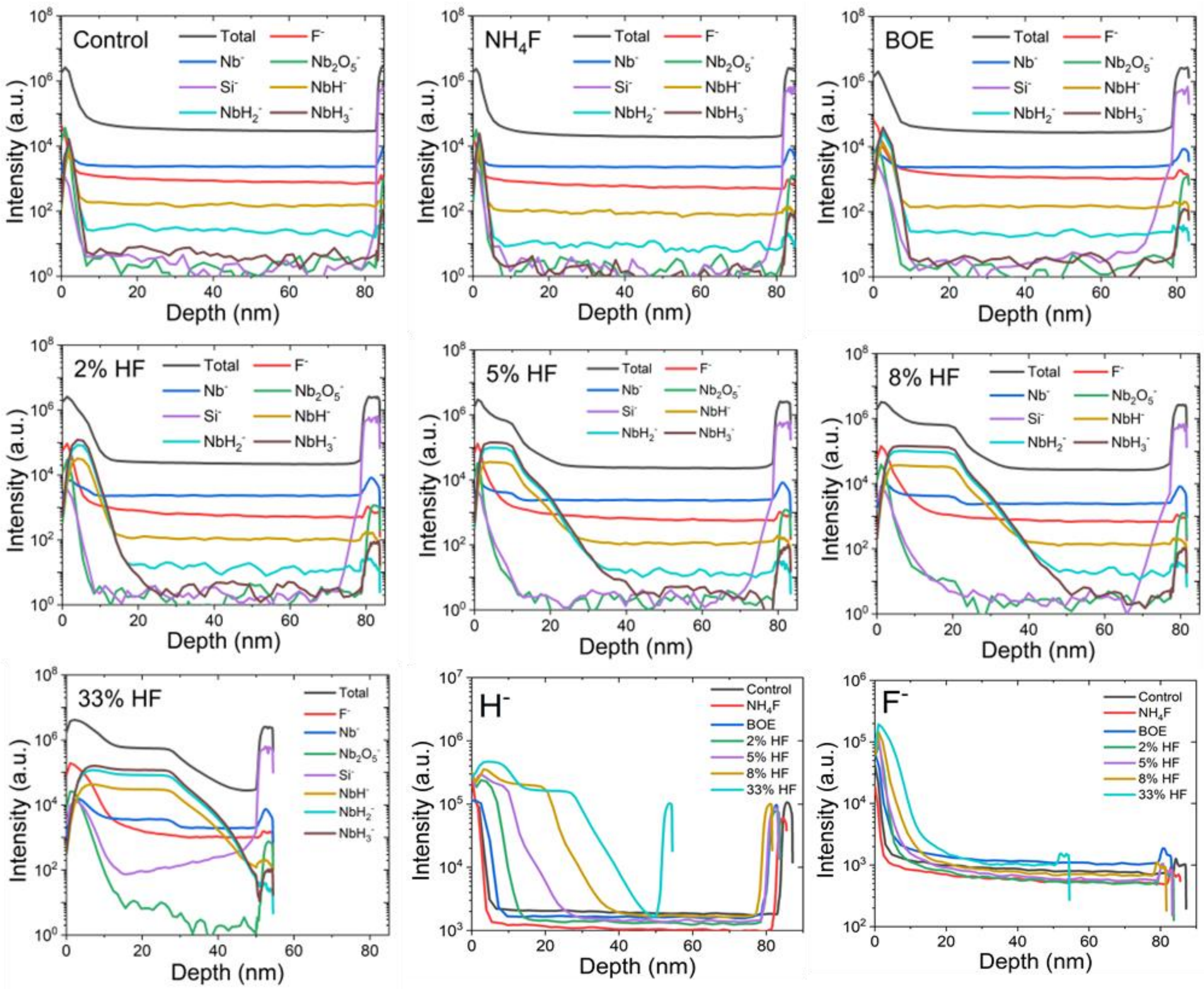

Figure 7.2. SIMS profiles of Nb thin films after 20 min etch treatments for selected ions.

The post-plateau intensity decline suggested excess hydrogen escape during the Cs^+ etching, exposing bare Nb to vacuum after the native oxide removal.[284] Furthermore, SIMS detected signals for other niobium hydride clusters, such as NbH_2^-, NbH_3^-, and H- ions, which all follow a similar trend as NbH^- (**Figure 7.2**). The F^- ion shows an increasing incorporation into the film but at a lower degree than the $(Nb)H^-$ species.

The identical set of samples was analyzed with XRD and XRR to examine further the impact of hydrogen incorporation on the structure of Nb film (**Figure 7.1 B** and **7.3**). XRD patterns exhibited a discernable shift in the Bragg peak towards lower scattering vector q ($q=4\pi sin\theta/\lambda$) with increasing aggressiveness of the etchant exposure, indicating a lattice expansion with the increment in the lattice spacing d ($d=2\pi/q_{peak}$). By tracking the change in d, the expansion of the lattice parameter a was traced from Nb body-centered-cubic (BCC) metal to α-NbH_x (BCC), a consequence of interstitially dissolved hydrogen in tetrahedral sites. As hydrogen content is increased, a phase transition to β-NbH_x face-centered-orthorhombic (FCO) occurs due to the ordering of the H atoms on a subset of tetrahedral interstitial sites.[285, 286] **Figure 7.1 B** depicts the regions of hydride phases, implying that hydrogen increasingly occupied tetrahedral sites in both BCC and FCO unit cells with increasing etchant acidity. Prior research found that the increase in lattice parameter in the Nb BCC structure as a function of hydrogen content was approximately 0.0023 Å per at.% of hydrogen.[287]

Table 7.1 detailed the volume fractions derived from the Bragg peaks for Nb (110), α-NbH_x (110), and β-NbH_x (020), alongside the at.% of hydrogen based on the lattice expansion of α-NbH_x (110).[7] **Figure 7.1 B** revealed nearly identical Bragg peaks for untreated and NH_4F-treated films, suggesting minimal to non-hydrogen incorporation from the NH_4F treatment. Conversely, the

Sample	Nb (110)	α-NbH_x(110) x=0.005-0.25	β-NbH_x (020) X>0.80
Control	100%		
NH_4F	100%		
BOE (5:1)	86.4%	13.6% (x≈0.03)	
2% HF		100% (x≈0.10)	
5% HF		84.7% (x≈0.19)	15.3%
8% HF		62.7% (x≈0.25)	37.3%
33% HF			100%

Table 7.1. Volume fractions for the Nb and NbH_x phases of the etched Nb thin films. Fractions extracted from the integrated area of the Bragg peaks and using kinematical diffraction theory. The volume fraction was calculated by multiplying the area by $V_{uc}/(LP*|FF|^2)$, where V_{uc} is the volume of the unit cell, LP is the Lorentz polarization factor and FF is the atomic form factor.

BOE-treated sample showed a slight lattice expansion, while the 2% HF sample confirmed an intensified shift, indicating a significant presence of α-NbH_x. Substantial compositional changes started with the 5% HF treatment, with a secondary Bragg peak corresponding to β-NbH_x. This trend persisted with the 8% HF treatment. In the case of 33% HF, the XRD pattern revealed a complete conversion to β-NbH_x.

XRR revealed an increased NbH_x concentration in films with more aggressive etchants, depicted in the inset in **Figure 7.3**. The decreasing critical angle corresponded to the electron density transitioning from Nb to NbH_x. Additionally, XRR facilitated the extraction of thicknesses and interfacial roughnesses of the various layers in the film, including the surface oxide, bulk Nb, and Nb/Si substrate interface (**Table 7.2**). These values indicated a relatively constant thickness of Nb, except for a slight deviation at 8% HF and more abruptly at 33% HF.

Critical temperature (T_c) was extracted from temperature-dependent resistivity measurements, as shown in **Figure 7.1 C**, to assess the impact of hydrides on superconducting properties. The T_c

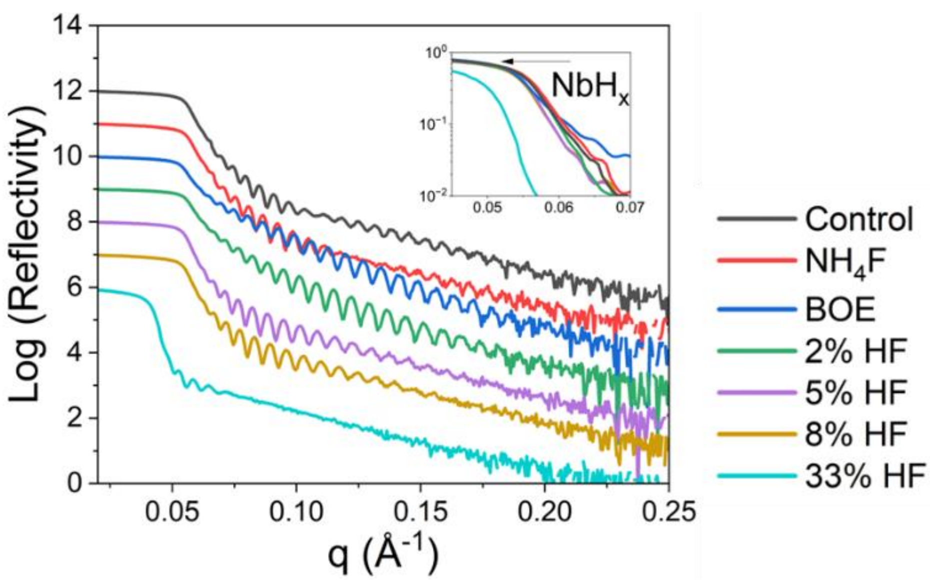

Figure 7.3. XRR of the etched Nb thin films. The inset shows the decrease of the critical angle from Nb to NbHx. Each profile has a constant offset.

Sample	Nb_xSi_y	Nb	Nb_xO_y	Total
Control	1.3	79.8	3.0	84.1
NH_4F	1.3	78.9	2.5	82.7
BOE (5:1)	1.3	76.2	2.5	80.0
2% HF	1.3	76.0	2.5	79.8
5% HF	1.3	76.1	2.5	79.9
8% HF	1.3	72.9	4.3	78.5
33% HF	1.3	43.8	6.2	51.3

Table 7.2. Thicknesses extracted from XRR fittings of the etched Nb thin films.

trend aligns with the SIMS and XRD findings, where the control and NH_4F samples exhibit almost identical behavior, followed by a gradual reduction in T_c as hydrogen incorporation increases. The depression in T_c within the α-NbH_x phase is explained by an increase in resistance due to interstitial hydrogen and disruption of local superconductivity caused by ε-NbH_x precipitates formed at low temperatures.[288, 289]

A notable deviation is observed in the 8% HF-treated film compared to samples treated by less aggressive etchants. This deviation is characterized by a significant broadening in the superconducting transition (ΔT) and an increase in normalized resistivity ($\rho(T)/\rho_{300K}$). This phenomenon is attributed to an inhomogeneous system comprising regions of the superconducting phase (α-NbH) and non-superconducting phase (ε-NbH_x).[290] In the extreme limit of the 33% HF-treated film, no superconducting transition is observed down to the measurement limit of 2.4 K.

Sample	T_c (K)	RRR	ΔT (K)
Control	8.99	5.08	0.015
NH_4F	8.97	5.64	0.015
BOE	8.87	5.13	0.033
2% HF	8.76	4.18	0.035
5% HF	8.65	3.34	0.065
8% HF	8.61	3.09	0.465
33% HF	<2.4	1.96	-

Table 7.3. Critical temperature, residual resistance ratio, and transition width of the etched Nb thin films.

This aligns with previous work indicating the absence of superconductivity for β-NbH_x/ε-NbH_x down to 1.3 K.[289] **Table 7.3** summarizes T_c, residual resistance ratio (RRR = R_{300K}/R_{10K}), and ΔT values. The depression of T_c and RRR, along with the broadening of ΔT, collectively serve as indicators of hydride formation, compromising the superconducting properties of the Nb thin films.

7.3 Time Evolution of Nb Hydrides

Nb films (~40 nm) were employed to investigate the time scales of hydrogen incorporation. Thinner samples were used to improve sensitivity to hydride concentration changes. **Figure 7.4** displays the XRD measurements for five different etchants at different exposure times (45 s, 3 min, 20 min, 42 min, 2 h, and 13 h). **Figure 7.5** summarizes the volume fraction evolution of the

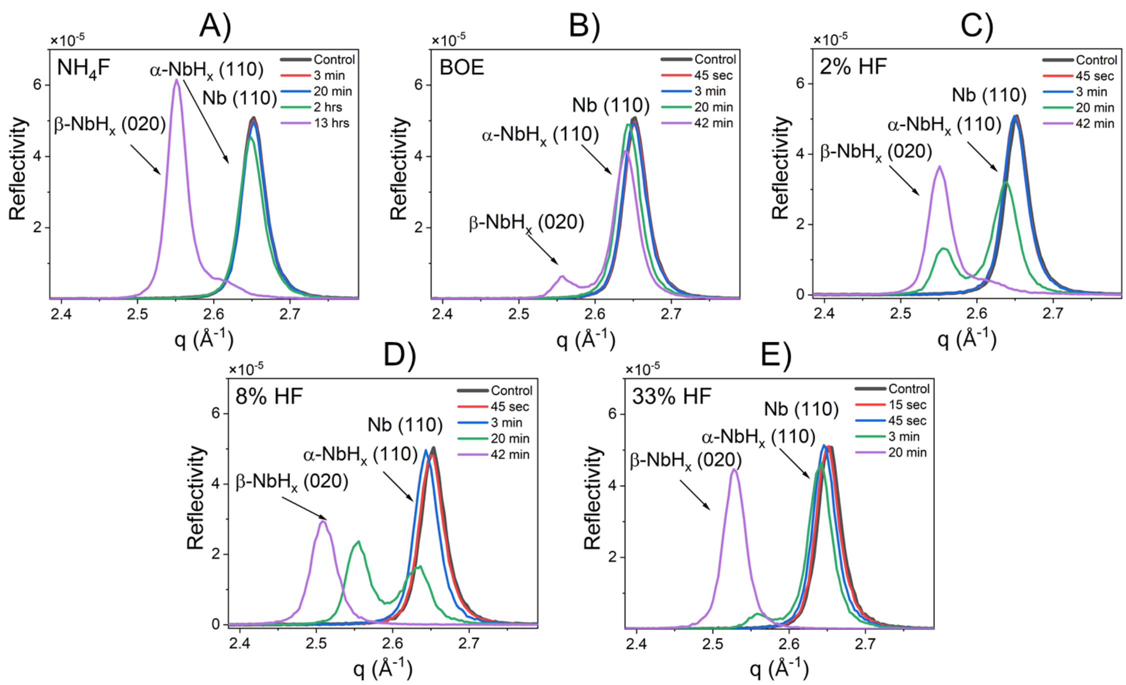

Fig. 7.4. X-ray diffraction of 40 nm Nb thin films treated with different etching times and etchants. The etchants include (A) NH_4F, (B) BOE, (C) 2% HF, (D) 8% HF, and (E) 33% HF.

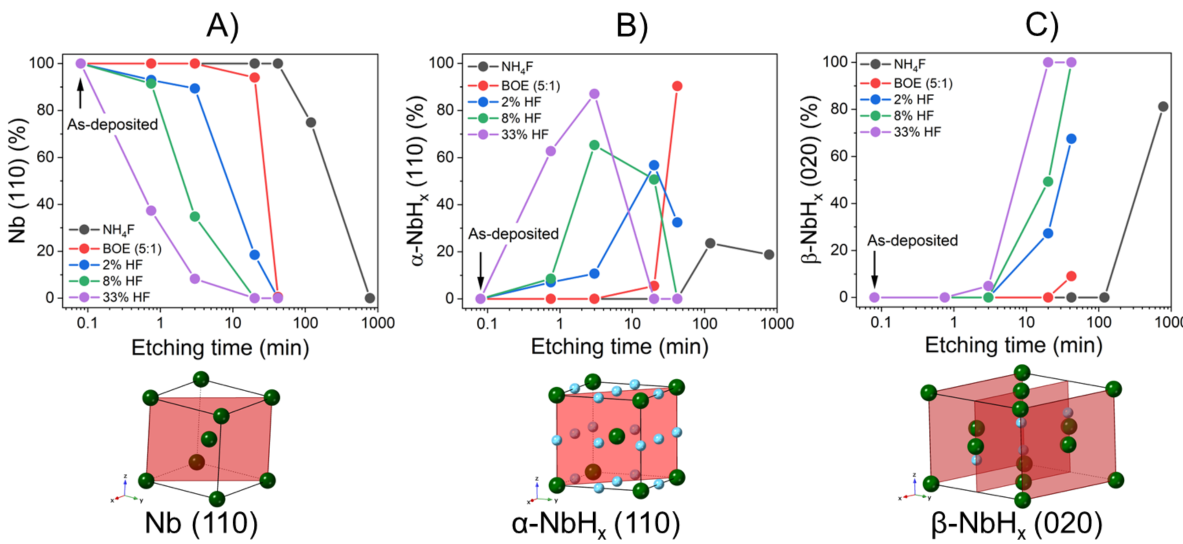

Figure 7.5. Nb hydride phase evolution during etching. Volume fractions of (A) Nb (110), (B) α-NbH_x (110), and (C) β-NbH_x (020) of the 40-nm-thick Nb thin films treated with different etchants and times as extracted from XRD data of Figure S5. The volume fractions were calculated from the integrated area of the Bragg peaks using kinematical diffraction theory. The diffraction planes for each phase are shown below their respective phase volume fraction plots.

different phases (Nb (110), α-NbHx (110), and β-NbHx (020). The 33% HF condition fully converts the Nb film to β-NbHx after only 20 min. For the 8% HF condition, α-NbHx (110) evidence is observed after just 45 sec, a mix of hydride phases after 20 min, and a complete conversion to β-NbHx after 42 min. Less aggressive etchants show slower hydrogen incorporation and NbH_x phase transformation. The 2% HF sample exhibits a noticeable peak shift after 3 min, BOE after 20 min, and NH_4F only after significantly longer exposure (13 hr). In all cases, the formation of the β-NbHx phase forms after saturation of the α-NbHx phase. The reduction in β-NbHx peak intensity for higher acidity etchants is attributed to Nb film etching and subsequent thickness reduction,

The nanoscale distribution of NbH_x phases in 40-nm-thick Nb thin films was examined using multimodal electron microscopy techniques (**Figure 7.6**). Analyzed samples include the untreated

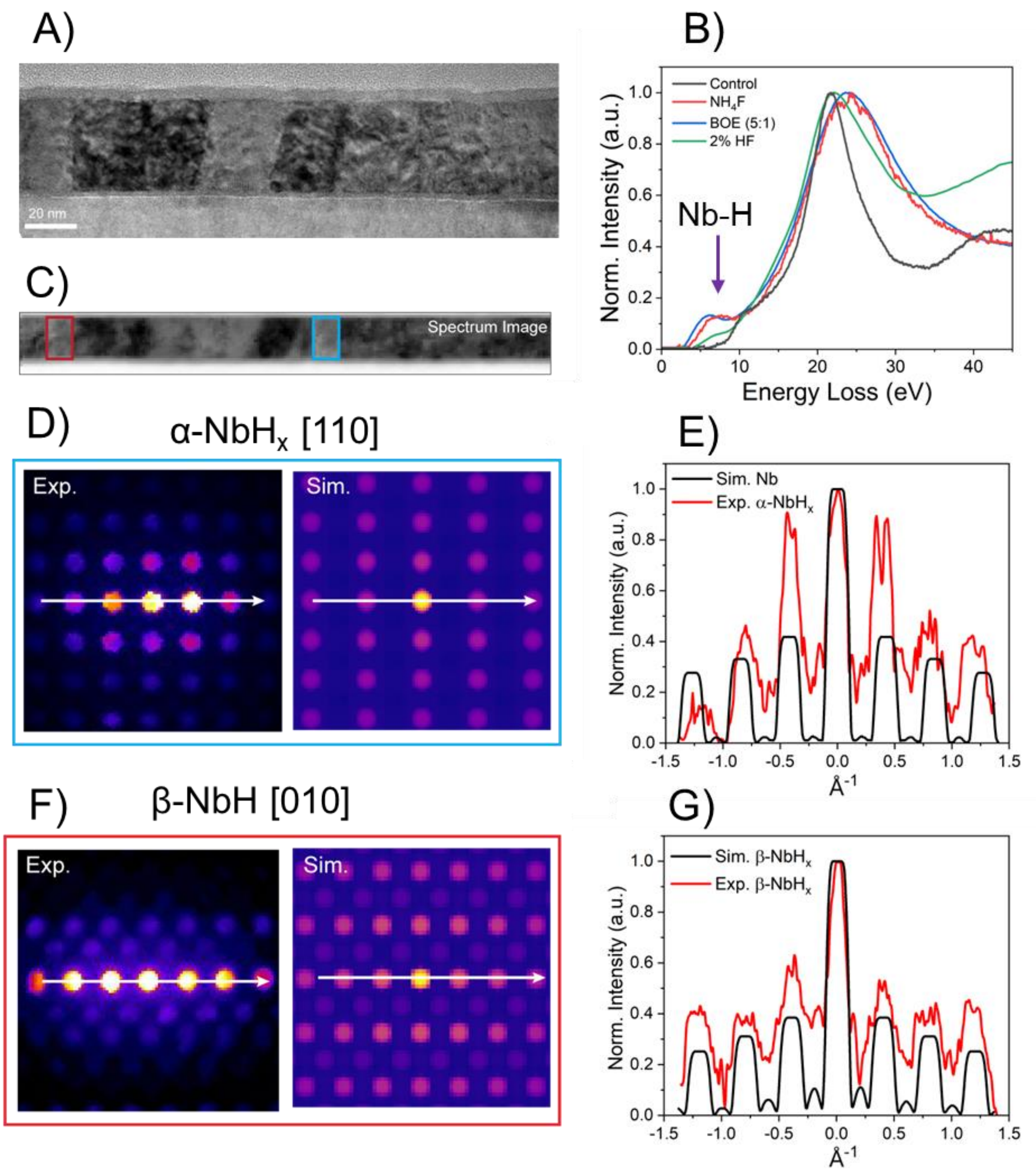

Figure 7.6. Nanoscale distribution of NbH_x phases. (A) Bright-field TEM image of NH_4F-treated Nb thin film showing its columnar grain structure. (B) EELS of the untreated control and chemically-treated Nb thin films. (C) A spectrum image of the NH_4F-treated Nb sample. The pixels within the blue and red boxes (20×35 nm^2) are used to generate the average CBED patterns in (D) and (F), respectively. (D) CBED patterns of Nb [110] were obtained by experiment (left) and multislice simulation (right). (E) Line profiles of patterns in (D) show a lattice expansion in the experimental pattern. (F) CBED patterns of β-NbH [010] were obtained by experiment (left) and multislice simulation (right). (G) Line profiles of patterns in (F).

control, BOE exposure for 42 min, 2% HF exposure for 20 min, and NH_4F exposure for 13 hr, in order of hydrogen content based on XRD results (**Figure 7.4**). All Nb films have a columnar structure with grain sizes of 20-40 nm in width (**Figure 7.4 A**).

In **Figure 7.4 B**, representative EELS spectra in the low-loss region reveal a shoulder at 5-8 eV (highlighted with a purple arrow), indicating metal-hydrogen bonding.[291-294] Conversely, the control samples show a distinct Nb plasmon peak ~10 eV.[292] The other Nb plasmon peak in control at ~21 eV shifts to higher energies (23-25 eV) in processed samples, suggesting Nb-H bonding and confirming its presence in treated films.[291, 292]

To investigate the nanoscale distribution of NbH_x phases detected by the XRD, 4D-STEM is employed, acquiring two-dimensional electron diffraction patterns at each probe scanning position,[295, 296], creating a spectrum image (**Figure 7.6 C**). This method provides structural information from a nanoscale volume, localizing phases embedded within the Nb matrix with sub-angstrom resolution. **Figures 7.6 D** and **F** show integrated 4D-STEM data summed over two areas in the 13 hr NH_4F-treated sample enclosed by the blue and red boxes in **Figure 7.6 C**, respectively. The line profiles in **Figure 7.6 E** comparing experimental and simulated Nb [110] patterns reveal a lattice expansion (~2.5 %), suggesting that the blue area is an expanded Nb phase (i.e., α-NbH_x). On the other hand, the line profiles of the observed and simulated patterns for the red area in **Figure 7.6 E** match reasonably well, indicating β-NbH_x (**Figure 7.6 G**).

7.5 Role of Nb_2O_5 in the Formation of Nb Hydrides

To understand the role of the primary Nb surface oxide, Nb_2O_5, in incorporating hydrogen into the Nb films, standalone 40-nm-thick Nb_2O_5 films were produced by PLD. As observed by XPS,

Nb_2O_5 is the predominant oxide for the Nb thin films. (**Figure 7.7 A**). The PLD deposition was optimized using XPS and XRR to track the film composition under different deposition conditions. XPS for the optimized film is shown in **Figure 7.7 B**. Then, the etch rate of the Nb_2O_5 was measured by XRR for the different etchants and times. XRR was used to determine the etch rate of Nb_2O_5 during progressively longer etching treatments. **Figure 7.8 A** reveals that the etch rate of Nb_2O_5 increases etchant acidity, strongly correlating with the rate of hydrogen incorporation into the Nb film.

Further investigation involved a two-step sequential etch procedure on an Nb film: a short etch (2 min) in 2% HF to remove the surface oxide and an immediate transfer to NH_4F solution for extended treatment (42 min). XRD results (**Figure 7.8 B**) show that while a film treated only with NH_4F for 42 min remains unchanged, a film first etched in 2% HF and then in NH_4F for 42 min now exhibits a mix of α-NbH_x and β-NbH_x. Following a fast etch of Nb_2O_5 in 2% HF, the exposed Nb surface undergoes hydrogen incorporation upon exposure to NH_4F. Compared to the 42-minute treatment using 2% HF only, where mainly β-NbH is observed, less hydrogen is captured in the

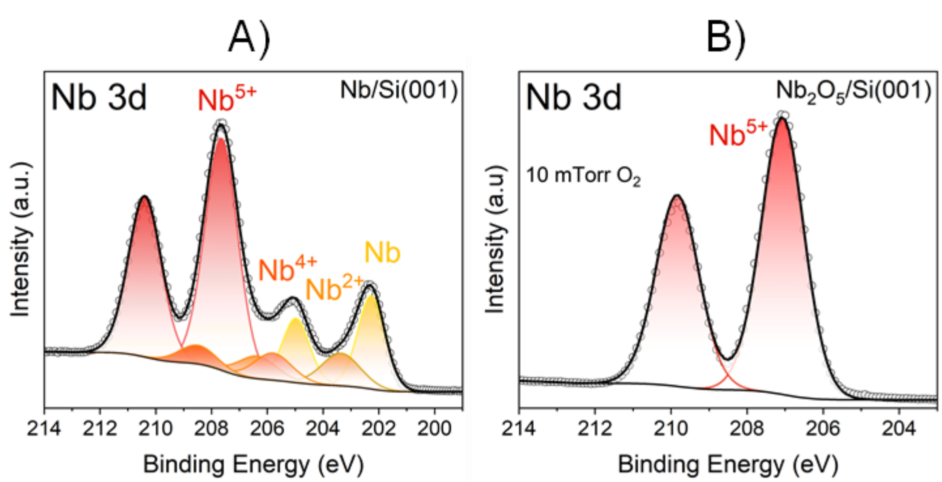

Fig. 7.7. XPS of the A) Nb/Si(001) and B) Nb_2O_5/Si(001) thin films. Both films are ~40 nm thick.

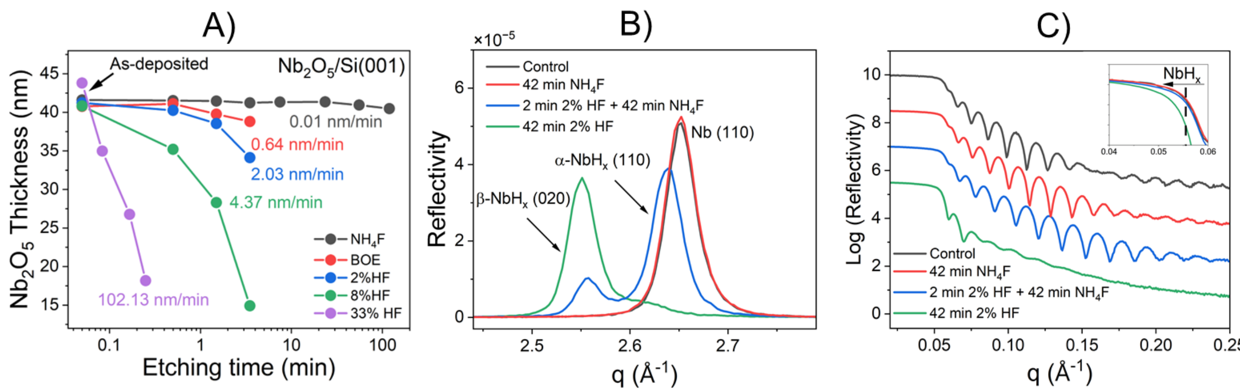

Figure 7.8. Nb_2O_5 etching and proposed sequential etching procedure. (A) XRR-determined etching rate of Nb_2O_5 thin films for different etchants. (B) XRD and (C) XRR of sequentially etched (2 min 2% HF and 42 min NH_4F) Nb thin films.

Nb for the NH_4F case due to the lower concentration of H^+ in the NH_4F solution. These findings were supported by XRR (**Figure 7.8 C**), revealing a decrease in electron density associated with increased hydrogen for the sequentially etched sample and, more markedly, for the 42 min 2% HF sample. These results conclude that the rate at which an etchant can incorporate hydrogen into an Nb film is determined by the rate of Nb_2O_5 removal and the available hydrogen concentration in the etching solution.

7.6 Loss Mechanisms Associated with Nb Hydrides

To asses the impact of Nb hydrides on superconducting devices, λ/4 CPW Nb resonators were fabricated, and microwave measurements were conducted after treating the resonators with the same etching conditions as the Nb films. CPW measurements can effectively explore defects associated with losses.[231] Power-dependent measurements of the internal quality factor (Q_i) were performed, and power-independent (δ_{PI}) and two-level system (δ_{TLS}) loss tangents were extracted,[231] (**Figure 7.9**). Resonators under different etching conditions exhibited varying degrees

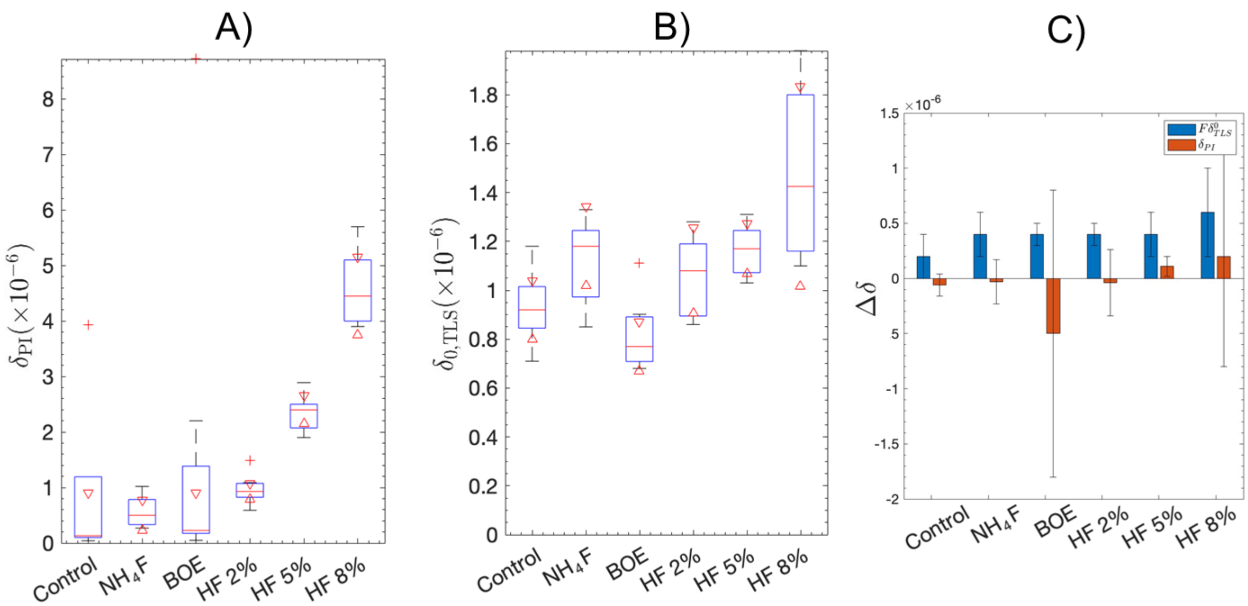

Figure 7.9. CPW Nb resonator results. (A) Power-independent (PI) and (B) two-level systems (TLS) losses of Nb CPW resonators after 20 min treatments in the indicated etchants. Losses were extracted from the nonlinear least square fit to the TLS power-dependent model. The blue boxes contain the 25th and 75th percentiles, the red horizontal lines indicate the median values, the red triangles show the 95% confidence intervals about the median, the red plus signs are outliers, and the black horizontal lines are the minimum and maximum values excluding outliers. (C) Change in PI and TLS losses after two months of aging in air.

of PI losses, indicating a clear trend corresponding to increasing hydride concentration. (**Figure 7.9 A**) Control, NH_4F, and BOE resonators showed similar low PI losses, consistent with low hydrogen loading. However, from the 2% HF condition onwards, there was a noticeable increase in PI loss, peaking at 8% HF, where the loss tangent exceeded four times that of the control. 33% HF-treated resonators did not yield measurable signals, suggesting non-superconductivity or extremely low internal quality factors.

The increased PI loss, coupled with the T_c depressions discussed in Section 7.3, implies increased quasiparticle generation due to higher hydrogen loading. Potential mechanisms could explain this increased quasiparticle generation. Potential mechanisms include hydrides acting as magnetic scattering impurities, though the magnetism in NbH_x phases remains uncertain. The increased quasiparticle and reduced T_c align with recent theoretical findings by Sauls and collaborators.[297] Their study indicates that due to the anisotropic superfluid gap of Nb, impurities (e.g., NbH_x precipitates) can still act as pair-breakers even when non-magnetic. Lastly, another theoretical result by Sauls and collaborators shows that TLSs embedded in bulk superconductors can generate dissipative quasiparticles at GHz frequencies.[298]

In contrast, the impact of Nb hydrides on TLS losses is less pronounced (**Figure 7.9 B**). Control, NH_4F, 2% HF, and 5% HF samples exhibit similar levels of TLS loss. BOE treatment slightly decreases TLS losses, likely due to the reduced Nb surface oxide thickness with minimal hydride introduction. The 8% HF condition shows increased TLS associated with a rise in the surface roughness and surface oxide thickness.

AFM was used to analyze the surface of the Nb and Si areas on the fabricated resonator chips after each treatment protocol. (**Figure 7.10**). While a slight smoothening effect on Si surfaces was observed with increasing etchant acidity, the overall change in the RMS is minimal. In contrast, the Nb surface exhibited substantial roughening with increasing etchant acidity, leading to thicker

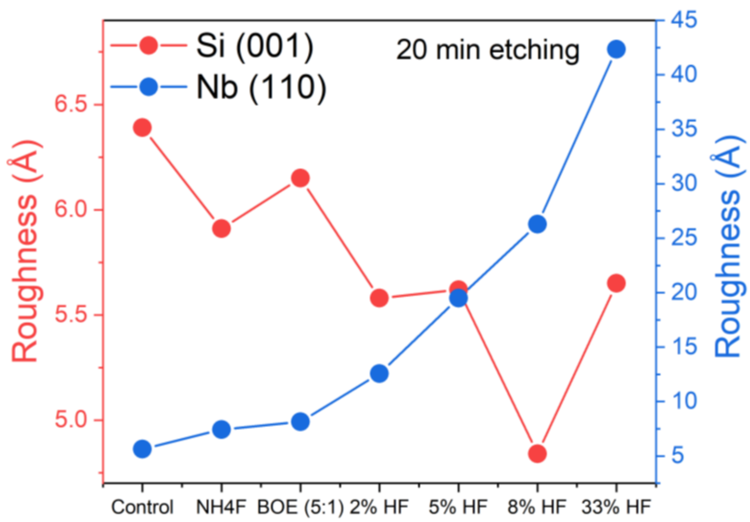

Fig. 7.10. AFM-determined RMS roughness of the Nb and Si surfaces in the Nb resonators after 20 min wet etch treatments.

Nb_2O_5, which is expected to increase TLS losses. Previously, a decrease in Nb_2O_5 thickness has been linked to an overall improvement in resonator loss.[262] However, in that study, both Nb_2O_5 and SiO_2 were found to host TLS losses. SiO_2 in the samples is expected to be uniform across the different resonators due to the similarity in Si surface roughness and since the samples were exposed to air for the same time before microwave measurements.

A second series of resonator measurements investigated aging effects linked to hydrogen loading. The identical resonators (**Figure 7.9 A** and **B**) were aged over two months in ambient laboratory conditions, and microwave characterization was repeated. **Figure 7.9 C** shows the difference ($\Delta\delta$) between PI and TLS losses before and after aging. PI losses showed minimal change after aging, consistent with unaltered hydrogen loading since Nb_2O_5 prevents hydrogen intake or escape.[279] For TLS losses, a uniform increase was observed across all resonators and treatment conditions following aging, suggesting increased TLS loss sources due to oxide thickening[274] and additional contamination during storage.[299] Previous reports have also observed increased TLS losses after long exposure of Nb to air,[274] It should be noted that earlier studies on Nb cavities and 2D Nb qubits have shown that hydride precipitates disorder the Nb surface,[281, 283] which has led to hydrides being hypothesized to be sources for both TLS and PI losses in addition to contributing to aging mechanisms.[283] However, our results suggest that while Nb hydride correlates with increased PI losses, it does not significantly contribute to TLS losses or aging.

7.6 Summary

This study investigated the formation of Nb hydrides in thin films induced by fluorine-based etchant, namely NH4F, BOE, and HF (2%, 5%, 8%, and 33%). As the etchant acidity increased, SIMS revealed a proportional rise in hydride concentration. Concurrently, X-ray and electron diffraction showcased phase transitions from Nb metal to α-NbH_x and eventually to β-NbH_x under more aggressive etching conditions. The time evolution of Nb hydrides for different etchants was presented. Examining Nb CPW resonators with varying hydrogen loading, PI loss tangents exhibited a clear correlation with hydride concentration. In contrast, TLS loss tangents remained largely unaffected despite roughening of the Nb surface induced by aggressive etching, leading to increased Nb_2O_5 and associated TLS losses. Aged resonators in the air indicated stable PI loss, linked to a constant hydride concentration, and a uniform increase in TLS across all hydrogen loading conditions due to additional oxide growth and contamination during storage.

The investigation of Nb_2O_5 films revealed a direct correlation between the rate of hydride formation and the Nb_2O_5 etch rate for a given etching solution. Combining this insight with the results on sequential etching with 2% HF and NH_4F, two main factors were identified to influence the hydrogen incorporation into Nb films: (1) Removal of the Nb_2O_5 surface oxide, a hydrogen diffusion barrier; (2) Hydrogen concentration in the etching solution exposed to the oxide-free Nb surface. Therefore, effective cleaning and etching strategies should consider these factors to minimize detrimental hydride formation in superconducting devices. This comprehensive exploration of Nb hydride formation and its association with loss mechanisms enhances the understanding of the interplay between materials processing and superconducting device performance, thus guiding the development of fabrication procedures in quantum information technologies.

7.7 Experimental Methods

7.7.1 Sample Preparation

For structural and chemical characterization, as well as cryogenic microwave measurements, 80 nm thick Nb films were deposited on double-side polished intrinsic 3-inch Si (001) wafers (WaferPro 380 μm, >10 MΩ) using DC sputtering. The wafers underwent standard RCA1/RCA2 cleaning and BOE (6:1) etching for 2 min. The Nb deposition took place in a Multi Tool Deposition System (PVD Products) chamber with specific conditions, including an initial base pressure $<1\times10^{-8}$ Torr and a deposition condition of 3 mTorr of Ar and 300 W from a 2-inch diameter Nb target (JX Nippon, 5N).

For interfacial and bulk studies, 40 nm thick Nb films were deposited HiPIMS on intrinsic 6-inch Si (001) wafers. The wafers underwent standard RCA1/RCA2 cleaning and BOE (5:1) etching for 30 sec. The Nb deposition occurred in a system with a base pressure $\sim 2\text{x}10^{-9}$ Torr, utilizing a 5N Nb target (JX Nippon, 5N). The substrate received a bakeout at 150 °C in the loadlock before transfer into the main deposition chamber.

Amorphous Nb_2O_5 thin films were on one-side polished intrinsic Si (001) wafer by PLD in a PVD Products PLD/MBE 2300 equipped with a 248 nm KrF excimer laser. The PLD process was conducted at room temperature in a 10 mTorr O_2 atmosphere with a pulse frequency of 10 Hz. The 40-nm-thick films were produced form a Nb_2O_5 target, and the laser was focused on a 2×4 mm^2 spot size with an energy of ~160 mJ/pulse.

Etching treatments were carried out using different HF (KMG Electronic Chemicals, 49% aqueous) and NH_4F (KMG Chemicals, 40% Aqueous) solutions: NH_4F, BOE (5:1), 2% HF, 5%

HF, 8% HF, and 33% HF in descending pH order. The 80-nm-thick Nb films were etched for 20 min under the different etchants. The 40-nm-thick Nb and 40-nm-thick-Nb_2O_5 films were subjected to varied etching times and specific etchants. All samples, including the Nb resonators, were etched at room temperature on an orbital shaker rotating at 60 rpm to ensure uniform etching. All thin film samples were approximately 10×10 mm^2 in area.

7.7.2 X-ray Diffraction and X-ray Reflectivity

XRR and XRD were conducted using a Smartlab Gen 2 diffractometer with a 9 kW Cu rotating anode and a Ge (220) 2-bounce monochromator (λ = 1.5406 Å). The Motofit software aided in fitting XRR data with a multiple-slab model. All the XRR and XRD data were normalized with the straight-to-beam intensity. Quantification and identification of the crystallographic phases (Nb, α-NbH_x, and β-NbH_x) were determined by Gaussian fittings in the three 2θ regions of interest. The phase volume was calculated considering kinematical theory, integrating the areas from the Gaussian fits and considering each phase's differential cross-section, including the unit cell structure, unit cell volume, and polarization factor.[7] Specifically, the Bragg peak area was multiplied by $V_{uc}/(LP^*|FF|^2)$, where V_{uc} is the volume of the unit cell, LP is the Lorentz polarization factor, and FF is the atomic form factor.

7.7.3 Transmission Electron Microscopy

For the TEM analysis, lamella cross-sections were prepared using a dual-beam FIB FEI-SEM Helios Nanolab. The lift-off involved 30 kV Ga^+ ions, followed by a final cleaning step at 2 kV to eliminate surface damage on the area of interest, resulting in a sample thickness of 50-100 nm. TEM and STEM data were collected on a probe-corrected JEOL ARM200 S/TEM at 200 kV. A convergent angle of 25 mrad was employed for ADF-STEM imaging.

EELS spectra were obtained at 200 kV using a Gatan GIF Quantum on a K2 pixelated detector. Data processing steps, including background subtraction, plural scattering removal, and signal mapping, were carried out using Gatan GMS software. 4D-STEM data were collected using a OneView camera with a 512 × 512 or 256 × 256 pixels software bin size. Convergent angles of 3-5 mrad and a camera length of 20 cm were applied, with a 5-10 Å step size. Virtual-detector images for NbH phase mapping were generated through the Gatan GMS 4D-STEM package and the open-source py4dstem package. 4D-STEM patterns were simulated using the abTEM package with input parameters from the experimental conditions.

7.7.4 Atomic Force Microscopy

An Asylum Cypher atomic force microscope, equipped with a Si cantilever having a resonant frequency ranging between 320-340 kHz, was employed in tapping mode. High-resolution imaging was achieved with a pixel resolution of 512 × 512 pixels and a scanning rate of 1 Hz.

7.7.5 X-ray Photoelectron Spectroscopy

XPS spectra were obtained using a Thermo Scientific ESCALAB 250Xi XPS spectrometer with a monochromated Al Kα X-ray source with an energy of 1486.6 eV. The measurement spot size was ~500 µm, and charge compensation was achieved using a flood gun. Avantage software (Thermo Scientific) facilitated the analysis. Core levels were fitted using a modified Shirley background and a Gaussian-Lorentzian product (70% Gaussian and 30% Lorentzian). Peak positions were charged-corrected to adventitious carbon (C 1s) at 284.8 eV.

7.7.6 Time-of-flight Secondary-ion Mass Spectrometry

An IONTOF M6 dual-beam system (IONTOF GmbH) was used to analyze the concentrations and depth distribution of the Nb thin films. Bi^+ ions at 30 keV were employed for negative polarity measurements on a 25× 25 μm^2 area, while Cs^+ ions with an energy of 500 eV facilitated sputtering a 150 × 150 μm^2 area for depth profiling. The resulting data were processed using SurfaceLab7 software.

7.7.7 Electrical Resistivity at Low Temperatures

Electrical transport measurements were conducted using a Quantum Design PPMS (Dynacool) in a four-probe geometry. Chip carriers were utilized, and devices were wire-bonded to them using a homebuilt In-Au bonder. T_c was determined by the intersection of linear fits on either side of the sharp transition. RRR was calculated from the ratio of the resistances at 300 K and 10 K. ΔT was derived from the temperature interval between points corresponding to 10% and 90% of the resistance during the superconducting phase transition.

7.7.8 Niobium Resonator Fabrication

80-nm-thick Nb films underwent CPW resonator pattering through standard photolithography and dry etching. The fabrication involved solvent cleaning of the Nb-coated wafer, spin coating with P20 primer and SPR660 photoresist, and subsequent patterning using direct laser writing. After development and cleaning, the wafer was etched in an inductively coupled plasma (ICO) tool with SF_6 and monitored optically for etching through Nb and approximately 100 nm into the Si substrate. An established CPW resonator design that consisted of eight frequency-multiplexed, inductively-coupled, quarter-wave resonators in hanger mode off a central feedline was utilized.[300] The CPW conductor/gap dimensions were 6 μm/3 μm, so the resonance frequencies fell between 4-8 GHz. The photoresist was removed using an NMP-based remover held at 80 °C with ultrasonication followed by rinsing in isopropanol. The Nb resonators were treated for 20 min in different solutions before measurements.

7.7.9 Resonator Microwave Measurements

Microwave transmission measurements were conducted on CPW hanger resonators using a vector network analyzer over several decades of input power. The resonators were enclosed in gold-plated, oxygen-free copper sample boxes with pogo pins for stabilization and grounding. Initial measurements occurred in a cryogen-free dilution refrigerator at a base temperature of 13 mK. The resonators were measured again in a second cooldown after two months of exposure to air. The transmission data were fitted using the diameter correction method (DCM)[301], incorporating a circle fit normalization routine to address asymmetric resonances.[302] This approach facilitated the extraction of internal quality factors as a function of input power. The subsequent fit of inverse quality factors versus the estimated number of photons[303] in each resonator to a TLS model provided the power-independent and TLS losses.[304] The entire measurement process, including data analysis, is available on GitHub: https://github.com/Boulder-Cryogenic-Quantum-Testbed/scresonators

CHAPTER 8:

FUTURE WORK

8.1 Overview

This chapter presents an overview of the future work centered around superconducting qubits. Proposed future efforts originate from results and protocols developed during the latter half of the Ph.D. The short-term aim is to finalize these open-ended projects.

8.2 Epitaxial Encapsulation of Nb by PLD

Niobium thin films, commonly used in superconducting qubits, are prone to rapid oxidation, forming amorphous Nb_2O_5 and other Nb_xO_y-complexes within seconds when exposed to air or low vacuum conditions.[305] The presence of these oxides at the metal-air interface adversely affects qubit coherence times. Various strategies have been proposed to address this issue to mitigate losses associated with amorphous oxides, with HF-based etching and UHV annealing proving effective in enhancing coherence in 2D and 3D quantum devices. [262, 275]

This study employs titanium nitride (TiN) superconducting films to cap Nb thin films. TiN is an ideal capping candidate due to its superconducting properties, stability against oxidation, and resilience against HF-based chemistries.[306] The capping process utilizes epitaxial Nb thin films on Al_2O_3 (110) substrates. Oxides are removed through annealing in a vacuum within the PLD system, and the TiN layer is deposited at the same temperature to prevent Nb oxide formation. This process exposes a NbO (111) surface,[307] facilitating the epitaxial growth of TiN (111). Additional materials like Pt (111) and Au (111) can be deposited on TiN to minimize post-oxidation risk. The resulting capped films effectively suppress the formation of Nb_2O_5/NbO_2 when exposed to air, and CPW resonators and superconducting qubits are fabricated to establish a connection between material properties and device performance.

8.3 Annealing of Nb Thin Films in UHV

Superconducting metallic thin films, including Nb, are crucial in 2D superconducting qubit fabrication, with film crystalline quality potentially affecting coherence. Conventional deposition methods result in textured Nb (110) thin films. While these textured Nb (110) thin films are suitable for superconducting transmons, they are limited in coherence times due to material defects. Crystal quality improvement via annealing is a possible pathway to increase coherence.

This study focuses on UHV annealed Nb thin films deposited by DC Sputtering at base pressures of ~10^{-10} Torr and temperatures up to 1000°C. Specular and off-specular X-ray scattering measurements suggest improvements in crystal quality, epitaxy, and roughness following UHV annealing. The impact of these Nb thin films on superconducting properties is investigated using cryogenic charge transport measurements at different crystallographic orientations and conditions.

8.4 Nb/Si Interfacial Studies

The Nb/Si interface undergoes intermixing and growth during different annealing procedures. Intermixing starts at only 300°C after one hour of annealing in a vacuum, [308] requiring low O2 pressure to circumvent Nb_xO_y formation, requiring low O_2 pressure to avoid oxidation. Annealing in a UHV chamber at 10^(-10) Torr is employed to diminish oxidation. However, this leads to Nb/Si interface interdiffusion processes.

In this study, different annealing time conditions modify the Nb/Si interface, and the effect on structure and superconducting properties in Nb is evaluated. XRR was used to elucidate such interface's thickness and electron density evolution. Annealing of Nb thin films on α-Al_2O_3 (006) is performed to exclude the Nb/Si intermixing effect. The study concludes with an evaluation of CPW resonators.

8.5 Epitaxial NbO_2 Thin Films Deposited by PLD

PLD is utilized to optimize the deposition of epitaxial NbO_2 films on various Al_2O_3 substrate orientations. Precise control over target composition and O2 background pressure allows for the growth of oxide films with specific properties.[309] NbO_2 is a stable oxide formed when Nb is exposed to air. Its crystalline form has a semiconductor n-type behavior with a small bandgap (0.5-1.2 eV). [310] These films will be used as model systems to understand the Nb/air interface mechanisms and propose strategies to passivate Nb, for instance, by selenizing a high crystalline NbO_2 film. Additionally, NbO_2 is the most investigated material for neuromorphic computing,[311] presenting a metal-to-insulator transition at 1070 K.[312]

In this study, high-quality NbO_2 thin films with different crystal orientations are obtained for various substrate orientations and deposition parameters. The highest quality epitaxial film was obtained for NbO_2 (222) deposited on Al_2O_3 (012) at 650°C and 1 mTorr of O_2. The study systematically optimizes the crystal growth of these films, showing higher quality than those reported in the literature, mostly grown on Al_2O_3 (006).[313, 314]

CHAPTER 9:

CONCLUSIONS

The dissertation is focused on the interfacial engineering of materials with applications in LIBs and superconducting qubits. The study encompasses various thin film systems, including epitaxial $LiMn_2O_4$ cathode cycled in different liquid electrolytes and an ionogel, epitaxial Pt thin films serving as current collector templates, and Nb hydrides generated through wet chemical etching. Valuable insights into engineering strategies examining the role of interfaces in diverse phenomena such as Mn^{2+} dissolution in different electrolytes, growth optimization of ultra-smooth Pt surfaces, and losses associated with Nb hydrides are described in detail.

In **Chapter 1**, the significance of interfaces in energy storage and quantum information devices is briefly discussed. **Chapter 2** provides an overview of the synthesis and characterization techniques used in the projects, focusing on X-ray diffraction and reflectivity. **Chapter 3** introduces Li-ion batteries, emphasizing components like $LiMn_2O_4$ cathode, ionic liquid electrolytes, and current collectors.

Chapter 4 presents the first research project, exploring epitaxial $LiMn_2O_4$ thin films cycled in a conventional electrolyte ($LiPF_6$+EC/DMC) and an ionic liquid electrolyte (LiTFSI+EMIM-TFSI). The ionic liquid proved effective in suppressing Mn dissolution, the root cause of capacity fade, leading to improved electrochemical and structural stability. X-ray techniques were instrumental in monitoring structural and interfacial changes during operation. Extensive *ex situ* characterization was employed to corroborate the suppression of Mn dissolution via ICP-MS and

STEM and to observe the formation of the irreversible $Li_2Mn_2O_4$ phase. Minimal amounts of overlithiated phase were found in the film cycled in ionic liquid. In contrast, severe Mn dissolution and overlithiated phase were found in the conventional electrolyte, proving the importance of electrolyte selection and compatibility with the cathode.

Additionally to studying the $LiMn_2O_4$/liquid interface, an ionogel composed of the same ionic liquid and h-BN nanoplatelets was employed to investigate the interfacial and structural evolution of the LMO cathode. Similar to the ionic liquid case, the Mn dissolution was prevented. However, an irreversible $Li_2Mn_2O_4$ phase was observed after cycling, a similar result when using a conventional electrolyte. This result suggested an inadequate physical contact between the gel and the surface of the $LiMn_2O_4$. The repercussion is the formation of voids where high Li^+ current densities are concentrated, facilitating the localized generation of $Li_2Mn_2O_4$.

Chapter 5 details another LIB project in which the Pt thin film growth was optimized for use as current collectors in LIB applications. A two-step temperature process (500/300°C) in an Ar+O_2 atmosphere emerged as the optimal condition, showcasing improved film crystallinity without 3D island growth. The optimized process yielded ultra-smooth films (<2 Å), exhibiting high conductivity (~7×10^6 S/m) and a high degree of epitaxy, serving as excellent templates for subsequent epitaxial growth. $LiMn_2O_4$ was epitaxially grown on the Pt thin film and cycled in an ionogel electrolyte.

Chapter 6 shifts focus to superconducting qubits, explaining quantum computing and coherence-limiting loss mechanisms. The different possible sources, including the substrates, tunnel junctions, metallic films, and surface treatments, are presented. **Chapter 7** presents the Nb hydride research project, investigating fluorine-based etching in superconducting qubits. This study identified that hydrogen incorporation happens after removing the native oxide surface and that the amount of hydrogen incorporated is proportional to the solution's acidity. Based on the Nb CPW resonator measurements, it was established that the PI loss tangents exhibit a clear correlation with the hydrogen loading, while TLS loss tangents do not. The aging of the resonators shows a stable PI loss tangent and an overall increase in the TLS due to additional oxide growth and contamination during storage.

Chapter 8 concludes the dissertation by highlighting ongoing projects in interfacial engineering for superconducting qubits. Interfaces like Nb/air and Nb/substrate are studied to understand and mitigate loss mechanisms.

The findings presented in this thesis contribute valuable knowledge to interfacial engineering, offering practical insights for understanding complex mechanisms in LIBs and superconducting qubits.

REFERENCES

(1) Eason, R. *Pulsed Laser Deposition of Thin Films: Applications-led Growth of Functional Materials*; John Wiley & Sons, 2007.
(2) De Bonis, A.; Teghil, R. Ultra-short Pulsed Laser Deposition of Oxides, Borides and Carbides of Transition Elements. *Coatings* **2020**, *10* (5), 501.
(3) Wang, F.; Zhao, H.; Liang, J.; Li, T.; Luo, Y.; Lu, S.; Shi, X.; Zheng, B.; Du, J.; Sun, X. Magnetron Sputtering Enabled Synthesis of Nanostructured Materials for Electrochemical Energy Storage. *Journal of Materials Chemistry A* **2020**, *8* (39), 20260-20285.
(4) Anders, A. Discharge Physics of High Power Impulse Magnetron Sputtering. *Surface and Coatings Technology* **2011**, *205*, S1-S9.
(5) Tan, W.; Li, B.; Lu, X.; Xiao, L.; Li, B.; Yang, D.; Yang, Y.; Ye, C.; Xie, D. Superiority of High Power Impulse Magnetron Sputtering in Niobium Films Deposition on Copper. *Materials Research Express* **2018**, *6* (2), 026418.
(6) Harrington, G. F.; Santiso, J. Back-to-Basics Tutorial: X-ray Diffraction of Thin Films. *Journal of Electroceramics* **2021**, *47* (4), 141-163.
(7) Als-Nielsen, J.; McMorrow, D. *Elements of Modern X-ray Physics*; John Wiley & Sons, 2011.
(8) Ohbuchi, A. Applications of the Two-dimensional Detector HyPix-3000 in X-ray Diffractometry. *Rigaku J* **2015**, *31* (4).
(9) Muniz, F. T. L.; Miranda, M. R.; Morilla dos Santos, C.; Sasaki, J. M. The Scherrer Equation and the Dynamical Theory of X-ray Diffraction. *Acta Crystallographica Section A: Foundations and Advances* **2016**, *72* (3), 385-390.
(10) Everitt, D. L.; Miller, W. J.; Abbott, N.; Zhu, X. Evolution of a Preferred Orientation of Polycrystalline Grains in Obliquely Deposited Gold Films on an Amorphous Substrate. *Physical Review B* **2000**, *62* (8), R4833.
(11) Yasaka, M. X-ray Thin-film Measurement Techniques. *The Rigaku Journal* **2010**, *26* (2), 1-9.
(12) Steinrück, H.-G. Surface Specific X-ray Scattering. X-ray Reflectivity: Theory, Application and Sample Preparation. 9th SSRL School on Synchrotron X-Ray Scattering Techniques in Materials and Environmental Sciences: Theory and Application: 2018.
(13) Birkholz, M. *Thin Film Analysis by X-ray Scattering*; John Wiley & Sons, 2006.
(14) Nelson, A. Co-refinement of Multiple-contrast Neutron/X-ray Reflectivity Data Using MOTOFIT. *Journal of Applied Crystallography* **2006**, *39* (2), 273-276.
(15) Schreiber, F.; Gerlach, A. X-ray and Neutron Reflectivity for the Investigation of Thin films. 2013.
(16) Chason, E.; Mayer, T. Thin Film and Surface Characterization by Specular X-ray Reflectivity. *Critical Reviews in Solid State and Material Sciences* **1997**, *22* (1), 1-67.
(17) Elgrishi, N.; Rountree, K. J.; McCarthy, B. D.; Rountree, E. S.; Eisenhart, T. T.; Dempsey, J. L. A Practical Beginner's Guide to Cyclic Voltammetry. *Journal of Chemical Education* **2018**, *95* (2), 197-206.
(18) Kissinger, P. T.; Heineman, W. R. Cyclic Voltammetry. *Journal of Chemical Education* **1983**, *60* (9), 702.
(19) Fister, T. T.; Esbenshade, J.; Chen, X.; Long, B. R.; Shi, B.; Schlepütz, C. M.; Gewirth, A. A.; Bedzyk, M. J.; Fenter, P. Lithium Intercalation Behavior in Multilayer Silicon Electrodes. *Advanced Energy Materials* **2014**, *4* (7), 1301494.
(20) Deitrick, K.; Krafft, G.; Terzić, B.; Delayen, J. High-brilliance, High-flux Compact Inverse Compton Light Source. *Physical Review Accelerators and Beams* **2018**, *21* (8), 080703.
(21) Henke, B. L.; Gullikson, E. M.; Davis, J. C. X-ray Interactions: Photoabsorption, Scattering, Transmission, and Reflection at E= 50-30,000 eV, Z= 1-92. *Atomic Data and Nuclear Data Tables* **1993**, *54* (2), 181-342.

(22) Measuring, N.; Ltd., I. 2018. https://www.novami.com/nova-technology/x-ray-photoelectron-spectroscopy-xps/ (accessed 2023 12/13/2023).
(23) Stevie, F. A.; Donley, C. L. Introduction to X-ray Photoelectron Spectroscopy. *Journal of Vacuum Science & Technology A* **2020**, *38* (6).
(24) Watts, J. F.; Wolstenholme, J. *An Introduction to Surface Analysis by XPS and AES*; John Wiley & Sons, 2019.
(25) Pantano, C.; Madey, T. E. Electron Beam Damage in Auger Electron Spectroscopy. *Applications of Surface Science* **1981**, *7* (1-2), 115-141.
(26) Ohring, M. *Materials Science of Thin Films: Depositon and Structure*; Elsevier, 2001.
(27) Jia, F.; Zhao, X.; Zhao, Y. Advancements in ToF-SIMS Imaging for Life Sciences. *Frontiers in Chemistry* **2023**, *11*.
(28) Vickerman, J. C. ToF-SIMS—An Overview. *ToF-SIMS: Surface Analysis by Mass Spectrometry* **2001**, 1-40.
(29) Priebe, A.; Michler, J. Review of Recent Advances in Gas-Assisted Focused Ion Beam Time-of-Flight Secondary Ion Mass Spectrometry (FIB-TOF-SIMS). *Materials* **2023**, *16* (5), 2090.
(30) Kim, S.-H.; Lee, Y.-H.; Jeong, M.-J.; Gwon, D.-Y.; Lee, J.-H.; Shin, Y.; Choi, H. LC-MS/MS Method Minimizing Matrix Effect for the Analysis of Bifenthrin and Butachlor in Chinese Chives and Its Application for Residual Study. *Foods* **2023**, *12* (8), 1683.
(31) Ammann, A. A. Inductively Coupled Plasma Mass Spectrometry (ICP MS): A Versatile Tool. *Journal of Mass Spectrometry* **2007**, *42* (4), 419-427.
(32) Alunda, B. O.; Lee, Y. J. Cantilever-based Sensors for High Speed Atomic Force Microscopy. *Sensors* **2020**, *20* (17), 4784.
(33) Cappella, B.; Dietler, G. Force-distance Curves by Atomic Force Microscopy. *Surface Science Reports* **1999**, *34* (1-3), 1-104.
(34) Eaton, P.; West, P. *Atomic Force Microscopy*; Oxford university press, 2010.
(35) Giessibl, F. J. Advances in Atomic Force Microscopy. *Reviews of Modern Physics* **2003**, *75* (3), 949.
(36) Tseng, A. A. Advancements and Challenges in Development of Atomic Force Microscopy for Nanofabrication. *Nano Today* **2011**, *6* (5), 493-509.
(37) Ichinose, H.; Sawada, H.; Takuma, E.; Osaki, M. Atomic Resolution HVEM and Environmental Noise. *Microscopy* **1999**, *48* (6), 887-891.
(38) Egerton, R. F. Choice of Operating Voltage for a Transmission Electron Microscope. *Ultramicroscopy* **2014**, *145*, 85-93.
(39) Li, G.; Zhang, H.; Han, Y. Applications of Transmission Electron Microscopy in Phase Engineering of Nanomaterials. *Chemical Reviews* **2023**, *123* (17), 10728-10749.
(40) Gauvin, R. Review of Transmission Electron Microscopy for the Characterization of Materials. In *Materials Characterization and Optical Probe Techniques: A Critical Review*, 1997; SPIE: Vol. 10291, pp 196-225.
(41) Zuo, J. M.; Spence, J. C. *Advanced Transmission Electron Microscopy*; Springer, 2017.
(42) Gloter, A.; Badjeck, V.; Bocher, L.; Brun, N.; March, K.; Marinova, M.; Tencé, M.; Walls, M.; Zobelli, A.; Stéphan, O. Atomically Resolved Mapping of EELS Fine Structures. *Materials Science in Semiconductor Processing* **2017**, *65*, 2-17.
(43) Sohlberg, K.; Pennycook, T. J.; Zhou, W.; Pennycook, S. J. Insights into the Physical Chemistry of Materials from Advances in HAADF-STEM. *Physical Chemistry Chemical Physics* **2015**, *17* (6), 3982-4006.
(44) Clément, L.; Pantel, R.; Kwakman, L.; Rouvière, J. Strain Measurements by Convergent-beam Electron Diffraction: The Importance of Stress Relaxation in Lamella Preparations. *Applied Physics Letters* **2004**, *85* (4), 651-653.
(45) Savitzky, B. H.; Zeltmann, S. E.; Hughes, L. A.; Brown, H. G.; Zhao, S.; Pelz, P. M.; Pekin, T. C.; Barnard, E. S.; Donohue, J.; DaCosta, L. R. py4DSTEM: A Software Package for Four-dimensional

Scanning Transmission Electron Microscopy Data Analysis. *Microscopy & Microanalysis* **2021**, *27* (4), 712-743.
(46) Li, M.; Lu, J.; Chen, Z.; Amine, K. 30 years of Lithium-ion Batteries. *Advanced Materials* **2018**, *30* (33), 1800561.
(47) Yu, X.; Manthiram, A. Electrode–electrolyte Interfaces in Lithium-based Batteries. *Energy & Environmental Science* **2018**, *11* (3), 527-543.
(48) Energy, U. S. D. o. *How Lithium-ion Batteries Work*. 2023. https://www.energy.gov/energysaver/articles/how-lithium-ion-batteries-work (accessed 2024 01/07/2024).
(49) Liu, W.; Oh, P.; Liu, X.; Lee, M. J.; Cho, W.; Chae, S.; Kim, Y.; Cho, J. Nickel-rich layered lithium transition-metal oxide for high-energy lithium-ion batteries. *Angewandte Chemie International Edition* **2015**, *54* (15), 4440-4457.
(50) Massé, R. C.; Liu, C.; Li, Y.; Mai, L.; Cao, G. Energy Storage Through Intercalation Reactions: Electrodes for Rechargeable Batteries. *National Science Review* **2016**, *4* (1), 26-53. DOI: 10.1093/nsr/nww093 (acccessed 1/8/2024).
(51) Daniel, C.; Mohanty, D.; Li, J.; Wood, D. L. Cathode Materials Review. In *AIP Conference Proceedings*, 2014; American Institute of Physics: Vol. 1597, pp 26-43.
(52) University, B. *BU-205: Types of Lithium-ion*. 2023. https://batteryuniversity.com/article/bu-205-types-of-lithium-ion (accessed 2024 01/08/2024).
(53) Zhang, S.; Deng, W.; Momen, R.; Yin, S.; Chen, J.; Massoudi, A.; Zou, G.; Hou, H.; Deng, W.; Ji, X. Element Substitution of a Spinel $LiMn_2O_4$ Cathode. *Journal of Materials Chemistry A* **2021**, *9* (38), 21532-21550.
(54) Li, X.; Xu, Y.; Wang, C. Suppression of Jahn–Teller Distortion of Spinel $LiMn_2O_4$ cathode. *Journal of Alloys and Compounds* **2009**, *479* (1-2), 310-313.
(55) Liu, T.; Dai, A.; Lu, J.; Yuan, Y.; Xiao, Y.; Yu, L.; Li, M.; Gim, J.; Ma, L.; Liu, J.; et al. Correlation Between Manganese Dissolution and Dynamic Phase Stability in Spinel-based Lithium-ion Battery. *Nature Communications* **2019**, *10* (1), 4721.
(56) Radzi, Z. I.; Arifin, K. H.; Kufian, M. Z.; Balakrishnan, V.; Raihan, S. R. S.; Abd Rahim, N.; Subramaniam, R. Review of Spinel $LiMn_2O_4$ Cathode Materials Under High Cut-off Voltage in Lithium-ion Batteries: Challenges and Strategies. *Journal of Electroanalytical Chemistry* **2022**, 116623.
(57) Xiao, L.; Zhao, Y.; Yang, Y.; Cao, Y.; Ai, X.; Yang, H. Enhanced Electrochemical Stability of Al-doped $LiMn_2O_4$ Synthesized by a Polymer-pyrolysis Method. *Electrochimica Acta* **2008**, *54* (2), 545-550.
(58) Zhu, J.; Liu, Q.; Xiang, M.; Guo, J.; Bai, H.; Liu, X.; Su, C.; Bai, W. Facile Synthesis of Truncated Octahedron $LiNi_{0.10}Mn_{1.90}O_4$ for High-performance Li-ion Batteries. *Ceramics International* **2020**, *46* (10), 14516-14522.
(59) Jeong, M.; Lee, M. J.; Cho, J.; Lee, S. Surface Mn Oxidation State Controlled spinel $LiMn_2O_4$ as a Cathode Material for High-energy Li-ion Batteries. *Advanced Energy Materials* **2015**, *5* (13), 1500440.
(60) Jiang, R.; Huang, Y.; Jia, D.; Wang, L.; Wang, L. High-capacity, High-cycling Cathode Material Synthesized by Low-temperature Solid-state Coordination Method for Lithium Rechargeable Batteries. *Journal of The Electrochemical Society* **2007**, *154* (7), A698.
(61) Guan, D.; Jeevarajan, J. A.; Wang, Y. Enhanced Cycleability of $LiMn_2O_4$ Cathodes by Atomic Layer Deposition of Nanosized-thin Al_2O_3 Coatings. *Nanoscale* **2011**, *3* (4), 1465-1469.
(62) Walz, K. A.; Johnson, C. S.; Genthe, J.; Stoiber, L. C.; Zeltner, W. A.; Anderson, M. A.; Thackeray, M. M. Elevated Temperature Cycling Stability and Electrochemical Impedance of $LiMn_2O_4$ Cathodes with Nanoporous ZrO_2 and TiO_2 coatings. *Journal of Power Sources* **2010**, *195* (15), 4943-4951.
(63) Zhao, J.; Wang, Y. Atomic Layer Deposition of Epitaxial ZrO_2 Coating on $LiMn_2O_4$ Nanoparticles for High-rate Lithium Ion Batteries at Elevated Temperature. *Nano Energy* **2013**, *2* (5), 882-889.
(64) Jaber-Ansari, L.; Puntambekar, K. P.; Kim, S.; Aykol, M.; Luo, L.; Wu, J.; Myers, B. D.; Iddir, H.; Russell, J. T.; Amine, K.; et al. Suppressing Manganese Dissolution from Lithium Manganese Oxide Spinel Cathodes with Single-Layer Graphene. *Advanced Energy Materials* **2015**, *5* (17), 1500646.

(65) Michalska, M.; Buchberger, D. A.; Jasiński, J. B.; Thapa, A. K.; Jain, A. Surface Modification of Nanocrystalline $LiMn_2O_4$ Using Graphene Oxide Flakes. *Materials* **2021**, *14* (15), 4134.
(66) Ray, A.; Saruhan, B. Application of Ionic Liquids for Batteries and Supercapacitors. *Materials* **2021**, *14* (11), 2942.
(67) Giordano, L.; Karayaylali, P.; Yu, Y.; Katayama, Y.; Maglia, F.; Lux, S.; Shao-Horn, Y. Chemical Reactivity Descriptor for the Oxide-electrolyte Interface in Li-ion Batteries. *The Journal of Physical Chemistry Letters* **2017**, *8* (16), 3881-3887.
(68) Balducci, A. Ionic Liquids in Lithium-ion Batteries. *Ionic Liquids II* **2018**, 1-27.
(69) Xu, K. Nonaqueous Liquid Electrolytes for Lithium-based Rechargeable Batteries. *Chemical Reviews* **2004**, *104* (10), 4303-4418.
(70) Choudhury, S. A Highly Reversible Room-Temperature lithium Metal Battery Based on Cross-linked Hairy Nanoparticles. *Rational Design of Nanostructured Polymer Electrolytes and Solid–liquid Interphases for Lithium Batteries* **2019**, 35-57.
(71) Hyun, W. J.; De Moraes, A. C. M.; Lim, J.-M.; Downing, J. R.; Park, K.-Y.; Tan, M. T. Z.; Hersam, M. C. High-modulus Hexagonal Boron Nitride Nanoplatelet Gel Electrolytes for Solid-state Rechargeable Lithium-ion Batteries. *ACS Nano* **2019**, *13* (8), 9664-9672.
(72) Guo, L.; Thornton, D. B.; Koronfel, M. A.; Stephens, I. E.; Ryan, M. P. Degradation in Lithium Ion Battery Current Collectors. *Journal of Physics: Energy* **2021**, *3* (3), 032015.
(73) Zhu, P.; Gastol, D.; Marshall, J.; Sommerville, R.; Goodship, V.; Kendrick, E. A Review of Current Collectors for Lithium-ion Batteries. *Journal of Power Sources* **2021**, *485*, 229321.
(74) Hendriks, R.; Cunha, D. M.; Singh, D. P.; Huijben, M. Enhanced Lithium Transport by Control of crystal Orientation in Spinel $LiMn_2O_4$ Thin Film Cathodes. *ACS Applied Energy Materials* **2018**, *1* (12), 7046-7051.
(75) Borkiewicz, O. J.; Wiaderek, K. M.; Chupas, P. J.; Chapman, K. W. Best Practices for Operando Battery Experiments: Influences of X-ray Experiment Design on Observed Electrochemical Reactivity. **2015**, *6* (11), 2081-2085.
(76) Xu, L.; Tang, S.; Cheng, Y.; Wang, K.; Liang, J.; Liu, C.; Cao, Y.-C.; Wei, F.; Mai, L. Interfaces in Solid-State Lithium Batteries. *Joule* **2018**, *2* (10), 1991-2015. DOI: https://doi.org/10.1016/j.joule.2018.07.009.
(77) Zhan, C.; Wu, T.; Lu, J.; Amine, K. Dissolution, Migration, and Deposition of Transition Metal Ions in Li-ion Batteries Exemplified by Mn-based Cathodes–A Critical Review. *Energy & Environmental Science* **2018**, *11* (2), 243-257.
(78) Zhao, L.; Chénard, E.; Çapraz, Ö. Ö.; Sottos, N. R.; White, S. R. Direct Detection of Manganese Ions in Organic Electrolyte by UV-vis Spectroscopy. *Journal of The Electrochemical Society* **2018**, *165* (2), A345-A348. DOI: 10.1149/2.1111802jes.
(79) Qiao, Y.; Zhou, Z.; Chen, Z.; Du, S.; Cheng, Q.; Zhai, H.; Fritz, N. J.; Du, Q.; Yang, Y. Visualizing Ion Diffusion in Battery Systems by Fluorescence Microscopy: A Case Study on the Dissolution of $LiMn_2O_4$. *Nano Energy* **2018**, *45*, 68-74. DOI: https://doi.org/10.1016/j.nanoen.2017.12.036.
(80) Kitta, M.; Kohyama, M. Stability of the $LiMn_2O_4$ Surface in a $LiPF_6$-based Non-aqueous Electrolyte Studied by In-situ Atomic Force Microscopy. *Japanese Journal of Applied Physics* **2016**, *55* (6), 065801. DOI: 10.7567/jjap.55.065801.
(81) Zhuo, Z.; Olalde-Velasco, P.; Chin, T.; Battaglia, V.; Harris, S. J.; Pan, F.; Yang, W. Effect of Excess Lithium in $LiMn_2O_4$ and $Li_{1.15}Mn_{1.85}O_4$ Electrodes Revealed by Quantitative Analysis of Soft X-ray Absorption Spectroscopy. *Applied Physics Letters* **2017**, *110* (9), 093902.
(82) Jena, A.; Tong, Z.; Bazri, B.; Iputera, K.; Chang, H.; Hu, S.-F.; Liu, R.-S. In Situ/Operando Methods of Characterizing All-Solid-State Li-Ion Batteries: Understanding Li-Ion Transport during Cycle. *The Journal of Physical Chemistry C* **2021**, *125* (31), 16921-16937.
(83) Bak, S.-M.; Shadike, Z.; Lin, R.; Yu, X.; Yang, X.-Q. In Situ/operando Synchrotron-based X-ray Techniques for Lithium-ion Battery Research. *NPG Asia Materials* **2018**, *10* (7), 563-580. DOI: 10.1038/s41427-018-0056-z.

(84) Masquelier, C.; Tabuchi, M.; Ado, K.; Kanno, R.; Kobayashi, Y.; Maki, Y.; Nakamura, O.; Goodenough, J. B. Chemical and Magnetic Characterization of Spinel Materials in the $LiMn_2O_4$–$Li_2Mn_4O_9$–$Li_4Mn_5O_{12}$ System. *Journal of Solid State Chemistry* **1996**, *123* (2), 255-266. DOI: https://doi.org/10.1006/jssc.1996.0176.
(85) Mishra, S. K.; Ceder, G. Structural Stability of Lithium Manganese Oxides. *Physical Review B* **1999**, *59* (9), 6120.
(86) Okumura, T.; Yamaguchi, Y.; Shikano, M.; Kobayashi, H. Further Findings of X-ray Absorption Near-edge Structure in Lithium Manganese Spinel Oxide Using First-Principles Calculations. *Journal of Materials Chemistry A* **2014**, *2* (21), 8017-8025, 10.1039/C3TA15412B. DOI: 10.1039/C3TA15412B.
(87) Ammundsen, B.; Paulsen, J. Novel lithium-ion Cathode Materials Based on Layered Manganese Oxides. *Advanced Materials* **2001**, *13* (12-13), 943-956.
(88) Amatucci, G.; Du Pasquier, A.; Blyr, A.; Zheng, T.; Tarascon, J. M. The Elevated Temperature Performance of the LiMn2O4/C System: Failure and Solutions. *Electrochimica Acta* **1999**, *45* (1), 255-271. DOI: https://doi.org/10.1016/S0013-4686(99)00209-1.
(89) Xia, Y.; Zhou, Y.; Yoshio, M. Capacity Fading on Cycling of 4 V Li/$LiMn_2O_4$ Cells. *Journal of The Electrochemical Society* **1997**, *144* (8), 2593-2600.
(90) Zhan, C.; Lu, J.; Kropf, A. J.; Wu, T.; Jansen, A. N.; Sun, Y.-K.; Qiu, X.; Amine, K. Mn (II) Deposition on Anodes and its Effects on Capacity Fade in Spinel Lithium Manganate–carbon Systems. *Nature Communications* **2013**, *4* (1), 1-8.
(91) Gauthier, M.; Carney, T. J.; Grimaud, A.; Giordano, L.; Pour, N.; Chang, H.-H.; Fenning, D. P.; Lux, S. F.; Paschos, O.; Bauer, C.; et al. Electrode–Electrolyte Interface in Li-Ion Batteries: Current Understanding and New Insights. *The Journal of Physical Chemistry Letters* **2015**, *6* (22), 4653-4672. DOI: 10.1021/acs.jpclett.5b01727.
(92) Tang, C.-Y.; Leung, K.; Haasch, R. T.; Dillon, S. J. $LiMn_2O_4$ Surface Chemistry Evolution During Cycling Revealed by In Situ Auger Electron Spectroscopy and X-ray Photoelectron Spectroscopy. *ACS Applied Materials & Interfaces* **2017**, *9* (39), 33968-33978.
(93) Banerjee, A.; Shilina, Y.; Ziv, B.; Ziegelbauer, J. M.; Luski, S.; Aurbach, D.; Halalay, I. C. On the Oxidation State of Manganese Ions in Li-ion Battery Electrolyte Solutions. *Journal of the American Chemical Society* **2017**, *139* (5), 1738-1741.
(94) Banerjee, A.; Ziv, B.; Shilina, Y.; Luski, S.; Aurbach, D.; Halalay, I. C. Acid-scavenging Separators: A Novel Route for Improving Li-ion Batteries' Durability. *ACS Energy Letters* **2017**, *2* (10), 2388-2393.
(95) Wotango, A. S.; Su, W.-N.; Leggesse, E. G.; Haregewoin, A. M.; Lin, M.-H.; Zegeye, T. A.; Cheng, J.-H.; Hwang, B.-J. Improved Interfacial Properties of MCMB Electrode by 1-(trimethylsilyl) imidazole as New Electrolyte Additive to Suppress $LiPF_6$ Decomposition. *ACS Applied Materials & Interfaces* **2017**, *9* (3), 2410-2420.
(96) Giffin, G. A. Ionic Liquid-based Electrolytes for "Beyond Lithium" Battery Technologies. *Journal of Materials Chemistry A* **2016**, *4* (35), 13378-13389, 10.1039/C6TA05260F. DOI: 10.1039/C6TA05260F.
(97) Choudhury, S.; Mangal, R.; Agrawal, A.; Archer, L. A. A Highly Reversible Room-temperature Lithium Metal Battery Based on Crosslinked Hairy Nanoparticles. *Nature Communications* **2015**, *6* (1), 10101. DOI: 10.1038/ncomms10101.
(98) Stone, G. M.; Mullin, S. A.; Teran, A. A.; Hallinan, D. T.; Minor, A. M.; Hexemer, A.; Balsara, N. P. Resolution of the Modulus Versus Adhesion Dilemma in Solid Polymer Electrolytes for Rechargeable Lithium Metal Batteries. *Journal of The Electrochemical Society* **2012**, *159* (3), A222-A227. DOI: 10.1149/2.030203jes.
(99) Warburton, R. E.; Castro, F. C.; Deshpande, S.; Madsen, K. E.; Bassett, K. L.; Dos Reis, R.; Gewirth, A. A.; Dravid, V. P.; Greeley, J. Oriented $LiMn_2O_4$ Particle Fracture from Delithiation-driven Surface Stress. *ACS Applied Materials & Interfaces* **2020**, *12* (43), 49182-49191.
(100) Koster, G.; Klein, L.; Siemons, W.; Rijnders, G.; Dodge, J. S.; Eom, C.-B.; Blank, D. H. A.; Beasley, M. R. Structure, Physical Properties, and Applications of $SrRuO_3$ Thin Films. *Reviews of Modern Physics* **2012**, *84* (1), 253-298. DOI: 10.1103/RevModPhys.84.253.

(101) Chen, X.; Vörös, M. r.; Garcia, J. C.; Fister, T. T.; Buchholz, D. B.; Franklin, J.; Du, Y.; Droubay, T. C.; Feng, Z.; Iddir, H. Strain-Driven Mn-Reorganization in Overlithiated $Li_xMn_2O_4$ Epitaxial Thin-Film Electrodes. *ACS Applied Energy Materials* **2018**, *1* (6), 2526-2535.
(102) Kim, D.; Park, S.; Chae, O. B.; Ryu, J. H.; Kim, Y.-U.; Yin, R.-Z.; Oh, S. M. Re-deposition of Manganese Species on Spinel $LiMn_2O_4$ Electrode After Mn Dissolution. *Journal of the Electrochemical Society* **2011**, *159* (3), A193.
(103) Wu, X.; Li, X.; Wang, Z.; Guo, H.; Yue, P.; Zhang, Y. Improvement on the Storage Performance of $LiMn_2O_4$ with the Mixed Additives of Ethanolamine and Heptamethyldisilazane. *Applied Surface Science* **2013**, *268*, 349-354.
(104) Sharova, V.; Moretti, A.; Diemant, T.; Varzi, A.; Behm, R. J.; Passerini, S. Comparative Study of Imide-based Li Salts as Electrolyte Additives for Li-ion Batteries. *Journal of Power Sources* **2018**, *375*, 43-52.
(105) Rath, P. C.; Wu, C.-J.; Patra, J.; Li, J.; Lee, T.-C.; Yeh, T.-J.; Chang, J. K. Hybrid Electrolyte Enables Safe and Practical 5 V $LiNi_{0.5}Mn_{1.5}O_4$ Batteries. *Journal of Materials Chemistry A* **2019**, *7* (27), 16516-16525.
(106) Dai, Y.; Cai, L.; White, R. E. Capacity Fade Model for Spinel $LiMn_2O_4$ Electrode. *Journal of The Electrochemical Society* **2012**, *160* (1), A182.
(107) Cho, C.-W.; Pham, T. P. T.; Jeon, Y.-C.; Yun, Y.-S. Influence of Anions on the Toxic Effects of Ionic Liquids to a Phytoplankton Selenastrum Capricornutum. *Green Chemistry* **2008**, *10* (1), 67-72.
(108) Zhou, G.; Sun, X.; Li, Q.-H.; Wang, X.; Zhang, J.-N.; Yang, W.; Yu, X.; Xiao, R.; Li, H. Mn Ion Dissolution Mechanism for Lithium-ion Battery with $LiMn_2O_4$ Cathode: In situ Ultraviolet–visible Spectroscopy and Ab Initio Molecular Dynamics Simulations. *The Journal of Physical Chemistry Letters* **2020**, *11* (8), 3051-3057.
(109) He, P.; Luo, J.-Y.; He, J.-X.; Xia, Y.-Y. Electrochemical Profile of Oxygen-Deficient $LiMn_2O_4$ in Aqueous Electrolyte. *Journal of The Electrochemical Society* **2009**, *156* (3), A209. DOI: 10.1149/1.3058591.
(110) Chigane, M.; Ishikawa, M. Manganese Oxide Thin Film Preparation by Potentiostatic Electrolyses and Electrochromism. *Journal of the Electrochemical Society* **2000**, *147* (6), 2246.
(111) Erichsen, T.; Pfeiffer, B.; Roddatis, V.; Volkert, C. A. Tracking the Diffusion-controlled Lithiation Reaction of LiMn2O4 by In Situ TEM. *ACS Applied Energy Materials* **2020**, *3* (6), 5405-5414.
(112) Torres-Castanedo, C. G.; Evmenenko, G.; Luu, N. S.; Das, P. M.; Hyun, W. J.; Park, K.-Y.; Dravid, V. P.; Hersam, M. C.; Bedzyk, M. J. Enhanced $LiMn_2O_4$ Thin-Film Electrode Stability in Ionic Liquid Electrolyte: A Pathway to Suppress Mn Dissolution. *ACS Applied Materials & Interfaces* **2023**, *15* (29), 35664-35673.
(113) Cho, Y.-G.; Jung, S.-H.; Joo, S. H.; Jeon, Y.; Kim, M.; Lee, K. M.; Kim, S.; Park, J. M.; Noh, H. K.; Kim, Y.-S. A Metal-ion-chelating Organogel Electrolyte for Le Chatelier Depression of Mn^{3+} Disproportionation of Lithium Manganese Oxide Spinel. *Journal of Materials Chemistry A* **2018**, *6* (45), 22483-22488.
(114) Du, M.; Liao, K.; Lu, Q.; Shao, Z. Recent Advances in the Interface Engineering of Solid-state Li-ion Batteries with Artificial Buffer Layers: Challenges, Materials, Construction, and Characterization. *Energy & Environmental Science* **2019**, *12* (6), 1780-1804.
(115) Lee, S.; Oshima, Y.; Hosono, E.; Zhou, H.; Kim, K.; Chang, H. M.; Kanno, R.; Takayanagi, K. In situ TEM Observation of Local Phase Transformation in a Rechargeable $LiMn_2O_4$ Nanowire Battery. *The Journal of Physical Chemistry C* **2013**, *117* (46), 24236-24241.
(116) Biswas, A.; Rossen, P. B.; Yang, C. H.; Siemons, W.; Jung, M. H.; Yang, I. K.; Ramesh, R.; Jeong, Y. H. Universal Ti-rich Termination of Atomically Flat $SrTiO_3$ (001), (110), and (111) Surfaces. *Applied Physics Letters* **2011**, *98* (5), 051904.
(117) Hong, W.; Lee, H. N.; Yoon, M.; Christen, H. M.; Lowndes, D. H.; Suo, Z.; Zhang, Z. Persistent Step-flow Growth of Strained Films on Vicinal Substrates. *Physical Review Letters* **2005**, *95* (9), 095501.

(118) Sánchez, F.; Lüders, U.; Herranz, G.; Infante, I.; Fontcuberta, J.; García-Cuenca, M.; Ferrater, C.; Varela, M. Self-organization in complex oxide thin films: from 2D to 0D nanostructures of $SrRuO_3$ and $CoCr_2O_4$. *Nanotechnology* **2005**, *16* (5), S190.
(119) Siera, J.; Cobden, P.; Tanaka, K.; Nieuwenhuys, B. The NO-H_2 Reaction Over Pt (100) Oscillatory Behaviour of Activity and Selectivity. *Catalysis Letters* **1991**, *10*, 335-342.
(120) Campbell, C.; Ertl, G.; Kuipers, H.; Segner, J. A Molecular Beam Study of the Catalytic Oxidation of CO on a Pt (111) Surface. *The Journal of Chemical Physics* **1980**, *73* (11), 5862-5873.
(121) Gambardella, P.; Rusponi, S.; Veronese, M.; Dhesi, S.; Grazioli, C.; Dallmeyer, A.; Cabria, I.; Zeller, R.; Dederichs, P.; Kern, K. Giant Magnetic Anisotropy of Single Cobalt Atoms and Nanoparticles. *Science* **2003**, *300* (5622), 1130-1133.
(122) Furuya, N.; Motoo, S. Arrangement of Ad-atoms of Various Kinds on Substrates: Part I. Platinum Substrate. *Journal of Electroanalytical Chemistry Interfacial Electrochemistry* **1979**, *98* (2), 189-194.
(123) Farrow, R.; Harp, G.; Marks, R.; Rabedeau, T.; Toney, M.; Weller, D.; Parkin, S. Epitaxial Growth of Pt on Basal-plane Sapphire: A Seed Film for Artificially Layered Magnetic Metal Structures. *Journal of Crystal Growth* **1993**, *133* (1-2), 47-58.
(124) Barbier, A.; Bezencenet, O.; Mocuta, C.; Moussy, J.-B.; Magnan, H.; Jedrecy, N.; Guittet, M.-J.; Gautier-Soyer, M. Dislocation Network Driven Structural Relaxation in Hematite Thin Films. *Materials Science Engineering: B* **2007**, *144* (1-3), 19-22.
(125) Bauer, S.; Rodrigues, A.; Horák, L.; Jin, X.; Schneider, R.; Baumbach, T.; Holý, V. Structure Quality of $LuFeO_3$ Epitaxial Layers Grown by Pulsed-Laser Deposition on Sapphire/Pt. *Materials* **2019**, *13* (1), 61.
(126) Chen, Y.; Li, Y.; Zheng, D.; Li, L.; Zeng, M.; Qin, M.; Hou, Z.; Fan, Z.; Gao, X.; Lu, X. Domain Structure and Multiferroic Properties of Epitaxial Hexagonal $ErMnO_3$ Films. *Journal of Alloys & Compounds* **2020**, *821*, 153529.
(127) Gómez, R.; Orts, J. M.; Álvarez-Ruiz, B.; Feliu, J. M. Effect of Temperature on Hydrogen Adsorption on Pt (111), Pt (110), and Pt (100) Electrodes in 0.1 M $HClO_4$. *The Journal of Physical Chemistry B* **2004**, *108* (1), 228-238.
(128) de Araujo, C. A.-P.; Cuchiaro, J.; McMillan, L.; Scott, M.; Scott, J. Fatigue-free Ferroelectric Capacitors with Platinum Electrodes. *Nature* **1995**, *374* (6523), 627-629.
(129) Kern, R.; Sastrawan, R.; Ferber, J.; Stangl, R.; Luther, J. Modeling and Interpretation of Electrical Impedance Spectra of Dye Solar Cells Operated Under Open-circuit Conditions. *Electrochimica Acta* **2002**, *47* (26), 4213-4225.
(130) Toupin, M.; Brousse, T.; Bélanger, D. Charge Storage Mechanism of MnO_2 Electrode Used in Aqueous Electrochemical Capacitor. *Chemistry of Materials* **2004**, *16* (16), 3184-3190.
(131) Dube, D.; Baborowski, J.; Muralt, P.; Setter, N. The Effect of Bottom Electrode on the Performance of Thin Film Based Capacitors in the Gigahertz Region. *Applied Physics Letters* **1999**, *74* (23), 3546-3548.
(132) Beck, G.; Fischer, H.; Mutoro, E.; Srot, V.; Petrikowski, K.; Tchernychova, E.; Wuttig, M.; Rühle, M.; Luerßen, B.; Janek, J. Epitaxial Pt (111) Thin Film Electrodes on YSZ(111) and YSZ(100)—Preparation and Characterization. *Solid State Ionics* **2007**, *178* (5-6), 327-337.
(133) Hilse, M.; Wang, K.; Engel-Herbert, R. Growth of Ultrathin Pt Layers and Selenization into $PtSe_2$ by Molecular Beam Epitaxy. *2D Materials* **2020**, *7* (4), 045013.
(134) Zhou, H.; Wochner, P.; Schöps, A.; Wagner, T. Investigation of Platinum Films Grown on Sapphire (0001) by Molecular Beam Epitaxy. *Journal of Crystal Growth* **2002**, *234* (2-3), 561-568.
(135) Braunschweig, B.; Mitin, A.; Daum, W. Pt (111) Thin-layer Electrodes on α-Al_2O_3 (0001): Morphology and Atomic Structure. *Surface Science* **2011**, *605* (11-12), 1082-1089.
(136) Hildner, M.; Minvielle, T.; Wilson, R. Epitaxial Growth of Ultrathin Pt Films on Basal-plane Sapphire: the Emergence of a Continuous Atomically Flat Film. *Surface Science* **1998**, *396* (1-3), 16-23.

(137) Schmidt, S.; Ok, Y.-W.; Klenov, D. O.; Lu, J.; Keane, S. P.; Stemmer, S. Microstructure of Epitaxial $SrTiO_3$/Pt/Ti/ Sapphire Heterostructures. *Journal of Materials Research* **2005**, *20* (9), 2261-2265. From Cambridge University Press Cambridge Core.
(138) Vargas, R.; Goto, T.; Zhang, W.; Hirai, T. Epitaxial Growth of Iridium and Platinum Films on Sapphire by Metalorganic Chemical Vapor Deposition. *Applied Physics Letters* **1994**, *65* (9), 1094-1096.
(139) Kwak, B.; First, P.; Erbil, A.; Wilkens, B.; Budai, J.; Chisholm, M.; Boatner, L. Study of Epitaxial Platinum Thin Films Grown by Metalorganic Chemical Vapor Deposition. *Journal of Applied Physics* **1992**, *72* (8), 3735-3740.
(140) Sacré, N.; Hufnagel, G.; Galipaud, J.; Bertin, E.; Hassan, S. A.; Duca, M.; Roué, L.; Ruediger, A.; Garbarino, S.; Guay, D. Pt Thin Films with Nanometer-Sized Terraces of (100) Orientation. *The Journal of Physical Chemistry C* **2017**, *121* (22), 12188-12198.
(141) Yıldırım, O.; Borzì, A.; Falub, C. V.; Rohrmann, H.; Jaeger, D.; Rechsteiner, M.; Schneider, D.; Neels, A.; Hug, H. J.; Marioni, M. Tuning the Microstructure of the Pt Layers Grown on Al_2O_3 (0001) by Different Sputtering Methods. *Scripta Materialia* **2021**, *194*, 113689.
(142) Okamoto, S.; Watanabe, T.; Akiyama, K.; Kaneko, S.; Funakubo, H.; Horita, S. Epitaxial Pt films with Different Orientations Grown on (100) Si Substrates by RF Magnetron Sputtering. *Japanese Journal of Applied Physics* **2005**, *44* (7R), 5102.
(143) Ryll, T.; Galinski, H.; Schlagenhauf, L.; Elser, P.; Rupp, J. L.; Bieberle-Hutter, A.; Gauckler, L. J. Microscopic and Nanoscopic Three-phase-boundaries of Platinum Thin-film Electrodes on YSZ Electrolyte. *Advanced Functional Materials* **2011**, *21* (3), 565-572.
(144) Leuchtner, R.; Chrisey, D.; Horwitz, J.; Grabowski, K. The Preparation of Epitaxial Platinum Films by Pulsed Laser Deposition. *Surface Coatings Technology* **1992**, *51* (1-3), 476-482.
(145) Morcrette, M.; Gutierrez-Llorente, A.; Seiler, W.; Perrière, J.; Laurent, A.; Barboux, P. Epitaxial Growth of Pt and Oxide Multilayers on MgO by Laser Ablation. *Journal of Applied Physics* **2000**, *88* (9), 5100-5106.
(146) Takai, Y.; Sato, M. Epitaxial Growth of Platinum Thin Films on (100) MgO by Pulsed Laser Deposition. *Superconductor Science Technology* **1999**, *12* (8), 486.
(147) Galinski, H.; Ryll, T.; Reibisch, P.; Schlagenhauf, L.; Schenker, I.; Gauckler, L. J. Temperature-Dependent 2-D to 3-D Growth Transition of Ultra-thin Pt Films Deposited by PLD. *Acta Materialia* **2013**, *61* (9), 3297-3303.
(148) Duclère, J.-R.; Mc Loughlin, C.; Fryar, J.; O'Haire, R.; Guilloux-Viry, M.; Meaney, A.; Perrin, A.; McGlynn, E.; Henry, M.; Mosnier, J.-P. ZnO Thin Films Grown on Platinum (111) Buffer Layers by Pulsed Laser Deposition. *Thin Solid Films* **2006**, *500* (1-2), 78-83.
(149) Barbieri, A.; Weiss, W.; Van Hove, M.; Somorjai, G. Magnetite Fe_3O_4 (111): Surface Structure by LEED Crystallography and Energetics. *Surface Science* **1994**, *302* (3), 259-279.
(150) Verguts, K.; Defossez, Y.; Leonhardt, A.; De Messemaeker, J.; Schouteden, K.; Van Haesendonck, C.; Huyghebaert, C.; De Gendt, S.; Brems, S. Growth of Millimeter-sized Graphene Single Crystals on Al_2O_3 (0001) / Pt (111) Template Wafers Using Chemical Vapor Deposition. *ECS Journal of Solid State Science Technology* **2018**, *7* (12), M195.
(151) Tachibana, T.; Yokota, Y.; Miyata, K.; Onishi, T.; Kobashi, K.; Tarutani, M.; Takai, Y.; Shimizu, R.; Shintani, Y. Diamond Films Heteroepitaxially Grown on Platinum (111). *Physical Review B* **1997**, *56* (24), 15967.
(152) Francis, A. J.; Salvador, P. A. Crystal Orientation and Surface Morphology of Face-centered-cubic Metal Thin Films Deposited Upon Single-crystal Ceramic Substrates Using Pulsed Laser Deposition. *Journal of Materials Research* **2007**, *22* (1), 89-102.
(153) Asthagiri, A.; Niederberger, C.; Francis, A. J.; Porter, L. M.; Salvador, P. A.; Sholl, D. S. Thin Pt Films on the Polar $SrTiO_3$ (111) Surface: an Experimental and Theoretical Study. *Surface Science* **2003**, *537* (1-3), 134-152.
(154) Trassin, M.; Viart, N.; Ulhaq-Bouillet, C.; Versini, G.; Barre, S.; Leuvrey, C.; Pourroy, G. Ultraflat Monocrystalline Pt (111) Electrodes. *Journal of Applied Physics* **2009**, *105*.

(155) Tanaka, H.; Taniguchi, M. Single Crystalline Epitaxial Platinum Film on Al_2O_3 (0001) Prepared by Oxygen-doped Sputtering Deposition. *Japanese Journal of Applied Physics* **2017**, *56* (5), 058001.
(156) Minvielle, T. J.; White, R. L.; Hildner, M. L.; Wilson, R. J. Temperature Dependence of the Epitaxial Growth of Pt on Basal-plane Sapphire. *Surface Science* **1996**, *366* (3), L755-L759.
(157) Yoshimoto, M.; Maeda, T.; Ohnishi, T.; Koinuma, H.; Ishiyama, O.; Shinohara, M.; Kubo, M.; Miura, R.; Miyamoto, A. Atomic-scale Formation of Ultrasmooth Surfaces on Sapphire Substrates for High-quality Thin-film Fabrication. *Applied Physics Letters* **1995**, *67* (18), 2615-2617.
(158) Nefedov, A.; Abromeit, A.; Morawe, C.; Stierle; Abromeit, A. High-resolution X-ray Scattering Study of Platinum Thin Films on Sapphire. *Journal of Physics: Condensed Matter* **1998**, *10* (4), 717.
(159) Fox, G.; Trolier-McKinstry, S.; Krupanidhi, S.; Casas, L. Pt/Ti/SiO_2/Si Substrates. *Journal of Materials Research* **1995**, *10* (6), 1508-1515.
(160) Mackus, A. J.; Verheijen, M. A.; Leick, N. m.; Bol, A. A.; Kessels, W. M. Influence of Oxygen Exposure on the Nucleation of Platinum Atomic Layer Deposition: Consequences for Film Growth, Nanopatterning, and Nanoparticle Synthesis. *Chemistry of Materials* **2013**, *25* (9), 1905-1911.
(161) Miller, A. M.; Lemon, M.; Choffel, M. A.; Rich, S. R.; Harvel, F.; Johnson, D. C. Extracting Information from X-ray Diffraction Patterns Containing Laue Oscillations. *Zeitschrift für Naturforschung B* **2022**, *77* (4-5), 313-322.
(162) Esch, S.; Hohage, M.; Michely, T.; Comsa, G. Origin of Oxygen Induced Layer-by-layer Growth in Homoepitaxy on Pt (111). *Physical Review Letters* **1994**, *72* (4), 518.
(163) Bauer, S.; Rodrigues, A.; Horák, L. s.; Nergis, B.; Jin, X.; Schneider, R.; Gröger, R.; Baumbach, T.; Holy, V. Time-Resolved Morphology and Kinetic Studies of Pulsed Laser Deposition-Grown Pt Layers on Sapphire at Different Growth Temperatures by in Situ Grazing Incidence Small-Angle X-ray Scattering. *Langmuir* **2021**, *37* (2), 734-749.
(164) Gammer, C.; Kacher, J.; Czarnik, C.; Warren, O.; Ciston, J.; Minor, A. M. Local and Transient Nanoscale Strain Mapping During in situ Deformation. *Applied Physics Letters* **2016**, *109* (8), 081906.
(165) Ozdol, V.; Gammer, C.; Jin, X.; Ercius, P.; Ophus, C.; Ciston, J.; Minor, A. Strain Mapping at Nanometer Resolution Using Advanced Nano-beam Electron Diffraction. *Applied Physics Letters* **2015**, *106* (25), 253107.
(166) Wölfing, B.; Theis-Bröhl, K.; Sutter, C.; Zabel, H. AFM and X-ray Studies on the Growth and Quality of Nb (110) on Al_2O_3 (11-20). *Journal of Physics: Condensed Matter* **1999**, *11* (13), 2669.
(167) Chaney, L. E.; Hyun, W. J.; Khalaj, M.; Hui, J.; Hersam, M. C. Fully Printed, High-Temperature Micro-Supercapacitor Arrays Enabled by a Hexagonal Boron Nitride Ionogel Electrolyte. *Advanced Materials* **2023**, 2305161.
(168) Hyun, W. J.; Thomas, C. M.; Chaney, L. E.; Mazarin de Moraes, A. C.; Hersam, M. C. Screen-printable Hexagonal Boron Nitride Ionogel Electrolytes for Mechanically Deformable Solid-state Lithium-ion Batteries. *Nano Letters* **2022**, *22* (13), 5372-5378.
(169) Hyun, W. J.; Thomas, C. M.; Luu, N. S.; Hersam, M. C. Layered Heterostructure Ionogel Electrolytes for High-performance Solid-state Lithium-ion Batteries. *Advanced Materials* **2021**, *33* (13), 2007864.
(170) Thomas, C. M.; Hyun, W. J.; Huang, H. C.; Zeng, D.; Hersam, M. C. Blade-coatable Hexagonal Boron Nitride Ionogel Electrolytes for Scalable Production of Lithium Metal Batteries. *ACS Energy Letters* **2022**, *7* (4), 1558-1565.
(171) Soeparno, H.; Perbangsa, A. S. Cloud Quantum Computing Concept and Development: A Systematic Literature Review. *Procedia Computer Science* **2021**, *179*, 944-954. DOI: https://doi.org/10.1016/j.procs.2021.01.084.
(172) Matthews, D. J. N. How to get started in quantum computing. **2021**, *591* (7848), 166-167.
(173) Monroe, C.; Raymer, M. G.; Taylor, J. J. S. The us national quantum initiative: From act to action. **2019**, *364* (6439), 440-442.
(174) Vopson, M. M. Estimation of the Information Contained in the Visible Matter of the Universe. *AIP Advances* **2021**, *11* (10).

(175) Yung, M.-H. Quantum Supremacy: Some Fundamental Concepts. *National Science Review* **2018**, *6* (1), 22-23. DOI: 10.1093/nsr/nwy072 %J National Science Review (acccessed 7/22/2021).
(176) Reiher, M.; Wiebe, N.; Svore, K. M.; Wecker, D.; Troyer, M. J. P. o. t. N. A. o. S. Elucidating reaction mechanisms on quantum computers. **2017**, *114* (29), 7555-7560.
(177) Patil, B.; Wang, Q.; Hessel, V.; Lang, J. J. C. t. Plasma N2-fixation: 1900–2014. **2015**, *256*, 49-66.
(178) Devoret, M. H.; Wallraff, A.; Martinis, J. M. J. a. p. c.-m. Superconducting qubits: A short review. **2004**.
(179) Müller, C.; Cole, J. H.; Lisenfeld, J. J. R. o. P. i. P. Towards understanding two-level-systems in amorphous solids: insights from quantum circuits. **2019**, *82* (12), 124501.
(180) Martinis, J. M.; Cooper, K. B.; McDermott, R.; Steffen, M.; Ansmann, M.; Osborn, K.; Cicak, K.; Oh, S.; Pappas, D. P.; Simmonds, R. W. J. P. r. l. Decoherence in Josephson qubits from dielectric loss. **2005**, *95* (21), 210503.
(181) Kane, B. E. J. n. A silicon-based nuclear spin quantum computer. **1998**, *393* (6681), 133-137.
(182) Loss, D.; DiVincenzo, D. P. J. P. R. A. Quantum computation with quantum dots. **1998**, *57* (1), 120.
(183) Häffner, H.; Roos, C. F.; Blatt, R. J. P. r. Quantum computing with trapped ions. **2008**, *469* (4), 155-203.
(184) Marcos, D.; Wubs, M.; Taylor, J.; Aguado, R.; Lukin, M. D.; Sørensen, A. S. J. P. r. l. Coupling nitrogen-vacancy centers in diamond to superconducting flux qubits. **2010**, *105* (21), 210501.
(185) Wasielewski, M. R.; Forbes, M. D. E.; Frank, N. L.; Kowalski, K.; Scholes, G. D.; Yuen-Zhou, J.; Baldo, M. A.; Freedman, D. E.; Goldsmith, R. H.; Goodson, T.; et al. Exploiting Chemistry and Molecular Systems for Quantum Information Science. *Nature Reviews Chemistry* **2020**, *4* (9), 490-504. DOI: 10.1038/s41570-020-0200-5.
(186) Wang, Y.; Li, J.; Zhang, S.; Su, K.; Zhou, Y.; Liao, K.; Du, S.; Yan, H.; Zhu, S.-L. J. N. P. Efficient quantum memory for single-photon polarization qubits. **2019**, *13* (5), 346-351.
(187) Zhong, H.-S.; Wang, H.; Deng, Y.-H.; Chen, M.-C.; Peng, L.-C.; Luo, Y.-H.; Qin, J.; Wu, D.; Ding, X.; Hu, Y.; et al. Quantum computational advantage using photons. **2020**, *370* (6523), 1460-1463. DOI: 10.1126/science.abe8770 %J Science.
(188) Krantz, P.; Kjaergaard, M.; Yan, F.; Orlando, T. P.; Gustavsson, S.; Oliver, W. D. J. A. P. R. A quantum engineer's guide to superconducting qubits. **2019**, *6* (2), 021318.
(189) Josephson, B. D. J. P. l. Possible new effects in superconductive tunnelling. **1962**, *1* (7), 251-253.
(190) Jaklevic, R.; Lambe, J.; Silver, A.; Mercereau, J. J. P. R. L. Quantum interference effects in Josephson tunneling. **1964**, *12* (7), 159.
(191) Nakamura, Y.; Pashkin, Y. A.; Tsai, J. J. n. Coherent control of macroscopic quantum states in a single-Cooper-pair box. **1999**, *398* (6730), 786-788.
(192) Berkley, A.; Xu, H.; Gubrud, M.; Ramos, R.; Anderson, J.; Lobb, C.; Wellstood, F. J. P. R. B. Decoherence in a Josephson-junction qubit. **2003**, *68* (6), 060502.
(193) Yu-Lin, W.; Hui, D.; Hai-Feng, Y.; Guang-Ming, X.; Ye, T.; Jie, L.; Ying-Fei, C.; Shi-Ping, Z.; Dong-Ning, Z. J. C. P. B. Fabrication of Al/AlOx/Al Josephson junctions and superconducting quantum circuits by shadow evaporation and a dynamic oxidation process. **2013**, *22* (6), 060309.
(194) Blais, A.; Huang, R.-S.; Wallraff, A.; Girvin, S. M.; Schoelkopf, R. J. J. P. R. A. Cavity quantum electrodynamics for superconducting electrical circuits: An architecture for quantum computation. **2004**, *69* (6), 062320.
(195) Gao, Y. Y.; Rol, M. A.; Touzard, S.; Wang, C. J. a. p. a. A practical guide for building superconducting quantum devices. **2021**.
(196) McRae, C. R. H.; Wang, H.; Gao, J.; Vissers, M. R.; Brecht, T.; Dunsworth, A.; Pappas, D. P.; Mutus, J. J. R. o. S. I. Materials loss measurements using superconducting microwave resonators. **2020**, *91* (9), 091101.

(197) Kjaergaard, M.; Schwartz, M. E.; Braumüller, J.; Krantz, P.; Wang, J. I.-J.; Gustavsson, S.; Oliver, W. D. Superconducting Qubits: Current State of Play. **2020**, *11* (1), 369-395. DOI: 10.1146/annurev-conmatphys-031119-050605.
(198) Lisenfeld, J.; Bilmes, A.; Matityahu, S.; Zanker, S.; Marthaler, M.; Schechter, M.; Schön, G.; Shnirman, A.; Weiss, G.; Ustinov, A. V. J. S. r. Decoherence spectroscopy with individual two-level tunneling defects. **2016**, *6* (1), 1-8.
(199) Quintana, C.; Megrant, A.; Chen, Z.; Dunsworth, A.; Chiaro, B.; Barends, R.; Campbell, B.; Chen, Y.; Hoi, I.-C.; Jeffrey, E. J. A. P. L. Characterization and reduction of microfabrication-induced decoherence in superconducting quantum circuits. **2014**, *105* (6), 062601.
(200) Bouchiat, V.; Vion, D.; Joyez, P.; Esteve, D.; Devoret, M. J. P. S. Quantum coherence with a single Cooper pair. **1998**, *1998* (T76), 165.
(201) Orlando, T.; Mooij, J.; Tian, L.; Van Der Wal, C. H.; Levitov, L.; Lloyd, S.; Mazo, J. J. P. R. B. Superconducting persistent-current qubit. **1999**, *60* (22), 15398.
(202) Martinis, J. M.; Devoret, M. H.; Clarke, J. J. P. r. l. Energy-level quantization in the zero-voltage state of a current-biased Josephson junction. **1985**, *55* (15), 1543.
(203) Kockum, A. F.; Nori, F. Quantum Bits with Josephson Junctions. In *Fundamentals and Frontiers of the Josephson Effect*, Springer, 2019; pp 703-741.
(204) Wallraff, A.; Schuster, D. I.; Blais, A.; Frunzio, L.; Huang, R.-S.; Majer, J.; Kumar, S.; Girvin, S. M.; Schoelkopf, R. J. J. N. Strong coupling of a single photon to a superconducting qubit using circuit quantum electrodynamics. **2004**, *431* (7005), 162-167.
(205) Houck, A. A.; Koch, J.; Devoret, M. H.; Girvin, S. M.; Schoelkopf, R. J. J. Q. I. P. Life after charge noise: recent results with transmon qubits. **2009**, *8* (2), 105-115.
(206) Koch, J.; Terri, M. Y.; Gambetta, J.; Houck, A. A.; Schuster, D. I.; Majer, J.; Blais, A.; Devoret, M. H.; Girvin, S. M.; Schoelkopf, R. J. J. P. R. A. Charge-insensitive qubit design derived from the Cooper pair box. **2007**, *76* (4), 042319.
(207) Rigetti, C.; Gambetta, J. M.; Poletto, S.; Plourde, B. L.; Chow, J. M.; Córcoles, A. D.; Smolin, J. A.; Merkel, S. T.; Rozen, J. R.; Keefe, G. A. J. P. R. B. Superconducting qubit in a waveguide cavity with a coherence time approaching 0.1 ms. **2012**, *86* (10), 100506.
(208) Paik, H.; Schuster, D.; Bishop, L. S.; Kirchmair, G.; Catelani, G.; Sears, A.; Johnson, B.; Reagor, M.; Frunzio, L.; Glazman, L. J. P. R. L. Observation of high coherence in Josephson junction qubits measured in a three-dimensional circuit QED architecture. **2011**, *107* (24), 240501.
(209) Premkumar, A.; Weiland, C.; Hwang, S.; Jäck, B.; Place, A. P.; Waluyo, I.; Hunt, A.; Bisogni, V.; Pelliciari, J.; Barbour, A. J. C. M. Microscopic relaxation channels in materials for superconducting Qubits. **2021**, *2* (1), 1-9.
(210) Calusine, G.; Melville, A.; Woods, W.; Das, R.; Stull, C.; Bolkhovsky, V.; Braje, D.; Hover, D.; Kim, D. K.; Miloshi, X. J. A. P. L. Analysis and mitigation of interface losses in trenched superconducting coplanar waveguide resonators. **2018**, *112* (6), 062601.
(211) Jurcevic, P.; Javadi-Abhari, A.; Bishop, L. S.; Lauer, I.; Bogorin, D. F.; Brink, M.; Capelluto, L.; Günlük, O.; Itoko, T.; Kanazawa, N. J. Q. S.; et al. Demonstration of quantum volume 64 on a superconducting quantum computing system. **2021**, *6* (2), 025020.
(212) Sheldon, S.; Magesan, E.; Chow, J. M.; Gambetta, J. M. J. P. R. A. Procedure for systematically tuning up cross-talk in the cross-resonance gate. **2016**, *93* (6), 060302.
(213) Murray, C. E. J. a. p. a. Material matters in superconducting qubits. **2021**.
(214) Mallet, F.; Ong, F. R.; Palacios-Laloy, A.; Nguyen, F.; Bertet, P.; Vion, D.; Esteve, D. J. N. P. Single-shot qubit readout in circuit quantum electrodynamics. **2009**, *5* (11), 791-795.
(215) Wallraff, A.; Schuster, D.; Blais, A.; Frunzio, L.; Majer, J.; Devoret, M.; Girvin, S.; Schoelkopf, R. J. P. r. l. Approaching unit visibility for control of a superconducting qubit with dispersive readout. **2005**, *95* (6), 060501.

(216) Place, A. P.; Rodgers, L. V.; Mundada, P.; Smitham, B. M.; Fitzpatrick, M.; Leng, Z.; Premkumar, A.; Bryon, J.; Vrajitoarea, A.; Sussman, S. J. N. c. New material platform for superconducting transmon qubits with coherence times exceeding 0.3 milliseconds. **2021**, *12* (1), 1-6.
(217) Wang, C.; Li, X.; Xu, H.; Li, Z.; Wang, J.; Yang, Z.; Mi, Z.; Liang, X.; Su, T.; Yang, C. J. a. p. a. Transmon qubit with relaxation time exceeding 0.5 milliseconds. **2021**.
(218) de Leon, N. P.; Itoh, K. M.; Kim, D.; Mehta, K. K.; Northup, T. E.; Paik, H.; Palmer, B. S.; Samarth, N.; Sangtawesin, S.; Steuerman, D. W. Materials Challenges and Opportunities for Quantum Computing Hardware. *Science* **2021**, *372* (6539), eabb2823. DOI: 10.1126/science.abb2823 (acccessed 2023/05/01).
(219) Dial, O.; McClure, D. T.; Poletto, S.; Keefe, G.; Rothwell, M. B.; Gambetta, J. M.; Abraham, D. W.; Chow, J. M.; Steffen, M. J. S. S.; Technology. Bulk and surface loss in superconducting transmon qubits. **2016**, *29* (4), 044001.
(220) Gao, J.; Daal, M.; Vayonakis, A.; Kumar, S.; Zmuidzinas, J.; Sadoulet, B.; Mazin, B. A.; Day, P. K.; Leduc, H. G. J. A. P. L. Experimental evidence for a surface distribution of two-level systems in superconducting lithographed microwave resonators. **2008**, *92* (15), 152505.
(221) Wang, C.; Axline, C.; Gao, Y. Y.; Brecht, T.; Chu, Y.; Frunzio, L.; Devoret, M.; Schoelkopf, R. J. J. A. P. L. Surface participation and dielectric loss in superconducting qubits. **2015**, *107* (16), 162601.
(222) Pappas, D. P.; Vissers, M. R.; Wisbey, D. S.; Kline, J. S.; Gao, J. J. I. T. o. A. S. Two level system loss in superconducting microwave resonators. **2011**, *21* (3), 871-874.
(223) O'Connell, A. D.; Ansmann, M.; Bialczak, R. C.; Hofheinz, M.; Katz, N.; Lucero, E.; McKenney, C.; Neeley, M.; Wang, H.; Weig, E. M. Microwave Dielectric Loss at Single Photon Energies and Millikelvin Temperatures. *Applied Physics Letters* **2008**, *92* (11).
(224) Lahtinen, V.; Möttönen, M. Effects of Device Geometry and Material Properties on Dielectric Losses in Superconducting Coplanar-waveguide Resonators. *Journal of Physics: Condensed Matter* **2020**, *32* (40), 405702.
(225) Wenner, J.; Barends, R.; Bialczak, R.; Chen, Y.; Kelly, J.; Lucero, E.; Mariantoni, M.; Megrant, A.; O'Malley, P.; Sank, D. J. A. P. L. Surface loss simulations of superconducting coplanar waveguide resonators. **2011**, *99* (11), 113513.
(226) Murray, C. E.; Gambetta, J. M.; McClure, D. T.; Steffen, M. J. I. T. o. M. T.; Techniques. Analytical determination of participation in superconducting coplanar architectures. **2018**, *66* (8), 3724-3733.
(227) Pop, I. M.; Geerlings, K.; Catelani, G.; Schoelkopf, R. J.; Glazman, L. I.; Devoret, M. H. Coherent Suppression of Electromagnetic Dissipation due to Superconducting Quasiparticles. *Nature* **2014**, *508* (7496), 369-372.
(228) Vepsäläinen, A. P.; Karamlou, A. H.; Orrell, J. L.; Dogra, A. S.; Loer, B.; Vasconcelos, F.; Kim, D. K.; Melville, A. J.; Niedzielski, B. M.; Yoder, J. L. Impact of Ionizing Radiation on Superconducting Qubit Coherence. *Nature* **2020**, *584* (7822), 551-556.
(229) Cardani, L.; Valenti, F.; Casali, N.; Catelani, G.; Charpentier, T.; Clemenza, M.; Colantoni, I.; Cruciani, A.; D'Imperio, G.; Gironi, L. Reducing the Impact of Radioactivity on Quantum circuits in a Deep-Underground Facility. *Nature Communications* **2021**, *12* (1), 2733.
(230) De Visser, P.; Goldie, D.; Diener, P.; Withington, S.; Baselmans, J.; Klapwijk, T. Evidence of a Nonequilibrium Distribution of Quasiparticles in the Microwave Response of a Superconducting Aluminum Resonator. *Physical Review Letters* **2014**, *112* (4), 047004.
(231) McRae, C. R. H.; Wang, H.; Gao, J.; Vissers, M. R.; Brecht, T.; Dunsworth, A.; Pappas, D. P.; Mutus, J. Materials Loss Measurements Using Superconducting Microwave Resonators. *Review of Scientific Instruments* **2020**, *91* (9), 091101. DOI: 10.1063/5.0017378 (acccessed 5/12/2023).
(232) de Leon, N. P.; Itoh, K. M.; Kim, D.; Mehta, K. K.; Northup, T. E.; Paik, H.; Palmer, B.; Samarth, N.; Sangtawesin, S.; Steuerman, D. J. S. Materials challenges and opportunities for quantum computing hardware. **2021**, *372* (6539).

(233) Harris, D. C. A Century of Sapphire Crystal Growth: Origin of the EFG Method. In *Optical Materials and Structures Technologies IV*, 2009; International Society for Optics and Photonics: Vol. 7425, p 74250P.
(234) Zulehner, W. J. M. S.; B, E. Historical overview of silicon crystal pulling development. **2000**, *73* (1-3), 7-15.
(235) Chen, W.; Bennett, D. A.; Patel, V.; Lukens, J. E. J. S. S.; Technology. Substrate and process dependent losses in superconducting thin film resonators. **2008**, *21* (7), 075013.
(236) Kostylev, N.; Goryachev, M.; Bulanov, A. D.; Gavva, V. A.; Tobar, M. E. J. S. r. Determination of low loss in isotopically pure single crystal 28 Si at low temperatures and single microwave photon energy. **2017**, *7* (1), 1-8.
(237) Golding, B.; Schickfus, M. v.; Hunklinger, S.; Dransfeld, K. J. P. R. L. Intrinsic electric dipole moment of tunneling systems in silica glasses. **1979**, *43* (24), 1817.
(238) Holder, A. M.; Osborn, K. D.; Lobb, C.; Musgrave, C. B. J. P. r. l. Bulk and surface tunneling hydrogen defects in alumina. **2013**, *111* (6), 065901.
(239) Pohl, R. O.; Liu, X.; Thompson, E. J. R. o. M. P. Low-temperature thermal conductivity and acoustic attenuation in amorphous solids. **2002**, *74* (4), 991.
(240) Paik, H.; Osborn, K. D. J. A. P. L. Reducing quantum-regime dielectric loss of silicon nitride for superconducting quantum circuits. **2010**, *96* (7), 072505.
(241) Weides, M. P.; Kline, J. S.; Vissers, M. R.; Sandberg, M. O.; Wisbey, D. S.; Johnson, B. R.; Ohki, T. A.; Pappas, D. P. J. A. P. L. Coherence in a transmon qubit with epitaxial tunnel junctions. **2011**, *99* (26), 262502.
(242) Stoutimore, M.; Khalil, M.; Lobb, C.; Osborn, K. J. A. P. L. A Josephson junction defect spectrometer for measuring two-level systems. **2012**, *101* (6), 062602.
(243) Nakamura, Y.; Terai, H.; Inomata, K.; Yamamoto, T.; Qiu, W.; Wang, Z. J. A. P. L. Superconducting qubits consisting of epitaxially grown NbN/AlN/NbN Josephson junctions. **2011**, *99* (21), 212502.
(244) Kim, S.; Terai, H.; Yamashita, T.; Qiu, W.; Fuse, T.; Yoshihara, F.; Ashhab, S.; Inomata, K.; Semba, K. J. a. p. a. Enhanced-coherence all-nitride superconducting qubit epitaxially grown on Si Substrate. **2021**.
(245) Murray, C. E. Material Matters in Superconducting Qubits. *Materials Science and Engineering: R: Reports* **2021**, *146*, 100646. DOI: https://doi.org/10.1016/j.mser.2021.100646.
(246) McRae, C.; McFadden, A.; Zhao, R.; Wang, H.; Long, J.; Zhao, T.; Park, S.; Bal, M.; Palmstrøm, C.; Pappas, D. J. J. o. A. P. Cryogenic microwave loss in epitaxial Al/GaAs/Al trilayers for superconducting circuits. **2021**, *129* (2), 025109.
(247) Chu, Y.; Kharel, P.; Renninger, W. H.; Burkhart, L. D.; Frunzio, L.; Rakich, P. T.; Schoelkopf, R. J. J. S. Quantum acoustics with superconducting qubits. **2017**, *358* (6360), 199-202.
(248) Kamal, A.; Yoder, J. L.; Yan, F.; Gudmundsen, T. J.; Hover, D.; Sears, A. P.; Welander, P.; Orlando, T. P.; Gustavsson, S.; Oliver, W. D. J. a. p. a. Improved superconducting qubit coherence with high-temperature substrate annealing. **2016**.
(249) Megrant, A.; Neill, C.; Barends, R.; Chiaro, B.; Chen, Y.; Feigl, L.; Kelly, J.; Lucero, E.; Mariantoni, M.; O'Malley, P. J. J. A. P. L. Planar superconducting resonators with internal quality factors above one million. **2012**, *100* (11), 113510.
(250) Sage, J. M.; Bolkhovsky, V.; Oliver, W. D.; Turek, B.; Welander, P. B. J. J. o. A. P. Study of loss in superconducting coplanar waveguide resonators. **2011**, *109* (6), 063915.
(251) Vissers, M. R.; Gao, J.; Wisbey, D. S.; Hite, D. A.; Tsuei, C. C.; Corcoles, A. D.; Steffen, M.; Pappas, D. P. J. A. P. L. Low loss superconducting titanium nitride coplanar waveguide resonators. **2010**, *97* (23), 232509.
(252) Ohya, S.; Chiaro, B.; Megrant, A.; Neill, C.; Barends, R.; Chen, Y.; Kelly, J.; Low, D.; Mutus, J.; O'Malley, P. J. S. S.; et al. Room temperature deposition of sputtered TiN films for superconducting coplanar waveguide resonators. **2013**, *27* (1), 015009.

(253) Dumur, E.; Delsol, B.; Weißl, T.; Kung, B.; Guichard, W.; Hoarau, C.; Naud, C.; Hasselbach, K.; Buisson, O.; Ratter, K. J. I. T. o. A. S. Epitaxial rhenium microwave resonators. **2016**, *26* (3), 1-4.
(254) Richardson, C. J.; Siwak, N. P.; Hackley, J.; Keane, Z. K.; Robinson, J. E.; Arey, B.; Arslan, I.; Palmer, B. S. J. S. S.; Technology. Fabrication artifacts and parallel loss channels in metamorphic epitaxial aluminum superconducting resonators. **2016**, *29* (6), 064003.
(255) Goetz, J.; Deppe, F.; Haeberlein, M.; Wulschner, F.; Zollitsch, C. W.; Meier, S.; Fischer, M.; Eder, P.; Xie, E.; Fedorov, K. G. J. J. o. A. P. Loss mechanisms in superconducting thin film microwave resonators. **2016**, *119* (1), 015304.
(256) Earnest, C. T.; Béjanin, J. H.; McConkey, T. G.; Peters, E. A.; Korinek, A.; Yuan, H.; Mariantoni, M. J. S. S.; Technology. Substrate surface engineering for high-quality silicon/aluminum superconducting resonators. **2018**, *31* (12), 125013.
(257) Bruno, A.; De Lange, G.; Asaad, S.; Van Der Enden, K.; Langford, N.; DiCarlo, L. J. A. P. L. Reducing intrinsic loss in superconducting resonators by surface treatment and deep etching of silicon substrates. **2015**, *106* (18), 182601.
(258) Nersisyan, A.; Poletto, S.; Alidoust, N.; Manenti, R.; Renzas, R.; Bui, C.-V.; Vu, K.; Whyland, T.; Mohan, Y.; Sete, E. A. Manufacturing low dissipation superconducting quantum processors. In *2019 IEEE International Electron Devices Meeting (IEDM)*, 2019; IEEE: pp 31.31. 31-31.31. 34.
(259) Verjauw, J.; Potočnik, A.; Mongillo, M.; Acharya, R.; Mohiyaddin, F.; Simion, G.; Pacco, A.; Ivanov, T.; Wan, D.; Vanleenhove, A. J. P. R. A. Investigation of Microwave Loss Induced by Oxide Regrowth in High-Q Niobium Resonators. **2021**, *16* (1), 014018.
(260) Altoé, M.; Banerjee, A.; Berk, C.; Hajr, A.; Schwartzberg, A.; Song, C.; Ghadeer, M. A.; Aloni, S.; Elowson, M. J.; Kreikebaum, J. M. J. a. p. a. Localization and reduction of superconducting quantum coherent circuit losses. **2020**.
(261) Zhong, Q.; Cao, W.; Li, J.; Zhong, Y.; Wang, X. Study of dry etching process using SF 6 and CF 4/O 2 for Nb/Nb x Si 1− x/Nb Josephson-junction fabrication. In *2012 Conference on Precision electromagnetic Measurements*, 2012; IEEE: pp 46-47.
(262) Altoé, M. V. P.; Banerjee, A.; Berk, C.; Hajr, A.; Schwartzberg, A.; Song, C.; Alghadeer, M.; Aloni, S.; Elowson, M. J.; Kreikebaum, J. M.; et al. Localization and Mitigation of Loss in Niobium Superconducting Circuits. *PRX Quantum* **2022**, *3* (2), 020312. DOI: 10.1103/PRXQuantum.3.020312.
(263) Dunsworth, A.; Megrant, A.; Quintana, C.; Chen, Z.; Barends, R.; Burkett, B.; Foxen, B.; Chen, Y.; Chiaro, B.; Fowler, A. J. A. P. L. Characterization and reduction of capacitive loss induced by sub-micron Josephson junction fabrication in superconducting qubits. **2017**, *111* (2), 022601.
(264) Romanenko, A.; Pilipenko, R.; Zorzetti, S.; Frolov, D.; Awida, M.; Belomestnykh, S.; Posen, S.; Grassellino, A. J. P. R. A. Three-Dimensional Superconducting Resonators at T< 20 mK with Photon Lifetimes up to τ= 2 s. **2020**, *13* (3), 034032.
(265) Barkov, F.; Romanenko, A.; Grassellino, A. J. P. R. S. T.-A.; Beams. Direct observation of hydrides formation in cavity-grade niobium. **2012**, *15* (12), 122001.
(266) Barkov, F.; Romanenko, A.; Trenikhina, Y.; Grassellino, A. J. J. o. A. P. Precipitation of hydrides in high purity niobium after different treatments. **2013**, *114* (16), 164904.
(267) Kjaergaard, M.; Schwartz, M. E.; Braumüller, J.; Krantz, P.; Wang, J. I. J.; Gustavsson, S.; Oliver, W. D. Superconducting Qubits: Current State of Play. *Annual Review of Condensed Matter Physics* **2020**, *11* (1), 369-395. (acccessed 2023/04/27).
(268) DiVincenzo, D. P. The Physical Implementation of Quantum Computation. *Fortschritte der Physik: Progress of Physics* **2000**, *48* (9-11), 771-783.
(269) Devoret, M. H.; Schoelkopf, R. J. Superconducting Circuits for Quantum Information: An Outlook. *Science* **2013**, *339* (6124), 1169. DOI: 10.1126/science.1231930.
(270) Burnett, J. J.; Bengtsson, A.; Scigliuzzo, M.; Niepce, D.; Kudra, M.; Delsing, P.; Bylander, J. Decoherence Benchmarking of Superconducting Qubits. *npj Quantum Information* **2019**, *5* (1), 54.
(271) Verjauw, J.; Acharya, R.; Van Damme, J.; Ivanov, T.; Lozano, D. P.; Mohiyaddin, F. A.; Wan, D.; Jussot, J.; Vadiraj, A. M.; Mongillo, M.; et al. Path Toward Manufacturable Superconducting Qubits with

Relaxation Times Exceeding 0.1 ms. *npj Quantum Information* **2022**, *8* (1), 93. DOI: 10.1038/s41534-022-00600-9.
(272) Nersisyan, A.; Poletto, S.; Alidoust, N.; Manenti, R.; Renzas, R.; Bui, C.-V.; Vu, K.; Whyland, T.; Mohan, Y.; Sete, E. A.; et al. Manufacturing Low Dissipation Superconducting Quantum Processors. 2019; p arXiv:1901.08042.
(273) Tolpygo, S. K.; Bolkhovsky, V.; Weir, T. J.; Johnson, L. M.; Gouker, M. A.; Oliver, W. D. Fabrication Process and Properties of Fully-Planarized Deep-Submicron Nb/AlOx/Nb Josephson Junctions for VLSI Circuits. *IEEE Transactions on Applied Superconductivity* **2015**, *25* (3), 1-12.
(274) Verjauw, J.; Potočnik, A.; Mongillo, M.; Acharya, R.; Mohiyaddin, F.; Simion, G.; Pacco, A.; Ivanov, T.; Wan, D.; Vanleenhove, A.; et al. Investigation of Microwave Loss Induced by Oxide Regrowth in High-Q Niobium Resonators. *Physical Review Applied* **2021**, *16* (1), 014018. DOI: 10.1103/PhysRevApplied.16.014018.
(275) Romanenko, A.; Pilipenko, R.; Zorzetti, S.; Frolov, D.; Awida, M.; Belomestnykh, S.; Posen, S.; Grassellino, A. Three-Dimensional Superconducting Resonators at T< 20 mK with Photon Lifetimes up to τ= 2 s. *Physical Review Applied* **2020**, *13* (3), 034032.
(276) Kowsari, D.; Zheng, K.; Monroe, J.; Thobaben, N.; Du, X.; Harrington, P.; Henriksen, E.; Wisbey, D.; Murch, K. Fabrication and Surface Treatment of Electron-beam Evaporated Niobium for Low-loss Coplanar Waveguide Resonators. *Applied Physics Letters* **2021**, *119* (13), 132601.
(277) Gao, R.; Yu, W.; Deng, H.; Ku, H.-S.; Li, Z.; Wang, M.; Miao, X.; Lin, Y.; Deng, C. Epitaxial Titanium Nitride Microwave Resonators: Structural, Chemical, Electrical, and Microwave Properties. *Physical Review Materials* **2022**, *6* (3), 036202.
(278) Zeng, L.; Krantz, P.; Nik, S.; Delsing, P.; Olsson, E. The Atomic Details of the Interfacial Interaction Between the Bottom Electrode of Al/AlOx/Al Josephson Junctions and HF-Treated Si Substrates. *Journal of Applied Physics* **2015**, *117* (16), 163915.
(279) Ricker, R. E.; Myneni, G. R. Evaluation of the Propensity of Niobium to Absorb Hydrogen During Fabrication of Superconducting Radio Frequency Cavities for Particle Accelerators. *Journal of Research of the National Institute of Standards Technology* **2010**, *115* (5), 353.
(280) Barkov, F.; Romanenko, A.; Grassellino, A. Direct Observation of Hydrides Formation in Cavity-grade Niobium. *Physical Review Special Topics-Accelerators Beams* **2012**, *15* (12), 122001.
(281) Barkov, F.; Romanenko, A.; Trenikhina, Y.; Grassellino, A. Precipitation of Hydrides in High Purity Niobium After Different Treatments. *Journal of Applied Physics* **2013**, *114* (16), 164904.
(282) Romanenko, A.; Barkov, F.; Cooley, L.; Grassellino, A. Proximity Breakdown of Hydrides in Superconducting Niobium Cavities. *Superconductor Science Technology* **2013**, *26* (3), 035003.
(283) Lee, J.; Sung, Z.; Murthy, A. A.; Reagor, M.; Grassellino, A.; Romanenko, A. Discovery of Nb Hydride Precipitates in Superconducting Qubits. 2021; p arXiv:2108.10385.
(284) Asakawa, T.; Nagano, D.; Denda, S.; Miyairi, K. Influence of Primary Ion Beam Irradiation Conditions on the Depth Profile of Hydrogen in Tantalum Film. *J Applied Surface Science* **2008**, *255* (4), 1387-1390.
(285) Laudahn, U.; Pundt, A.; Bicker, M.; Hülsen, U. v.; Geyer, U.; Wagner, T.; Kirchheim, R. Hydrogen-induced Stress in Nb Single Layers. *Journal of Alloys and Compounds* **1999**, *293*, 490-494.
(286) Burlaka, V.; Wagner, S.; Hamm, M.; Pundt, A. Suppression of Phase Transformation in Nb–H Thin Films Below Switchover Thickness. *Nano Letters* **2016**, *16* (10), 6207-6212.
(287) Albrecht, W. M.; Goode, W. D.; Mallett, M. W. Reactions in the Niobium-Hydrogen System. *Journal of The Electrochemical Society* **1959**, *106* (11), 981.
(288) Welling, M.; Aegerter, C.; Westerwaal, R.; Enache, S.; Wijngaarden, R.; Griessen, R. Effect of Hydrogen Uptake and Substrate Orientation on the Flux Penetration in NbHx Thin Films. *Physica C: Superconductivity* **2004**, *406* (1-2), 100-106.
(289) Isagawa, S. Hydrogen Absorption and Its Effect on Low-temperature Electric Properties of Niobium. *Journal of Applied Physics* **1980**, *51* (8), 4460-4470.

(290) Welter, J.-M.; Johnen, F. Superconducting Transition Temperature and Low Temperature Resistivity in the Niobium-Hydrogen System. *Zeitschrift für Physik B Condensed Matter* **1977**, *27* (3), 227-232.
(291) Kim, Y.-J.; Tao, R.; Klie, R. F.; Seidman, D. N. J. A. n. Direct Atomic-scale Imaging of Hydrogen and Oxygen Interstitials in Pure Niobium Using Atom-probe Tomography and Aberration-Corrected Scanning Transmission Electron Microscopy. *ACS Nano* **2013**, *7* (1), 732-739.
(292) Tao, R.; Romanenko, A.; Cooley, L.; Klie, R. Low Temperature Study of Structural Phase Transitions in Niobium Hydrides. *Journal of Applied Physics* **2013**, *114* (4), 044306.
(293) Baldi, A.; Narayan, T. C.; Koh, A. L.; Dionne, J. A. In situ Detection of Hydrogen-induced Phase Transitions in Individual Palladium Nanocrystals. *Nature Materials* **2014**, *13* (12), 1143-1148.
(294) de Graaf, S.; Momand, J.; Mitterbauer, C.; Lazar, S.; Kooi, B. Resolving Hydrogen Atoms at Metal-metal Hydride Interfaces. *Science Advances* **2020**, *6* (5), eaay4312.
(295) Ophus, C. Four-dimensional Scanning Transmission Electron Microscopy (4D-STEM): From Scanning Nanodiffraction to Ptychography and Beyond. *Microscopy and Microanalysis* **2019**, *25* (3), 563-582.
(296) Savitzky, B. H.; Zeltmann, S. E.; Hughes, L. A.; Brown, H. G.; Zhao, S.; Pelz, P. M.; Pekin, T. C.; Barnard, E. S.; Donohue, J.; DaCosta, L. R. py4DSTEM: A Software Package for Four-dimensional Scanning Transmission Electron Microscopy Data Analysis. *Microscopy and Microanalysis* **2021**, *27* (4), 712-743.
(297) Zarea, M.; Ueki, H.; Sauls, J. Effects of Anisotropy and Disorder on the Superconducting Properties of Niobium. 2022; p arXiv:2201.07403.
(298) Sauls, J. A. personal communication. **July 28, 2023**.
(299) Zheng, K.; Kowsari, D.; Thobaben, N. J.; Du, X.; Song, X.; Ran, S.; Henriksen, E. A.; Wisbey, D. S.; Murch, K. W. Nitrogen Plasma Passivated Niobium Resonators for Superconducting Quantum Circuits. *Applied Physics Letters* **2022**, *120* (10).
(300) Kopas, C. J.; Lachman, E.; McRae, C. R. H.; Mohan, Y.; Mutus, J. Y.; Nersisyan, A.; Poudel, A. Simple Coplanar Waveguide Resonator Mask Targeting Metal-Substrate Interface. 2022; p arXiv:2204.07202.
(301) Khalil, M. S.; Stoutimore, M.; Wellstood, F.; Osborn, K. An Analysis Method for Asymmetric Resonator Transmission Applied to Superconducting Devices. *Journal of Applied Physics* **2012**, *111* (5), 054510.
(302) Probst, S.; Song, F.; Bushev, P. A.; Ustinov, A. V.; Weides, M. Efficient and Robust Analysis of Complex Scattering Data Under Noise in Microwave Resonators. *Review of Scientific Instruments* **2015**, *86* (2), 024706.
(303) Burnett, J.; Bengtsson, A.; Niepce, D.; Bylander, J. Noise and Loss of Superconducting Aluminium Resonators at Single Photon Energies. In *Journal of Physics: Conference Series*, 2018; IOP Publishing: Vol. 969, p 012131.
(304) de Graaf, S.; Faoro, L.; Burnett, J.; Adamyan, A.; Tzalenchuk, A. Y.; Kubatkin, S.; Lindström, T.; Danilov, A. Suppression of Low-frequency Charge Noise in Superconducting Resonators by Surface Spin Desorption. *Nature Communications* **2018**, *9* (1), 1143.
(305) Grundner, M.; Halbritter, J. On the Natural Nb_2O_5 Growth on Nb at Room Temperature. *Surface Science* **1984**, *136* (1), 144-154.
(306) Wang, X.; Bai, S.; Li, F.; Li, D.; Zhang, J.; Tian, M.; Zhang, Q.; Tong, Y.; Zhang, Z.; Wang, G. Effect of Plasma Nitriding and Titanium Nitride Coating on the Corrosion Resistance of Titanium. *The Journal of Prosthetic Dentistry* **2016**, *116* (3), 450-456.
(307) Zhussupbekov, K.; Walshe, K.; Bozhko, S. I.; Ionov, A.; Fleischer, K.; Norton, E.; Zhussupbekova, A.; Semenov, V.; Shvets, I. V.; Walls, B. Oxidation of Nb (110): Atomic Structure of the NbO Layer and its Influence on Further Oxidation. *Scientific reports* **2020**, *10* (1), 3794.

(308) Suresh, N.; Phase, D. M.; Gupta, A.; Chaudhari, S. M. Electron Density Fluctuations at Interfaces in Nb/Si Bilayer, Trilayer, and Multilayer Films: An X-ray Reflectivity Study. *Journal of Applied Physics* **2000**, *87* (11), 7946-7958. DOI: 10.1063/1.373479.
(309) Lowndes, D. H.; Geohegan, D.; Puretzky, A.; Norton, D.; Rouleau, C. Synthesis of Novel Thin-film Materials by Pulsed Laser Deposition. *Science* **1996**, *273* (5277), 898-903.
(310) Nico, C.; Monteiro, T.; Graça, M. P. Niobium Oxides and Niobates Physical Properties: Review and Prospects. *Progress in Materials Science* **2016**, *80*, 1-37.
(311) Pickett, M. D.; Medeiros-Ribeiro, G.; Williams, R. S. A Scalable Neuristor Built with Mott Memristors. *Nature Materials* **2013**, *12* (2), 114-117.
(312) Shapiro, S.; Axe, J.; Shirane, G.; Raccah, P. Neutron Scattering Study of the Structural Phase Transition in NbO_2. *Solid State Communications* **1974**, *15* (2), 377-381.
(313) Joshi, T.; Senty, T. R.; Borisov, P.; Bristow, A. D.; Lederman, D. Preparation, Characterization, and Electrical Properties of Epitaxial NbO_2 Thin Film Lateral Devices. *Journal of Physics D: Applied Physics* **2015**, *48* (33), 335308.
(314) Joshi, T.; Cirino, E.; Morley, S. A.; Lederman, D. Thermally Induced Metal-to-insulator Transition in NbO_2 Thin Films: Modulation of the Transition Temperature by Epitaxial Strain. *Physical Review Materials* **2019**, *3* (12), 124602.